Final Report

รายงานฉบับสมบูรณ์

Project Title Synthesis of Bis-N-heterocyclic carbene (NHC)-chelated palladium(II), nickel(II) complexes, and palldium(0) nanoparticles on silsesquioxane frameworks for C-C and C-S cross-coupling reactions

ชื่อโครงการ การสังเคราะห์สารประกอบเชิงซ้อนของโลหะพาลาเดียม นิกเกิล และ อนุภาคระดับนาโนเมตรของโลหะพาลาเดียม ด้วยสารประกอบ Bis-N-heterocyclic carbene ที่อยู่บนโครงสร้างสารประกอบ silsesquioxane สำหรับการเร่งปฏิกิริยา C-C และ C-S

By Associate Professor Dr. Vuthichai Ervithayasuporn

โดย รองศาสตราจารย์ ดร. วุฒิชัย เอื้อวิทยาศุภร

June 2019

มิถุนายน พ.ศ. 2562

Contract No. RSA5980018
สัญญาเลขที่ RSA5980018

Final Report
รายงานฉบับสมบูรณ์

Project Title Synthesis of Bis-N-heterocyclic carbene (NHC)-chelated palladium(II), nickel(II) complexes, and palldium(0) nanoparticles on silsesquioxane frameworks for C-C and C-S cross-coupling reactions

ชื่อโครงการ การสังเคราะห์สารประกอบเชิงซ้อนของโลหะพาลาเดียม นิกเกิล และ อนุภาคระดับนาโนเมตรของโลหะพาลาเดียม ด้วยสารประกอบ Bis-N-heterocyclic carbene ที่อยู่บนโครงสร้างสารประกอบ silsesquioxane สำหรับการเร่งปฏิกิริยา C-C และ C-S

Researcher (ผู้วิจัย)	Institute (สังกัด)
Associate Professor Dr. Vuthichai Ervithayasuporn	Mahidol University
รองศาสตราจารย์ ดร. วุฒิชัย เอื้อวิทยาศุภร	มหาวิทยาลัยมหิดล

This project granted by the Thailand Research Fund
สนับสนุนโดยสำนักงานกองทุนสนับสนุนการวิจัย

Abstract

Project Code : RSA5980018

Project Title : Synthesis of Bis-N-heterocyclic carbene (NHC)-chelated palladium(II), nickel(II) complexes, and palldium(0) nanoparticles on silsesquioxane frameworks for C-C and C-S cross-coupling reactions

Investigator : Associate Professor Dr. Vuthichai Ervithayasuporn

E-mail Address : vuthichai.erv@mahidol.edu

Project Period : 3 years (June 16, 2016 – June 15, 2019)

Abstract: The first part of this report focuses on the synthesis of polyhedral oligomeric silsesquioxanes (POSS), which can be used as a solid support to stabilize Palladium complexes and nanoparticles for a catalyst (Suzuki-Miyaura cross-coupling reaction, alcohol oxidation). Meanwhile, the functionalization of POSS (sulfonic acid, chiral pyrrolidinium) itself can be directly used as catalysts (ring-opening polymerization (ROP) of ε-caprolactone, asymmetric Michael addition, respectively) in green conditions (solventless).

The final part of this report, novel fluorescent small molecules were prepared to be used as a chemosensor to detect picric acid, fluoride, and cyanide. Meanwhile, polycyclic aromatic hydrocarbons conjugated silsesquioxane cages (SQ) can be synthesized *via* Heck reaction between bromo-derivatives (anthracene and pyrene) and octavinylsilsesquioxane (OVS) to obtain fluorescent SQs, which can be directly used to detect a fluoride sensor and even can distinguish each anion through changes of fluorescent color and intensity.

Keywords : Cage-rearrangement, Polyhedral Oligomeric Silsesquioxane, Nanocomposite, Nanoparticle, Palladium, Catalyst, Fluoride, Picric acid, Fluorescence, Anion, Sensor

บทคัดย่อ

รหัสโครงการ : RSA5980018

ชื่อโครงการ : การสังเคราะห์สารประกอบเชิงซ้อนของโลหะพาลาเดียม นิกเกิล และ อนุภาคระดับนาโนเมตรของโลหะพาลาเดียม ด้วยสารประกอบ Bis-N-heterocyclic carbene ที่อยู่บนโครงสร้างสารประกอบ silsesquioxane สำหรับการเร่งปฏิกิริยา C-C และ C-S

ชื่อนักวิจัย : รองศาสตราจารย์ ดร. วุฒิชัย เอื้อวิทยาศุภร มหาวิทยาลัยมหิดล

E-mail Address : vuthichai.erv@mahidol.edu

ระยะเวลาโครงการ : 3 ปี (16 มิ.ย. 2559 ถึง 15 มิ.ย. 2562)

งานวิจัยส่วนแรกนี้มุ่งเน้นไปที่การสังเคราะห์ สารประกอบ “ลูกผสม” หรือเรียกว่า polyhedral oligomeric silsesquioxanes (POSS) ซึ่งสามารถใช้เป็นของแข็งในการรองรับสารประกอบเชิงซ้อน หรืออนุภาคนาโนของโลหะพาลาเดียม เพื่อใช้ในการศึกษาเป็นตัวเร่งปฏิกิริยาแบบ Suzuki-Miyaura cross-coupling และ oxidation alcohol ในขณะเดียวกันได้มีการดัดแปลงหมู่ฟังก์ชันการทำงานของสารประกอบ POSS ให้เป็นกรดซัลโฟนิก หรือ ไพร์ริลิดิโนเนียม เพื่อสามารถนำมาใช้เป็นตัวเร่งปฏิกิริยาโดยตรง ได้แก่ การเกิดโพลีเมอไรเซชันแบบเปิดวงแหวน ของสารประกอบ ε-caprolactone และ การเร่งปฏิกิริยาไมเคิลแบบไม่สมมาตร ตามลำดับ ทำให้เกิดการเร่งปฏิกิริยาที่เป็นมิตรต่อสิ่งแวดล้อม เช่น ไม่มีการใช้ตัวทำละลายใดๆเลยระหว่างการเร่งปฏิกิริยาเคมี

ส่วนสุดท้ายของรายงานฉบับนี้ ยังได้มีการสังเคราะห์สารอินทรีย์แบบใหม่ที่มีโมเลกุลขนาดเล็ก และสามารถเปล่งแสงแบบฟลูออเรสเซนต์ใหม่ เพื่อทำให้เกิดการพัฒนาเป็นสารที่ใช้ตรวจวัดการปนเปื้อนของสสารอื่นๆด้วยตาเปล่า ได้แก่ การตรวจวัดกรดพิคริก ฟลูออไรด์ และไซยาไนด์ ในขณะเดียวกันได้พัฒนาโครงสร้างทางเคมีของสารประกอบ POSS โดยการนำสารประกอบโพลีไซคลิคอะโรมาติกไฮโดรคาร์บอน (จากอนุพันธ์แอนทราซีน และ ไพรีน) มาเชื่อมต่อกับโมเลกุล octavinylsilsesquioxane ด้วยปฏิกิริยาแบบ Heck แล้วจึงทำให้เกิดสารประกอบ POSS ชนิดใหม่ที่สามารถเปล่งแสงแบบฟลูออเรสเซนต์ได้ แล้วจึงมาประยุกต์ใช้ในการตรวจวัดทางเคมีเซ็นเซอร์ด้วยตาเปล่าของไอออนฟลูออไรด์ได้อย่างจำเพาะ รวมถึงยังสามารถนำสารประกอบที่สังเคราะห์ได้เหล่านี้มาใช้จำแนกประเภทของแอนไอออนชนิดต่างๆ จากการเปลี่ยนแปลงสีหรือความเข้มของแสงฟลูออเรสเซนต์

คำหลัก : การเปลี่ยนแปลงของกรง พอลิฮีดรอลโอลิโกเมอริกซิลเซสคิวออกเซน นาโนคอมโพสิท อนุภาคนาโน พาราเดียม ตัวเร่งปฏิกิริยา ฟลูออไรด์ กรดพิคริก ฟลูออเรสเซนต์ แอนไอออน เซ็นเซอร์

Final report content:

1. Abstract

The first part of this report focuses on the synthesis of polyhedral oligomeric silsesquioxanes (POSS), which can be used as a solid support to stabilize Palladium complexes and nanoparticles for a catalyst (Suzuki-Miyaura cross-coupling reaction, alcohol oxidation). Meanwhile, the functionalization of POSS (sulfonic acid, chiral pyrrolidinium) itself can be directly used as catalysts (ring-opening polymerization (ROP) of ε-caprolactone, asymmetric Michael addition, respectively) in green conditions (solventless).

The final part of this report, novel fluorescent small molecules were prepared to be used as a chemosensor to detect picric acid, fluoride, and cyanide. Meanwhile, polycyclic aromatic hydrocarbons conjugated silsesquioxane cages (SQ) can be synthesized *via* Heck reaction between bromo-derivatives and octavinylsilsesquioxane (OVS) to obtain a fluorescent SQ, which can be directly used to detect a fluoride sensor and even can distinguish in an anionic recognition.

2. Executive summary

One line of my previous research aimed to synthesize, isolate, and characterize novel silsesquioxane cages. Under this scope of basic chemistry, I have published 1 papers (*Dalton Trans.* **2016**, *45*, 16117) by using ^{1}H, ^{13}C and ^{29}Si Nuclear magnetic resonance (NMR) and single X-ray crystallography to identify a precise molecular structure of each pure product. Their high-resolution electrospray ionization mass spectrometry (HR ESI-MS) can be also used to confirm the exact molecular weight of our desired products.

In addition, my recent projects involved to use freshly prepared silsesesquioxane cages from projects mentioned above applying in catalytic application, especially using as a supporting material for stabilizing palladium complexes and nanoparticles for C-C coupling, alcohol oxidation, etc. under an environmental friendly (neat, water, ethanol as a solvent). By doing this project, X-ray photoelectron spectroscopy (XPS) is a key instrument to measure the elemental composition of desired catalysts, while solid-state NMR (SSNMR) spectroscopy can determine the molecular structure of silsesquioxane cages. Transmission electron microscopy (TEM) of desired catalysts can be also used to observe features and morphologies such as nanoparticles and nanoporous materials, while X-ray powder diffraction (XRD) is used for phase identification of a crystalline catalyst. In this application, I have published 4 papers (e.g. *Catal. Lett.* **2018**, *148*, 779; *ChemistrySelect* **2018**, *3*, 753.; *ACS Appl. Mater. Interfaces* **2017**, *9*, 12812; *ChemistrySelect* **2016**, *1*, 5353) Meanwhile, polymer-based silsesquioxane cages

can be prepared and published in *Polymer* **2017**, *108*, 173, which gel permeation chromatography (GPC) was used to measure the polydispersity index.

Importantly, my current projects also found some breakthrough to use silsesquioxane cages in supramolecular chemistry for the first time. In this application, silsesquioxane cages conjugated with fluorescent molecules were prepared, which the high molecular weight of desired product can be confirmed by matrix assisted laser desorption ionization-time of flight mass spectrometry (MALDI-TOF MS). In addition, UV-vis and fluorescent spectroscopies are the tools to study their photophysical properties of silsesquioxane cages through anionic sensing behavior. Finally, my supramolecular studies recently were reported in *Chem. Commun.* **2017**, *53*, 12108 and *Chem. Sci.* **2018**, *9*, 7753. Meanwhile, small organic molecule of imidazolylmethylpyrene as a chemosensor can be found to selectively detect the picric acid and other anions by a change of fluorescence and naked-eye color, published in (*Sens. Actuators B Chem.* **2017**, *245*, 665; *Journal of Photochemistry and Photobiology A: Chemistry* **2018**, *358*, 215)

3. Objective

3.1 To study base catalyzed-silsesquioxane cages formation.

3.2 To prepare and study a catalytic activity of silsesquioxane cages-based nanocatalysts for ring-opening polymerization of Ɛ-caprolactone, alcohol oxidation, Suzuki-Miyaura cross-coupling reaction.

3.3 To prepare silsesquioxane cages-based fluorescent materials and their sensing applications

4. Research methodology

Project 1

Synthesis and isolation of non-chromophore cage-rearranged silsesquioxanes from base-catalyzed reactions

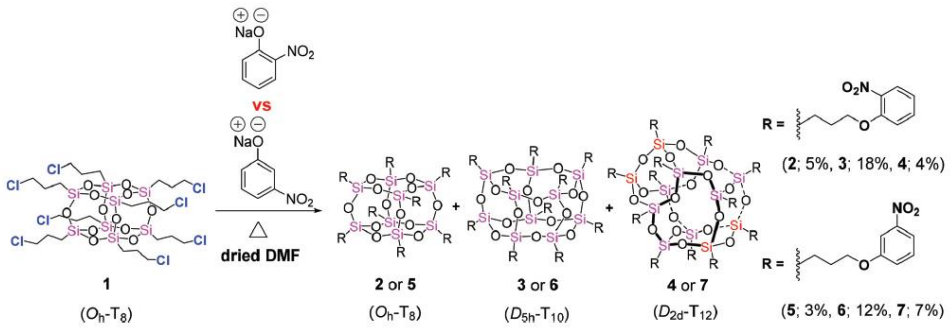

Scheme 1 Comparative reactivity of nucleophiles towards compound 1 (T_8) resulting in full incorporation of *ortho*- and *meta*-oxynitrobenzene functions in POSS, leading to (a) compounds 2–4 (100 °C, 1 day, 0.129 mol L^{-1} 1, 1.7 equiv. of 2-nitrophenol sodium salt/$RSiO_{3/2}$) and (b) compounds 5–7 (70 °C, 1 day, 0.129 mol L^{-1} 1, 1.5 equiv. of 3-nitrophenol sodium salt/$RSiO_{3/2}$), respectively.

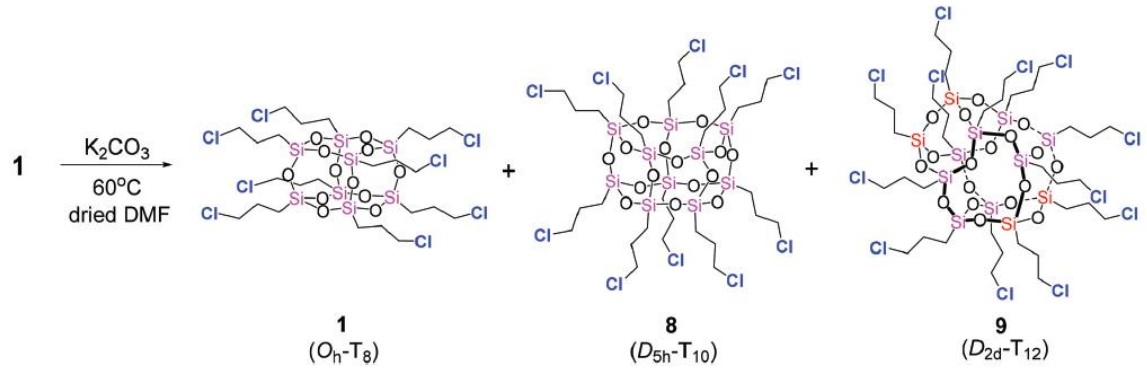

Scheme 2 Cage-rearrangement on exposure of compound 1 (T_8) to a base leading to a mixture of octa-, deca-, and dodecameric silsesquioxanes (T_8, T_{10}, and T_{12}).

The nucleophilicity of both *ortho*- and *meta*-nitrophenolate anions is strong enough to give substituted products, but their basicity also facilitates cage-rearrangement reactions in polyhedral oligomeric silsesquioxanes (POSS). Anions having a stronger basicity, but weaker nucleophilicity, such as CO_3^{2-}, gave products only from cage-rearrangement, with the cage expansion products being isolable in multi-gram quantities using conventional column chromatography.

Project 2

Solid–state Synthesis of Polyhedral Oligomeric Silsesquioxane-Supported N-Heterocyclic Carbenes/Imidazolium salts on Palladium Nanoparticles: Highly Active and Recyclable Catalyst

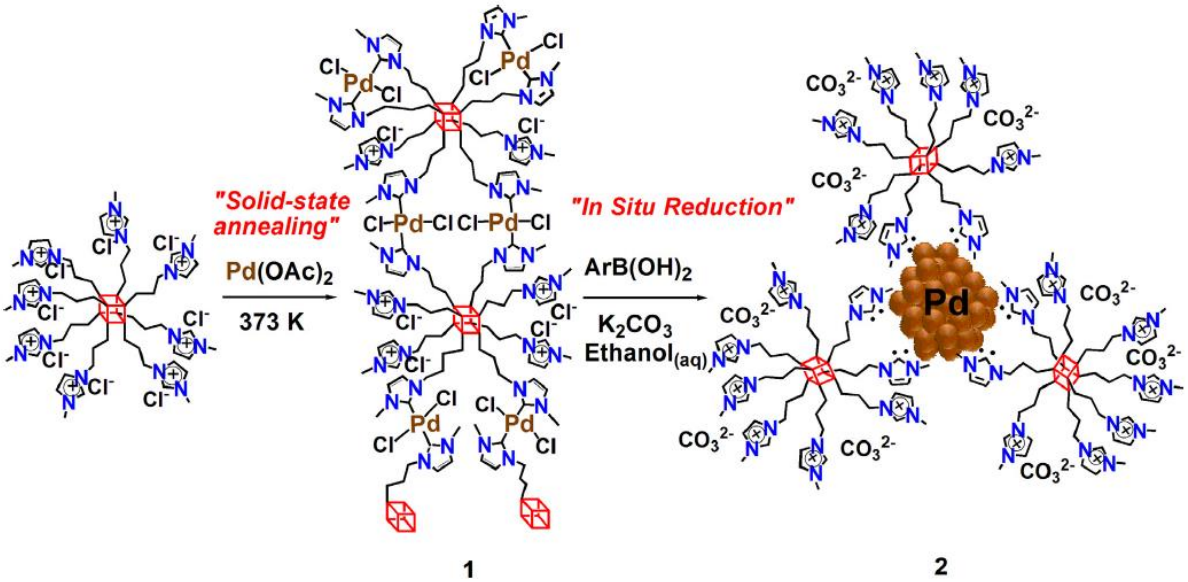

Scheme 1. Solvent-free synthesis of Pd(II)-MPIm-POSS composite (1) and a subsequent reduction to fabricate Pd(0)-nano-POSS nanocomposite (2) (red cube: POSS).

We describe a novel and green synthetic methodology for the fabrication of polyhedral oligomeric silsesquioxane-supported N-heterocyclic carbenes/imidazolium salts on palladium(II) complexes; Pd(II)-MPIm-POSS (**1**) composite by solid-state annealing between $Pd(OAc)_2$ and octakis(3-(1-methylimidazolium)propyl) octasilsesquioxane without added base. Subsequently, arylboronic acid based in situ or ex situ reduction of 1 in aqueous ethanol produces polyhedral oligomeric silsesquioxane supported N-heterocyclic carbenes/imidazolium salts on palladium nanoparticles; Pd(0)-nano-POSS (**2**) composite, consisting of monodispersed and N-heterocyclic carbene (NHC) stabilized Pd nanoparticles of very small size (3.0 ± 1.5 nm). Nanocatalyst **2** is a highly efficient and easily recyclable homogeneous catalyst for Suzuki-Miyaura cross-coupling reactions with TOF up to 1670 h^{-1}.

Project 3

Polyhedral oligomeric silsesquioxane (POSS) containing sulfonic acid groups as a metal-free catalyst to prepare polycaprolactone

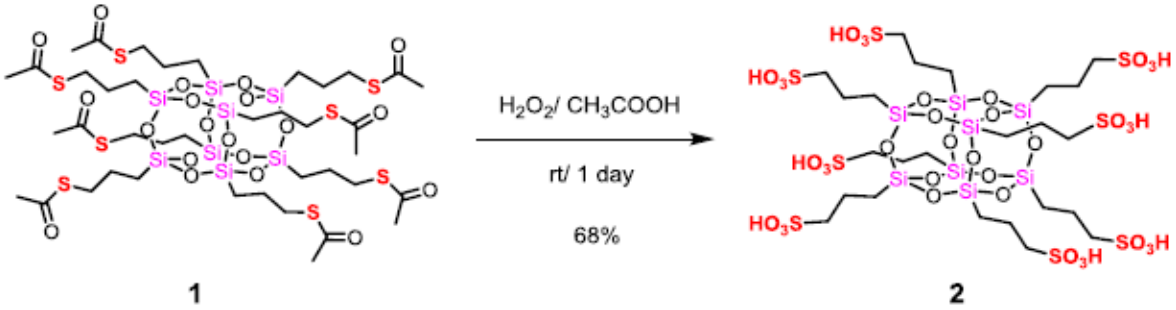

Scheme 1. Synthesis of octakis(3-sulfopropyl)octasilsesquioxane (**2**) *via* oxidation reaction.

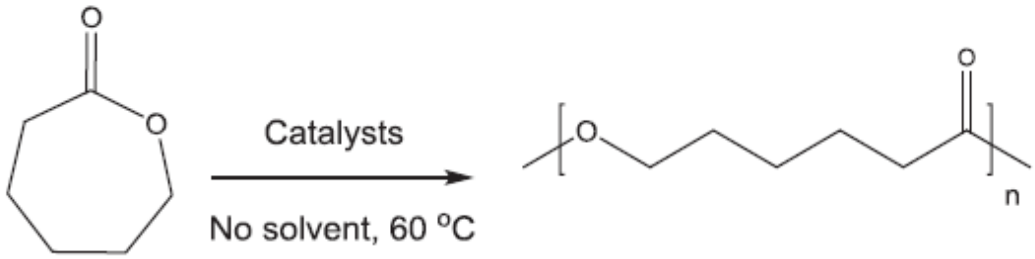

Scheme 2. Acid-catalyzed polymerization of ε-caprolactone using POSS **2**, amberlyst® 15, and zeolite Y, hydrogen as a catalyst.

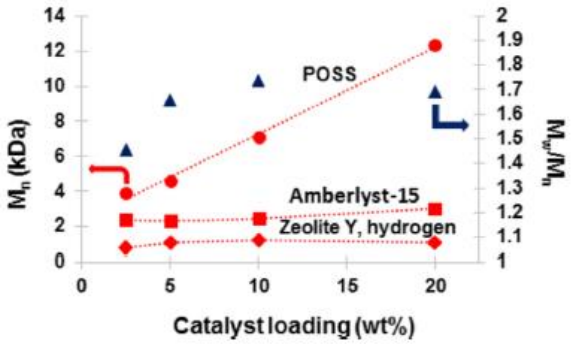

Fig. 3. Plot of number average molecular weight (M_n) (red labels) and PDI (blue triangles) versus catalyst loading of POSS (red circles), amberlyst® 15 (red squares), and zeolite Y, hydrogen (red diamond) in ε-caprolactone monomer for the synthesis of polycaprolactone (see Scheme 2). (For interpretation of the references to colour in this figure legend, the reader is referred to the web version of this article.)

Organic-inorganic hybrid nano-building block of polyhedral oligomeric silsesquioxane (POSS) containing hyperbranched sulfonic acid groups was easily prepared within a day through oxidation reaction at room temperature. The desired product was fully characterized by ^{1}H, $^{13}C\{^{1}H\}$ NMR, ^{29}Si CP/MAS NMR, FT-IR spectroscopy, and TGA-DSC analysis, confirming the complete formation of sulphonic acids while retaining the cubic structure of silsesquioxanes cage. Furthermore, the proton exchange capacities of POSS catalyst were determined to be 5.39 meq of H^{+}/g, much greater than any previous silicon-based materials, leading to the catalytic preparation of polycaprolactone with well-controlled polymerization under the metal-free system and without the addition of any co-catalysts and solvents.

Project 4

Tunable Porosity of Cross-Linked-Polyhedral Oligomeric Silsesquioxane Supports for Palladium-Catalyzed Aerobic Alcohol Oxidation in Water

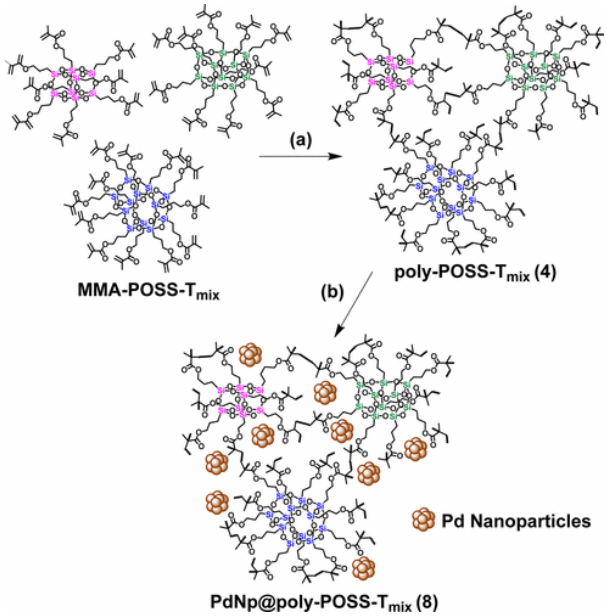

Scheme 1. A representative example for the synthesis of poly-POSS-T_{mix} (**4**) and PdNp@poly-POSS-T_{mix} (**8**).

We have recently prepared and isolated methyl methacrylate-functionalized-POSS (MMA-POSS-T_n) monomers in pure form of T_8, T_{10}, and T_{12} cages (Scheme 1). Our findings show a relationship between the chemical structure of each pure silsesquioxane cage and its physical properties. Particularly, the packing of cubic T_8 structure of MMA-POSS-T_8 led to highly crystalline materials, whereas the other MMA-POSS-T_{10} and T_{12} packed less efficiently and were amorphous. Moreover, those compounds can be used as a comonomer to prepare various types of polymer–silsesquioxane hybrid nanocomposites. Despite these studies, differences in properties of the resulting polymers obtained from using pure forms of POSS-T_n have not been explored nor taken into consideration in any previous studies. Herein, we prepare a series of novel POSS-based porous materials from free radical polymerization of pure MMA-POSS-T_n (n = 8, 10, 12) and MMA-POSS-T_{mix} monomers. Also, for the first time, the effects of POSS cage sizes on physical properties including porosity, surface areas, thermal properties, and catalytic activities toward Pd-catalyzed aerobic alcohol oxidation in water are evaluated as shown in Table 1.

Table 1. Substrate Scope for Aerobic Alcohol Oxidation Catalyzed by PdNp@poly-POSS-T_{mix} (**8**) in Water[a]

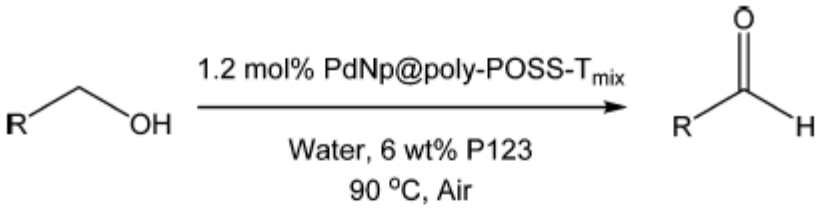

entry[a]	R–	time (h)	yield (%)[b]
1[c]	C_6H_5–	6	>99
2[c]	4-HOC_6H_4–	6	>99
3	2-$CH_3OC_6H_4$–	6	70
4	3-$CH_3OC_6H_4$–	6	90
5	4-$CH_3OC_6H_4$–	6	81
6	$C_6H_5CH{=}CH$–	6	95
7[d]	4-$NO_2C_6H_4$–	96	91
8[d]	4-BrC_6H_4–	48	88
9[d]	2-furyl–	6	94

[a]Reaction conditions: 0.50 mmol of RCH_2OH, 2.0 mL of H_2O with P123 (6 wt %, 0.12 g), 1.2 mol % Pd (14 mg of **8**) at 90 °C with air bubbling. [b]GC yield. [c]0.43 mol % Pd (5.2 mg of **8**). [d]With 1 equiv of K_2CO_3 additive.

In conclusion, polymeric POSS-based porous materials, poly-POSS-T_n [*n* = 8 (**1**), 10 (**2**), 12 (**3**), and mix (**4**)], were prepared *via* free radical polymerization from the corresponding pure forms of MMA-POSS-T_n (*n* = 8, 10, 12) and the mixture form (*n* = mix). BET analysis revealed that POSS cage sizes exert a significant effect on polymer surface areas and porosities, as poly-POSS-T_{12} (**3**) possesses the highest surface areas, pore volumes, and also amount of mesopores, as compared to other poly-POSS-T_n. Interestingly, although these differences show no effect on Pd nanoparticles stabilization, they have an influence on the catalytic activities toward Pd-catalyzed aerobic alcohol oxidation. In particular, due to higher surface areas, pore volumes, and amount of mesopores, PdNp@poly-POSS-T_n [*n* = 10 (**6**), 12 (**7**), and mix (**8**)] were more effective heterogeneous oxidation catalysts than PdNp@poly-POSS-T_8 (**5**) in the P123/water medium. In addition, the substrate scope study revealed that electron-rich benzyl alcohol derivatives were more readily oxidized than the related electron-withdrawing substrates. Catalyst **8** can also be reused for at least five reaction cycles without a significant loss in activities.

This work, for the first time, provides insights into the effects of POSS cage sizes on POSS-based polymer properties and consequently their efficiency as catalyst supports for Pd-catalyzed aerobic alcohol oxidation. These findings should pave a way for the preparation of POSS-based materials for stabilization of metal nanoparticles. Efforts to include other stabilizing functional groups at the POSS organic linkers and investigation of different catalytic reactions are ongoing in our laboratory.

Project 5

Heterogeneous Pd/POSS Nanocatalysts for C–C Cross-Coupling Reactions

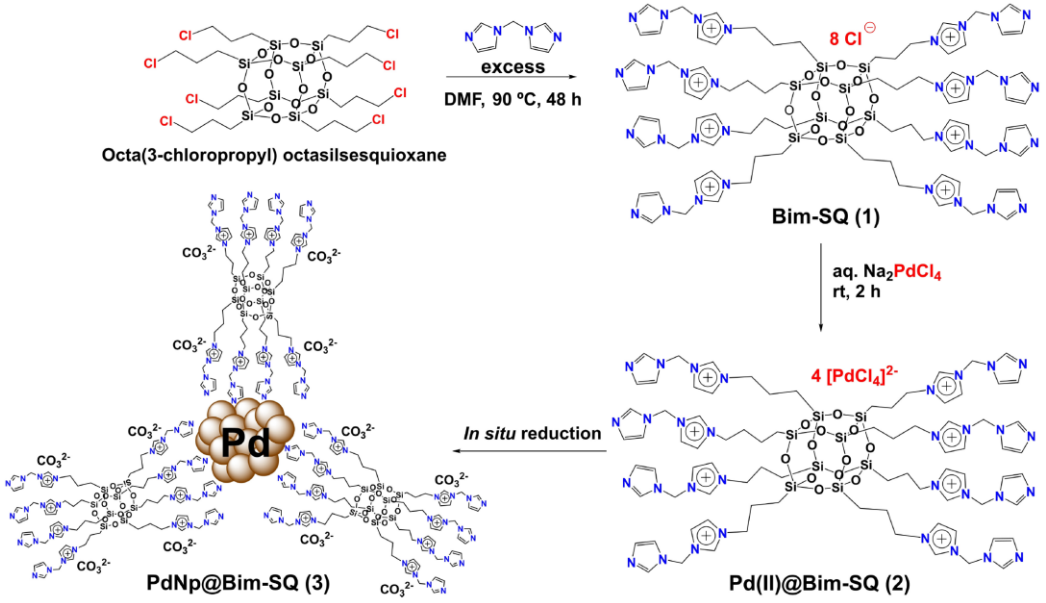

Scheme 1. Synthetic approach to prepare Bim-SQ (**1**), the pre-catalyst of Pd(II)@Bim-SQ (**2**), and PdNp@Bim-SQ (**3**).

An insoluble solid support of N-heterocyclic imidazoliumfunctionalized cage-like silsesquioxane (SQ); Bim-SQ, was synthesized by nucleophilic substitution of octakis(3-chloropropyl)octasilsesquioxane with an excess bis-(imidazol-1-yl)methane and investigated as a new organic-inorganic hybrid support. In the presence of Bim-SQ, Pd(II) from $[PdCl_4]^{2-}$ can be stabilized via both electrostatic interactions and imidazole-Ncoordination, giving an amorphous material of Pd(II)@Bim-SQ. Subsequent in situ reduction of Pd(II)@Bim-SQ during Suzuki-Miyaura cross-coupling reactions afforded monodispersed Pd nanoparticles (2.33 $\pm$ 1.50 nm) stablized on Bim-SQ support, PdNp@Bim-SQ with Pd loading up to 14% w/w. Catalytic studies revealed that the pre-catalyst Pd(II)@Bim-SQ was active heterogeneous catalyst for Suzuki-Miyaura cross-coupling reactions, having the maximum TOFs of 5400 h^{-1} under mild conditions and in aqueous ethanol medium. Furthermore, PdNp@Bim-SQ was also shown to be an efficient catalyst for Heck reactions. Simple catalyst recovery and reusability of PdNp@Bim-SQ for at least 5 catalytic cycles without loss of activity were also demonstrated.

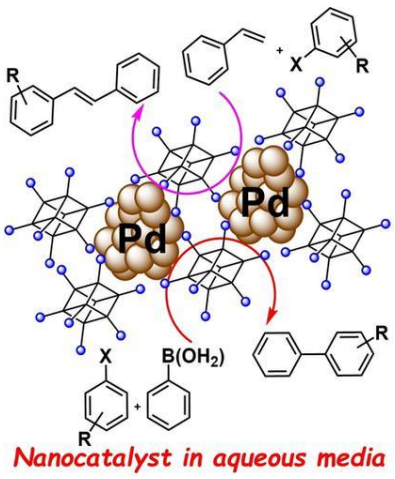

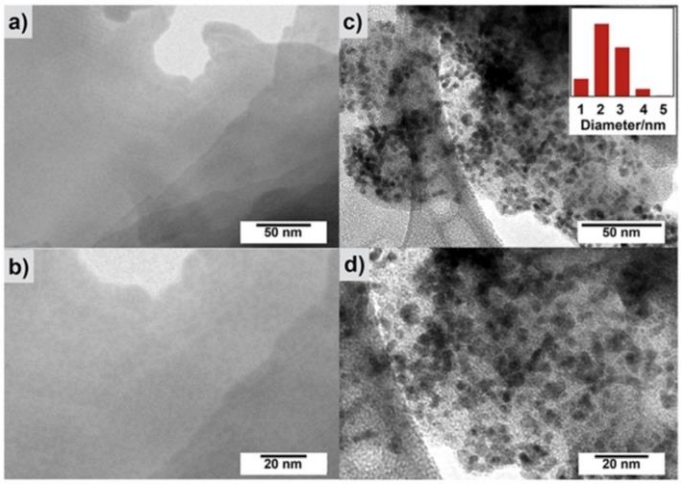

Project 6

Chiral Pyrrolidine Bridged Polyhedral Oligomeric Silsesquioxanes as Heterogeneous Catalysts for Asymmetric Michael Additions

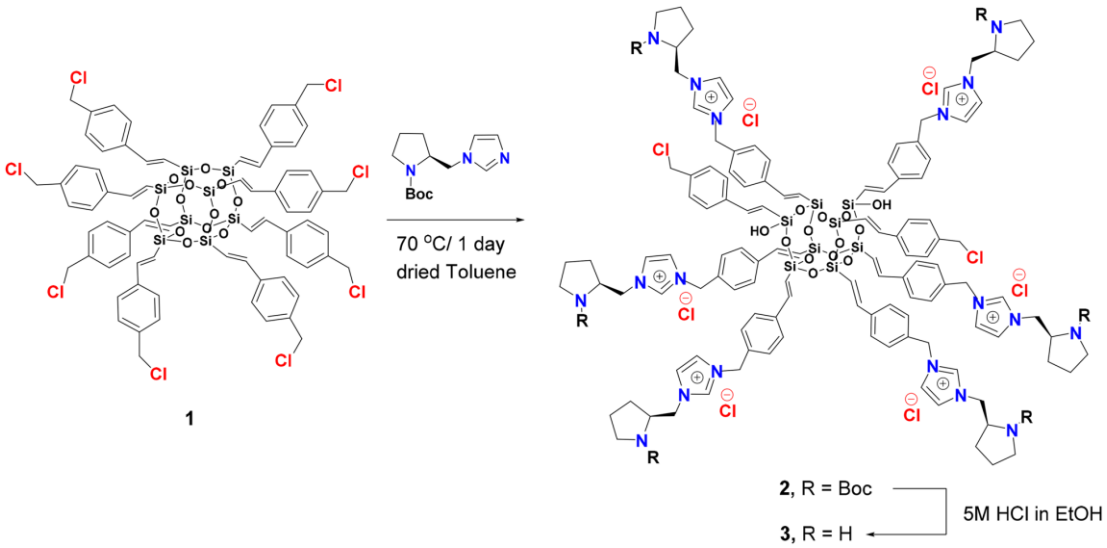

Scheme 1 Synthesis of a chiral pyrrolidine bridged polyhedral oligomeric SQ, the SQ supported catalyst (**3**)

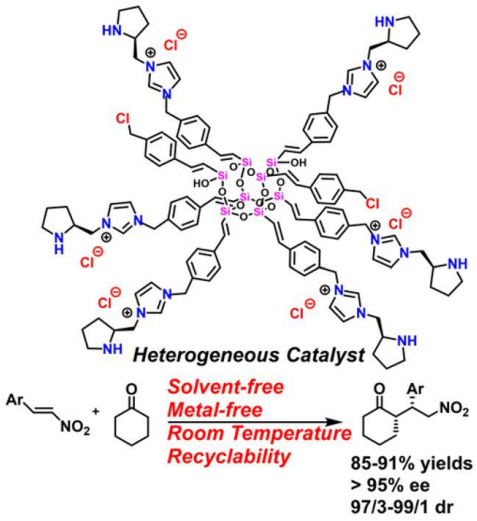

A chiral pyrrolidine bridged polyhedral oligomeric silsesquioxane (SQ) was synthesized, characterized, and used as an effective heterogeneous catalyst. The synthesis involves two simple steps: nucleophilic substitution between benzylchloride functionalized SQ and imidazoyl pyrrolidine carboxylate and subsequent deprotection. The catalyst was isolated by simple filtration. The SQ-supported chiral pyrrolidine catalyst was used as a heterogeneous catalyst in an asymmetric Michael addition into nitrostyrenes under room temperature and neat condition, giving the product in excellent yields (85–91%), diastereoselectivities (up to 99:1) and enantioselectivities (95–98%). The catalyst can be recycled by a simple filtration without a significant loss in its reactivity and selectivity.

Project 7

Silsesquioxane Cages as Fluoride Sensors

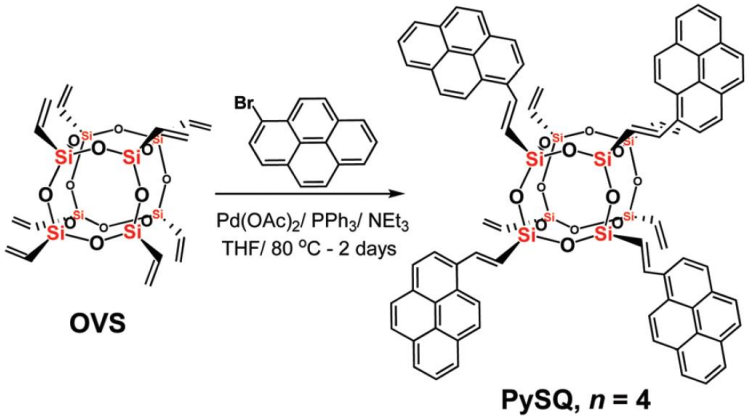

Scheme 1 Synthesis of a pyrene functionalized-silsesquioxane cage (PySQ) *via* the Heck reaction.

Herein, pyrene functionalized silsesquioxane cages (PySQ) were successfully synthesized, which can provide different fluorescence properties depending on the polarity of the solvent. For example, PySQ in DMSO potentially generates a significant fluorescence of the pyrene–pyrene excimer through space, while p–p* fluorescence emission of PySQ in THF can be dominant. Upon the addition of the fluoride ion, the highly negatively charged F^- was pulled into the confined silsesquioxane cage through the electrostatic interactions of electron deficient elements (i.e., silicon). Subsequently, the fluoride ion was centralized within a silsesquioxane cage, which can also compress the cage. Therefore, fluorescence responses of PySQ to F^- in DMSO and THF can also be used to detect the fluoride ion by turning the fluorescence ON–OFF and OFF–ON, respectively, including detection by the naked eye.

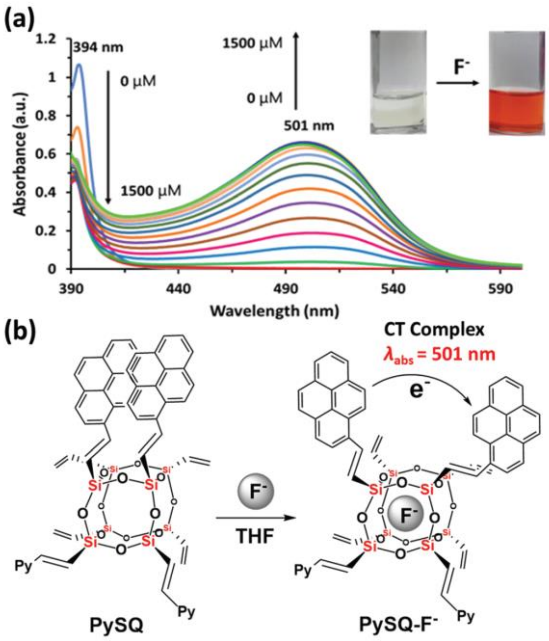

Project 8

Anion identification using silsesquioxane cages

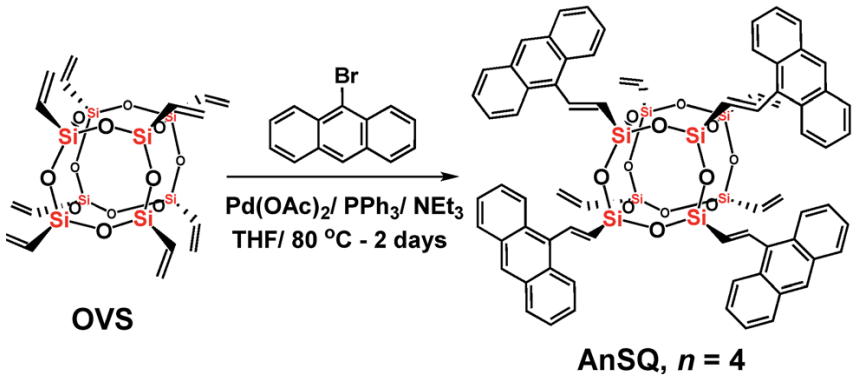

Scheme 1 Synthesis of anthracene-conjugated octameric silsesquioxane (AnSQ) cages.

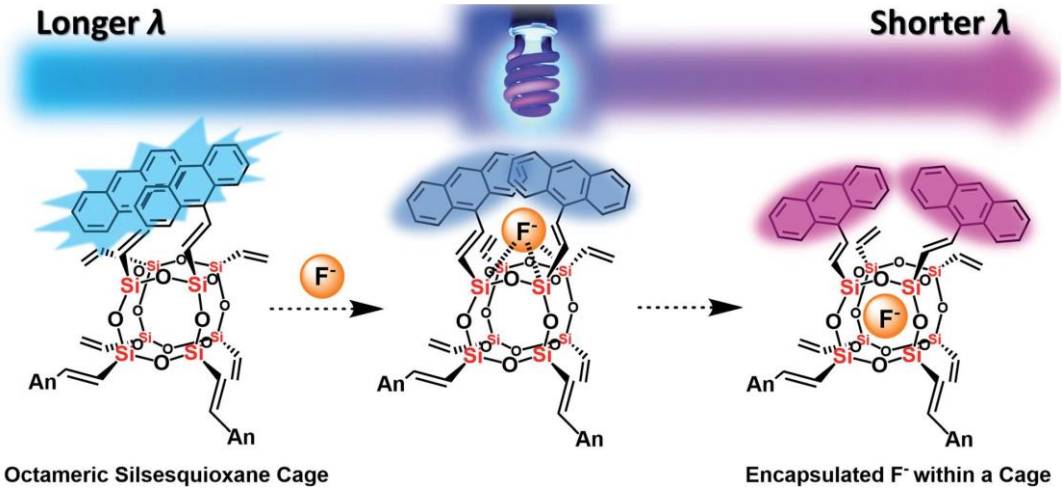

Anthracene-conjugated octameric silsesquioxane (AnSQ) cages, prepared via Heck coupling between octavinylsilsesquioxane (OVS) and 9-bromoanthracene, thermodynamically display intramolecular excimer emissions. More importantly, these hosts are sensitive to each anionic guest, thereby resulting in change of anthracene excimer formation, displaying the solvent-dependent fluorescence and allowing us to distinguish up to four ions such as F^-, OH^-, CN^- and PO_4^{3-} by fluorescence spectroscopy. Depending on the solvent polarity, for example, both F^- and CN^- quenched the fluorescence emission intensity in THF, but only F^- could enhance the fluorescence in all other solvents. The presence of PO_4^{3-} results in fluorescence enhancements in high polarity solvents such as DMSO, DMF, and acetone, while OH^- induces enhancements only in low polarity solvents (e.g. DCM and toluene). A picture of the anion recognizing ability of AnSQ was obtained through principal component analysis (PCA) with NMR and FTIR confirming the presence of host–guest interactions. Computational modeling studies demonstrate the conformation of host–guest complexation and also the change of excimer formation. Detection of F^-, CN^- and OH^- by AnSQ hosts in THF is noticeable with the

naked eye, as indicated by strong color changes arising from charge transfer complex formation upon anion addition.

Project 9

Green synthesis of fluorescent N,O-chelating hydrazone Schiff base for multi-analyte sensing in Cu^{2+}, F^{-} and CN^{-} ions

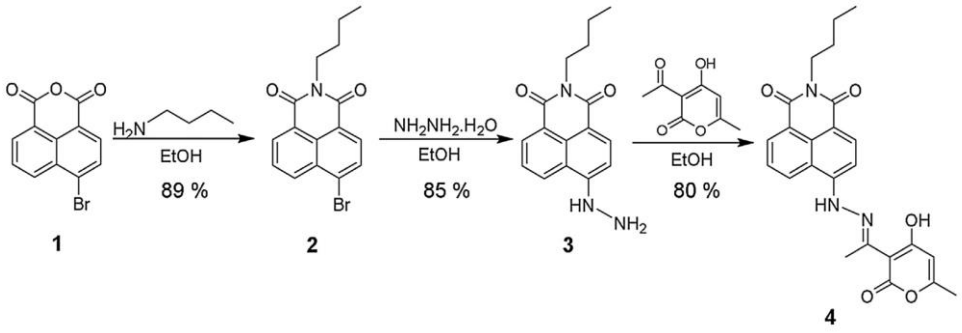

Scheme 1. Synthetic approach to prepare the hydrazone Schiff base of chemosensor **4** derived from 1,8-naphthalimide and dehydroacetic acid.

A colorimetric and fluorometric hydrazone Schiff's base derived from dehydroacetic acid by three-stepsand high-yield syntheses under green approach employing ethanol as a solvent has been prepared. Multi-analyte sensing for both metal cation (Cu^{2+}) and anions (F^{-} and CN^{-}), with high sensitivity andcompetitive selectivity, was encountered. The sensing mechanism of anion detection found to bedeprotonation of N-H and O-H moieties in the presence of ions. However, metal cation like copper(II)ions chelation with sensor, leads to diminish intra-molecular charge transfer (ICT) with chelation inducedquenching of fluorescence (CHQF). Contrary, anionic interaction ensued in heightened ICT as well asphoto-induced electron transfer (PET) processes. The Job's plots interpretation rendered stoichiometry of 2:1 with Cu2+/F- and 1:1 with CN^{-}. Moreover, the detection limits of 0.962 ppm (Cu^{2+}), 0.023 ppm (F-)and 0.073 ppm (CN^{-}) were much lower than WHO guidelines. Further, either water or methanol wasemployed to differentiate F^{-}/CN^{-} ions with sensor in THF, with prominent visible naked eye and fluorometric responses.

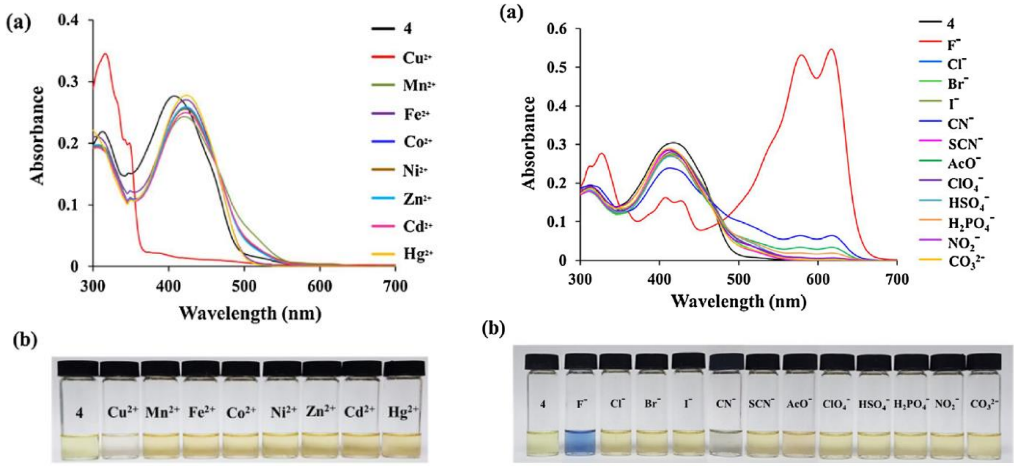

Project 10

Imidazolylmethylpyrene sensor for dual optical detection of explosive chemical: 2,4,6-Trinitrophenol

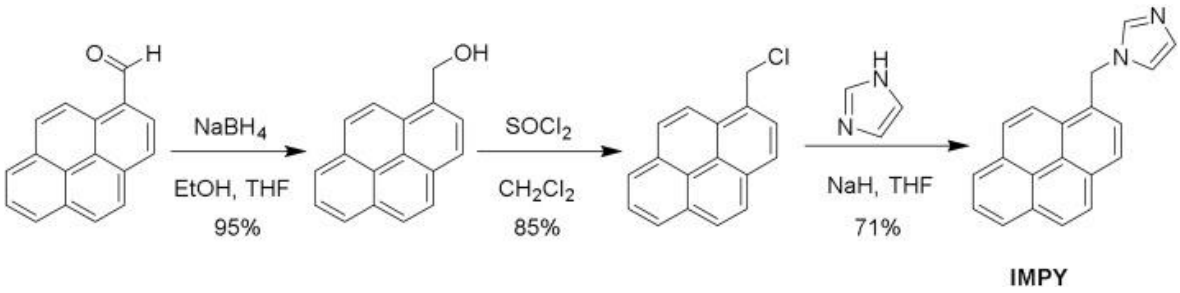

Scheme 1. Synthetic approach to prepare 1-imidazolylmethylpyrene (**IMPY**).

Herein, we found that the designed sensor of 1-imidazolylmethylpyrene (**IMPY**) as shown in Scheme 1 could be used as a **PA** fluorescent chemosensor and could be operated through both enhancement and quenching of fluorescence by simply switching the solvent systems. Importantly, the sensor exhibited high selectivity and sensitivity to **PA** and also exhibited chromogenic change from colorless to yellow in the presence of PA. Therefore, the developed sensor could also serve as a “naked-eye” indicator.

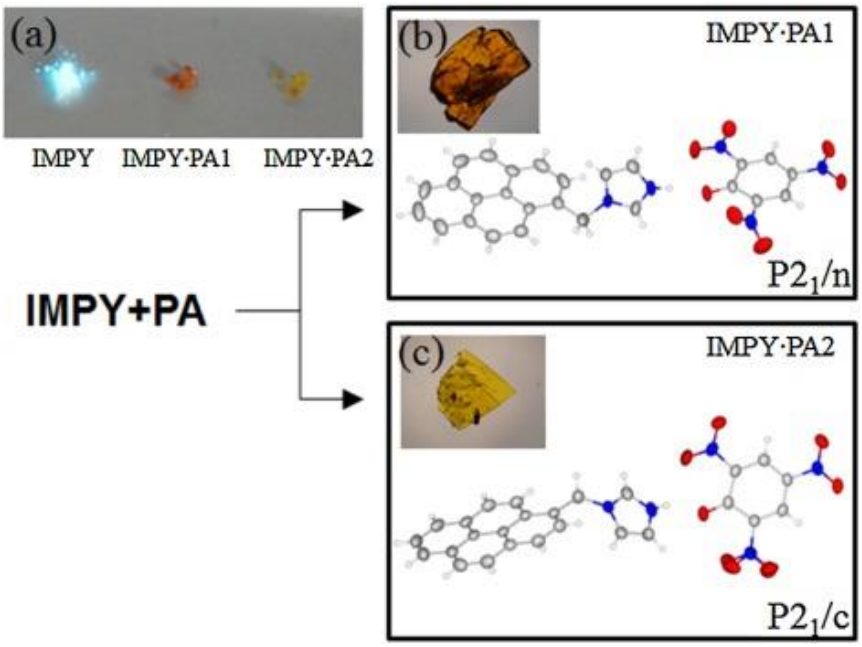

Fig 1. (a) Photos of IMPY, IMPY·PA1 and IMPY·PA2 under UV lamp (λ = 366 nm), X-ray structures of host-guest complexes of IMPY·PA in (b) $P2_1/n$ and (c) $P2_1/c$ space groups.

Single-crystal X-ray diffraction of co-crystalline structures of **IMPY** and picric acid complexes revealed a host-guest complex of 1:1 (Fig. 1). The appearance of orange and yellow crystals was formed during the slow evaporation of methanol (Figs. 1). The nitrogen atoms of imidazole groups on **IMPY** in both crystal structures exhibited the protonation in cation form, while picric acid was deprotonated into a picrate anion. Consequently, the nitrogen of **IMPY** was switched from H-bond acceptor into donor, while picrate anion was transformed into H-bond acceptor. The X-ray crystal structures affirmed the formation of hydrogen bond between protonated **IMPY** and deprotonated form of picric acid.

In conclusion, we have successfully found a new type of fluorescent sensor, **IMPY**, for 2,4,6-trinitrophenol or picric acid (**PA**) detection based on 1-imidazolylmethylpyrene. To confirm highly interactive affinity of the sensor molecule to picric acid, two different types of crystal structures of **IMPY·PA** complexes were successfully recrystallized and characterized. Sensor **IMPY** exhibited high sensitivity and selectivity toward picric acid over a wide range of phenolic compounds due to the presence of H-bondings and π-π interactions. Not only, **IMPY** sensor could be operated *via* both OFF–ON and ON–OFF responses, but also exhibited the chromogenic change by changing the color of the solution from colorless to yellow, which could be noticeable by the naked eye. The designed sensor reported here has several advantages in terms of synthetic simplicity, economical cost of starting materials which make it possible for commercial uses, high sensitivity and selectivity to picric acid which will be benefit for on-site detection of this powerful explosive chemical.

5. Result

The first part of this report focuses on the synthesis of polyhedral oligomeric silsesquioxanes (POSS), which can be used as a solid support to stabilize Palladium complexes and nanoparticles for a catalyst (Suzuki-Miyaura cross-coupling reaction, alcohol oxidation). Meanwhile, the functionalization of POSS (sulfonic acid, chiral pyrrolidinium) itself can be directly used as catalysts (ring-opening polymerization (ROP) of Ɛ-caprolactone, asymmetric Michael addition, respectively) in green conditions (solventless).

The final part of this report, novel fluorescent small molecules were prepared to be used as a chemosensor to detect picric acid, fluoride, and cyanide. Meanwhile, polycyclic aromatic hydrocarbons conjugated silsesquioxane cages (SQ) can be synthesized *via* Heck reaction between bromo-derivatives (anthracene and pyrene) and octavinylsilsesquioxane (OVS) to obtain fluorescent SQs, which can be directly used to detect a fluoride sensor and even can distinguish each anion through changes of fluorescent color and intensity.

6. Conclusion and Discussion

One line of my previous research aimed to synthesize, isolate, and characterize novel silsesquioxane cages. Under this scope of basic chemistry, I have published 1 papers (*Dalton Trans.* **2016**, *45*, 16117) by using ^{1}H, ^{13}C and ^{29}Si Nuclear magnetic resonance (NMR) and single X-ray crystallography to identify a precise molecular structure of each pure product. Their high-resolution electrospray ionization mass spectrometry (HR ESI-MS) can be also used to confirm the exact molecular weight of our desired products.

In addition, my recent projects involved to use freshly prepared silsesesquioxane cages from projects mentioned above applying in catalytic application, especially using as a supporting material for stabilizing palladium complexes and nanoparticles for C-C coupling, alcohol oxidation, etc. under an environmental friendly (neat, water, ethanol as a solvent). By doing this project, X-ray photoelectron spectroscopy (XPS) is a key instrument to measure the elemental composition of desired catalysts, while solid-state NMR (SSNMR) spectroscopy can determine the molecular structure of silsesquioxane cages. Transmission electron microscopy (TEM) of desired catalysts can be also used to observe features and morphologies such as nanoparticles and nanoporous materials, while X-ray powder diffraction (XRD) is used for phase identification of a crystalline catalyst. In this application, I have published 4 papers (e.g. *Catal. Lett.* **2018**, *148*, 779; *ChemistrySelect* **2018**, *3*, 753.; *ACS Appl. Mater. Interfaces* **2017**, *9*, 12812; *ChemistrySelect* **2016**, *1*, 5353) Meanwhile, polymer-based silsesquioxane cages can be prepared and published in *Polymer* **2017**, *108*, 173, which gel permeation chromatography (GPC) was used to measure the polydispersity index.

Importantly, my current projects also found some breakthrough to use silsesquioxane cages in supramolecular chemistry for the first time. In this application, silsesquioxane cages conjugated with fluorescent molecules were prepared, which the high molecular weight of desired product can be confirmed by matrix assisted laser desorption ionization-time of flight mass spectrometry (MALDI-TOF MS). In addition, UV-vis and fluorescent spectroscopies are the tools to study their photophysical properties of silsesquioxane cages through anionic sensing behavior. Finally, my supramolecular studies recently were reported in *Chem. Commun.* **2017**, *53*, 12108 and *Chem. Sci.* **2018**, *9*, 7753. Meanwhile, small organic molecule of imidazolylmethylpyrene as a chemosensor can be found to selectively detect the picric acid and other anions by a change of fluorescence and naked-eye color, published in (*Sens. Actuators B Chem.*

2017, *245*, 665; *Journal of Photochemistry and Photobiology A: Chemistry* **2018**, *358*, 215)

7. Appendix

8. Output (Acknowledge the Thailand Research Fund)

8.1 International Journal Publication

1. Mohapatra, S.; Chaiprasert, T.; Sodkhomkhum, R.; Kunthom, R.; Hanprasit, S.; Sangtrirutnugul, P.; **Ervithayasuporn, V.*** *ChemistrySelect* **2016**, *1*, 5353-5357.
2. Hanprasit, S.; Tungkijanansin, N.; Prompawilai, A.; Eangpayunga, S.; **Ervithayasuporn, V.*** *Dalton Trans*. **2016**, *45*, 16117-16120.
3. Kunthom, R.; Jaroentomeechai, T.; **Ervithayasuporn, V.*** *Polymer* **2017**, *108*, 173-178.
4. Sangtrirutnugul, P.; Chaiprasert, T.; Hunsiri, W.; Jitjaroendee, T.; Songkhum, P.; Laohhasurayotin, K.; Osotchan, T. and **Ervithayasuporn, V.*** *ACS Appl. Mater. Interface* **2017**, *9*, 12812-12822**.**
5. Sodkhomkhum, R.; Masik, M.; Watchasit, S.; Suksai, C.; Boonmak, J.; Youngme, S.; Wanichacheva, N.; **Ervithayasuporn, V.*** *Sens. Actuators B: Chem.* **2017**, *245*, 665–673.
6. Chanmungkalakul, S.; **Ervithayasuporn, V.***; Hanprasit, S.; Masik, M.; Prigyai, N.; Kiatkamjornwong, S. *Chem. Commun*., **2017**, *53*, 12108.
7. Somjit, V.; Man, M.W.C.; Ouali, A.; Sangtrirutnugul, P.; **Ervithayasuporn, V.*** *ChemistrySelect*, **2018**, *3*, 753–759.
8. Saini, N.; Prigyai, N.; Wannasiri, C.; **Ervithayasuporn, V.***; Kiatkamjornwong, S. *Journal of Photochemistry and Photobiology A: Chemistry* **2018**, *358*, 215–225.
9. Luanphaisarnnont, T.; Hanprasit, S.; Somjit, V.; **Ervithayasuporn, V.*** *Catal. Lett.* **2018**, *148*, 779-786.
10. Chanmungkalakul, S.; **Ervithayasuporn, V.***; Boonkitti, P.; Phuekphong, A.; Prigyai, N.; Kladsomboon, S.; Kiatkamjornwong, S. *Chem. Sci.* **2018**, *9*, 7753-7765.

8.2 Application

8.3 Others e.g. national journal publication, proceeding, international conference, book chapter, patent

ChemPubSoc Europe

DOI: 10.1002/slct.201600878

Chemistry SELECT Communications

Materials Science inc. Nanomaterials & Polymers

Solid–state Synthesis of Polyhedral Oligomeric Silsesquioxane-Supported N-Heterocyclic Carbenes/Imidazolium salts on Palladium Nanoparticles: Highly Active and Recyclable Catalyst

Sudip Mohapatra, Thanawat Chaiprasert, Rapheepraew Sodkhomkhum, Rungthip Kunthom, Sasikarn Hanprasit, Preeyanuch Sangtrirutnugul, and Vuthichai Ervithayasuporn*[a]

We describe a novel and green synthetic methodology for the fabrication of polyhedral oligomeric silsesquioxane-supported N-heterocyclic carbenes/imidazolium salts on palladium(II) complexes; Pd(II)-MPIm-POSS (**1**) composite by solid-state annealing between $Pd(OAc)_2$ and octakis(3-(1-methylimidazolium) propyl) octasilsesquioxane without added base. Subsequently, arylboronic acid based *in situ* or *ex situ* reduction of **1** in aqueous ethanol produces polyhedral oligomeric silsesquioxane-supported N-heterocyclic carbenes/imidazolium salts on palladium nanoparticles; Pd(0)-nano-POSS (**2**) composite, consisting of monodispersed and N-heterocyclic carbene (NHC) stabilized Pd nanoparticles of very small size (3.0 ± 1.5 nm). Nanocatalyst **2** is a highly efficient and easily recyclable homogeneous catalyst for Suzuki-Miyaura cross-coupling reactions with TOF up to 1670 h^{-1}.

Palladium nanoparticles stabilized on solid supports have been used in various applications including chemical sensor and catalysis, particularly for reduction and C–C coupling reactions.[1] Over the past decades, development of an efficient and environmentally friendly method to fabricate monodispersed metal nanoparticles with definite size and shape, high catalytic activity, exceptional stability, and multiple recyclability is highly desirable for practical applications. In particular, novel methods for the fabrication of palladium nanocomposites on a non-toxic support and stabilizer have been actively pursued.[2] In this context due to strong σ donating properties and coordinating ability to the metal center, the N-heterocyclic carbene (NHC) has shown to be an excellent ligand for transition metals as well as metal nanoparticles.[3] Despite many examples of NHC ligands in homogeneous metal-catalyzed chemical transformations and polymer synthesis, fewer reports involving carbene stabilized *d* block metal nanoparticles are known with limited applications.[4]

Although, polyhedral oligomeric silsesquioxanes (POSS), a silicon derived nanoscopic, building block consisting of Si–O–Si bond with tunable surface functional groups, are promising as supports, their applications for nanoparticle immobilization have been largely unexplored.[5] There are a few reports of the immobilization of metal ions on POSS surface involving N and/or O donating ligands for catalytic application available in the literature, but most of these are solution based, have low atom economies and often require hazardous reagents.[2i–l] Recently, we found pyridine–triazole functionalized POSS/Pd(II) complexes as a highly active and stable heterogeneous catalyst for C–C cross-coupling reactions.[5a] However, the catalyst preparation was costly, complicated, and considered to be unfriendly environmental practices. Furthermore, although a number of porous materials with coordinating groups have been previously investigated as supports for nanoparticles,[1h] examples of POSS based materials which stabilize transition metal complexes or metal nanoparticles (NPs) through metal-ligand bonds by adopting an efficient atom economic solid-state synthetic approach is unknown and yet to be explored properly.[2b,c,m,3c]

Moreover, the high stability of such complex is detrimental in terms of catalytic activity or as a precursor of nanoparticle. In order to develop a better and greener synthetic method for Pd/POSS synthesis, we judiciously choose dendritic N-methyl imidazolium groups anchored POSS as a supporting material with a rich source of N-heterocyclic carbene (NHC) ligands and metal acetate salt as a source of metal atom as well as base. To the best of our knowledge, this is the first report of solid-state annealing technique adopted to fabricate metal nanocomposite in the POSS-based system. In addition, the derived composite exhibited high catalytic activity for C–C coupling reactions, because of in situ generation of small size Pd nanoparticles which has been reused for more than ten reaction cycles without a loss in activity.

Octakis(3-(1-methylimidazolium)propyl)octasilsesquioxane, POSS-MPIm–Cl was synthesized according to the literature report.[6] Solid-state annealing of POSS-MPIm-Cl and $Pd(OAc)_2$ at 100 °C for 72 hours without added base afforded the desired material as a yellow solid **1** in a quantitative yield. After the annealing process, we noticed liberation of acetic acid from the

[a] *S. Mohapatra, T. Chaiprasert, R. Sodkhomkhum, R. Kunthom, S. Hanprasit, P. Sangtrirutnugul, V. Ervithayasuporn*
Department of Chemistry, Center of Excellence for Innovation in Chemistry (PERCH-CIC), Center for Catalysis, Center for Inorganic and Materials Chemistry, and Center of Intelligent Materials and Systems, Nanotec Center of Excellence, Faculty of Science, Mahidol University, Rama VI road, Ratchathewi, Bangkok 10400, Thailand.
E-mail: vuthichai.erv@mahidol.ac.th

Supporting information for this article is available on the WWW under http://dx.doi.org/10.1002/slct.201600878

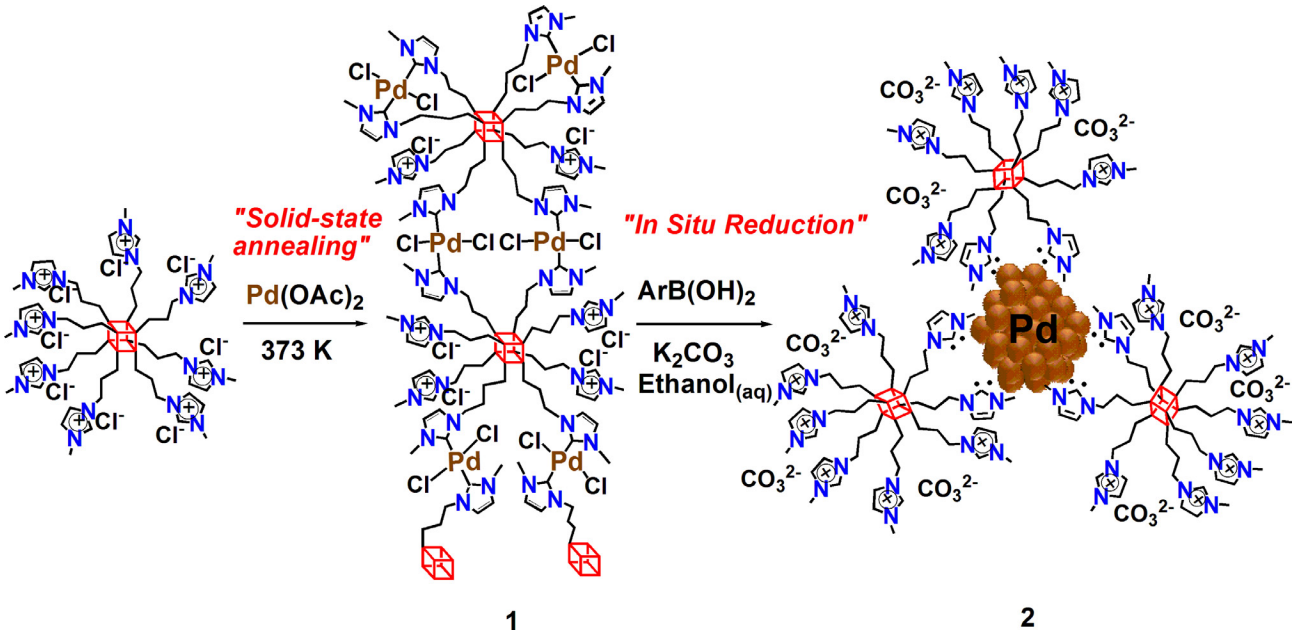

Scheme 1. Solvent-free synthesis of Pd(II)-MPIm-POSS composite (**1**) and a subsequent reduction to fabricate Pd(0)-nano-POSS nanocomposite (**2**) (red cube: POSS).

solid-state reaction mixture because acetate ion acts as a base to abstract the C-2 acidic protons from imidazolium rings of the side chains of POSS to generate carbene in situ. Composite **1** shows a unique solubility property due to the presence of pendent imidazolium moiety. In particular, this composite was insoluble in both polar and nonpolar solvents, possibly due to the formation of cross-linked, extended networks, as illustrated in Scheme 1.

On the contrary, **1** is highly soluble in aqueous alkaline medium. We anticipate that two NHC ligands coordinating to each Pd(II), namely a 1:2 mole ratio of POSS-MPIm-Cl:Pd(OAc)$_2$, should result in *ca.* 50% of unreacted methyl imidazolium groups. The ICP-OES results reveal 10.7 wt% of Pd content or 1.9 Pd(II) per POSS unit, which is consistent with the proposed structure (Scheme 1). The presence of the cationic imidazolium groups are believed to play a crucial role in solubilization of **1** in an alkaline medium and stabilization of Pd nanoparticles generated in the subsequent reaction. In fact, when more than two equiv of Pd(OAc)$_2$ were used, Pd black was observed in the reduction step. Furthermore, to evaluate the stability of the Pd (II) species, the compound **1** was dispersed in aqueous ethanol for a prolonged period of time at room temperature. After two months, no changes in colour and absorption spectrum (Fig. S1) were observed, suggesting high stability of Pd(II) species toward reduction by aqueous ethanol.

Composite **1** was investigated as the pre-catalyst for cross-coupling reactions (*vide infra*). During Suzuki–Miyaura reactions, we observed a vivid color change from yellow to brown upon an addition of arylboronic acid to **1**, indicating an in situ reduction of Pd(II) to Pd(0). A reaction between **1** and four equiv of PhB(OH)$_2$ in aqueous ethanol under alkaline conditions at room temperature was separately carried out, which yielded the product Pd(0)-nano-POSS (**2**) with the same brown color. Both solids obtained from Suzuki–Miyaura and stoichiometric reactions gave in the same UV-Vis spectra, which contain an absorption band at 290 nm, corresponding to the Surface Plasmon band of Pd nanoparticles (Figure S1).[8]

Transmission electron microscopy (TEM) images of **2** shows well dispersed Pd nanoparticles with an average size of 3.0 $\pm$ 1.5 nm with narrow size distribution (Figure 1). Moreover, powder XRD patterns of **1** and of the recovered catalyst after the first cycle of Suzuki–Miyaura reaction contain no peak in the 2θ range of 20–80°, indicating the amorphous nature of both materials (Figure S2). Notably, FT-IR spectra of both **1** and **2** reveal the disappearance of ν(COO) asymmetric band of acetate group, previously observed at 1600 cm^{-1} for Pd(OAc)$_2$, confirming complete displacement of OAc$^-$ after solid-state annealing.[7] In addition, the intensity of two bands at 621 and 1161 cm^{-1}, assignable to imidazolium units is sharply reduced or almost disappeared for both **1** and **2**, suggesting the formation of Pd(II)/Pd(0)-NHC bond (Figure S3).[3d,2h] We further characterized **1** and **2** using ^{29}Si and ^{13}C CP/MAS spectroscopy (Figure S4 and S5). The compound **1** feature two broad, distinct ^{29}Si CP/MAS resonances at –71 and –61 ppm, corresponding to T^3 and T^2 structured Si, respectively. These two peaks indicate that some degrees of cage opening occur during palladation in step 1. The ^{13}C CP/MAS spectrum of **1** also contains a broad signal characteristic of carbenic carbon from Pd(II)-NHC interactions at 155.9 ppm. Upon reduction, two broad peaks appears at 155.8 and 166.3 ppm, corresponding to carbenic carbons of residual Pd(II)-NHC and Pd(0)-NHC, respectively (Figure S5).[3c,1g,4f]

To gain an insight into the reduction of Pd(II) by PhB(OH)$_2$ we recorded XANES spectra of both **1** and **2.** XANES analyses

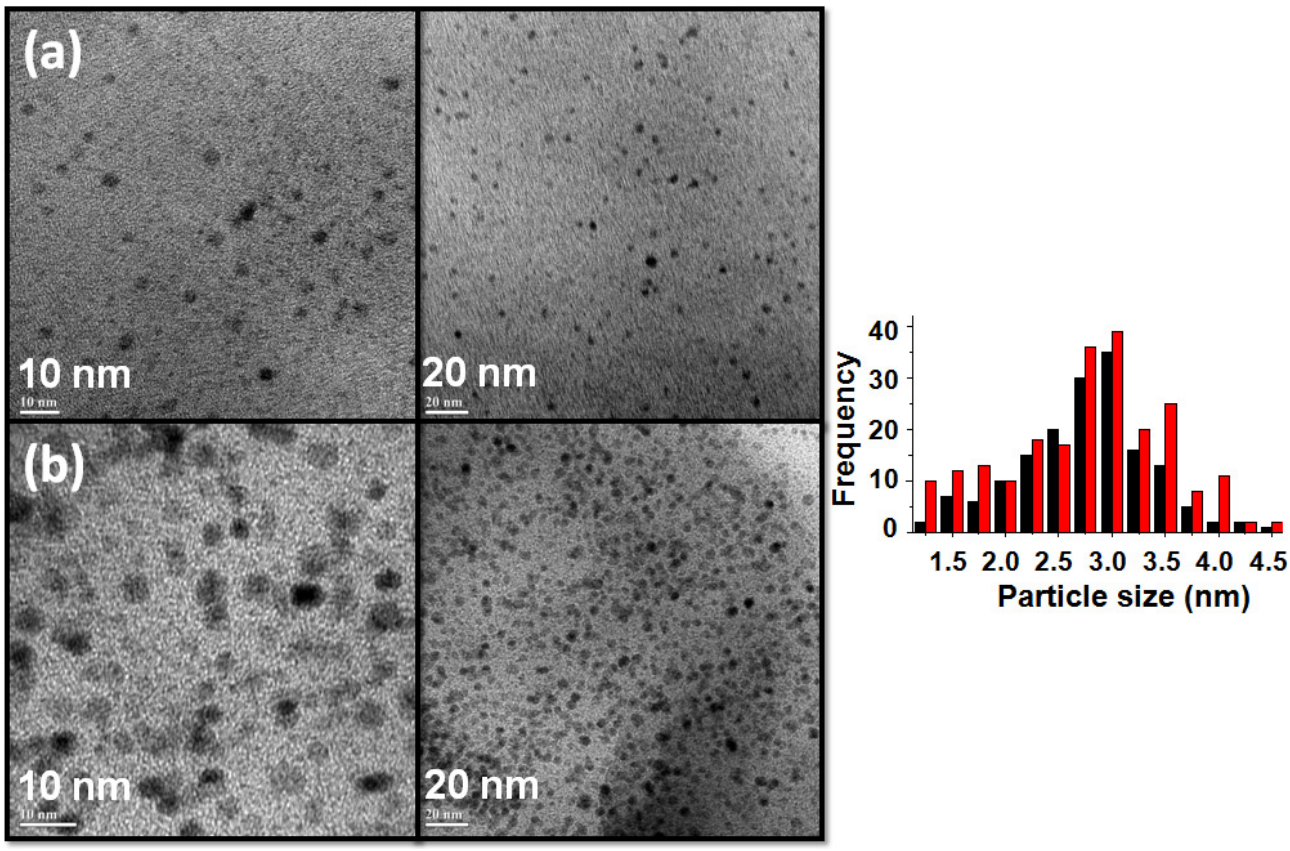

Figure 1. TEM images of the catalyst isolated from Suzuki–Miyaura reactions after (a) 1st cycle and (b) 10th cycle. Histogram obtained considering (a) 160 (black) and (b) 200 particles (red).

(Figure S6) reveal that **1** is a mixture of 86.3% Pd(II) and 13.7% Pd(0) whereas **2** consists of 21.1% Pd(II) and 78.9% Pd(0). The remaining amount of residual Pd(II) species in **2** after reduction is due to the incomplete reduction after the first cycle. Furthermore, we observe a little change in color of the recovered catalyst after subsequent cycles of the reaction. The elemental composition of the **1** and **2** were probed by XPS analysis. The peaks corresponding to the binding energies of Si2p & 2s, Cl2p & 2s, C1s, Pd3d & 3p, N1s, and O1s have been clearly observed in the full XPS spectra as shown in Figure S7a. Narrow scanned XPS spectra of **1** and **2** show two peaks centered at 337.4 eV and 342.9 eV corresponding to the binding energies of Pd, assignable to $3d_{5/2}$ and $3d_{3/2}$, respectively (Figure S7b).[9c, d] Furthermore, both spectra contain a peak at *ca.* 401 eV assignable to N 1s. This peak is deconvoluted into two peaks at 400.5 eV (sp^2 N) and 401.4 eV (quaternary N). The integrations suggest that the ratio of sp^2 N: quaternary N is 2.5:1 in **1** (compared to the calculated value of 3:1), which further increases to 4.5:1 in **2**, suggesting a conversion of quaternary to trivalent sp^2 N (Figure S8 and S9) through additional NHC formation in step 2. Moreover, the presence of quaternary N supports that some imidazolium cations still remain after both steps (Scheme 1).

To evaluate **1** as the pre-catalyst for Suzuki–Miyaura cross coupling reactions, the model substrates *p*-bromoanisole and $PhB(OH)_2$ in the presence of K_2CO_3 were chosen. Using as low as 0.8 mol% of Pd, the well dispersed pre-catalyst **1** exhibited high activity. Higher reaction temperatures (>60 °C) led to Pd black formation, possibly due to the inherent instability of POSS support in a strong alkaline solution.[5b–e, 9] Under optimal conditions, substrate scope was investigated in details as listed in Table 1. In general, with the exception of 1-bromonaphthalene, reactions between $PhB(OH)_2$ and aryl bromides containing functional groups including OH, COMe, NO_2, NH_2, Me, OCH_3, and CH_2OH at the *para* position afforded the corresponding coupled products in good to excellent conversions (76–100%; Table 1). In terms of the electronic effect, electron withdrawing substituents generally resulted in higher TOF values (entries 10, 13, 15). On the other hand, substituents on the aryl boronic acid resulted in lower activities (entries 17–23). As a result of steric hindrance, substituents at the *ortho* position of both aryl bromides and arylboronic acids impede coupling activities (entries 3, 9, 11, 18, 21, 23). We subjected both **1** and **2** to more challenging chloro substrates (e.g. chlorobenzene, *p*-chloroanisole). Unfortunately, the cross-coupling reaction did not occur at 60 °C.

Interestingly during the workup procedure, after an addition of EtOAc, we observed the solid catalyst **2** at the organic-aqueous interface (Figure 2b). This is due to self-aggregation of POSS-based molecules assisted by the pendent methyl imidazolium groups. Thus, the catalyst **2** can be simply recovered by

Table 1. Suzuki–Miyaura cross-coupling reactions[a]

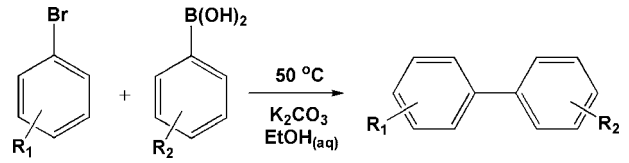

Entry	R_1	R_2	Conversion[b] (%)	Time (h)	TOF[c] (h^{-1})
1	*p*-OMe	H	99	2	620
2	*m*-OMe	H	99	2	560
3	*o*-OMe	H	45	10	301
4	H	H	99	2	570
5	*p*-Me	H	76	4	98
6	*p*-NH_2	H	78	10	
7	*p*-OH	H	85	6	135
8	*m*-OH	H	40	10	
9	*o*-OH	H	25	15	
10	*p*-NO_2	H	98	3	1670
11	*o*-NO_2	H	15	15	
12	*p*-CH_2OH	H	72	6	
13	*p*-CHO	H	100	2	1030
14	*m*-CHO	H	100	2	
15	*p*-COMe	H	100(99)[d]	2	1120
16	Napth[e]	H	78	6	53
17	*p*-OMe	*p*-F	76	2	750
18	*p*-OMe	*o*-OMe	56	10	
19	*p*-OMe	*m*-OMe	90	2	
20	*p*-OMe	*p*-OMe	99	2	
21	*o*-OMe	*p*-OMe	23	15	
22	*m*-OMe	*m*-OMe	72	4	
23	*o*-OMe	*o*-OMe	3	15	
24[f]	*p*-COMe	H	100	2	

[a]ArBr (0.5 mmol), $ArB(OH)_2$ (0.6 mmol), K_2CO_3 (1.1 mmol), **1** (0.8 mol%), in 4 mL of EtOH:H_2O (1:1 v/v). [b]Conversion based on GC-MS. [c]TOF was determined from a different experiment using about 0.20 mol% of Pd at 50 °C for a certain time when the conversion was less than 25% (see the Supporting Information). [d]Isolated yield. [e]1-bromonapthalene. [f]using *ex-situ* generated catalyst **2** of 4 mg.

decantation of EtOAc and aqueous layers and used directly in subsequent reactions. Moreover, after addition of aqueous ethanol and K_2CO_3 to the recovered catalyst, a brown solution generated in subsequent cycles indicates that the particles get redissolved into the solution as shown in Figure 2. The reversible dispersion and re-aggregation characteristics of the catalyst **2** have an added advantage in using as a recyclable catalyst. Composite **2** has been studied for more than ten cycles of reaction without any loss in activity (Figure 2). A hot filtration experiment revealed no change in the reaction rate after filtration, compared to the reaction without filtration, an evidence that active species were present in the solution state rather than solid state (Figure S10). In agreement with this result, the aqueous phase of the catalytic reaction (1st cycle) contains 80 ppm of Pd based on ICP-OES analysis, confirming that there was a significant amount of Pd liberated into the aqueous alkaline solution and no aggregation of Pd nanoparticles under the catalytic conditions was observed (Figure 1). On the basis of these observations, we propose the Pd(0)-nano-POSS composite as a recyclable homogeneous catalyst or quasi homogeneous catalyst, where **2** serves as a Pd reservoir releasing active Pd species into the reaction solution during catalysis. The color change of the catalyst recovered after subsequent cycles of reaction is shown in Figure S11. The gradual, detectable color change is possibly due to the complete reduction of residual Pd(II) after many cycles of reaction and in fact, no significant changes in the particle size was observed even after ten catalytic cycles (Figure 2).

In summary, a solid-state synthetic method has been successfully implemented for the fabrication of POSS supported well dispersed palladium nanoparticles. The derived Pd nanocomposite exhibits high catalytic activity for C–C coupling reactions with TOF up to 1670 h^{-1}. The reusability for more than ten reaction cycles without a loss in activity indicates exceptional stability of the nanoparticles. Furthermore, the imidazo-

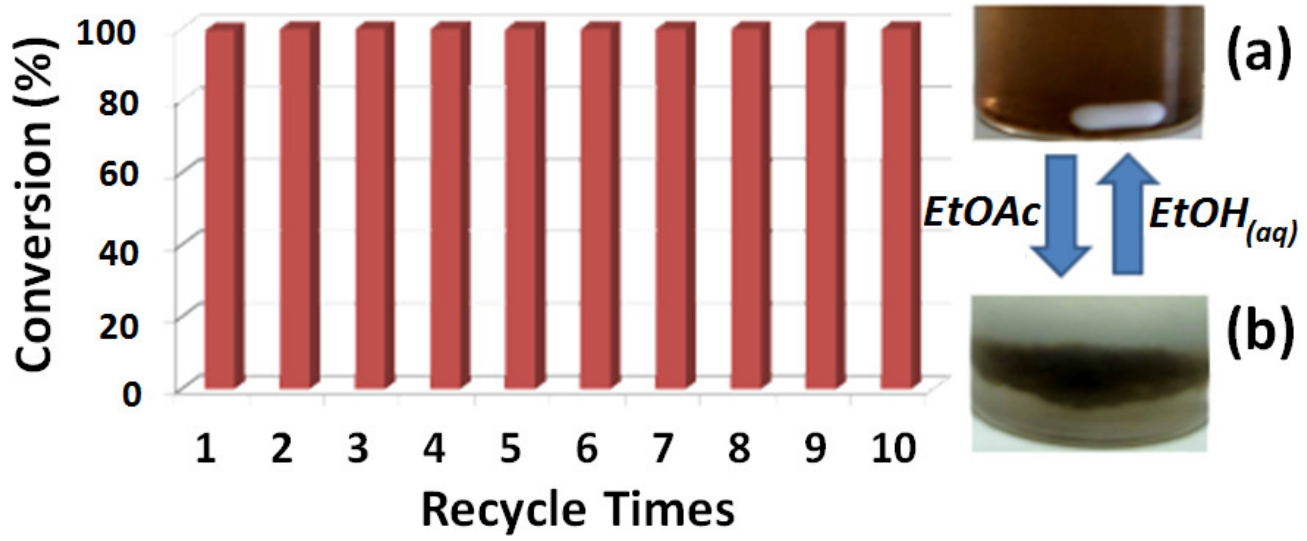

Figure 2. Recyclability test under reaction conditions: 4-bromoacetophenone (0.5 mmol), $PhB(OH)_2$ (0.6 mmol), K_2CO_3 (1.1 mmol), Pd(II)-MPIm-POSS (1.5 mg) in 4 mL of H_2O:EtOH (1:1 v/v) at 50°C for 1 h.; (a) before and (b) after EtOAc addition.

lium functional groups on POSS play a key role in the unique solubility properties of the catalyst **2.** Interestingly, a significant amount of Pd nanoparticles stabilized by NHC groups are liberated into an alkaline aqueous EtOH solution and act as an active homogeneous catalyst. After EtOAc addition, the Pd nanoparticles are driven to the organic-aqueous interface where they can be conveniently separated out and reused. The method is low cost, environmentally friendly in nature, and potentially useful for fabrication of similar composites with other transition metals. We are currently exploring similar protocol to fabricate POSS-based composite materials with other less expensive and catalytically active metals by tuning organic linkages including stabilizing functional groups. Furthermore, the related POSS-based composite can be further explored for other palladium catalyzed reactions.

Supporting information includes materials, instruments, syntheses and characterizations of **1** and **2**, and general procedure for Suzuki–Miyaura cross-coupling reaction.

Acknowledgements

S.M. is grateful to Mahidol University for the postdoctoral fellowship (MU-PD_2015_05). This research is financially supported by the Thailand Research Fund (RSA5980018), Faculty of Science, Mahidol University and Mahidol University under the National Research Universities Initiative, Center of Excellence for Innovation in Chemistry (PERCH-CIC), and the Nanotechnology Center (NANOTEC), NSTDA, Ministry of Science and Technology, Thailand, through its program of Center of Excellence Network. Authors are also thankful to Natthapat Sungchawek, Suttiporn Pikulthong, and Assoc. Prof. Dr. Ekasith Somsook for help and support.

Keywords: Carbene ligands · Catalysts · Nanoparticles · Silsesquioxane · Solid-phase synthesis

[1] a) R. J. White, R. Luque, V. L. Budarin, J. H. Clark, D. J. MacQuarrie, *Chem. Soc. Rev.*, **2009**, *38*, 481–494; b) D. Astruc, F. Lu, J. R. Aranzaes, *Angew. Chem., Int. Ed.*, **2005**, *44*, 7852–7872; c) C. Deraedt, D. Astruc, *Acc. Chem. Res.*, **2014**, *47*, 494–503; d) A. Balanta, C. Godard, C. Claver, *Chem. Soc. Rev.*, **2011**, *40*, 4973–4985; e) J. Guerra, M. A. Herrero, *Nanoscale*, **2010**, *2*, 1390–1400; f) D. Astruc, *Inorg. Chem.*, **2007**, *46*, 1884–1894; g) S. Omar, R. Abu-Reziq, *J. Phys. Chem. C*, **2014**, *118*, 30045–30056; h) H. Zhao, Y. Wang, R. Wang, *Chem. Commun.*, **2014**, *50*, 10871–10874; i) V. P. Ananikov, I. P. Beletskaya, *Organometallics* **2012**, *31*, 1595–1604; j) Ã. Molnar, *Chem. Rev.* **2011**, *111*, 2251–2320.

[2] a) I. Saldan, Y. Semenyuk, I. Marchuk, O. eshetnyak, *J. Mater. Sci.*, **2015**, *50*, 2337–2354; b) C.-H. Lu, F.-C. Chang, *ACS Catal.*, **2011**, *1*, 481–488; c) S. E. Letant, A. Maiti, T. V. Jones, J. L. Herberg, R. S. Maxwell, A. P. Saab, *J. Phys. Chem. C*, **2009**, *113*, 19424–19431; d) E. A. Baquero, S. Tricard, J. C. Flores, J. E. de Jesus, B. Chaudret, *Angew. Chem., Int. Ed.*, **2014**, *53*, 13220–13224; e) K. V. S. Ranganath, A. H. Schaefer, F. Glorius, *ChemCatChem*, **2011**, *3*, 1889–1891; f) K. V. S. Ranganath, J. Kloesges, A. H. Schaefer, F. Glorius, *Angew. Chem., Int. Ed.*, **2010**, *49*, 7786–7789; g) V. Kogan, Z. Aizenshtat, R. Popovitz-Biro, R. Neumann, *Org. Lett.*, **2002**, *4*, 3529–3532; h) N. Sharma, G. Sekar, *Adv. Synth. Catal.*, **2016**, *358*, 314–320; i) B. Karimi, M. Khorasani, H. Vali, C. Vargas, R. Luque, *ACS Catal.*,**2015**, *5*, 4189–4200; j) Y. Zhou, G. Yang, C. Lu, J. Nie, Z. Chen, J. Ren, *Catal. Commun.*, **2016**, *75*, 23–27; k) S. Tang, R. Jin, H. Zhang, H. Yao, J. Zhuang, G. Liu, H. Li, *Chem. Commun.*, **2012**, *48*, 6286–6288.; l) K. Naka, M. Sato, Y. Chujo, *Langmuir*, **2008**, *24*, 2719–2726.; m) L. A. Bivona, F. Giacalone, E. Carbonell, M. Gruttadauria, C. Aprile, *ChemCatChem*, **2016**, *8*, 1685–1691.

[3] a) M. N. Hopkinson, C. Richter, M. Schedler, F. Glorius, *Nature (London, U. K.)*, **2014**, *510*, 485–496; b) C. M. Crudden, J. H. Horton, I. I. Ebralidze, O. V. Zenkina, A. B. McLean, B. Drevniok, Z. She, H.-B. Kraatz, N. J. Mosey, T. Seki, E. C. Keske, J. D. Leake, A. Rousina-Webb, G. Wu, *Nat Chem*, **2014**, *6*, 409–414; c) H. Zhao, L. Li, Y. Wang, R. Wang, *Sci. Rep.*, **2014**, *4*, 5478; d) Y. He, C. Cai, *Chem. Commun.*, **2011**, *47*, 12319–12321.

[4] a) Y. G. Kolyagin, V. N. Zakharov, A. V. Yatsenko, K. A. Paseshnichenko, S. V. Savilov, L. A. Aslanov, *J. Nanopart. Res.*, **2016**, *18*, 1–11; b) P. Lara, A. Suarez, V. Colliere, K. Philippot, B. Chaudret, *ChemCatChem*, **2014**, *6*, 87–90; c) L. M. Martinez-Prieto, C. Urbaneja, P. Palma, J. Campora, K. Philippot, B. Chaudret, *Chem. Commun.*, **2015**, *51*, 4647–4650; d) A. V. Zhukhovitskiy, J. A. Johnson, *Polym. Prepr.* **2012**, *53*, 450–451; e) J. Vignolle, T. D. Tilley, *Chem. Commun.*, **2009**, 7230–7232., f) A. L. Ferry, K. Schaepe, P. Tegeder, C. Richter, K. M. Chepiga, B. J. Ravoo, F. Glorius, *ACS Catal*, **2015**, *5*, 5414–5420; g) E. C. Hurst, K. Wilson, I. J. S. Fairlamb, V. Chechik, *New J. Chem.*, **2009**, *33*, 1837–1840; h) C. J. Serpell, J. Cookson, A. L. Thompson, C. M. Brown, P. D. Beer, *Dalton Trans.*, **2013**, *42*, 1385–1393; i) M. J. MacLeod, J. A. Johnson, *J. Am. Chem. Soc.*, **2015**, *137*, 7974–7977; j) P. Lara, O. Rivada-Wheelaghan, S. Conejero, R. Poteau, K. Philippot, B. Chaudret, *Angew. Chem., Int. Ed.*, **2011**, *50*, 12080–12084; k) D. Gonzalez-Galvez, P. Lara, O. Rivada-Wheelaghan, S. Conejero, B. Chaudret, K. Philippot, P. W. N. M. van Leeuwen, *Catal. Sci. Technol.*, **2013**, *3*, 99–105.

[5] a) V. Ervithayasuporn, K. Kwanplod, J. Boonmak, S. Youngme, P. Sangtrirutnugul, *J. Catal.*, **2015**, *332*, 62–69; b) M.C.B. Jaimes, C. R. N. Bohling, J. M. Serrano-Becerra, and A. S. K. Hashmi, *Angew. Chem. Int. Ed.* **2013**, *52*, 7963–7966; c) S. Chimjarn, R. Kunthom, P. Chancharone, R. Sodkhomkhum, P. Sangtrirutnugul, V. Ervithayasuporn, *Dalton Trans.* **2015**, *44*, 916–919; d) M. Janeta, Ł. John, J. Ejfler, T. Lis, S. Szafert, *Dalton Trans.*, **2016**, *45*, 12312–12321; e) J.C. Furgal, T. Goodson III, and R. M. Laine, *Dalton Trans.*, **2016**, *45*, 1025–1039; f) W. Yang, Y. Gan, X. Jiang, H. Liu, *Eur. J. Inorg. Chem.* **2015**, 99–103.

[6] J. Tan, D. Ma, X. Sun, S. Feng, C. Zhang, *Dalton Trans.*, **2013**, *42*, 4337–4339.

[7] D. D. Kragten, R. A. van Santen, M. K. Crawford, W. D. Provine, J. J. Lerou, *Inorg. Chem.*, **1999**, *38*, 331–339.

[8] A. Henglein, *J. Phy. Chem. B*, **2000**, *104*, 6683–6685.

[9] a) J. P. Contour, G. Mouvier, M. Hoogewys, C. Leclere, *J. Catal.*, **1977**, *48*, 217–228; b) J. Escard, G. Mavel, J. E. Guerchais, R. Kergoat, *Inorg. Chem.*, **1974**, *13*, 695–701; c) S. O. Grim, L. J. Matienzo, W. E. Swartz, *Inorg. Chem.*, **1974**, *13*, 447–449.

[10] S. Fabritz, D. Heyl, V. Bagutski, M. Empting, E. Rikowski, H. Frauendorf, I. Balog, W.-D. Fessner, J. J. Schneider, O. Avrutina, H. Kolmar, *Org. Bio. Chem.*, **2010**, *8*, 2212–2218.

[11] B. Ravel, M. Newville, *J. Synchrotron Rad.*, **2005**, *12*, 537–541.

Submitted: July 6, 2016
Accepted: October 5, 2016

Dalton Transactions

COMMUNICATION

View Article Online
View Journal | View Issue

Cite this: *Dalton Trans.*, 2016, **45**, 16117

Received 29th June 2016,
Accepted 22nd July 2016

DOI: 10.1039/c6dt02585d

www.rsc.org/dalton

Synthesis and isolation of non-chromophore cage-rearranged silsesquioxanes from base-catalyzed reactions†

Sasikarn Hanprasit, Nuttanee Tungkijanansin, Arisa Prompawilai, Supattra Eangpayung and Vuthichai Ervithayasuporn*

The nucleophilicity of both *ortho*- and *meta*-nitrophenolate anions is strong enough to give substituted products, but their basicity also facilitates cage-rearrangement reactions in polyhedral oligomeric silsesquioxanes (POSS). Anions having a stronger basicity, but weaker nucleophilicity, such as CO_3^{2-}, gave products only from cage-rearrangement, with the cage expansion products being isolable in multi-gram quantities using conventional column chromatography.

Polyhedral oligomeric silsesquioxanes (POSS) are one of the most interesting organic–inorganic hybrid materials because their molecular structures contain the smallest inorganic Si–O core that is covalently bonded to organic substituents.[1] Their potential recent applications (*e.g.* in biomedicine,[2] catalysis,[3] and electronics[4]) are driven by the ability to append large numbers of organic functional groups onto the core, especially in the case of the octameric silsesquioxane or T_8 (O_h) cube. During the hydrolytic condensation reactions of alkoxysilanes under appropriate conditions, cubic T_8 cages are commonly found as a major product which separate from the reaction through precipitation or crystallisation.[5] This phenomenon can be explained by the higher degree of symmetry in T_8 cubes (O_h), resulting in efficient close-packing. Only very few cases of other symmetry silsesquioxanes, *e.g.* decameric T_{10} (D_{5h}) and dodecameric T_{12} (D_{2d}) systems, have been isolated through crystallization, due to the stacking effects between phenyl substituents.[6] Most lower symmetry molecules (T_{10} and T_{12}) are amorphous and exhibit higher solubilities in organic solvents.[7] Recently, we have highlighted that chromatography is an excellent purification technique for the separation of POSS molecules. The isolation of high purity T_{10} and T_{12} POSS systems may open a new direction of research into silsesquioxane materials, since these possess higher degrees of reactive functionalization than smaller cages[8] and interesting solubility behaviour in some cases.[9] In addition, their physical and thermal properties are totally distinct from those of the T_8 cube.

Octakis(3-chloropropyl)octasilsesquioxane (**1**) has been demonstrated to be a highly reactive precursor towards substitution reactions. During functionalization of the alkyl substituents in **1**, the degree of inorganic cage-rearrangement relies on the nature of the nucleophile used. Soft nucleophiles (*e.g.* RS^-, Br^-, and I^-) resulted in the structural integrity of the octameric T_8 cage being retained,[5b,c] while mixtures of cage-rearranged silsesquioxanes (T_8, T_{10}, and T_{12} cages) were found due to the action of strong nucleophiles (*e.g.* ArO^-, N_3^-, and $RCOO^-$).[7] Recently, we have found that if the electron density of hard nucleophiles is stabilized by resonance, the distribution of cage-rearranged silsesquioxanes can be effectively controlled.[7c] Herein, this report probes the effect of nucleophile basicity on cage-rearrangements during substitution reactions on **1**, to derive a series of chromophoric POSS systems. Treatment of **1** with a non-nucleophilic carbonate results in core expansion to highly functional T_{10} and T_{12} cages, which can be isolated in gram-scale synthesis using conventional column chromatography.

To achieve complete substitution (>98%) of the primary alkyl chlorides in **1**, the nature of the nucleophile used must be carefully considered. As an example, the nucleophilicities of each nitrophenol sodium salt (*ortho* and *meta*), as defined by the pK_a values of their conjugate acids, can be used to predict their reactivities in substitution reactions on **1** to obtain *ortho*- and *meta*-oxynitrobenzene-functionalized POSS (Scheme 1).

The lower pK_a (7.23) of *ortho*-nitrophenol results in the conjugate phenolate being more weakly basic and less nucleophilic than that of *meta*-nitrophenol (pK_a = 8.36). As a result, milder conditions (70 °C, 1 day) were required for complete substitution on **1** using *meta*-nitrophenolate, whereas *ortho*-nitrophenolate required harsher conditions (100 °C, 1 day) as shown in Scheme 1. The resonance effect arising from the electron withdrawing nitro-group at the *ortho* position results in

Department of Chemistry, Center of Excellence for Innovation in Chemistry (PERCH-CIC), Center for Catalysis, Center for Inorganic and Materials Chemistry, and Center of Intelligent Materials and Systems, Nanotec Center of Excellence, Faculty of Science, Mahidol University, Rama VI road, Ratchathewi, Bangkok 10400, Thailand. E-mail: vuthichai.erv@mahidol.ac.th

†Electronic supplementary information (ESI) available: Experimental sections, ^1H, $^{13}C\{^1H\}$, $^{29}Si\{^1H\}$ NMR spectra and high resolution ESI-MS analyses of compounds **1–9**. See DOI: 10.1039/c6dt02585d

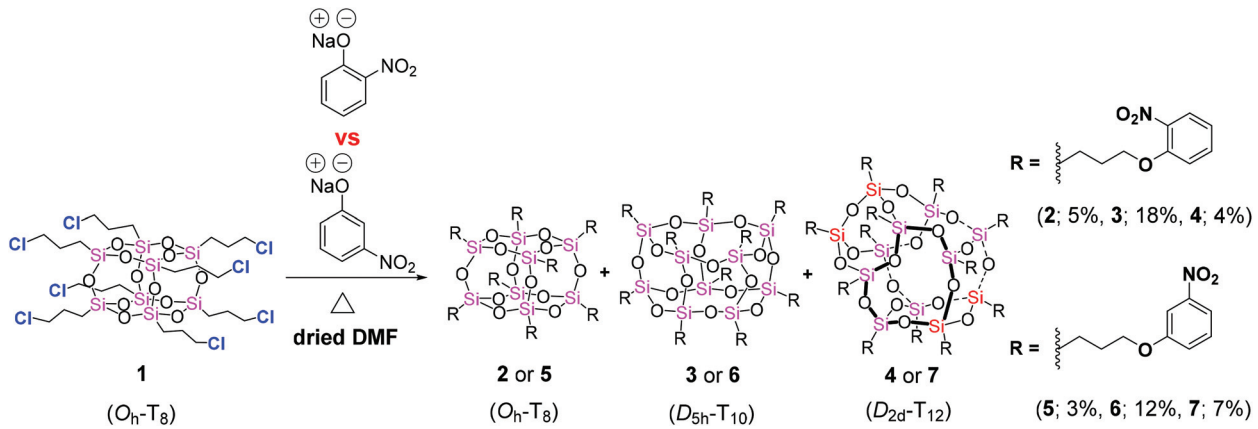

Scheme 1 Comparative reactivity of nucleophiles towards compound **1** (T_8) resulting in full incorporation of *ortho*- and *meta*-oxynitrobenzene functions in POSS, leading to (a) compounds **2–4** (100 °C, 1 day, 0.129 mol L^{-1} **1**, 1.7 equiv. of 2-nitrophenol sodium salt/$RSiO_{3/2}$) and (b) compounds **5–7** (70 °C, 1 day, 0.129 mol L^{-1} **1**, 1.5 equiv. of 3-nitrophenol sodium salt/$RSiO_{3/2}$), respectively.

lower nucleophilicity in *ortho*-nitrophenolate; this is not evident in the *meta*-isomer (inductive effect only). In our previous report, *para*-oxynitrobenzene-functionalized POSS could be prepared from **1** under similar conditions to that used for *ortho*-nitrophenolate substitution (70 °C, 3 days). *para*-Nitrophenol has a pK_a (7.16) close to that of *ortho*-nitrophenol and exhibits the same resonance effect. However, while both conjugate bases are of comparable strength, the *para*-isomer is less sterically hindered, enhancing its nucleophilicity over the *ortho*-nitrophenolate as reflected under the milder reaction conditions. As such, we suggest that a position-controlled reactivity series for nitrophenolate nucleophile substitution on **1** follows the order *meta*- > *para*- > *ortho*-. In all cases however, substitution reactions led to additional cage-rearrangement products in moderate yields. Of these, the decameric T_{10} cage was observed as a major product, while octa- and dodecameric (T_8 and T_{12}) cages were identified as minor constituents.

According to previous reports on POSS substitution, nucleophile basicity may play an important role in promoting cage-rearrangement reactions at the inorganic Si–O–Si core.[7] Hard nitrogen (*e.g.* azide, phthalimide) and oxygen (*e.g.* acrylate, methacrylate, and phenolate) nucleophiles, which show pK_a values in the range of 4.25–9.17, almost always lead to the formation of cage-rearranged products (T_8, T_{10}, and T_{12}). However, saccharinate and thioacetate anions, which have low pK_a values (1.6 and 3.33), respectively, produce only a T_8 cage substitution product.[5c,7b] In order to confirm the influence of the nucleophile basicity on the cage-rearrangement, potassium carbonate (K_2CO_3) was employed as a non-nucleophilic base due to its high pK_a (10.25), which may promote cage-rearranged reactions, but avoid substitution.[9] As shown in Scheme 2, cubic T_8 **1** was exposed to K_2CO_3 in dry DMF at 60 °C. Although **1** contains no UV-active chromophore, we found that thin layer chromatography could be used to monitor the reaction as products were detectable through exposure to iodine vapour.

After conducting a series of reactions for different time periods, the consumption of T_8 tends to reach a maximum level after 20 minutes, as shown in Fig. 1, suggesting that K_2CO_3 can catalyse the cage-rearrangement process. The

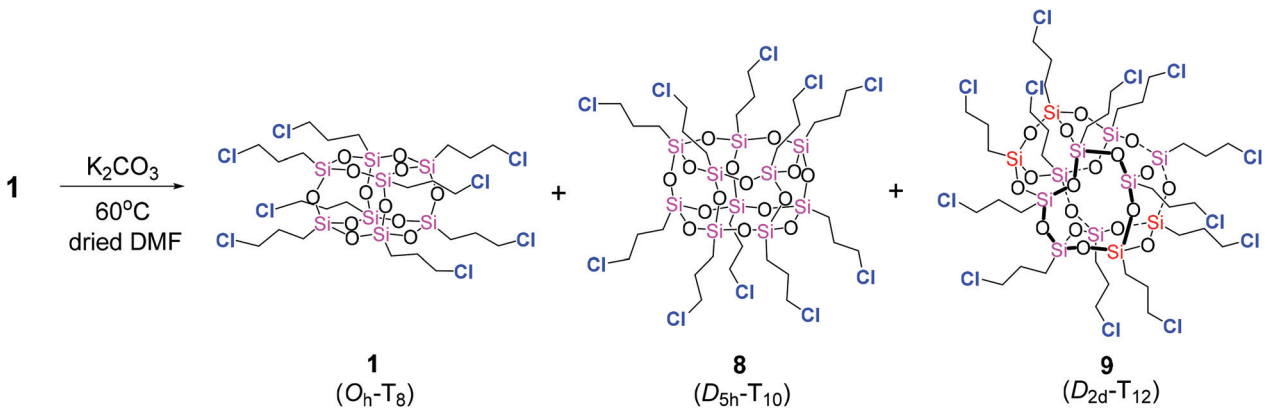

Scheme 2 Cage-rearrangement on exposure of compound **1** (T_8) to a base leading to a mixture of octa-, deca-, and dodecameric silsesquioxanes (T_8, T_{10}, and T_{12}).

highest overall yield of such products is thus achieved at this stage on quenching, giving decakis(3-chloropropyl)decasilsesquioxane (**8**) as a major product (42%, R_f = 0.35) that can be simply isolated using conventional column chromatography (CH_2Cl_2/hexane 3.0 : 7.0). T_8 (**1**) (25%; R_f = 0.41) is recovered from equilibrium with dodecakis(3-chloropropyl)dodecasilsesquioxane, T_{12}, (**9**) (24%; R_f = 0.28) being isolated as a minor product.

The $^{29}Si\{^1H\}$ NMR spectra of compounds **1** (T_8) and **8** (T_{10}) confirm their purity through the presence of distinct singlets at −67.07 and −68.94 ppm (Fig. 2a and b), respectively, which correspond to the values expected based on symmetry, for T_8 and T_{10} cages. Compound **9** (T_{12}) shows two singlets at −68.74 and −71.34 ppm consistent with its lower symmetry (D_{2d}) (Fig. 2c). We suggest that the reaction pathways driving cage-rearrangements in **1** are favourable for bases that are strong enough to allow attack on the cage silicon atoms. In the case of the carbonate, cleavage of silicon–oxygen bonds can thus occur followed by incorporation of oxygen atoms from CO_3^{2-} into Si–O fragments. Subsequently, the molecular self-organization of such reactive fragments (precursors) would lead to condensation of the most thermodynamically controlled cage-like silsesquioxanes.[6a,10]

However, isolated yields of POSS decrease with time, such that after a 24 h (as shown in Fig. S1†) exposure to the carbonate, only broad and poorly defined NMR signals in the crude product are evident, similar to those observed in random polymeric silsesquioxanes. This result suggests that stronger bases should be avoided in POSS substitution reactions as extensive cage degradation is possible.

In conclusion, *ortho*- and *meta*-oxynitrobenzene functionalized-polyhedral oligomeric silsesquioxanes (T_8, T_{10}, and T_{12}) can be simply prepared through substitution reaction on **1** with nitrophenolate anions. However, the basicity of these anions also facilitates cage-rearrangement reactions. Carbonate, a stronger but lower nucleophilicity base results in the extensive formation of cage-rearrangement products. Surprisingly, the highly reactive alkyl chloride functionalities are not affected, and cage expansion from T_8 to higher T_{10} and T_{12} functionalised POSS materials can be enabled, and the materials isolated in gram scale quantities through conventional column chromatography. The feasibility to prepare gram-scale quantities of these previously rare (T_{10} and T_{12}) silsesquioxanes should be a key driver for researching into preparation of other highly functionalized cages for materials applications.

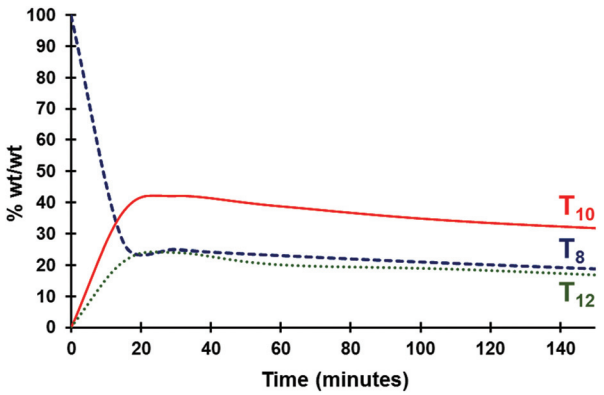

Fig. 1 Weight percentages of compounds **1** (T_8), **8** (T_{10}), and **9** (T_{12}) with time for base-catalyzed reactions. Isolated yields determined using conventional liquid chromatography.

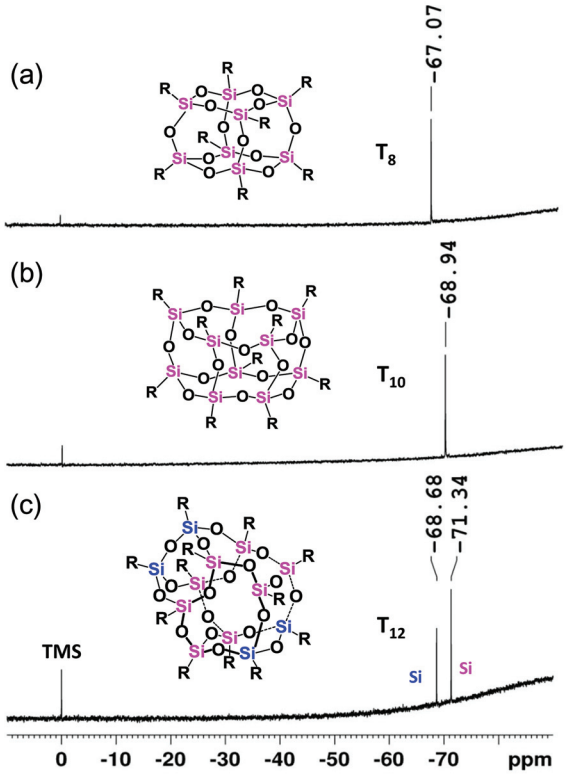

Fig. 2 $^{29}Si\{^1H\}$ NMR spectra of isolated POSS (a) octa-, (b) deca-, and (c) dodecameric silsesquioxanes (**1**, **8**, and **9**).

Acknowledgements

This research is financially supported by the Thailand Research Fund (RSA5980018), Faculty of Science, Mahidol University, Center of Excellence for Innovation in Chemistry (PERCH-CIC), and the Nanotechnology Center (NANOTEC), NSTDA, Ministry of Science and Technology, Thailand, through its program of Center of Excellence Network. Authors also thank Dr Christopher Brooke Smith for his valuable advice in scientific discussion.

References

1 (*a*) K. Tanaka and Y. Chujo, *J. Mater. Chem.*, 2012, **22**, 1733–1746; (*b*) D. B. Cordes, P. Lickiss and F. Rataboul, *Chem. Rev.*, 2010, **110**, 2081.

2 (*a*) M. E. Pérez-Ojeda, B. Trastoy, Á. Rol, M. D. Chiara, I. García-Moreno and J. L. Chiara, *Chem. – Eur. J.*, 2013, **19**, 6630; (*b*) S. Fabritz, S. Hörner, O. Avrutina and H. Kolmar, *Org. Biomol. Chem.*, 2013, **11**, 222.

3 (*a*) Y. Leng, J. Zhao, P. Jiang and D. Lu, *Catal. Sci. Technol.*, 2016, **6**, 875; (*b*) L. A. Bivona, O. Fichera, L. Fusaro, F. Giacalone, M. Buaki-Sogo, M. Gruttadauria and C. Aprile, *Catal. Sci. Technol.*, 2015, **5**, 5000–5007; (*c*) Y. Zhou, G. Yang, C. Lu, J. Nie, Z. Chen and J. Ren, *Catal. Commun.*, 2016, **75**, 23.

4 (*a*) N. Konnertz, M. Böhning and A. Schönhals, *Polymer*, 2016, **90**, 89; (*b*) Y. Ie, T. Sakurai, S. Jinnai, M. Karakawa, K. Okuda, S. Mori and Y. Aso, *Chem. Commun.*, 2013, **49**, 8386–8388; (*c*) C. L. Chan, P. Sonar and A. Sellinger, *J. Mater. Chem.*, 2009, **19**, 9103; (*d*) T. Zhang, J. Wang, M. Zhou, L. Ma, G. Yin, G. Chen and Q. Li, *Tetrahedron*, 2014, **70**, 2478.

5 (*a*) M. F. Roll, J. W. Kampf and R. M. Laine, *Cryst. Growth Des.*, 2011, **11**, 4360–4367; (*b*) V. Ervithayasuporn, N. Pornsamutsin, P. Prangyoo, K. Sammawutthichai, T. Jaroentomeechai, C. Phurat and T. Teerawatananond, *Dalton Trans.*, 2013, **42**, 13747–13753; (*c*) V. Ervithayasuporn, T. Tomeechai, N. Takeda, M. Unno, A. Chaiyanurakkul, R. Hamkool and T. Osotchan, *Organometallics*, 2011, **30**, 4475; (*d*) B. Marciniec, M. Dutkiewicz, H. Maciejewski and M. Kubicki, *Organometallics*, 2008, **27**, 793.

6 (*a*) J. C. Furgal, T. Goodson III and R. M. Laine, *Dalton Trans.*, 2016, **45**, 1025; (*b*) A. S. Lee, S.-S. Choi, H. S. Lee, K. Y. Baek and S. S. Hwang, *Dalton Trans.*, 2012, **41**, 10585.

7 (*a*) S. Chimjarn, R. Kunthom, P. Chancharone, R. Sodkhomkhum, P. Sangtrirutnugul and V. Ervithayasuporn, *Dalton Trans.*, 2015, **44**, 916–919; (*b*) V. Ervithayasuporn and S. Chimjarn, *Inorg. Chem.*, 2013, **52**, 13108–13112; (*c*) T. Jaroentomeechai, P. Yingsukkamol, C. Phurat, E. Somsook, T. Osotchan and V. Ervithayasuporn, *Inorg. Chem.*, 2012, **51**, 12266–12272; (*d*) V. Ervithayasuporn, X. Wang and Y. Kawakami, *Chem. Commun.*, 2009, 5130–5132.

8 V. Ervithayasuporn, K. Kwanplod, J. Boonmak, S. Youngme and P. Sangtrirutnugul, *J. Catal.*, 2015, **332**, 62.

9 E. Rikowski and H. C. Marsmann, *Polyhedron*, 1997, **16**, 3357.

10 R. Franco, A. K. Kandalam and R. Pandey, *J. Phys. Chem. B*, 2002, **106**, 1709–1713.

Polymer 108 (2017) 173–178

Contents lists available at ScienceDirect

Polymer

journal homepage: www.elsevier.com/locate/polymer

Short communication

Polyhedral oligomeric silsesquioxane (POSS) containing sulfonic acid groups as a metal-free catalyst to prepare polycaprolactone

Rungthip Kunthom [a, b], Thapakorn Jaroentomeechai [a, b], Vuthichai Ervithayasuporn [a, b, *]

[a] Department of Chemistry, Center of Excellence for Innovation in Chemistry (PERCH-CIC), Center for Catalysis, Center for Inorganic and Materials Chemistry, Faculty of Science, Mahidol University, Rama VI Road, Ratchathewi, Bangkok 10400, Thailand
[b] Center of Intelligent Materials and Systems, Nanotec Center of Excellence, Faculty of Science, Mahidol University, Rama VI Road, Ratchathewi, Bangkok 10400, Thailand

ARTICLE INFO

Article history:
Received 19 September 2016
Received in revised form
9 November 2016
Accepted 17 November 2016
Available online 19 November 2016

Keywords:
Polyhedral oligomeric silsesquioxane
Sulfonic acid
Polycaprolactone
Metal-free catalyst
Ring-opening polymerization

ABSTRACT

Organic-inorganic hybrid nano-building block of polyhedral oligomeric silsesquioxane (POSS) containing hyperbranched sulfonic acid groups was easily prepared within a day through oxidation reaction at room temperature. The desired product was fully characterized by ^{1}H, $^{13}C\{^{1}H\}$ NMR, ^{29}Si CP/MAS NMR, FT-IR spectroscopy, and TGA-DSC analysis, confirming the complete formation of sulphonic acids while retaining the cubic structure of silsesquioxanes cage. Furthermore, the proton exchange capacities of POSS catalyst were determined to be 5.39 meq of H^{+}/g, much greater than any previous silicon-based materials, leading to the catalytic preparation of polycaprolactone with well-controlled polymerization under the metal-free system and without the addition of any co-catalysts and solvents.

1. Introduction

Polycaprolactone (PCL) is commonly considered as a class of biodegradable polyester that appears in a wide range of functional properties, e.g. highly controlled degradability, miscibility with other polymers, and biocompatible in tissue engineering stability [1,2]. To prepare PCL, the ring-opening polymerizations (ROP) with a step-growth process lead to a formation of PCL with different chain lengths to give a variety of building materials. In the most extensive case, metals such as Tin, Aluminium, and Zinc are used as a catalyst to synthesize polycaprolactone [3,4]. Nevertheless, metal contamination can be a problematic seriousness if polyesters are used in food and biomedical applications [5]. Therefore, developing the metal-free catalyst with a heterogeneous nature for preparing the polymers is considered as a potential alternative route with a broader application, especially to “organocatalysts” [6]. One example in this field is the development of enzymatic ring-opening polymerization (eROP). However, there is much concern about enzyme stability during eROP of ε-caprolactone (ε-CL) [7]. Together with several drawbacks of enzyme's stability including pH, temperature, and water content that may influence its ability to bind the substrate and catalyze the reaction. Organic acids and some amino acids (e.g. serine, proline, and glycine) have been reported their ability to catalyze the ROP of ε-CL to obtain polymers [8,9]. However, a molecular weight of PCL made by these catalysts was found up to only 2800 g mol^{-1}, partly due to the narrow range of pK_a values, from 3 to 5, of those acid catalysts. Meantime, other organic materials like graphene oxide (GO) containing acid functions have been found as a promising catalyst to prepare PCL, confirming that the acidic behaviour on GO's surface was the source of the polymerization [10].

Meanwhile, polyhedral oligomeric silsesquioxanes (POSS) considered as one of silicon-based materials in nano-sized skeleton, consist of inorganic Si-O core and organic substituents [11]. Their applications recently involve in catalysis [12], sensors [13], biomedicines [14], and optical materials [15]. Previously, several attempts preparing sulfonic acid-functionalized POSS can be found through either nucleophilic or electrophilic substitution reactions [16,17]. Herein, we found that the complete formation of alkyl sulfonic acid moieties on POSS molecule could be simply achieved

* Corresponding author. Department of Chemistry, Center of Excellence for Innovation in Chemistry (PERCH-CIC), Center for Catalysis, Center for Inorganic and Materials Chemistry, Faculty of Science, Mahidol University, Rama VI Road, Ratchathewi, Bangkok 10400, Thailand.
E-mail address: vuthichai.erv@mahidol.ac.th (V. Ervithayasuporn).

http://dx.doi.org/10.1016/j.polymer.2016.11.038
0032-3861/

via oxidation reaction from the thioester (R-S-CO-R) precursor for the first time. Thus, our aim is to develop robust and efficient synthesis method of the hyperbranched acids based-silsesquioxane materials, named octakis(3-sulfopropyl)octasilsesquioxane (**2**). To the best of our knowledge, however, such organic-inorganic hybrid materials like polyhedral oligomeric silesesquioxanes (POSS) as a metal-free catalyst have not been applied to prepare PCL with well-controlled average molecular weight and without the use of any co-catalysts and solvents.

2. Experimental section

2.1. Materials and methods

Octakis(3-propyl ethanethioate)octasilsesquioxane (**1**), prepared according to our previous report [18], was used as a starting material for preparing the catalyst **2**. ε-Caprolactone (ε-CL) was purchased from Sigma Aldrich, dried over CaH_2 and distilled prior to use, hydrogen peroxide (30%) and glacial acetic acid were purchased from QREC and used as received. L-Menthol, 1-octanol, methyl acetoacetate, and amberlyst® 15 hydrogen form were purchased from Sigma Aldrich and used as recieved, toluene was bought from Honeywell B&J. Ethyl acetate and hexane were of commercial grade and distilled prior to use. Zeolite Y, hydrogen (powder, S.A. 780 m^2/g, 80:1 mole ratio of SiO_2:Al_2O_3) was purchased from Alfa Aesar, precoated silica gel 60 F254 plates and silica gel (No. 60) used for chromatography were purchased from Merck & Co., Inc.

The solution-state NMR spectra were obtained by using a Bruker-Ascend™ 400 high-resolution magnetic resonance spectrometer for ^1H (400 MHz) and $^{13}C\{^1H\}$ (100 MHz) nuclei. ^{29}Si CP/MAS NMR (59.606 MHz) experiment was recorded on a Varian VNMRS 300 MHz spectrometer using a two channel probe with 7.5 mm diameter size ZrO_2 rotors, while ^{29}Si CP/MAS NMR (79.51 MHz) experiment was measured from a Bruker-Ascend™ 400 WB spectrometer. Fourier transform infrared (FT-IR) spectra were collected using an attenuated total reflectance (ATR) technique with Bruker model Alpha spectrometer. DSC-TGA measurement was carried out by using a SDT 2960 Simultaneous DSC-TGA instrument. Approximately, 18 mg of the sample was capsulated in aluminum pans and was performed under oxygen atmosphere. The ion-exchange capacity (IEC) of **2** was confirmed by acid−base titrations with Denver model 215 pH meter. Approximately, 10 mg of the sample was dissolved and equilibrated in 15 mL of NaCl (2.0 M). The solution was stirred at room temperature for 1 h. Then, the solution was titrated by dropwise addition of NaOH (0.01 M). Gel permeation chromatography (GPC) analysis were performed on a Waters e2695 instrument equipped with Model 3580 refractive index detectors (Viscotek) and two 10 μm PL Gel columns. Tetrahydrofuran as a solvent was used to elute GPC columns with flow rate of 1.0 mL/min at 35 °C. Molecular weights and molecular weight distributions were also calibrated with polystyrene standards ranging from 500 to 10,000,000 amu.

3. Synthesis of octakis(3-sulfopropyl)octasilsesquioxane (2)

The starting material of octakis(3-propyl ethanethioate)octasilsesquioxane (**1**) (0.30 g, 0.22 mmol), prepared according to an established procedure [18], was firstly dissolved in 9.0 mL of glacial acetic acid in a round-bottom flask. Then, 1.5 mL of 30% hydrogen peroxide solution was slowly dropped into the reaction solution *via* a transfer syringe with continuing stir. The solution was kept stirred at room temperature for another 24 h. Evaporation of solvent gave a yellow solid, which was then redissolved in deionized water (10 mL). Insoluble contaminants were removed by extracting with 3×10 mL of CH_2Cl_2. The aqueous solution was kept and water was evaporated to obtain the pure product **2**. Finally, **2** was dried over vacuum to afford a white solid (0.21 g, 0.15 mmol, 68% yield). This hygroscopic material will tend to become dampand cakey when exposed to moist air.

^1H NMR (400 MHz, D_2O, 25 °C): $\delta = 1.88$ (tt, ^3J (H,H) = 6.40 and 5.20 Hz, 16H; CCH_2C), 2.88 (t, ^3J (H,H) = 5.20 Hz, 16H; SiCH_2), 3.61 (t, ^3J (H,H) = 6.40 Hz, 16H; CH_2S) ppm; $^{13}C\{^1H\}$ NMR (100 MHz, D_2O, 25 °C, DSS): $\delta = 29.68$ (CCH_2C), 50.66 (SiCH_2C), 62.90 (CCH_2S) ppm; ^{29}Si CP/MAS NMR (59 MHz, solid state, 25 °C): $\delta = -68.53$ ppm. The TGA ceramic yield was 31.3 versus 34.3 wt % theory.

4. POSS-catalyzed polymerization of ε-caprolactone

In a glove box, ε-caprolactone (1.0 g) in a thick-wall reaction-tube under argon atmosphere was introduced with 2.5, 5, 10, and 20 wt% of compound **2** as a POSS catalyst. The solution suspension was stirred at 60 °C for 14 h, until highly viscous polymer was observed. The reaction mixture was cooled down to room temperature, polycaprolactone/POSS composites appeared as a white solid. Catalyst **2** in polycaprolactone matrix was simply separated out by dissolving in 10 mL of CH_2Cl_2, following by filtration. The catalyst was further washed with 3×10 mL of CH_2Cl_2. Evaporation of combined CH_2Cl_2 layers gave pure polycaprolactone as a white solid in 95% yield (GPC (polystyrene standards): M_n = 3950, M_w = 5750, PDI = 1.46), 96% (M_n = 4580, M_w = 7610, PDI = 1.66), 96% (M_n = 7080, M_w = 12300, PDI = 1.74), and 97% (M_n = 12350, M_w = 20920, PDI = 1.69) yields, respectively.

5. Results and discussion

Octakis(3-propyl ethanethioate)octasilsesquioxane (**1**), prepared according to our previous report [18], was used as a starting material because of its ease of preparation and greater stability over thiol compounds. By performing oxidation reaction upon thioester, we can then bypass an important step of oxidizing the thiol group and disulfide bond, which is a major thermodynamic hindrance to achieve sulfonic acid. Notably, our synthesis route can efficiently prepare sulfonic acid functionalized-material using thiol-free precursors, solvent-omitted reaction, and environmentally friendly reagents [19]. Owing to our relatively mild condition and carefully chosen precursor, all eight thioester groups of the octasilsesquioxanes molecule were efficiently oxidized into sulfonic acids, while Si-O cage was left untouched.

In Scheme 1, complete oxidation reaction on **1** (0.30 g) in the presence of a solution mixture (1:6 v/v) of 1.5 mL of hydrogen peroxide solution 30% (w/w) in H_2O and 9.0 mL of glacial acetic acid was easily achieved within a day at an ambient temperature to obtain **2** (0.21 g) in high yield (68%). As the oxidation goes to completion, ^1H NMR spectroscopy of a key signal at 2.36 ppm (Fig. 1a) of methyl groups on **1** completely disappears, while a new set of signals of propyl linkages at 3.61, 2.88, and 1.88 ppm (Fig. 1b) of **2** in D_2O is all shifted downfield from 2.90, 1.66, and 0.71 ppm (Fig. 1a) of **1** in $CDCl_3$ because of the deshielding effect of electron withdrawing groups, thus confirming the formation of super-hydrophilic sulfonic acid groups. The reaction smoothly proceeds without any cage-decomposition or cage rearrangement as a result of clear, sharp, and correct coupling pattern from the NMR signals. As well as being confirmed by ^{29}Si CP/MAS NMR (Fig. S3), its spectrum appears only a single peak at −68.5 ppm, indicating that a symmetric environment for silicon atoms stably remain within a silsesquioxane T_8 cage. Interestingly, the signal detection from $^{29}Si\{^1H\}$ solution NMR could not be found. This observation is also consistent with a previous report for the presence of highly electrolytic nature or multiple charges on POSS molecule in polar

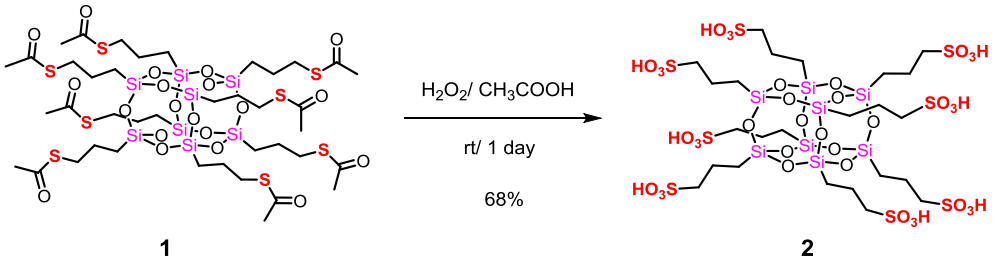

Scheme 1. Synthesis of octakis(3-sulfopropyl)octasilsesquioxane (**2**) *via* oxidation reaction.

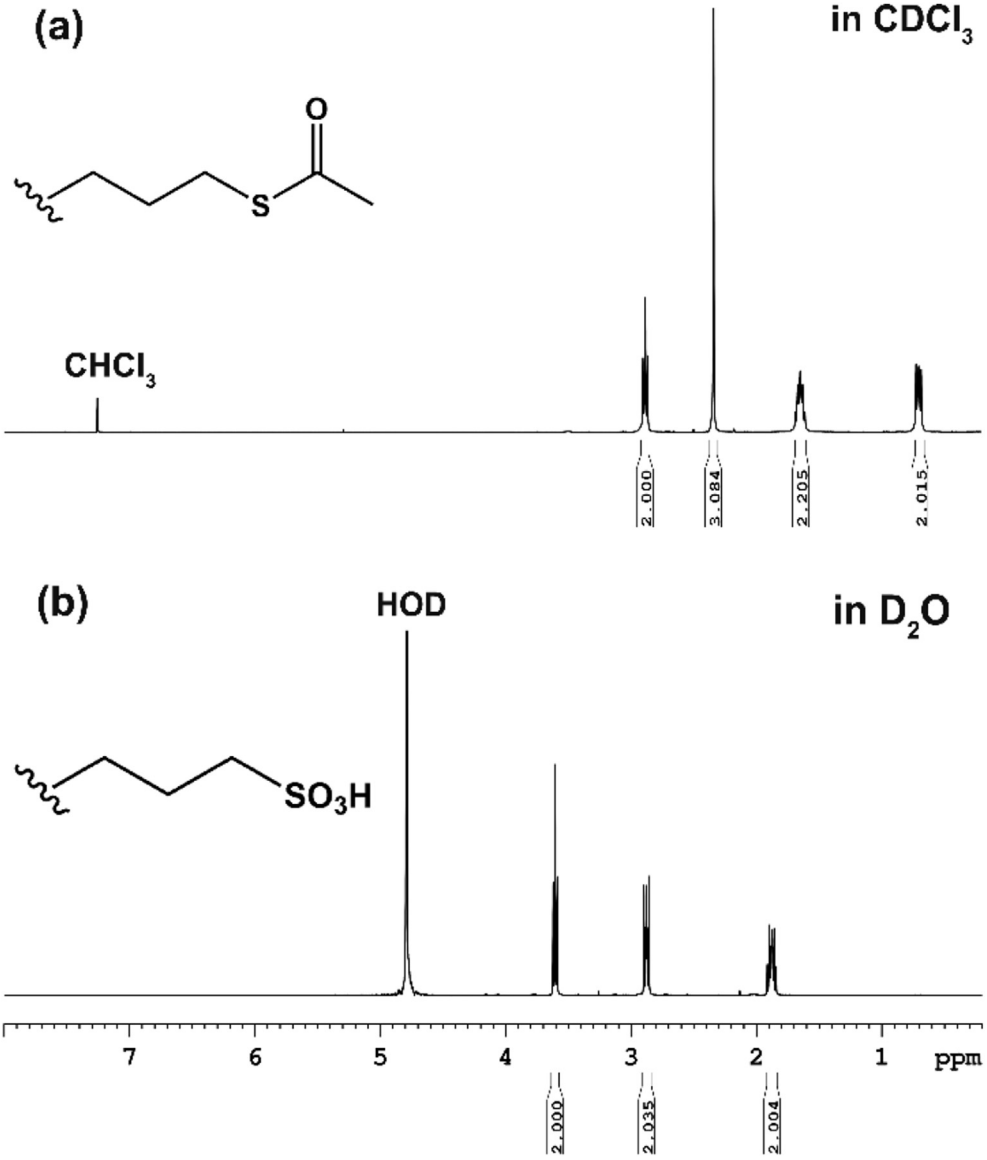

Fig. 1. ^{1}H NMR spectra of compounds (a) **1** in $CDCl_3$ and (b) **2** in D_2O.

solvents (e.g. imidazolium functionalized POSS) [20]. ^{29}Si isotope of those compounds and in our case can be, however, detected by using ^{29}Si CP/MAS NMR. It is noteworthy to mention that a side reaction could be observed when inappropriate amount of H_2O_2 ratio was introduced. We found that a lesser amount of H_2O_2 led to a formation of crosslinking silsesquioxane in a gel form, while a longer reaction time or higher amount of H_2O_2 gave an insoluble white precipitation, suggesting the overoxidation/degradation of product into the formation of inorganic silica.

Further evidenced by the changes in their infrared spectra, the characteristic peak at 1685 cm^{-1} from C=O stretching (carbonyl) and at 1370 cm^{-1} from CH_3 rocking of the propyl ethanethioate side chains of **1** in Fig. S4a disappeared, while the broad absorption bands at 3500–2500 cm^{-1} from O-H stretching and at 1700 cm^{-1}

from O-H bending of **2** become apparent in Fig. S4b. Regarding to the absorption of silica core, the key vibrational mode of silsesquioxane characteristic on both **1** and **2** is the strong broad band at 1080 and 1105 cm^{-1} assigned to Si-O stretching vibrations of the Si-O-Si network, respectively [21]. Thermogravimetric curve of **2** (Fig. S5) shows ~20% weight loss up to 180 °C, corresponding to the dehydration and desulfurization processes. This thermal analysis reveals that compound **2** is a hygroscopic material as the desorption of water molecule must first occur, followed by decomposition of sulfonic acid functional groups. Further gradual increasing in the temperature up to 470 °C results in the last degradation period of ~50% mass lost. This period is due to the combustion of the remaining organic moieties. Finally, the measured ceramic yield is found to be 31.3% compared to a theoretical value of 34.3%.

To confirm acid density of this material, the number of sulfonic acid groups on **2** is determined by acid-base titration against sodium hydroxide. The largest value of proton exchange capacities of **2** (Fig. S6) is 5.39 meq of H^+/g, well agreed with theoretical values of 5.71 meq of H^+/g. This result corroborates the conclusion that all ethanethioate groups are completely oxidized to sulfonic acid groups. Notably, the proton exchange capacities of **2** is much greater than that of any other sulfonic acid anchored on silica materials (0.5–1.2 meq of H^+/g) [22], suggesting that **2** has a very promising application as rich in electrolytic nature. Previously, those hybrid materials are conventionally prepared by directly treating thiol groups (R-SH) on the materials' surface with strong oxidants such as nitric acid and hydrogen peroxide [23]. Although the acidic density of these materials has been found to increase with enlarging surface area under vigorous conditions, it has not always equaled to the concentrations of either the thiol groups or oxidizing agents [24,25]. This result is indicative of an incomplete oxidation reaction and the transformation to sulfonic acid groups from all sulfur atoms is hardly achieved. Often, thiol precursor is only partially oxidized to form disulfide bond (R-S-S-R) with an adjacent thiol group or even remains unreacted thiol groups, in the case of oxidative deficiency [26].

To investigate the potential application of **2**, we deem to use this material as a catalyst. Firstly, as expected, material **2** is extremely hygroscopic and can be only dissolved in polar solvents such as water, dimethyl sulfoxide, dimethylformamide, ethanol, and methanol, but did not dissolve in non-polar solvents (e.g. toluene, dichloromethane, ethyl acetate and hexane). Herein, our desired material in this case can be replaced from other conventional acidic catalysts (e.g. amberlyst® 15) due to their practical utility from

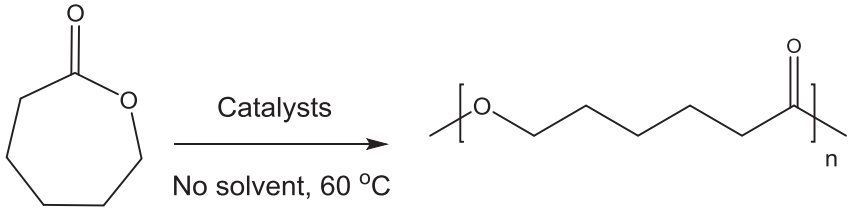

Scheme 2. Acid-catalyzed polymerization of ε-caprolactone using POSS **2**, amberlyst® 15, and zeolite Y, hydrogen as a catalyst.

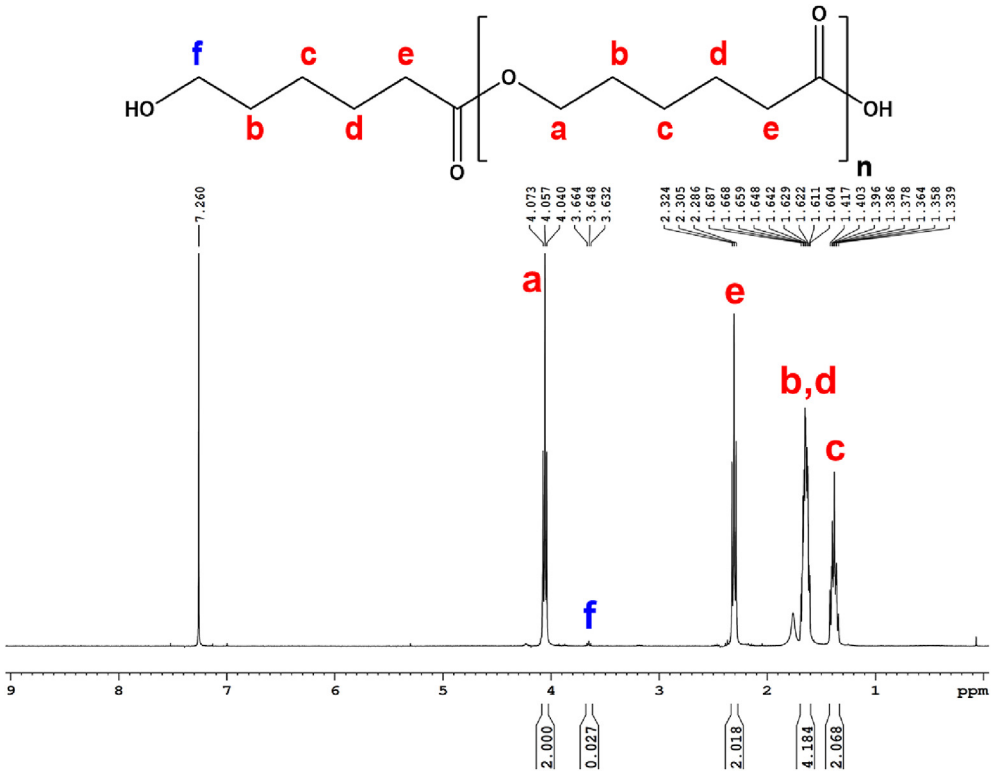

Fig. 2. ^{1}H NMR (400 MHz) spectrum of PCL in $CDCl_3$, synthesized by a ROP method using POSS catalyst at 2.5 wt%, and signal at 3.64 ppm illustrates the end methylene group labeled f.

similar conditions [27]. We preliminarily report that **2** has been effectively promising for a catalyst in transesterification of β-ketoesters with great yields and turnover frequencies (TOFs) (Scheme S1). Moreover, the recyclability of **2** was also determined in Table S2 and after recycling, moderate yields (47–54%) were obtained through three successive reactions with some loss of catalytic activity. It is well known that the sulfonated acid catalysts are subject to the catalyst deactivation in the presence of alcohols at higher temperature [28]. However, the catalyst **2** could be simply separated from the reaction mixtures *via* filtration after each catalytic run.

To widely explore a utility of material **2** used for the synthesis of PCL, we studied a range of catalytic loadings of POSS or how the molecular mass of a polymer varied as a function of the amount of POSS initiator employed in the ROP. Using POSS-catalyzed polymerization of ε-CL, pure ε-CL monomer in liquid state can be directly reacted with the POSS in a heterogeneous system (Scheme 2) to obtain PCL composite with POSS. After a complete polymerization reaction, the polymer was dissolved in dichloromethane and the suspension of insoluble POSS catalyst can be easily removed by filtration. The high yield of polymer was simply obtained by evaporation of solvent followed by vacuum drying, as characterized by ^{1}H NMR spectroscopy and GPC.

Using loadings at or above 2.5 wt%, conversion of the ε-CL monomer to PCL was highly quantitative. Characterization of PCL by ^{1}H NMR spectroscopy (Fig. 2), no by-product was observed, while ε-CL completely converted to PCL and the ^{1}H NMR spectrum of PCL showed a significant signal at δ 3.65 ppm (triplet) from the end chain; HO-CH_2- in PCL. This result shows that the successful polymerization of ε-CL monomer and increase of covalent attachment of PCL can be first initiated by the adsorpted H_2O *in situ* where that came from the surface of POSS material, as shown in Scheme S2 for a suggested mechanism. Indicating that POSS's acidic and superhydrophilic natures were the source of the polymerization reaction. Interestingly, as the loading of POSS was increased (from 2.5 up to 20.0 wt% in ε-CL monomer), number average molecular weight linearly increased (M_n range: 4.0–12.4 kDa, PDI range: 1.4–1.7) as shown in Fig. 3. With higher POSS loading (amount of catalyst), sulfonic acid functions would allow to increase the activation of the ε-CL monomer, resulting in a faster polymerization of ROP. As has been previously described in the synthesis of PCL from other acidic catalysts [29,30], we suggested that the PCL reaches an equilibrium chain length, dependent upon the number of acid catalyst and temperature.

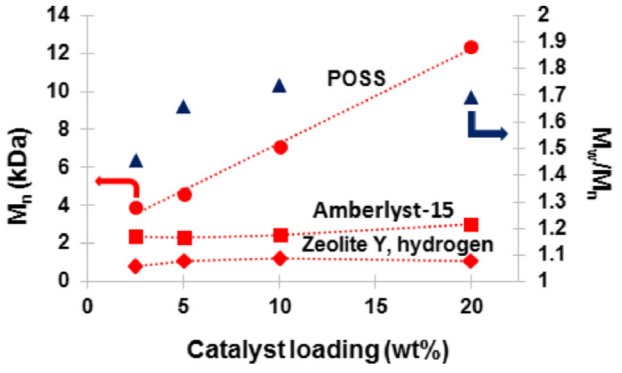

Fig. 3. Plot of number average molecular weight (M_n) (red labels) and PDI (blue triangles) versus catalyst loading of POSS (red circles), amberlyst® 15 (red squares), and zeolite Y, hydrogen (red diamond) in ε-caprolactone monomer for the synthesis of polycaprolactone (see Scheme 2). (For interpretation of the references to colour in this figure legend, the reader is referred to the web version of this article.)

To measure the catalytic stability after the synthesis of PCL, catalyst removal **2** appears additional features of two peaks, distinct ^{29}Si CP/MAS NMR resonances at −101 and −109 ppm (Fig. S10), corresponding to Q-type structured Si. These key signals indicate that some organic decomposition of POSS led to the formation of inorganic silica and its proton exchange capacities have been reduced to 3.89 meq of H^+/g. Therefore, the polymerization of ε-CL monomer is activated by the leaching of sulfonic species from a POSS catalyst existing as an acidic reservoir. However, the thermal degradation may lead to the reduction or even loss of the catalytic activities during polymerization [31]. In order to increase the molecular weight of PCL, only a certain amount of active catalyst must be sufficient. Undoubtedly, in this case, POSS catalyst loading is directly proportional to the extent polymerization, as well as sulfonic acid groups from POSS are considered as Brönsted acid-catalyzed reactions for living polymerizations [32].

Although, the leaching process of sulfonic species from acid catalyst is quite well-known [33], this ^{29}Si CP/MAS NMR of isolated catalyst reveals the first piece of direct evidence by partially turning T into Q types, as shown in Fig. 4. Since, our designed catalyst was made up from only pure T unit of a POSS molecule, the conventional catalyst of sulfonic acid functionalized-mesoporous silica is usually a combination of Q (silica) + T (silsesquioxane) types. Moreover, this phenomenon led to the higher catalytic activity (well-controlled polymerization of PCL) during a degradation catalyst of T into Q types. In order to compare to other solid acid catalysts,

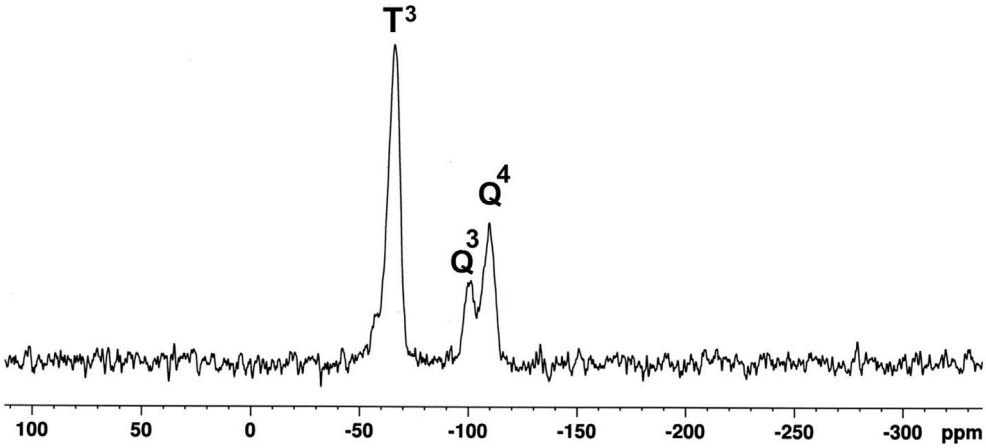

Fig. 4. ^{29}Si CP/MAS NMR (79.51 MHz) spectrum of catalyst **2** removed from POSS-catalyzed polymerization of ε-CL.

amberlyst® 15 containing sulfonic acids in macromolecular polymeric resin based on crosslinked styrene, was also tested for ROP of ε-CL monomer in a similar condition. As a result, it was shown that M_n of PCL was maintained in a range of 2–3 kDa. Moreover, lower molecular weight of PCL (M_n as low as 1 kDa) can be found using zeolite Y, hydrogen as shown in Fig. 3. In that case, those solid catalysts were less involved from leaching during the synthesis of PCL. Therefore, these results strongly support our hypothesis that POSS catalysts can be considered as an acidic reservoir. Their leaching process of sulfonic species is a key to increase the molecular weight of PCL and the contribution of homogeneous catalysis is not negligible.

6. Conclusions

We believe that this synthetic methodology describes the best prototype for preparation of silicon-based organic-inorganic hybrid materials containing the highest number of sulfonic acid groups in a pure form. Hence, this compound is considered as a hybrid molecule rich in Brönsted acid sites and is applicable for further use as a metal-free catalyst in neat condition. Moreover, this material shows the superior catalytic activity for a well-controlled polymerization of PCL under heterogeneous system, compared to other conventional acid catalysts.

Acknowledgements

This research is financially supported by the Thailand Research Fund (RSA5980018), Faculty of Science, Mahidol University, Center of Excellence for Innovation in Chemistry (PERCH-CIC), and the Nanotechnology Center (NANOTEC), NSTDA, Ministry of Science and Technology, Thailand, through its program of Center of Excellence Network.

Appendix A. Supplementary data

Supplementary data related to this article can be found at http://dx.doi.org/10.1016/j.polymer.2016.11.038.

References

[1] M. Labet, W. Thielemans, Chem. Soc. Rev. 38 (2009) 3484–3504.
[2] S. Chanda, S. Ramakrishnan, Polym. Chem. 6 (2015) 2108.
[3] A. Arbaoui, C. Redshaw, Polym. Chem. 1 (2010) 801–826.
[4] P. Christian, I.A. Jones, Polymer 42 (2001) 3989–3994.
[5] K. Kannan, K. Senthilkumar, J.P. Giesy, Environ. Sci. Technol. 33 (1999) 1776–1779.
[6] T.R. Blake, R.M. Waymouth, J. Am. Chem. Soc. 136 (2014) 9252–9255.
[7] S. Kobayashi, J. Polym Sci, Part A Polym. Chem. 37 (1999) 3041–3056.
[8] J. Casas, P.V. Persson, T. Iversen, A. Cordova, Adv. Synth. Catal. 346 (2004) 1087–1089.
[9] P.V. Persson, J. Schroder, K. Wickholm, E. Hedenstrom, T. Iverson, Macromolecules 37 (2004) 5889–5893.
[10] D.R. Dreyer, K.A. Jarvis, P.J. Ferreira, C.W. Bielawski, Polym. Chem. 3 (2012) 757–766.
[11] S. Chimjarn, R. Kunthom, P. Chancharone, R. Sodkhomkhum, P. Sangtrirutnugul, V. Ervithayasuporn, Dalton Trans. 44 (2015) 916–919.
[12] V. Ervithayasuporn, K. Kwanplod, J. Boonmak, S. Youngme, P. Sangtrirutnugul, J. Catal. 332 (2015) 62–69.
[13] L. Li, S. Feng, H. Liu, RSC Adv. 4 (2014) 39132–39139.
[14] C. Shen, Y. Han, B. Wang, J. Tang, H. Chen, Q. Lin, RSC Adv. 5 (2015) 53782.
[15] R. Sodkhomkhum, V. Ervithayasuporn, Polymer 86 (2016) 113–119.
[16] Y. Li, Q. Zhang, X. Zhao, P. Yu, L. Wu, D. Chen, J. Mater Chem. 22 (2012) 1884–1892.
[17] J.-H. Jeon, K. Tanaka, Y. Chujo, J. Mater Chem. A2 (2014) 624–630.
[18] V. Ervithayasuporn, T. Tomeechai, N. Takeda, M. Unno, A. Chaiyanurakkul, R. Hamkool, T. Osotchan, Organometallics 30 (2011) 4475–4478.
[19] D. Prat, A. Wells, J. Hayler, H. Sneddon, C.R. McElroy, S. Abou-Shehadad, P.J. Dunn, Green Chem. 18 (2016) 288–296.
[20] L.A. Bivona, O. Fichera, L. Fusaro, F. Giacalone, M. Buaki-Sogo, M. Gruttadauria, C. Aprile, Catal. Sci. Technol. 5 (2015) 5000–5007.
[21] E.S.H. Park, W. Ro, C.V. Nguyen, R.L. Jaffe, D.Y. Yoon, Chem. Mater 20 (2008) 1548–1554.
[22] J.A. Melero, R. van Grieken, G. Morales, Chem. Rev. 106 (2006) 3790–3812.
[23] E. Cano-Serrano, J.M. Campos-Martin, J.L.G. Fierro, Chem. Commun. (2003) 246–247.
[24] A. El Kadib, A. Finiels, D. Brunel, Chem. Commun. 49 (2013) 9073–9076.
[25] Y. Kaneko, H. Toyodome, T. Mizumo, K. Shikinaka, N. Iyi, Chem. Eur. J. 20 (2014) 9394–9399.
[26] V. Dufaud, M.E. Davis, J. Am. Chem. Soc. 125 (2003) 9403–9413.
[27] S.P. Chavan, Y.T. Subbarao, S.W. Dantale, R. Sivappa, Synth. Commun. 31 (2001) 289–294.
[28] J.M. Fraile, E. García-Bordejé, L. Roldán, J. Catal. 289 (2012) 73–79.
[29] G. Cheng, X. Fan, W. Pan, Y. Liu, J. Polym. Res. 17 (2010) 847–851.
[30] Q. Zhang, B. Wang, K. Hong, Q. Zhu, Macromol. Chem. Phys. 195 (1994) 2401–2407.
[31] J.M. Andersona, R.L. Johnsonb, K. Schmidt-Rohrb, B.H. Shanks, Catal. Commun. 51 (2014) 33–36.
[32] M. Oshimura, T. Tang, A. Takasu, J. Polym. Sci. A Polym. Chem. 49 (2011) 1210–1218.
[33] J. Juan-Alcañiz, R. Gielisse, A.B. Lago, E.V. Ramos-Fernandez, P. Serra-Crespo, T. Devic, N. Guillou, C. Serre, F. Kapteijn, J. Gascon, Catal. Sci. Technol. 3 (2013) 2311–2318.

Sensors and Actuators B 245 (2017) 665–673

Contents lists available at ScienceDirect

Sensors and Actuators B: Chemical

journal homepage: www.elsevier.com/locate/snb

Imidazolylmethylpyrene sensor for dual optical detection of explosive chemical: 2,4,6-Trinitrophenol

Rapheepraew Sodkhomkhum[a], Manlika Masik[a], Sarayut Watchasit[b], Chomchai Suksai[c], Jaursup Boonmak[d], Sujittra Youngme[d], Nantanit Wanichacheva[e], Vuthichai Ervithayasuporn[a,*]

[a] Department of Chemistry, Center of Excellence for Innovation in Chemistry (PERCH-CIC), Center for Catalysis, Center for Inorganic and Materials Chemistry, and Center of Intelligent Materials and Systems, Nanotec Center of Excellence, Faculty of Science, Mahidol University, Rama VI Road, Ratchathewi, Bangkok 10400, Thailand
[b] Nuclear Magnetic Resonance Spectroscopic Laboratory, Science Innovation Facility, Faculty of Science, Burapha University, Chonburi 20131, Thailand
[c] Department of Chemistry and Center for Innovation in Chemistry, Faculty of Science, Burapha University, Chonburi 20131, Thailand
[d] Materials Chemistry Research Center, Department of Chemistry and Center of Excellence for Innovation in Chemistry (PERCH-CIC), Faculty of Science, Khon Kaen University, Khon Kaen 40002, Thailand
[e] Department of Chemistry, Faculty of Science, Silpakorn University, Nakhon Pathom 73000, Thailand

ARTICLE INFO

Article history:
Received 22 August 2016
Received in revised form 11 January 2017
Accepted 20 January 2017
Available online 23 January 2017

Keywords:
Chemical sensor
Host-guest chemistry
Fluorescent sensor
Explosives
Fluorescence enhancement
Fluorescence quenching

ABSTRACT

Fluorescence and colorimetric sensor with simplistic synthesis method based on 1-imidazolylmethylpyrene (**IMPY**) was found to be a specific recognition for an explosive chemical: 2,4,6-trinitrophenol or picric acid (**PA**). The sensor did not only provide highly sensitive OFF–ON fluorescence enhancement toward **PA** in acetonitrile, but also offered ON–OFF fluorescence quenching upon **PA** binding in toluene solution. In addition, the sensor **IMPY** provided high selectivity to 2,4,6-trinitrophenol and was shown to discriminate various phenolic compounds such as *p*-iodophenol, *p*-bromophenol, *m*-hydroxybenzaldehyde, *o*-nitrophenol, *m*-nitrophenol, *p*-nitrophenol and 2,4-dinitrophenol. Upon binding to **PA**, the fluorogenic change of the sensor were observed and accompanied by the noticeable chromogenic change from colorless to yellow, therefore the sensor could also serve as a "naked-eye" indicator. Finally, two different types of crystal structures of **IMPY**·**PA** complexes were successfully recrystallized and characterized, which confirmed highly interactive affinity of the host-guest molecules.

1. Introduction

Nowadays, terrorists-attacks occur in countries around the world with an extensive use of explosive chemicals. Therefore, the detection of those explosives in a trace amount becomes great interests and necessary for social safety [1]. 2,4,6-Trinitrophenol or picric acid (**PA**) is one of the highly reactive compounds and its explosive power is almost similar to other nitroaromatic compounds (NACs) such as trinitrotoluene (TNT), and dinitrotoluene (DNT) [2]. Moreover, **PA** is widely used in many industries as a composition of the products such as firework, matches, leather, and dyes [3–5]. Currently, **PA** determination can be detected by gas chromatography, Raman spectroscopy, and fluorescence spectroscopy [6,7]. However, fluorescence detection of **PA** presents many promising approaches because it allows high sensitivity, rapid response and real-time monitoring [8,9]. In addition, fluorescent sensor for **PA** can allow the on-site preliminary screening which will greatly benefit prevention of the explosion and social security.

The continuous developments of probes for **PA** detection have been provided through the compounds with electron deficient phenyl ring and/or the acidic hydroxyl group [9–17]. Anthracene and pyrene were found to be potential fluorophores to detect NACs, due to the strong binding of the electron deficient phenyl ring of the nitro groups on the NACs to the polyaromatic hydrocarbon (PAHs) through π-π interaction [18,19]. In particularly, pyrene and their derivatives have been one of the most intensive-used fluorophores for **PA** fluorescent sensors due to their high fluorescent emission. Commonly, developed pyrene structures for **PA** sensor were based on several hydrogen bonding and π-π interactions. However, most of the reported **PA** fluorescent chemosensors operated

* Corresponding author.
E-mail addresses: vuthichai.erv@mahidol.ac.th, maldiniandg@hotmail.com (V. Ervithayasuporn).

http://dx.doi.org/10.1016/j.snb.2017.01.120
0925-4005/

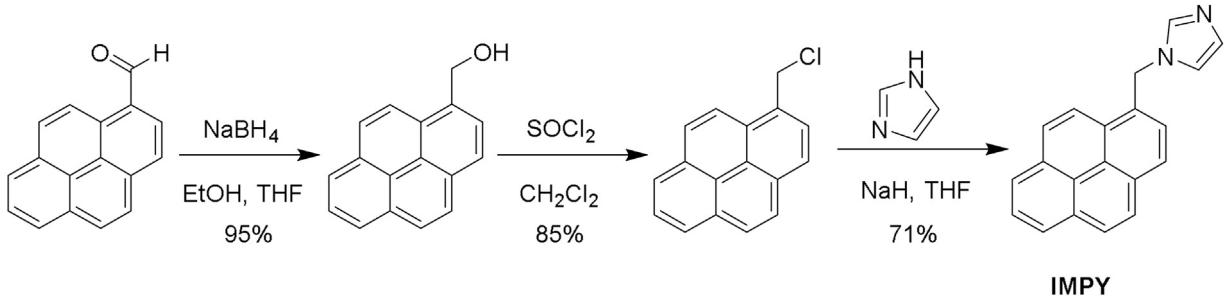

Scheme 1. Synthetic approach to prepare 1-imidazolylmethylpyrene (**IMPY**).

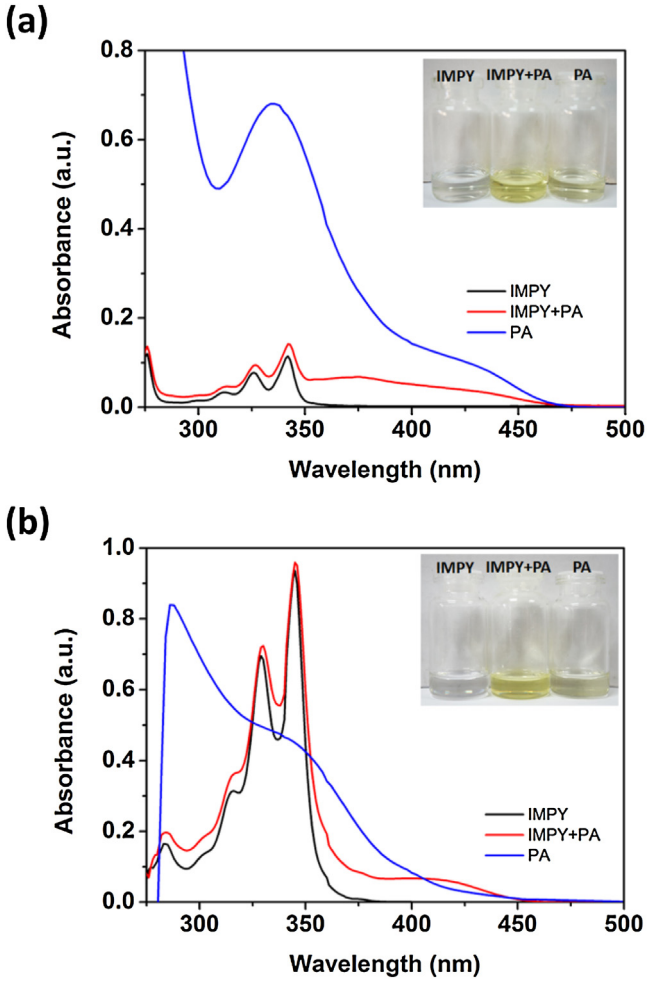

Fig. 1. Absorption spectra of **IMPY** in the presence and absence of **PA** in (a) toluene and (b) acetonitrile.

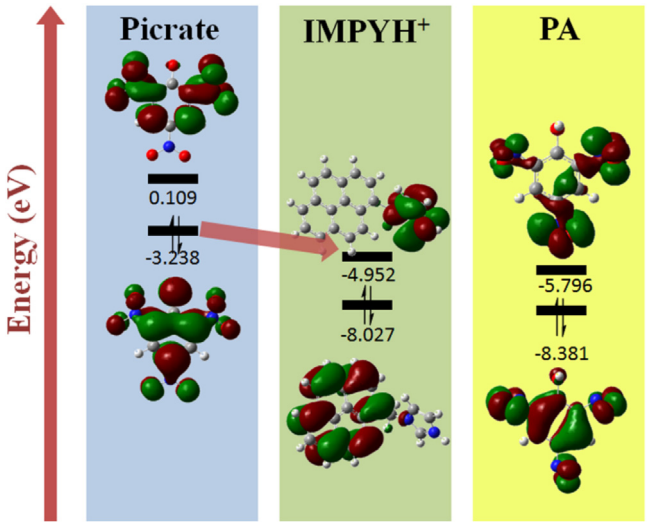

Fig. 2. Calculated energy level diagram of picrate anion, protonated **IMPY**, and picric acid (**PA**) [17].

via an ON–OFF fluorescent quenching mechanism without chromogenic change [17,20–22]. Therefore, the development of high sensitive and selective **PA** fluorescent sensor that could be operated *via* both OFF–ON and ON–OFF responses, which also exhibited the chromogenic change will be a great challenge, and could benefit on-site detection of **PA** due to the versatility to use the sensor.

Herein, we found that the designed sensor of 1-imidazolylmethylpyrene (**IMPY**) could be used as a **PA** fluorescent chemosensor and could be operated through both enhancement and quenching of fluorescence by simply switching the solvent systems. Importantly, the sensor exhibited high selectivity and sensitivity to **PA** and also exhibited chromogenic change from colorless to yellow in the presence of **PA**. Therefore, the developed sensor could also serve as a "naked-eye" indicator.

2. Experimental section

2.1. Materials and instruments

1-Pyrenecarboxaldehyde (purity, 99.0%), sodium borohydride (powder, ≥98.0%), imidazole (purity, ≥99.0%) and sodium hydride (60% dispersion in mineral oil) were purchased from Sigma-Aldrich. Thionyl chloride (purity, ≥99.0%) was purchased from Merck millipore. Precoated silica gel 60 F_{254} plates and silica gel (No. 60) used for chromatography were purchased from Merck & Co., Inc. Acetonitrile, toluene, tetrahydrofuran, and ethanol were purchased from Honeywell Burdick & Jackson® without further distillation, while the commercial grade of methanol and methylene chloride were further distilled at atmospheric pressure.

NMR spectra were obtained in $CDCl_3$ and DMSO-d_6 solutions using the known chemical shift of the residual ^1H solvent signal as the reference: $CDCl_3$ = 7.26 and DMSO-d_6 = 2.54 ppm by a Bruker-AV 400 of high-resolution magnetic resonance spectrometer for ^1H (400 MHz) nuclei. The mass spectrum of the **IMPY** product was acquired using a micro-TOF mass spectrometer of VQ-TOF 2. UV–Vis spectra were obtained on a UV–Vis spectrophotometer of JASCO Model V-530. Absorption spectra were collected in toluene and acetonitrile for molar concentrations used in **IMPY** (3 μM) and all phenolic compounds (1.2×10^{-4} M). Fluorescence spectra were obtained on a spectrofluorometer of JASCO FP-6200 using a 1 cm path length of quartz cell. In a fluorescence titration study

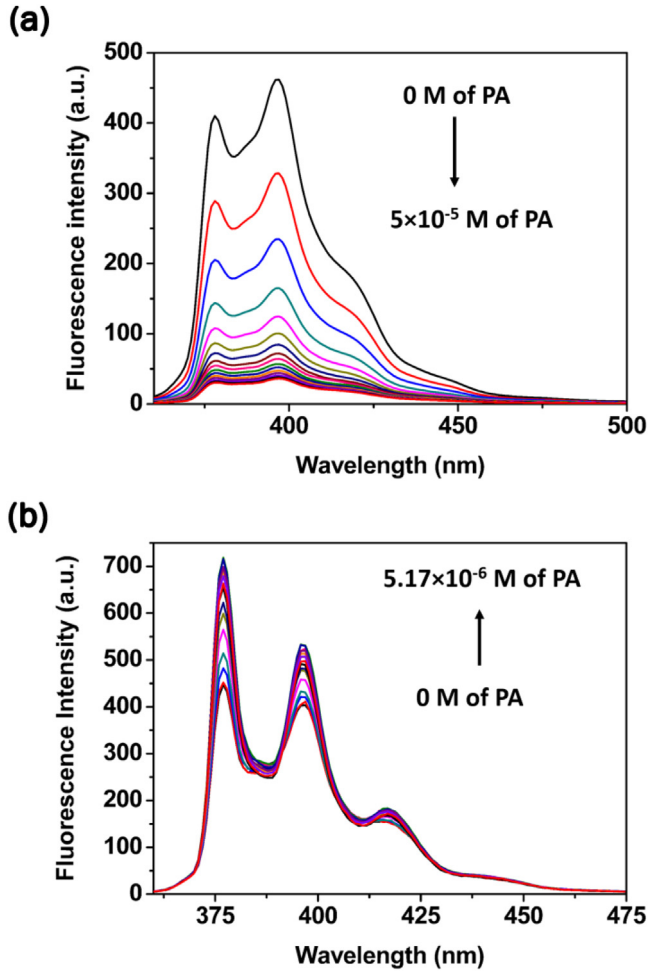

Fig. 3. Fluorescence emission spectra (λ_{ex} = 345 nm) of **IMPY** in (a) toluene, (b) acetonitrile as function of [**PA**].

between **IMPY** and picric acid (**PA**), the stock solution (2 mL) of **IMPY** (3 μM) was first placed in the quartz cell. Subsequently, **PA** (1.2×10^{-4} M) solution was added into an incremental fashion at 10 μL per time until unchanged spectrum was observed. For each titration experiment, the results were obtained by repeating twice [23]. For all fluorescence measurements, the experiments were excited at 342 nm due to highest peak in UV–Vis absorption. The limit of fluorescence sensing detection was also calculated from the titration plot of relative value as a function of log[**PA**]. Relative value can be determined from $(I_{max} - I_{obs})/(I_{max} - I_{min})$, in which I_{max} and I_{min} are the highest and lowest fluorescence intensities, respectively. The binding constant was calculated from the fluorescence sensing titration plot of $1/(I - I_o)$ as a function of 1/[**PA**] in moles, in which I_o and I are fluorescence intensities of the sensor without and with the presence of **PA**, respectively. A concentration of **IMPY** (3 μM) was used to study the fluorescence titration with **PA** (1.2×10^{-4} M) and was varied until the spectra were unchanged.

The apparent binding constant for the formation of the host-guest complex was calculated using a Benesi–Hildebrand plot [24]. Stern–Volmer (SV) quenching rate constants were estimated by plotting the ratio of I_o/I with a concentration of quencher [Q], where I_o and I are the maximum fluorescence intensity of the **IMPY** before and after the addition of analytes [25], respectively. The interaction of **IMPY** is confirmed by ^{1}H NMR titration study in DMSO-d_6. The solution (0.5 mL) of **IMPY** (5 mM) is added in NMR tube, followed by the addition of **PA** (50 mM) at 5 μL per time until the spectra were unchanged.

The fluorescence quantum yield (Φ_F) was calculated by using 9,10-diphenylanthracene in ethanol as the standard sample, which have a fixed and known fluorescence quantum yield (Φ_{ST} = 0.95) [26], to the following equation: $\Phi_x = (\Phi_{ST} \times Grad_x \times \eta_x^2)/(Grad_{ST} \times \eta_{ST}^2)$. Where the subscripts of ST and x refer to the standard and test samples, respectively, Φ is the fluorescence quantum yield; Grad is the gradient from the linear plot of integrated fluorescence intensity *vs* absorbance; η is the refractive index of the solvent [27–29]. For each test sample, the data of an absorption and emission were obtained from five different concentrations of **IMPY** (0.2, 0.4, 0.6, 0.8, and 1.0 μM), which was added with **PA** (0.1 mM)

Co-crystals of **IMPY·PA1** (CCDC 1493378) and **IMPY·PA2** (CCDC 1493387) were obtained by recrystallization in hot methanol suitable for X-ray structural analysis. X-ray data were collected by Bruker D8-Quest PHOTON-100 CMOS detector, with graphite-monochromated Mo K-alpha radiation (λ = 0.71073 Å) at 298 K using the APEX2 program. The full matrix least-squares procedures using SHELXTL2014 on F^2 anisotropic for all non-hydrogen atom was used to refine the crystal structures. Hydrogen atoms were placed in their calculated positions and refined following the riding model. The oxygen atoms (O2 and O3) of nitro group on picrate anion in **IMPY·PA2** were disordered over two positions, their occupancies were freely refined to be 70:30. The crystal data and structural refinement parameters are summarized in Table S1.

2.2. Synthesis of 1-imidazolylmethylpyrene (IMPY)

2.2.1. Synthesis of 1-hydroxymethylpyrene [30]

1-Pyrenecarboxaldehyde (500 mg, 2.17 mmol) was dissolved in anhydrous THF (2.5 mL) in 50 mL round bottom flask. Then, the mixture of $NaBH_4$ (250 mg, 6.61 mmol) in 95% ethanol (10 mL) was prepared in order to reduce vigorousness of the further reaction, and slowly added into the solution mixture of 1-pyrenecarboxaldehyde at 0 °C. The reaction solution was kept stirring at 0 °C for 5 min in an ice bath, after that the ice bath was taken off and continuously stirred at the room temperature for 30 min. After that the reaction mixture was quenched with 10 mL of HCl (1 M), diluted with deionized water (15 mL), and finally extracted with CH_2Cl_2 (3 × 20 mL). The combined organic fractions were dried with anhydrous Na_2SO_4. Evaporation of solvent gave the desired product, which could be used without further purification (480 mg, 2.07 mmol, 95%): ^{1}H NMR (400 MHz, $CDCl_3$), δ: 8.41 – 8.02 (m, 9H, Ar-*H*), 5.43 (s, 2H, Py-C*H*$_2$-OH).

2.2.2. Synthesis of 1-chloromethylpyrene [31]

1-Hydroxymethylpyrene (480 mg, 2.07 mmol) was stirred with thionyl chloride (174.1 μL, 2.4 mmol) in CH_2Cl_2 at room temperature. After 6 h, cracked ice and CH_2Cl_2 20 mL was added to the solution. The organic layer was washed with water and saturated $NaHCO_3$, and then dried with anhydrous Na_2SO_4. Evaporation of solvent afforded a dark green powder of desired product (440 mg, 1.75 mmol, 85%): ^{1}H NMR (400 MHz, $CDCl_3$), δ: 8.38 – 8.01 (m, 9H, Ar-*H*), 5.34 (s, 2H, Py-C*H*$_2$-Cl).

2.2.3. Synthesis of 1-imidazolylmethylpyrene (*IMPY*) [32]

A solution of imidazole (239 mg, 3.51 mmol) in dry THF (7 mL) was added into sodium hydride (60% dispersion in mineral oil, 140 mg, and 3.50 mmol) at 0 °C. Then, 1-chloromethylpyrene (440 mg, 1.75 mmol) in dry THF (13 mL) was subsequently added into the reaction mixture at 0 °C. After additional stirring for 12 h at room temperature, the reaction mixture was poured into 50 mL of deionized water and extracted with CH_2Cl_2 (3 × 20 mL). The combined organic layers were separated, dried over anhydrous Na_2SO_4, filtrate and dried under vacuum to provide a crude product (390 mg, 1.38 mmol, 79%). Purification by using column chromatography

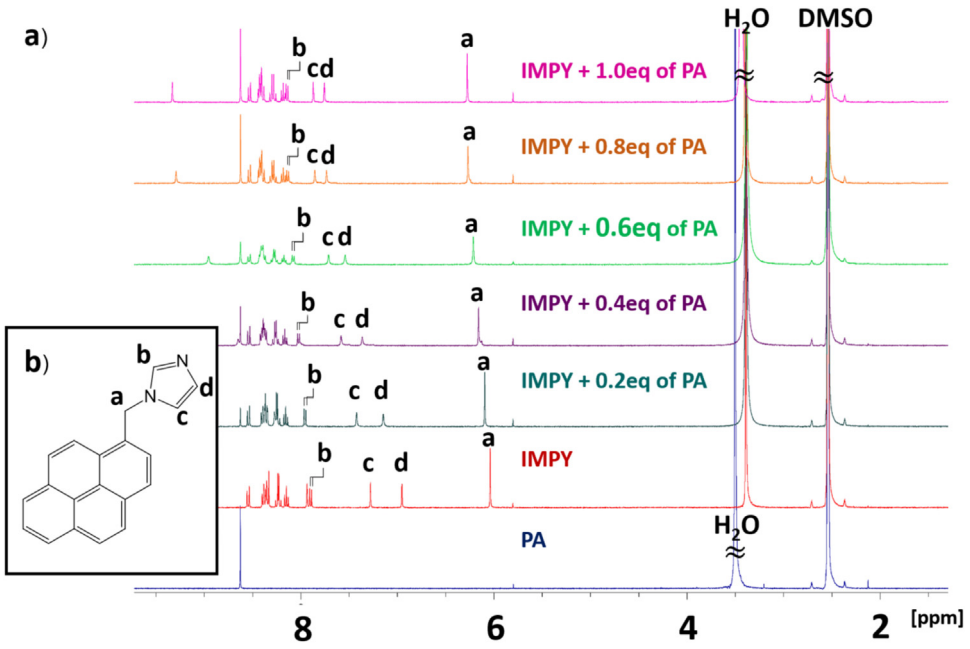

Fig. 4. ^{1}H NMR spectra of **IMPY** in DMSO-d_6 in the presence and absence of **PA.**

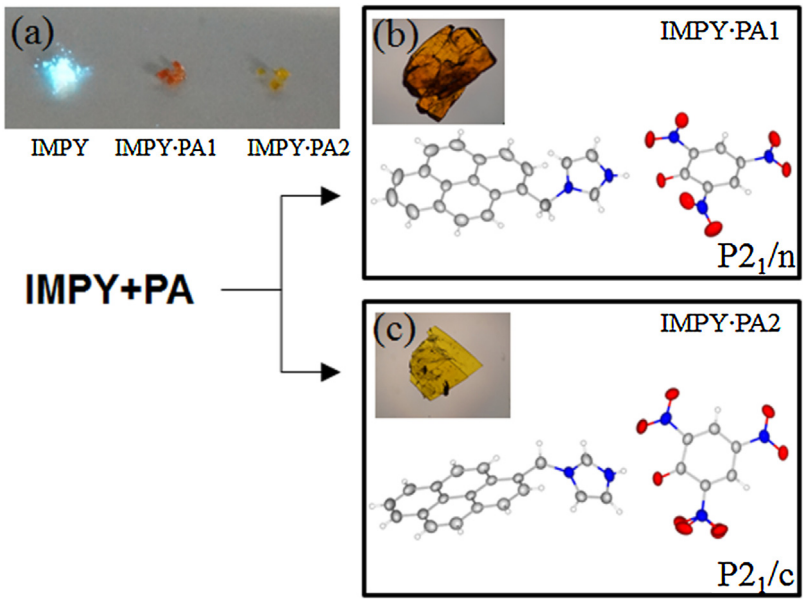

Fig. 5. (a) Photos of **IMPY**, **IMPY·PA1** and **IMPY·PA2** under UV lamp (λ = 366 nm), X-ray structures of host-guest complexes of **IMPY·PA** in (b) $P2_1/n$ and (c) $P2_1/c$ space groups.

with silica gel as a stationary phase (3% of methanol in CH_2Cl_2, R_f = 0.11) afforded **IMPY** product (350 mg, 1.24 mmol, 71%): ^{1}H NMR (400 MHz, $CDCl_3$), δ: 8.23 – 8.03 (m, 8H, Ar-*H*), 7.75 – 7.73 (d, *J* = 7.88 Hz, 1H, N-*CH*-N), 7.63 (s, 1H, Ar-*H*), 7.10 (s, 1H, N-*CH*), 6.95 (s, 1H, N-*CH*), 5.86 (s, 2H, Py-CH_2-N); ^{13}C NMR (400 MHz, $CDCl_3$), δ: 137.4 (N-CH-N, 131.6 (C_{py}), 131.2 (C_{py}), 130.54 (C_{py}), 129.7 (C_{py}), 128.8 (C_{py}), 128.6 (C_{py}), 128.3 (C_{py}), 127.9 (N-CH), 127.3 (C_{py}), 126.4 (C_{py}), 126.9 (C_{py}), 125.8 (C_{py}), 125.6 (C_{py}), 124.9 (C_{py}), 124.6 (C_{py}), 121.6 (N-CH), 119.4 (C_{py}), 48.84 (CH_2); HRMS (ESI-TOF) calcd for $C_{20}H_{15}N_2[M+H]^+$: *m/z* 283.1230; found, *m/z* 283.1290.

2.3. Computational methodology

Full geometry optimizations of picric acid, picrate anion and protonated 1-imidazolylmethylpyrene (**IMPYH**$^+$) were studied by density functional method (DFT) using B3LYP functional, 6-31G as the basic set in Gaussian (03) program [33].

3. Results and discussions

3.1. Synthesis and molecular design of *IMPY*

From the literatures [30–32], **IMPY** sensor could be simply prepared by a conventional three-step synthesis as shown in Scheme 1. 1-Pyrenecarboxaldehyde was reduced to 1-hydroxymethylpyrene in good yield (95%). Then, 1-hydroxymethylpyrene was treated with thionyl chloride to achieved 1-chloromethylpyrene (yield of 85%). After that, the 71% yield of sensor; **IMPY** was obtained from the *N*-alkylation of imidazole on 1-chloromethylpyrene (Additional characterizations shown in Figs. S2–S6). Herein, **IMPY** molecule

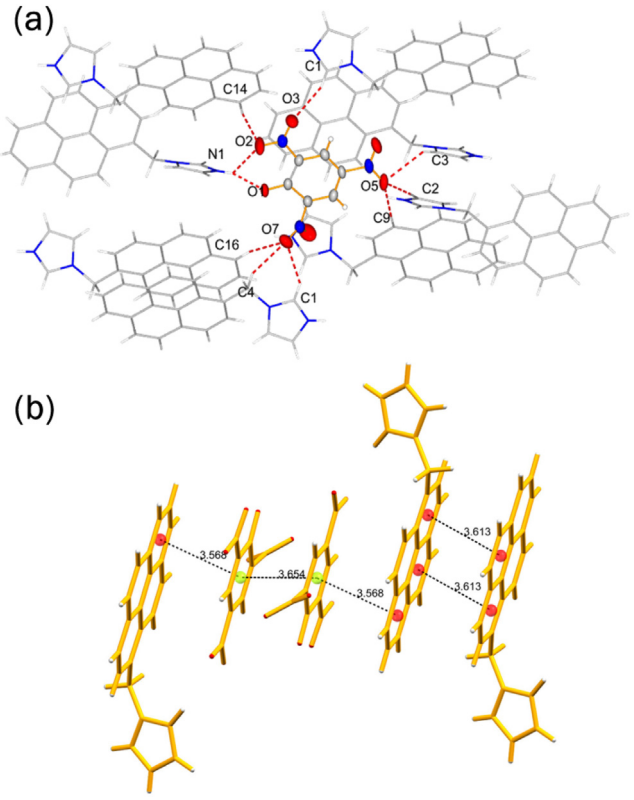

Fig. 6. (a) Picrate anion was connected with eight **IMPYs** *via* various intermolecular H-bonds in **IMPY·PA1** (The H-bondings are shown in red broken lines) and (b) Face-to-face π-π stacking interactions between pyrene rings and picrate anions in **IMPY·PA1**. (For interpretation of the references to color in this figure legend, the reader is referred to the web version of this article.)

contained one unit of imidazole, covalently bonding with pyrene fluorophore. As expected, the imidazole ring was employed to be a sensitive nitrogen heterocycle binding with **PA** *via* hydrogen bonding, as well as pyrene subunit and **PA** *via* π-π interactions.

3.2. Sensitivity studies

In this study, the sensing properties of sensor **IMPY** were examined by UV–Vis and fluorescence measurements in toluene and acetonitrile. It was found that **IMPY** provided colorless in both solvent systems. The UV–Vis absorption spectrum of **IMPY** displayed the absorption bands (λ_{max}) at around 283, 316, 329 and 345 nm ascribed mostly to $S_0 \rightarrow S_2$ transition of pyrene [34,35]. The addition of **PA** to the solutions of **IMPY** in toluene and acetonitrile resulted in an appearance of new absorption bands at approximately 420 nm and 377 nm, respectively, and induced a visual color change from colorless to yellow which could be easily detected by the naked eye. Fig. 1 shows absorption of **IMPY** in the presence and absence of **PA** in toluene and acetonitrile solvent systems.

From UV–Vis spectra, the appearance of a charge-transfer band ~420 nm (Fig. 1) after the addition picric acid is supported by theoretical calculation of ground-state charge-transfer complex formation that correlated with DFT (Density Function Theory) calculation in the gas phase (Fig. 2) [17]. The calculation exhibited electron migration from HOMO of picrate anion to LUMO of protonated **IMPY**, which was appropriated with the ground state charge transfer complex formation.

To clarify the quantitative binding affinity of **IMPY**, fluorescence titrations of **IMPY** with **PA** were gradually carried out in toluene and acetonitrile solutions. Fig. 3 shows the fluorescence spectra of

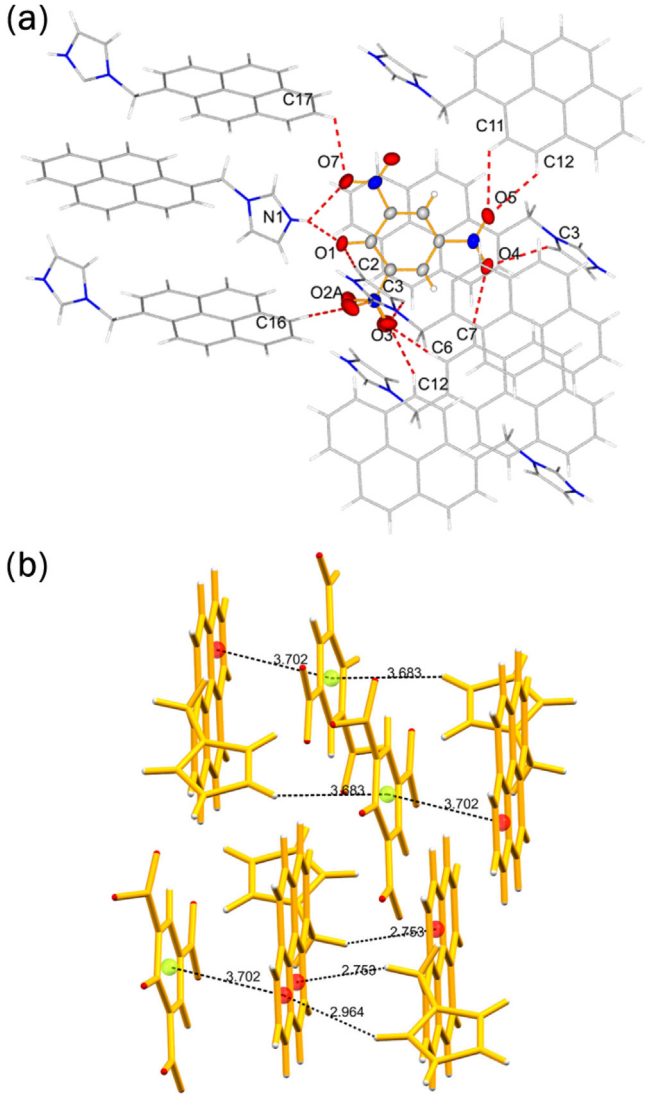

Fig. 7. (a) Picrate anion was connected with eight **IMPYs** *via* various intermolecular H-bonds in **IMPY·PA2** (The H-bonding are shown in red broken lines) and (b) several C—H-π, π-π stacking interactions between pyrene rings and picrate anions in **IMPY·PA2**. (For interpretation of the references to color in this figure legend, the reader is referred to the web version of this article.)

IMPY in the presence and absence of different concentrations of **PA**.

In toluene solution, it was found that **IMPY** provided colorless and strong fluorescence signal at 378 and 397 nm upon excitation at 345 nm, which are typical monomeric emission bands of pyrene in the term of quantum yield = 0.126 (Fig. S10). The addition of **PA** to the solution of **IMPY** results in a chromogenic change to the yellow color as well as quenching of the fluorescence ($\Phi_{IMPY+2eq\ of\ PA} = 0.068$ and $\Phi_{IMPY+10eq\ of\ PA} = 0.020$) (Fig. S10). The rapid decreasing of fluorescence signal clearly demonstrated the "ON-—OFF" switching mechanism occurred in response to **IMPY·PA** complexation. The quenching process of **IMPY** upon **PA** binding could be due to the formation of a ground state charge transfer complex and resonance energy transfer (RET). The quenching efficiency was estimated by Stern-Volmer (SV) rate constants (K_{SV}) = 8.47×10^4 M (Fig. S9). The detection limit of **IMPY** as a **PA**-fluorescent sensor was determined from the correlation between the fluorescence intensity and **PA** concentration and was found to be 576 ppb in toluene system. On the other hand, the titration of **PA** to the solution of **IMPY** in acetonitrile induced "OFF–ON" switching

mechanism and provided the fluorescence enhancement at 378 and 397 nm. Though only **IMPY** in acetonitrile exhibited a weak fluorescence signal (Φ_{IMPY} 0.056), after formation of **IMPY**·**PA** complex in acetonitrile the quantum yield slightly increased a fold-change of 1.25. The probability of the increased fluorescence intensity might be due to the inhibition of conformational change in excited state of **IMPYH**$^+$ upon of **IMPY**·**PA** complex in polar aprotic solvent as suggested in reference [36]. Thus, the detection limit was found to be 244 ppb for the determination of **PA**.

The binding constants of **IMPY** with **PA** in toluene and acetonitrile were calculated to be $6.58 \times 10^4\ M^{-1}$ and $1.85 \times 10^6\ M^{-1}$, respectively, according to the Benesi–Hildebrand plots (Fig. S8) of the signal changes in the fluorescence titration results. Therefore, the 1:1 complex formation of **IMPY**·**PA** was suggested and consistent with single-crystal X-ray diffraction result (Table S1).

3.3. Modes of binding

^{1}H NMR spectroscopy and X-ray diffraction were utilized to study binding mode of sensor **IMPY** and **PA**. ^{1}H NMR results of **IMPY** illustrated that the proton signals of both pyrene and methylimidazole units were shifted upon the addition of **PA** using DMSO-d_6 as a solvent (Fig. 4). The downfield shift of the methylimidazole protons (H_a, H_b, H_c and H_d) upon the addition of **PA** suggested an interaction between methylimidazole and picric acid. In addition, the downfield shifts of pyrene protons around 8.1–8.4 ppm were consistent with the π−π interaction between the pyrene and aromatic ring of **PA**.

Single-crystal X-ray diffraction of co-crystalline structures of **IMPY** and picric acid complexes revealed a host-guest complex of 1:1 (Fig. 5). The appearance of orange and yellow crystals was formed during the slow evaporation of methanol (Figs. 5, S11, and S12). The nitrogen atoms of imidazole groups on **IMPY** in both crystal structures exhibited the protonation in cation form, while picric acid was deprotonated into a picrate anion. Consequently, the nitrogen of **IMPY** was switched from H-bond acceptor into donor, while picrate anion was transformed into H-bond acceptor. The X-ray crystal structures affirmed the formation of hydrogen bond between protonated **IMPY** and deprotonated form of picric acid.

In both crystal structures, the negative charge at oxygen of picrate anion delocalized to aromatic ring though C—O bond that showed bond distances of 1.239(3)–1.255(3) Å, correlated with CO. These crystal structures crystallized in the same monoclinic crystal system but different space group. The protonated **IMPY** and picrate anions were self-assembled by multiple H-bond and π-π stacking interactions. The orange crystal crystallized in $P2_1/n$ space group (Fig. 5b). The dihedral angle between pyrene plane and imidazole ring was 71.2°. This structure showed that each picrate anion connected with eight **IMPYs** *via* ten H-bonds; and each **IMPY** also connected with eight picrate anions *via* ten H-bonds. The D···A distances of hydrogen bond and the DH···A angles were in the range 2.713(2)–3.598(2) Å and 117–176°, while weak CH···O interactions were included (Fig. 6 and Table S2). Hydrogen bonds of N1 with O1 and O2 were stronger than others with shorter distances. These results indicated that the protonated form of methylene imidazole part was an active site to respond with picrate anion. Two steps of mechanism were proposed for the specific key site. Firstly, the imidazole was protonated by stronger acid like picric acid. Then the assembly between protonated **IMPY** and picrate anions was formed *via* strong hydrogen bonds. ^{1}H NMR titration supported that methylene imidazole was a specific key site. In addition, this structure displayed three face-to-face π-π stacking interactions. The first one was between pyrene ring and picrate anion with $\pi_{centroid} - \pi_{centroid}$ in distance of 3.568(2) Å. The second one was between two picrate anions with $\pi_{centroid} - \pi_{centroid}$ in distance of 3.654(2) Å and the last one was π-π stacking interaction between two pyrene rings with $\pi_{centroid} - \pi_{centroid}$ in distance of 3.613(2) Å.

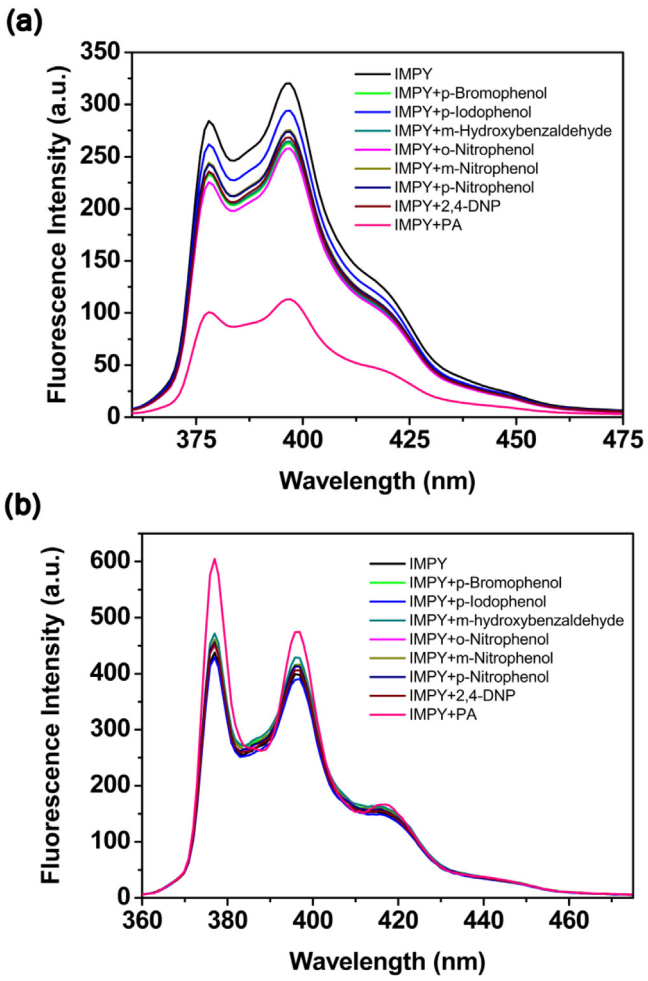

Fig. 8. Fluorescence spectra (λ_{ex} = 342 nm) of **IMPY** (3 μM) in (a) toluene and (b) acetonitrile with addition of phenolic compounds (1.2×10^{-4} M).

Another crystalline structure, the yellow one, was in $P2_1/c$ space group (Fig. 5c) showing distinct packing supramolecular motif. The dihedral angle between pyrene plane and imidazole ring was 86.8°. Each picrate anion connected with eight **IMPYs** *via* twelve H-bonds, as well as **IMPY** also connected with eight picrate anions *via* twelve H-bonds. The D···A distances of hydrogen bond and the DH···A angles were in the range 2.647(2)–3.647(8) Å and 114–164°, while weak CH···O interactions were included (Fig. 7). In addition, this structure revealed various intermolecular weak interactions, including face-to-face π-π stacking interaction between pyrene rings and picrate rings with $\pi_{centroid} - \pi_{centroid}$ distance of 3.702(2) Å, C—H-π interaction between imidazole CH and picrate ring with distance of 3.683(2) Å, as well as, many C—H-π interactions between two adjacent pyrene rings with distances of 2.753(2) and 2.964(2) Å. Contradictory, there was no π-π stacking interaction between two neighboring picrate anions observed in this case. Moreover, this structure had more interesting point as there were three electrostatic interactions observed for a picrate anion, which were also responsible for its packing motif. From this structure, H-bonding between picrate anion and protonated imidazole showed strongest interaction with the shortest distance of 2.647(2) Å. Therefore, the H-bonding was a specific site to respond with picrate anion as **IMPY**·**PA1**.

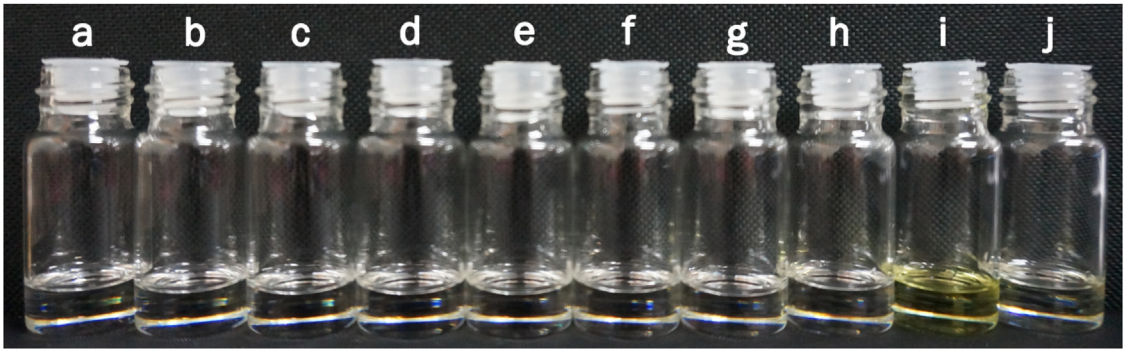

Fig. 9. Chromogenic change of **IMPY** (3 μM) in toluene. Legend: (a) **IMPY** (b) **IMPY** + *p*-iodophenol, (c) **IMPY** + *p*-bromophenol, (d) **IMPY** + *m*-hydroxybenzaldehyde, (e) **IMPY** + *o*-nitrophenol, (f) **IMPY** + *m*-nitrophenol, (g) **IMPY** + *p*-nitrophenol, (h) **IMPY** + 2,4-dinitrophenol, (i) **IMPY** + **PA**, and (j) **PA**.

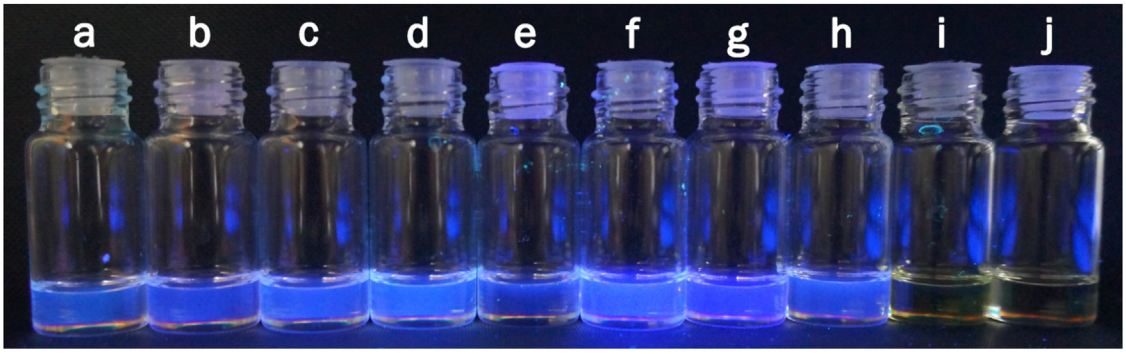

Fig. 10. The luminescence of **IMPY** (3 μM) in toluene. Legend: (a) **IMPY** (b) **IMPY** + *p*-iodophenol, (c) **IMPY** + *p*-bromophenol, (d) **IMPY** + *m*-hydroxybenzaldehyde, (e) **IMPY** + *o*-nitrophenol, (f) **IMP** + *m*-nitrophenol, (g) **IMPY** + *p*-nitrophenol, (h) **IMPY** + 2,4-dinitrophenol, (i) **IMPY** + **PA**, and (j) **PA** under a UV light.

3.4. Selectivity studies

The selectivity studies of **IMPY** to a series of phenolic compounds such as *p*-iodophenol, *p*-bromophenol, *m*-hydroxybenzaldehyde, *o*-nitrophenol, *m*-nitrophenol, *p*-nitrophenol, 2,4-dinitrophenol and picric acid were performed by observing the fluorescence spectra of the **IMPY** sensors solutions after addition of each representative phenolic compound. These studies were carried out by a similar method to the Separate Solution Method (SSM) used in ion-selective electrode applications [37,38]. This method involves the measurement of a series of separate solutions, each containing only a decided phenolic compound. Fig. 8 shows the fluorescence intensity of **IMPY** upon addition of various phenolic compounds in both toluene and acetonitrile systems.

The selectivity studies clearly revealed the high selectivity of **IMPY** to **PA** in comparison with other phenolic compounds. In toluene solutions, a remarkable quenching in fluorescence emission intensity of **IMPY** was observed when only **PA** was added to the solution of sensor. However, the fluorescence response of **IMPY** induced only small changes after the addition of *p*-iodophenol, *p*-bromophenol, *m*-hydroxybenzaldehyde, *o*-nitrophenol, *m*-nitrophenol, *p*-nitrophenol and 2,4-dinitrophenol under identical conditions (Fig. 8a). On the other hand, in acetonitrile system, the fluorescence of **IMPY** was selectively enhanced with **PA** and discriminated other phenolic compounds in this study (Fig. 8b).

The selectivity of sensor **IMPY** was not only demonstrated by rapid turn-off or turn-on fluorescence switches but also displayed by color changes. The addition of **PA** to the solution of sensor **IMPY** led to the change of color of the solution from colorless to yellow, which could be noticeable by the naked eye. In contrast, other phenolic compounds such as *p*-iodophenol, *p*-bromophenol, *m*-hydroxybenzaldehyde, *o*-nitrophenol, *m*-nitrophenol, *p*-nitrophenol and 2,4-dinitrophenol induced negligible color changes under identical conditions. This phenomenon can be confirmed by the absorption spectra as shown in Fig. S7. The selectivity of **IMPY** and **PA** are described by three specific points. First of all, the acidic proton of **PA** guest has to protonate at the N-imidazole unit in **IMPY**. Second, the deficiency of electron density in phenyl ring of **PA** involves in the term of π-π interaction with pyrene ring in **IMPY**. Lastly, the energy levels of their HOMO-LUMOs must be suitable for electron migration. The selective bindings of sensor **IMPY** indicated by both chromogenic and fluorogenic changes are demonstrated in Figs. 9 and 10, respectively.

4. Conclusions

We have successfully found a new type of fluorescent sensor, **IMPY**, for 2,4,6-trinitrophenol or picric acid (**PA**) detection based on 1-imidazolylmethylpyrene. To confirm highly interactive affinity of the sensor molecule to picric acid, two different types of crystal structures of **IMPY**·**PA** complexes were successfully recrystallized and characterized. Sensor **IMPY** exhibited high sensitivity and selectivity toward picric acid over a wide range of phenolic compounds due to the presence of H-bondings and π-π interactions. Not only, **IMPY** sensor could be operated *via* both OFF–ON and ON–OFF responses, but also exhibited the chromogenic change by changing the color of the solution from colorless to yellow, which could be noticeable by the naked eye. The designed sensor reported here has several advantages in terms of synthetic simplicity, economical cost of starting materials which make it possible for commercial uses, high sensitivity and selectivity to picric acid which will be benefit for on-site detection of this powerful explosive chemical.

Acknowledgements

This research is financially supported by the Thailand Research Fund (RSA5980018), Faculty of Science, Mahidol University, Center of Excellence for Innovation in Chemistry (PERCH-CIC), and the Nanotechnology Center (NANOTEC), NSTDA, Ministry of Science and Technology, Thailand, through its program of Center of Excellence Network.

Appendix A. Supplementary data

Supplementary data associated with this article can be found, in the online version, at http://dx.doi.org/10.1016/j.snb.2017.01.120.

References

[1] S. Madhu, A. Bandela, M. Ravikanth, BODIPY based fluorescent chemodosimeter for explosive picric acid in aqueous media and rapid detection in the solid state, RSC Adv. 4 (14) (2014) 7120–7123.
[2] P.W. Cooper, Explosives Engineering, Wiley-VCH, 1996.
[3] A.M. Brandt, Exploring the dangerous trades, Rev. Am. Hist. 17 (1) (1989) 101–107.
[4] T.L. Davis, The Chemistry of Powder and Explosives, Angriff Press, 1943.
[5] A. Hamilton, Exploring the Dangerous Trades – The Autobiography of Alice Hamilton, M.D., Read Books, 2007.
[6] Y. Salinas, et al., Optical chemosensors and reagents to detect explosives, Chem. Soc. Rev. 41 (3) (2012) 1261–1296.
[7] J.A. Caulfield, T.J. Bruno, K.E. Miller, Enthalpy of solution and Kováts retention indices for nitroaromatic compounds on stationary phases using gas chromatography, J. Chem. Eng. Data 54 (6) (2009) 1814–1822.
[8] M.E. Germain, M.J. Knapp, Optical explosives detection: from color changes to fluorescence turn-on, Chem. Soc. Rev. 38 (9) (2009) 2543–2555.
[9] S.J. Toal, W.C. Trogler, Polymer sensors for nitroaromatic explosives detection, J. Mater. Chem. 16 (28) (2006) 2871–2883.
[10] M.E. Germain, M.J. Knapp, Discrimination of nitroaromatics and explosives mimics by a fluorescent Zn (salicylaldimine) sensor array, J. Am. Chem. Soc. 130 (16) (2008) 5422–5423.
[11] A. Saxena, et al., Fluoroalkylated polysilane film as a chemosensor for explosive nitroaromatic compounds, Chem. Mater. 17 (8) (2005) 2181–2185.
[12] B. Xu, et al., Selective detection of TNT and picric acid by conjugated polymer film sensors with donor–acceptor architecture, Macromolecules 44 (13) (2011) 5089–5092.
[13] A.I. Costa, J.V. Prata, Substituted *p*-phenylene ethynylene trimers as fluorescent sensors for nitroaromatic explosives, Sens. Actuators B: Chem. 161 (1) (2012) 251–260.
[14] J.-F. Xiong, et al., Benzimidazole derivatives: selective fluorescent chemosensors for the picogram detection of picric acid, J. Organic Chem. 79 (23) (2014) 11619–11630.
[15] B. Roy, et al., Fluorescent tris-imidazolium sensors for picric acid explosive, J. Org. Chem. 78 (3) (2013) 1306–1310.
[16] K. Acharyya, P.S. Mukherjee, A fluorescent organic cage for picric acid detection, Chem. Commun. 50 (99) (2014) 15788–15791.
[17] S. Shanmugaraju, S.A. Joshi, P.S. Mukherjee, Fluorescence and visual sensing of nitroaromatic explosives using electron rich discrete fluorophores, J. Mater. Chem. 21 (25) (2011) 9130–9138.
[18] C.R. Martinez, B.L. Iverson, Rethinking the term pi-stacking, Chem. Sci. 3 (7) (2012) 2191–2201.
[19] C.A. Hunter, J.K.M. Sanders, The nature of.pi.-.pi. interactions, J. Am. Chem. Soc. 112 (14) (1990) 5525–5534.
[20] H. Du, et al., Preparation of pyrene-functionalized fluorescent film with a benzene ring in spacer and sensitive detection to picric acid in aqueous phase, J. Photochem. Photobiol. A: Chem. 217 (2) (2011) 356–362.
[21] N. Niamnont, et al., Tunable star-shaped triphenylamine fluorophores for fluorescence quenching detection and identification of nitro-aromatic explosives, Chem. Commun. 49 (8) (2013) 780–782.
[22] P. Sam-ang, et al., A nitroaromatic fluorescence sensor from a novel tripyrenyl truxene, RSC Adv. 4 (101) (2014) 58077–58082.
[23] D. Thongkum, T. Tuntulani, Fluoride-induced intermolecular excimer formation of bispyrenyl thioureas linked by polyethylene glycol chains, Tetrahedron 67 (42) (2011) 8102–8109.
[24] S. Goswami, et al., A highly selective and sensitive probe for colorimetric and fluorogenic detection of Cd2+ in aqueous media, Analyst 138 (6) (2013) 1903–1907.
[25] B. Gole, et al., Explosives sensing by using electron-rich supramolecular polymers: role of intermolecular hydrogen bonding in significant enhancement of sensitivity, Chem. Eur. J. 20 (42) (2014) 13662–13680.
[26] J.V. Morris, M.A. Mahaney, J.R. Huber, Fluorescence quantum yield determinations 9, 10-diphenylanthracene as a reference standard in different solvents, J. Phys. Chem. 80 (9) (1976) 969–974.
[27] M.W. Allen, Measurement of fluorescence quantum yields, Technical Note 52019 Thermo Fisher Scientific, Madison, WI, USA, 2010.
[28] S. Dhami, et al., Phthalocyanine fluorescence at high concentration: dimers or reabsorption effect? Photochem. Photobiol. 61 (4) (1995) 341–346.
[29] A.T.R. Williams, S.A. Winfield, J.N. Miller, Relative fluorescence quantum yields using a computer-controlled luminescence spectrometer, Analyst 108 (1290) (1983) 1067–1071.
[30] W. Chen, et al., Pyrene-functionalized ruthenium nanoparticles: novel fluorescence characteristics from intraparticle extended conjugation, J. Phys. Chem. C 113 (39) (2009) 16988–16995.
[31] J.L. Bartels, et al., Building addressable libraries: a site-selective click-reaction strategy for rapidly assembling mass spectrometry cleavable linkers, Chem. Commun. 2009 (37) (2016) 5573–5575.
[32] S.K. Kim, et al., A fluorescent cavitand for the recognition of GTP, Tetrahedron Lett. 46 (39) (2005) 6617–6620.
[33] M.J. Frisch, et al., Gaussian 03, Revision C.02, 2003.
[34] B.et al. Valderrama-García, Synthesis and characterization of novel polythiophenes containing pyrene chromophores: thermal, optical and electrochemical properties, Molecules 21 (2) (2016) 172.
[35] A.T. Haedler, et al., Controlling the π-stacking behavior of pyrene derivatives: influence of H-bonding and steric effects in different states of aggregation, ChemPhysChem 14 (9) (2013) 1818–1829.
[36] J. Ma, et al., A new coumarin-derived fluorescent sensor with red-emission for Zn^{2+} in aqueous solution, Sens. Actuators B: Chem. 197 (2014) 364–369.
[37] N. Wanichacheva, et al., Rhodamine B-based turn-on fluorescent and colorimetric chemosensors for highly sensitive and selective detection of mercury (II) ions, J. Lumin. 132 (1) (2012) 35–40.
[38] P. Piyanuch, et al., Highly sensitive and selective Hg^{2+}-chemosensor based on dithia-cyclic fluorescein for optical and visual-eye detections in aqueous buffer solution, Sens. Actuators B: Chem. 224 (2016) 201–208.

Biographies

Rapheepraew Sodkhomkhum received B.Sc. in Chemistry from Silpakorn University at 2010. In 2016, she received her a Ph.D. in Inorganic Chemistry at Mahidol University, Thailand with Associate Professor Dr. Vuthichai Ervithayasuporn and now continues her study as a postdoctoral fellowship with Professor Dr. Takumi Konno at Osaka University, Japan. Her research interest focuses on the synthesis and application of organic-inorganic hybrid polymer and coordination chemistry.

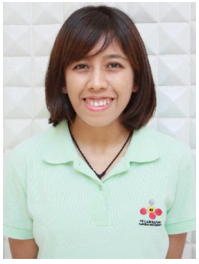

Manlika Masik received B.Sc. in Chemistry from Silpakorn University at 2014. Currently, she is a Master student under supervision of Associate Professor Dr. Vuthichai Ervithayasuporn at Department of Chemistry, Faculty of Science, Mahidol University. Her research interests involve synthesis of small molecules and organic-inorganic hybrid materials applying for a fluorescence chemosensor.

Sarayut Watchasit was born in 1985 and brought up in Trat, Thailand. He finished B.Sc. in chemistry and M.Sc. in inorganic chemistry at Burapha University. He then started a Ph.D. at Chulalongkorn University, working on sensing of anions and biological molecules by using an indicator displacement assay approach. Now, he is currently served as the scientist at Faculty of Science, Burapha University. His actual research interest involves the development of new sensing molecules for detection of metal ions, anions and biological molecules.

Chomchai Suksai received a B.Sc. in chemistry from Burapha University in 1998. She received a M.Sc. in applied analytical and inorganic chemistry from Mahidol University in 2001. She then pursued her PhD under the supervision of Professor Thawatchai Tuntulani at Chulalongkorn University and graduated in 2006. Since then, she has been working as an Assistant Professor in the Department of Chemistry, Faculty of Science, Burapha University. Her research is in the field of supramolecular chemistry focusing on syntheses of new mononuclear and dinuclear metal complexes to be used in optical sensing of relevant biological ions by using indicator displacement assay.

Jaursup Boonmak received his Ph.D. in Chemistry from Khon Kaen University. He is currently a full-time lecturer at Department of Chemistry, Faculty of Science, Khon Kaen University, Thailand. His main research interest includes small molecule X-ray crystallography, synthesis and crystal engineering of inorganic-organic hybrid frameworks.

Sujittra Youngme received her Ph.D. in Inorganic Chemistry from the National University of Ireland at University College Cork. She is now working as a Professor in Inorganic Chemistry at the Department of Chemistry, Faculty of Science, Khon Kaen University, Thailand. Her current research focuses on the design, synthesis, X-ray structure and functional properties of metal-organic frameworks.

Nantanit Wanichacheva is an Assistant Professor in Department of Chemistry at Silpakorn University, Thailand. She received her Ph.D. in Chemistry from Worcester Polytechnic Institute, Massachusetts, USA. She is currently served as the deputy head of Department of Chemistry, Faculty of Science, Silpakorn University, Thailand. Her current research interests include design, syntheses and development of new fluorescence sensors for metal ions detections, such as mercury ion, copper ion and zinc ion, and their utilization in solutions, polymer membrane, solid support-strip tests and portable monitoring devices.

Vuthichai Ervithayasuporn is an Associate Professor in Department of Chemistry, Faculty of Science, Mahidol University, Thailand. In 2010, he received his Ph.D. in Materials Chemistry from Japan Advanced Institute of Science and Technology (JAIST), Ishikawa, Japan. Recently, he won Young Scientist Award from Foundation for the Promotion of Science and Technology under the Patronage of H.M. the King of Thailand. His current research focuses on the synthesis and application of small molecules, polymers, and organic-inorganic hybrid materials.

ACS APPLIED MATERIALS & INTERFACES

Research Article

www.acsami.org

Tunable Porosity of Cross-Linked-Polyhedral Oligomeric Silsesquioxane Supports for Palladium-Catalyzed Aerobic Alcohol Oxidation in Water

Preeyanuch Sangtrirutnugul,[†] Thanawat Chaiprasert,[†] Warodom Hunsiri,[†] Thanudkit Jitjaroendee,[†] Patsaya Songkhum,[§] Kritapas Laohhasurayotin,[§] Tanakorn Osotchan,[‡] and Vuthichai Ervithayasuporn*[,†,‡]

[†]Department of Chemistry, Center of Excellence for Innovation in Chemistry (PERCH-CIC), Center for Catalysis Science and Technology, and Center for Inorganic and Materials Chemistry, and [‡]School of Materials Science and Engineering, and NANOTEC-MU Center of Intelligent Materials and Systems, Faculty of Science, Mahidol University, 272 RAMA VI road, Ratchathewi District, Bangkok 10400, Thailand

[§]National Nanotechnology Center, National Science and Technology Development Agency, Phaholyothin road, Patumthani 12120, Thailand

Supporting Information

ABSTRACT: Polyhedral oligomeric silsesquioxane (POSS)-based materials, poly-POSS-T_n [n = 8 (**1**), 10 (**2**), 12 (**3**), and mix (**4**)], were prepared in high yields *via* free radical polymerization of corresponding pure forms of methacrylate-functionalized POSS monomers, MMA-POSS-T_n (n = 8, 10, 12), and the mixture form, MMA-POSS-T_{mix}. Powder X-ray diffraction (XRD) spectra and BET analysis indicate that **1**−**4** are amorphous materials with high surface areas (683−839 $m^2 g^{-1}$). The surface areas and total pore volumes follow the trend: poly-POSS-T_{12} > poly-POSS-T_{10} > poly-POSS-T_{mix} > poly-POSS-T_8. In addition, on the basis of Barrett−Joyner−Halenda (BJH) analysis, poly-POSS-T_{12} contains the highest amount of mesopores. The Pd nanoparticles immobilized on poly-POSS-T_n [n = 8 (**5**), 10 (**6**), 12 (**7**), and mix (**8**)] are well dispersed with 4−6 wt % Pd content and similar average particle sizes of 6.2−6.5 nm, according to transmission electron microscopy-energy dispersive X-ray analysis (TEM-EDX) and microwave plasma-atomic emission spectroscopy (MP-AES). At 90 °C, the stabilized Pd nanoparticles in **5**−**8** catalyzed aerobic oxidation of benzyl alcohol to benzaldehyde in 72−100% yields at 6 h using a mixture of a H_2O/Pluronic (P123) solution. The PdNp@poly-POSS-T_8 catalyst (**5**) exhibited the lowest catalytic activity, as a result of its lowest surface areas, total pore volumes, and amounts of mesopores. With the catalyst **8**, various benzyl alcohol derivatives were converted to the corresponding aldehydes in good to excellent yields. However, with alcoholic substrates featuring electron-withdrawing substituents, high conversions were achieved with 1 equiv of K_2CO_3 additive and longer reaction times.

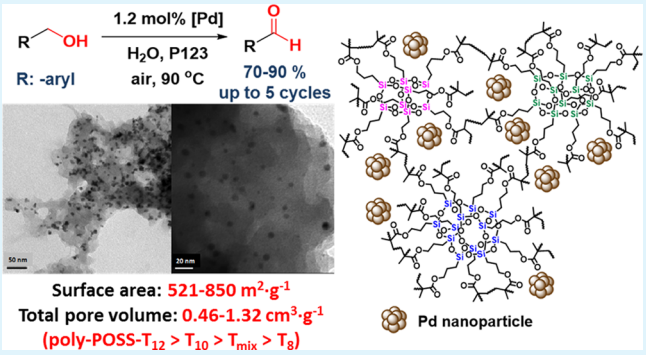

KEYWORDS: *polyhedral oligomeric silsesquioxane, free-radical polymerization, porous materials, palladium nanoparticle, alcohol oxidation*

INTRODUCTION

Inorganic−organic composite materials with porous structures and high surface areas have gained considerable research interest with potential industrial applications.[1−4] In particular, porous materials based on polyhedral oligomeric silsesquioxane (POSS), a hybrid compound with the formula $(RSiO_{1.5})_n$ consisting of a well-defined rigid silica core and peripheral organic substituents, have shown favorable characteristics such as high thermal stability,[5,6] adjustable functional groups within the materials,[7−12] and tunable pore sizes depending on the synthetic methods[13−15] and starting precursors.[16,17] As a result, POSS-based materials have been used in various applications including electronic devices, sensors, gas storage, and catalysis.[18−25]

In general, POSS-based materials exhibit exceptionally high surface areas as a result of the packing arrangement of nanometer-sized, rigid POSS cages, which creates spaces and voids among POSS molecules.[13,14,26] Furthermore, the presence of heteroatom-containing functional groups (i.e., N and O) at organic linkers within the materials makes

Received: March 19, 2017
Accepted: March 24, 2017
Published: March 24, 2017

DOI: 10.1021/acsami.7b03910
ACS Appl. Mater. Interfaces 2017, 9, 12812−12822

Scheme 1. Synthetic Approach To Prepare MMA-POSS-T_n (n = 8, 10, and 12)

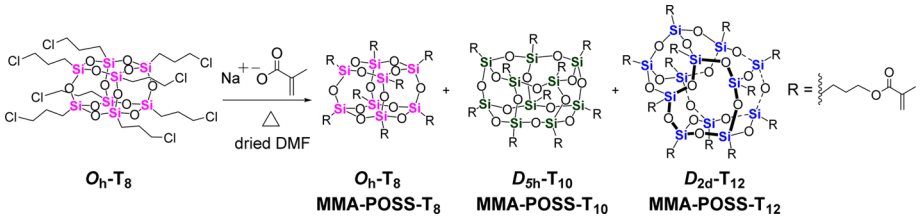

silsesquioxane-based materials potentially effective metal stabilizers.[27,28] For these reasons, thermally stable, high-surface-area POSS-based materials have recently been investigated as catalyst supports for a number of metal-promoted chemical transformation. Notably, several groups reported the synthesis of hybrid porous POSS-based materials (surface areas ranging from 680 to 1080 m^2 g^{-1}) *via* AIBN initiated free radical polymerization of octavinylsilsesquioxane (OVS) in THF.[13,14,26] Post functionalization of the free vinyl groups using thiol−ene addition and nucleophilic substitution, followed by Pd(II) complexation, yielded the Pd(II)-POSS porous materials, which served as active catalysts toward C−C cross coupling.[29] In addition, Nakanishi and Kanamori et al. prepared hydrogen silsesquioxane (HSQ) with high surface areas and well-defined meso- and macropores *via* the sol−gel process in the presence of poly(ethylene oxide) (PEO) under acidic conditions. Subsequent reduction of noble metal salts (i.e., Au, Ag, Pd, and Pt) by the Si−H groups present in the material framework was carried out.[30] Later work by the same group has shown that Pd nanoparticles supported on HSQ were effective catalysts for Heck reactions.[31] In another example, Leng and co-workers reported amphiphilic mesoporous POSS-based materials: POSS-BM_x prepared from free radical copolymerization of octa(3-(imidazol-1-yl)-propylsilsesquioxane) and bis(3-vinylimidazolium) bromide (BM).[25] Anion exchange with $H_3PW_{12}O_{40}$ (PW) resulted in the ionic hybrids POSS-BM_x-PW, which were active and recyclable catalysts for alkene epoxidation in the presence of H_2O_2 oxidant. Recently, our group also reported the synthesis of the homogeneous and heterogeneous catalysts of organo-palladium-functionalized-polyhedral oligomeric silsesquioxanes for Suzuki−Miyaura reaction.[23,32]

Water is nontoxic and readily available, making it an attractive alternative to organic solvents. As a result, catalytic reactions in an aqueous solution are highly desirable and considered important at the area of green chemistry.[33] In particular, we chose aerobic alcohol oxidation, which has potential industrial applications, in water for catalytic studies. Sheldon and co-workers have previously investigated the water-soluble Pd(II) bathophenanthroline complex of a homogeneous aerobic oxidation catalyst in aqueous solution.[34] There are also previous reports involving heterogeneous nano-palladium catalysts supported on inorganic silica[35] and polymeric networks[36−40] for alcohol oxidation under 1 atm of O_2 or air. However, to the best of our knowledge, activities of Pd nanoparticles stabilized by organic−inorganic silsesquioxanes for aerobic alcohol oxidation in water remain unexplored. We have recently prepared and isolated methyl methacrylate-functionalized-POSS (MMA-POSS-T_n) monomers in pure form of T_8, T_{10}, and T_{12} cages (Scheme 1).[41] Our findings show a relationship between the chemical structure of each pure silsesquioxane cage and its physical properties. Particularly, the packing of cubic T_8 structure of MMA-POSS-T_8 led to highly crystalline materials, whereas the other MMA-POSS-T_{10} and T_{12} packed less efficiently and were amorphous. Moreover, those compounds can be used as a comonomer to prepare various types of polymer−silsesquioxane hybrid nanocomposites.[42,43] Despite these studies, differences in properties of the resulting polymers obtained from using pure forms of POSS-T_n have not been explored nor taken into consideration in any previous studies. Herein, we prepare a series of novel POSS-based porous materials from free radical polymerization of pure MMA-POSS-T_n (n = 8, 10, 12) and MMA-POSS-T_{mix} monomers. Also, for the first time, the effects of POSS cage sizes on physical properties including porosity, surface areas, thermal properties, and catalytic activities toward Pd-catalyzed aerobic alcohol oxidation in water are evaluated.

EXPERIMENTAL SECTION

Materials. AIBN was purchased from Shanghai Chemical Reagent Co. Ltd., China. Other chemicals and solvents were obtained from Sigma-Aldrich and used without further purification. MMA-POSS-T_n (n = 8, 10, 12) monomers were prepared and isolated according to our previous report, while MMA-POSS-T_{mix} was a crude mixture and used without further purification.[41] All organic solvents in this work were dried using the standard procedures. The water used was DI water.

Physical Measurements and Instrumentation. Fourier transform nuclear magnetic resonance (NMR) spectra of sample solutions were obtained at 25 °C using a Bruker's Ascend 400 high-resolution magnetic resonance spectrometer for ^1H (400 MHz), $^{13}C\{^1H\}$ (100 MHz), and $^{29}Si\{^1H\}$ (79 MHz) nuclei. The ^{29}Si CP/MAS NMR spectra were acquired at 60 MHz frequency with AVANCE 300 MHz Digital NMR spectrometer (Bruker Biospin; DPX-300). Chemical shifts were reported in δ units (parts per million) relative to tetramethylsilane, and residual solvents peaks were used as a reference. The FT-IR spectra were recorded on a Bruker model Alpha spectrometer. The MP-AES spectra were recorded by microwave plasma-atomic emission spectrometer (MP-AES) Systems 4200 MP-AES. The samples for MP-AES were prepared as solutions in diluted aqua regia (2%). The emission spectra of Pd were recorded at 343.345 nm. Powder X-ray diffraction (XRD) was performed by Bruker D8 Advance with a monochromatic Cu K_α (40 kV, 40 mA) source, step size of 0.010°, and a step time of 3 s/step. Scanning electron microscopy (SEM) was performed on a JEOL JSM-6400 microscope equipped with EDX analyzer. A sample was coated with gold before performing SEM. Transmission electron microscopy (TEM) was recorded on a JEOL JEM-2010 equipped with EDX analyzer microscope and was operated at 200 kV. Samples for TEM were dispersed in ethanol and dropped onto a copper grid with Formvar film before recording data. X-ray photoelectron spectroscopy (XPS) measurements were obtained from a Kratos Axis Ultra DLD applied to determine the state of Pd. The measurements were carried out when the residual pressure was lower than 5×10^{-7} Torr with a monochromatic Al Kα radiation operating at 10 mA and 15 kV. The binding energies of catalysts were obtained by curve fitting and were referenced to the C 1s band at 284.6 eV. The molar ratio of Pd(0)/Pd(II) was approximately determined from the ratio of peak area of the Pd(0) species of Pd $3d_{5/2}$ to that of the Pd(II) species of Pd $3d_{5/2}$. Specific surface area and nitrogen adsorption−desorption were determined using an Autosorp-1 gas sorption system (Quantachrome

DOI: 10.1021/acsami.7b03910
ACS Appl. Mater. Interfaces 2017, 9, 12812−12822

Corp.) *via* the Brunauer–Emmett–Teller (BET) method at 77 K. The samples were thoroughly outgassed at 120 °C for 15 h prior to exposure to the adsorbent gas. Gas chromatography–mass spectrometry (GC–MS) was operated on a 6890N Agilent equipped with a 5973N Agilent quadrupole mass detector using anisole as internal standard. Differential scanning calorimetry (DSC) and thermo gravimetric analysis (TGA) were recorded on a SDT 2960 Simultaneous DSC-TGA instrument with a scan rate of 20 °C min^{-1} in the presence of oxygen atmosphere.

*General Procedure To Prepare Poly-POSS-T_n [n = 8 (**1**), 10 (**2**), 12 (**3**), Mix (**4**)].* Under Ar, MMA-POSS-T_n (n = 8 or 10 or 12 or mix) (20 wt %, 0.500 g) was completely dissolved in a solution mixture (2.5 mL) of PEG-200:THF (1:3 w/w). Next, the reaction mixture was stirred at room temperature for 10 min, after which AIBN (0.080 g, 0.49 mmol) was added. After 10 min of stirring, the reaction flask was immersed in a preheated oil bath at 60 °C. Note that the solution mixture became highly viscous and solidified after 20 min of heating. After 24 h, the white solid formed was crushed and repeatedly washed with 200 mL of THF in a Soxhlet apparatus. The resulting solids (**1**–**4**) were then dried under vacuum at 80 °C for 12 h. The percentage yields were calculated on the basis of the weights of the resulting products: % yield = [(weight of product)/(weight of POSS monomer + AIBN)] × 100; poly-POSS-T_8 (**1**) = 80%, poly-POSS-T_{10} (**2**) = 82%, poly-POSS-T_{12} (**3**) = 90%, and poly-POSS-T_{mix} (**4**) = 87%.

*Preparation of Poly-POSS-T_{mix} (No PEG-200) (**9**).* Under Ar, MMA-POSS-T_{mix} (20 wt %, 0.500 g) monomers were dissolved in 2.5 mL of THF. Next, the reaction mixture was stirred at room temperature for 10 min, after which AIBN (0.080 g, 0.49 mmol) was added. After 10 min of stirring, the reaction flask was immersed in a preheated oil bath at 60 °C. Note that the solution mixture became highly viscous and solidified after 20 min of heating. After 24 h, the resulting white solid was crushed, repeatedly washed with 200 mL of THF using a Soxhlet apparatus, and dried under vacuum at 80 °C for 12 h.

*Preparation of Pd Nanoparticles on Poly-POSS-T_n [Pd@poly-POSS-T_n (**5**–**8**)].* Poly-POSS-T_n [n = 8 (**5**), 10 (**6**), 12 (**7**), and mix (**8**)] (0.200 g) was first dissolved in CH_2Cl_2 (8 mL), followed by an addition of $Pd(OAc)_2$ (0.020 g, 0.089 mmol). The reaction mixture was stirred at room temperature for 24 h, after which all volatiles were completely evaporated resulting in an orange solid. The solid mixture then was dispersed in 8 mL of CH_3OH, and an excess amount of $NaBH_4$ (0.034 g, 0.89 mmol) was added to the reaction mixture, giving an immediate color change from orange to black solids. After being stirred for 3 h at room temperature, the black solution was centrifuged using 50% of CH_3OH in DI water five times to remove any starting reagents, and the gray solid was dried in vacuo at 80 °C for 12 h. The amount of Pd was determined by MP-AES (Table S1).

Preparation of Pd Nanoparticles on PMMA. Under Ar, MMA (20 wt %, 0.500 g) monomer was completely dissolved in a solution mixture (2.5 mL) of PEG-200:THF (1:3 w/w). Next, the reaction mixture was stirred at room temperature for 10 min, after which AIBN (0.080 g, 0.49 mmol) was added. After 10 min of stirring, the reaction flask was immersed in a preheated oil bath at 60 °C. After 24 h, the solution was precipitated using cold methanol. The resulting product (PMMA) was then dried under vacuum at 80 °C for 12 h. To generate Pd nanoparticles on PMMA, 20 mg of $Pd(OAc)_2$ was mixed with 200 mg of PMMA in 8 mL of methanol and stirred for 24 h, resulting in the black solution. Next, the black solution was centrifuged using 50% of CH_3OH in DI water five times to remove any starting reagents, and the dark gray solid was dried in vacuo at 80 °C for 12 h. The amount of Pd was determined by MP-AES (Table S1).

General Procedure for Pd-Catalyzed Aerobic Alcohol Oxidation. To a 25 mL round-bottom flask equipped with a stir bar and a condenser was dispersed a given amount of PdNp@poly-POSS-T_n (**5**–**8**) in solvents (2.0 mL), followed by an addition of alcoholic substrates (1.0 mmol). The reaction flask was then immersed in a preheated oil bath. In some optimized experiments, the reaction mixture was stirred with air bubbling at 90 °C. After a given time, the reaction mixture was allowed to cool to room temperature using a water bath. When the water was used as a solvent, the products were extracted with 10 mL of diethyl ether three times before GC analysis. The percent conversions were determined by GC–MS methods with anisole (0.10 mmol) as an internal standard. Because of the poor solubility of alcoholic substrates in water, a lower amount of an alcoholic substrate (0.50 mmol) was used in the substrate scope investigation.

Reusability Study of PdNp@poly-POSS-T_{mix}. In a two-necked round-bottomed flask (50 mL) equipped with a stir bar and a condenser was dissolved a solid mixture of PdNp@poly-POSS-T_{mix} (0.65 mol % Pd, 0.097 g) and P123 (0.72 g), which was then dispersed in water (12 mL), followed by an addition of benzyl alcohol (0.65 g, 6.0 mmol). The reaction mixture was stirred with air bubbling at 90 °C for 5 h, after which the product was extracted with diethyl ether (10 mL) three times. The percent conversions were analyzed using GC analysis with anisole as an internal standard. The catalyst was recovered by simple decantation. Next, it was washed with 50 mL of ethanol followed by centrifugation three times. The resulting solid was then dried under vacuum at 80 °C for 12 h before being used in the next reaction cycle.

Hot Filtration Experiment. To a two-necked round-bottom flask (50 mL) equipped with a stir bar and a condenser was added a mixture of PdNp@poly-POSS-T_{mix} (**8**) (0.65 mol % Pd, 0.097 g) and P123 (0.24 g) in water (4.0 mL), followed by an addition of benzyl alcohol (0.21 g, 2.0 mmol). The reaction mixture was then heated at 90 °C. After 90 min, the reaction mixture was quickly filtered through a silica gel to remove the catalyst **8**. After that, the filtrate was extracted with 10 mL of Et_2O and sampled for GC–MS analysis. The remaining aqueous solution was further heated at 90 °C. The product yields were determined at 90 and 240 min using GC–MS.

Leaching Test of PdNp@poly-POSS-T_{mix}. To a mixture of PdNp@poly-POSS-T_{mix} (**8**) (10 wt %, 0.021 g) and P123 (0.24 g) dissolved in water (4.0 mL) was added benzyl alcohol (0.21 g, 2.0 mmol). The reaction mixture was then stirred and bubbled with air at 90 °C for 5 h. After the first reaction cycle, the reaction was diluted with EtOH (200 mL) and filtered using a Büchner funnel, followed by syringe filtration (with 0.22 μm pore size filter paper). Next, the filtrate was dried under vacuum, and the remaining solid was digested in aqua regia (1 mL) before dilution with DI water to produce a stock solution with a total volume of 50 mL. The Pd content in the solution was then analyzed by MP-AES.

RESULTS AND DISCUSSION

Preparation of Highly Porous Poly-POSS-T_n (n = 8, 10, 12, and Mix). Pure forms of MMA-POSS-T_8, T_{10}, T_{12}, and the mixture of all three compounds (MMA-POSS-T_{mix}) were prepared according to the literature[41] and used as monomers in the subsequent step. Under Ar, the solution mixture of a given POSS monomer (17 wt %) in 1:3 ratio of PEG-200:THF, a porogenic solvent,[44] was polymerized with 16 wt % AIBN as an initiator at 60 °C for 24 h (Scheme 2). As the polymerization proceeded, the reaction solution turned from clear colorless to gelatinous, and eventually white precipitates were formed. Repeated washing with THF *via* the Soxhlet extraction technique and drying under vacuum afforded the respective polymer products of poly-POSS-T_n [n = 8 (**1**), 10 (**2**), 12 (**3**), and mix (**4**)] as white solids in 80–90% yields.

Based on FT-IR spectra, complete polymerizations were confirmed based on the disappearance of the absorption band corresponding to the C=C groups of methacrylate at 1637 cm^{-1} observed for the MMA-POSS-T_n monomers (Figures 1 and S1). In addition, FT-IR spectra of **1**–**4** exhibit the same absorption pattern in which each spectrum contains strong absorption bands at 1731 and 1113 cm^{-1}, assignable to stretching vibrations of C=O of the methacrylate ester and Si–O–Si groups in the POSS molecule, respectively (Figure S2). Furthermore, the absence of a broad absorption band at ca. 3400 cm^{-1} indicates a complete removal of PEG-200.[45] The ^{29}Si CP/MS NMR spectra of poly-POSS-T_n (**1**–**4**) contain a

DOI: 10.1021/acsami.7b03910
ACS Appl. Mater. Interfaces 2017, 9, 12812–12822

Scheme 2. A Representative Example for the Synthesis of Poly-POSS-T_{mix} (4) and PdNp@poly-POSS-T_{mix} (8)[a]

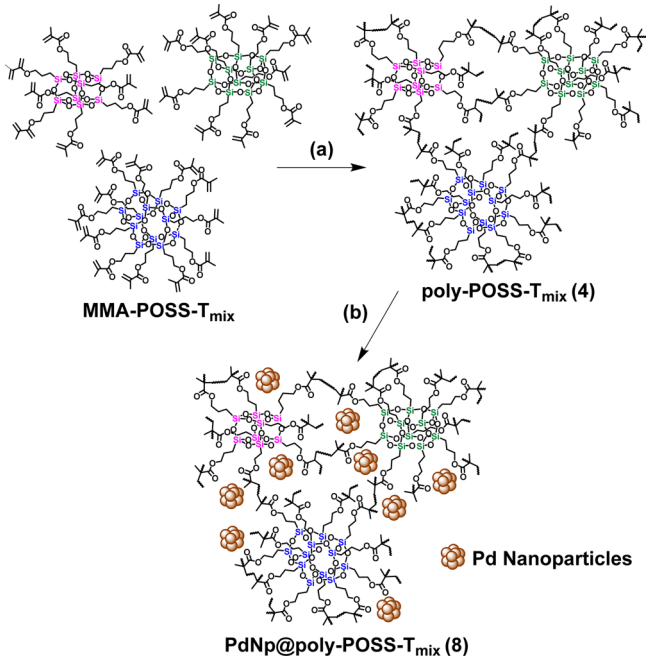

[a](a) AIBN, PEG-200:THF (1:3 w/w), 60 °C, 24 h; (b) $Pd(OAc)_2$, $NaBH_4$, CH_3OH, rt, 24 h.

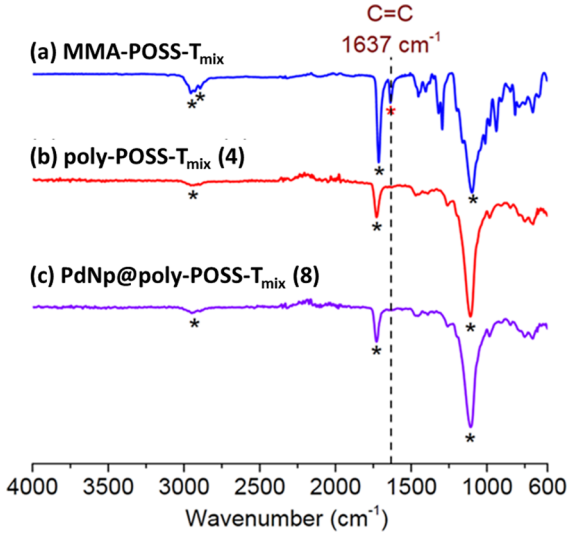

Figure 1. FT-IR spectra of MMA-POSS-T_{mix}, poly-POSS-T_{mix} (**4**), and PdNp@poly-POSS-T_{mix} (**8**).

uniformly broad signal at ca. −70 ppm, characteristic of the silsesquioxane T-unit of silicon cage compound as $RSiO_{1.5}$ unit (Figure S3). This result suggests that the cage structures of POSS remain intact (i.e., no cage opening) under the polymerization conditions investigated.

Preparation of PdNp@poly-POSS-T_n. To study the effect of POSS cage sizes on the immobilization of Pd nanoparticles, a mixture of $Pd(OAc)_2$ (10 wt %) in the presence of the supports **1**−**4** was reduced with excess $NaBH_4$ in CH_3OH to afford well-dispersed Pd nanoparticles on POSS-based supports, PdNp@poly-POSS-T_n [n = 8 (**5**), 10 (**6**), 12 (**7**), and mix (**8**)] (Scheme 2). Notably, the resulting products **5**−**8** appeared homogeneously dispersed in CH_3OH, whereas Pd nanoparticles generated in the absence of the poly-POSS-T_n support underwent aggregation after 5 min of stirring (see Figure S4). This observation confirms effective stabilization of Pd nanoparticles by the polymeric POSS-based supports, possibly *via* coordination at carbonyl (C═O) groups of the cross-linked MMA networks. In agreement with our findings, previous studies have suggested that ester C═O functional groups are capable of stabilizing Pd nanoparticles.[46−48] According to MP-AES, the PdNp@poly-POSS-T_n (**5**−**8**) contains 4−6 wt % of Pd on supporting materials (see Table S1).

Materials Characterizations. All powder XRD spectra of **1**−**4** reveal an amorphous nature of the resulting materials featuring two broad peaks at 2θ = 9° and 18° indicative of the silsesquioxane cage and poly(methacrylate) chain, respectively (Figure 2).[49] Apparently, the polymerizations resulted in more

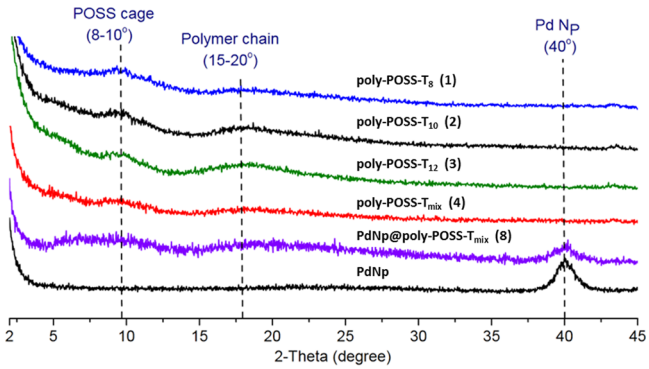

Figure 2. Powder XRD spectra of **1**−**4** and **8**.

disordered packing arrangements as the previously crystalline compound of MMA-POSS-T_8 monomer became amorphous after polymerization. The powder XRD spectra of PdNp@poly-POSS-T_8, T_{10}, T_{12}, and T_{mix} (**5**−**8**) exhibit an additional peak at 2θ = 40°, assignable to Pd nanoparticles (Figures 2 and S6).[50,51] Thermogravimetric analyses (TGA) of samples **1**−**4** reveal mass losses at 220−240 and 250−350 °C, associated with ester bond cleavage and polymer chain degradation, whereas ceramic yields of these materials are in the range of 33−36% (see Figure S7).[52,53] In addition, the DSC spectra of **1**−**4** contain no signal assignable to the glass transition temperature (T_g) and the melting temperature (T_m), suggesting rigid and cross-linked structures (see Figure S8).[54] In agreement with XRD spectra, TEM images of **1**−**4** are similar, showing amorphous structures with porous characteristics (Figure 3).

The porosities of **1**−**8** were determined using nitrogen adsorption at 77 K, as shown in Figure 4. All samples exhibit type IV isotherm patterns with H3-type hysteresis loop at higher relative pressures, suggesting the presence of both micropores and mesopores in the structure and nonrigid aggregates of plate-like particles.[55,56] The Brunauer−Emmett−Teller (BET) surface areas of the materials (683−839 $m^2\ g^{-1}$) are exceptionally large as compared to other silica-based materials (Table 1).[13,26,35,57] For poly-POSS-T_n, both surface areas and total pore volumes follow the trend: poly-POSS-T_{12} > T_{10} > T_{mix} > T_8. We speculate that POSS molecules with higher symmetry [POSS-T_8 (O_h) > POSS-T_{10} (D_{5h}) > POSS-T_{12} (D_{2d})] result in better packed materials and consequently lead to smaller pore volumes and lower surface areas.[17,48] In addition, because the poly-POSS-T_{mix} (**4**) consists of all three POSS cage sizes (T_8, T_{10}, and T_{12}), its porosities are roughly an

DOI: 10.1021/acsami.7b03910
ACS Appl. Mater. Interfaces 2017, 9, 12812−12822

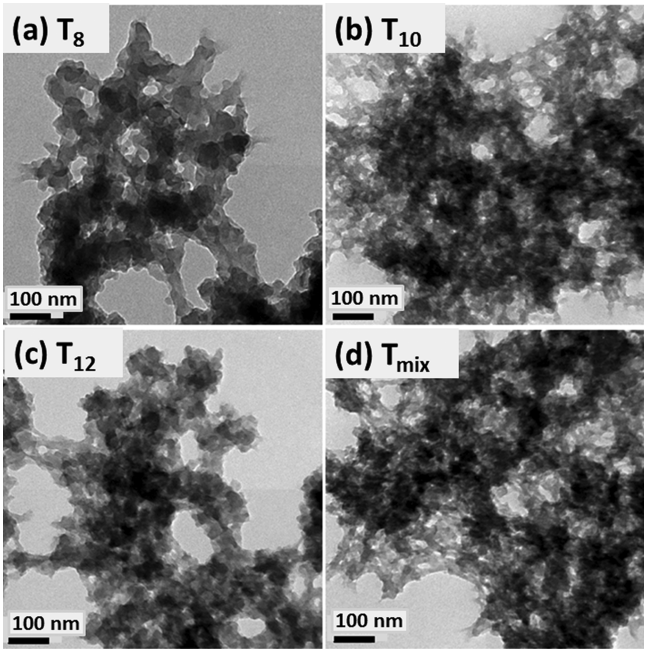

Figure 3. TEM images of (a) poly-POSS-T_8 (**1**), (b) poly-POSS-T_{10} (**2**), (c) poly-POSS-T_{12} (**3**), and (d) poly-POSS-T_{mix} (**4**).

Table 1. Porosity Data for Polymeric POSS-Based Supports and PdNp@poly-POSS-T_n

entry	samples	S_{BET} [a] ($m^2\ g^{-1}$)	S_{micro} [b] ($m^2\ g^{-1}$)	V_{total} [c] ($cm^3\ g^{-1}$)	V_{micro} [b] ($cm^3\ g^{-1}$)
1	poly-POSS-T_8 (**1**)	683	67	0.97	0.033
2	poly-POSS-T_{10} (**2**)	819	139	1.11	0.070
3	poly-POSS-T_{12} (**3**)	839	41	1.25	0.019
4	poly-POSS-T_{mix} (**4**)	719	50	0.99	0.024
5	PdNp@poly-POSS-T_8 (**5**)	521	160	0.49	0.083
6	PdNp@poly-POSS-T_{10} (**6**)	713	132	1.03	0.068
7	PdNp@poly-POSS-T_{12} (**7**)	850	83	1.32	0.042
8	PdNp@poly-POSS-T_{mix} (**8**)	695	45	1.04	0.021
9	poly-POSS-T_{mix} (no PEG-200) (**9**)	803	106	0.60	0.054
10	PdNp@poly-POSS-T_{mix} (no PEG-200) (**10**)	594	51	0.46	0.025

[a]Surface area derived from N_2 adsorption isotherm using multipoint BET analysis. [b]Microporous surface areas and micropore volumes were calculated from N_2 adsorption isotherm using *t*-plot method. [c]Total pore volumes were calculated from pores with diameter less than 160 nm at P/P_0 = 0.99.

average of all three pure compounds (Table 1, entry 4). According to BJH pore size distributions (Figure 5), **1**−**4** possess broad pore size distributions consisting of a mixture of micropores (<2 nm), mesopores (2−50 nm), and a small amount of macropores (>50 nm). In particular, poly-POSS-T_{12} (**3**) comparatively possesses the highest surface area and ratio of mesopores. In other words, it is explained that a larger cage size or lower structural symmetry of POSS-T_{12} results in less effective packing density of porous materials after polymerization, consequently leading to larger pore volumes and surface areas. To determine the effect of PEG-200 on porosity, we also prepared poly-POSS-T_{mix} in the absence of PEG-200. As compared to **4**, poly-POSS-T_{mix} (no PEG-200) (**9**) exhibits higher surface area and significantly larger micropore volume [803 $m^2\ g^{-1}$ and 0.054 $cm^3\ g^{-1}$, cf., 719 $m^2\ g^{-1}$ and 0.024 cm^3

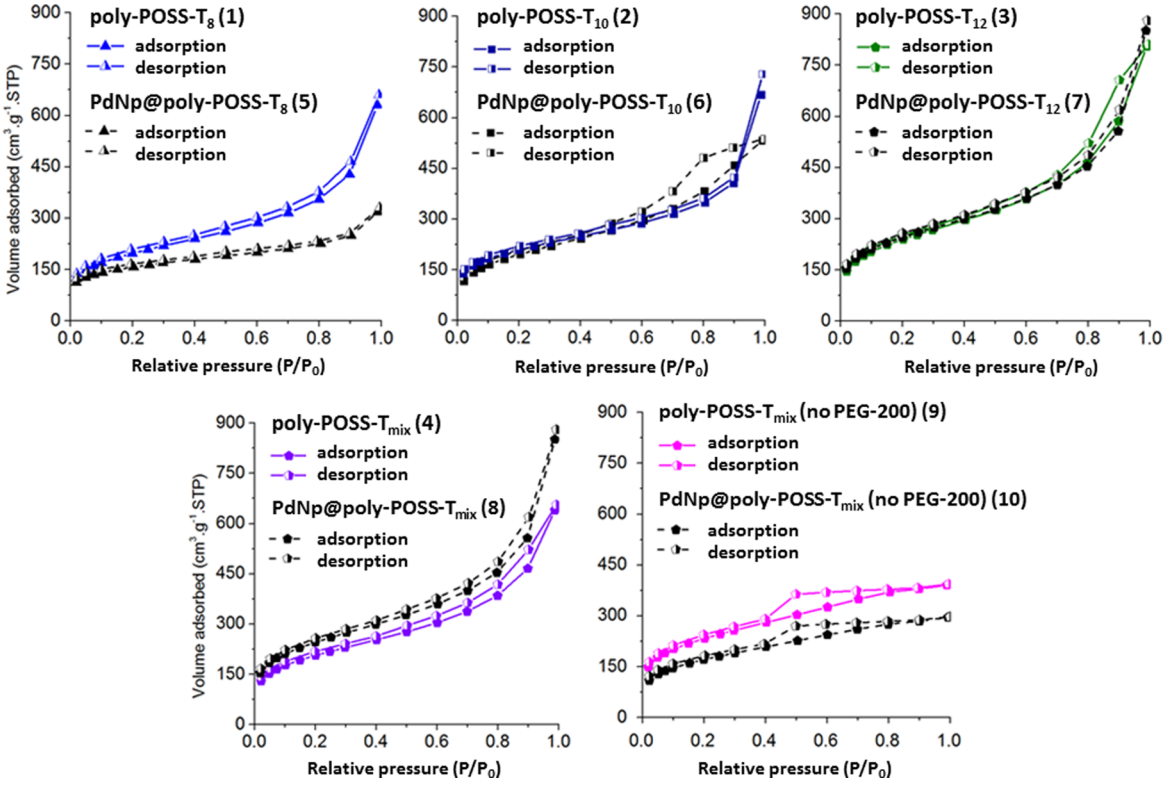

Figure 4. N_2 adsorption−desorption isotherms of **1**−**10**.

DOI: 10.1021/acsami.7b03910
ACS Appl. Mater. Interfaces 2017, 9, 12812−12822

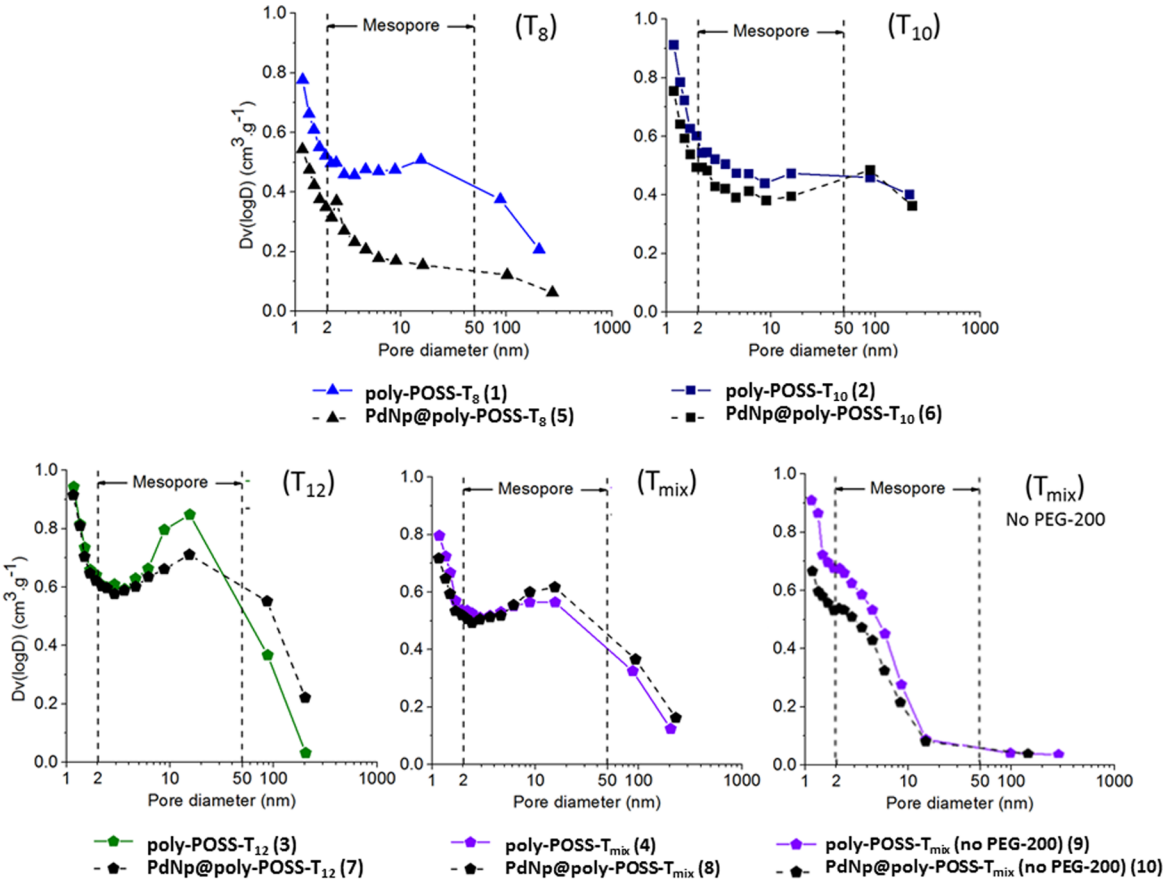

Figure 5. Pore size distributions by BJH adsorption of **1**−**10**.

g^{-1} (for **4**); Table 1]. However, the total pore volume decreases to 0.60 from 0.99 $cm^3\ g^{-1}$ (for **4**) with narrower BJH pore size distribution (Figure 5). These results confirm the role of PEG-200 as a porogenic solvent. After Pd nanoparticles immobilization, surface areas and total pore volumes of poly-POSS-T_8 were significantly reduced (from 683 to 521 $m^2\ g^{-1}$ and from 0.97 to 0.49 $cm^3\ g^{-1}$, respectively), whereas, for other POSS-based polymers, only slight reductions were observed (entries 1−8, Table 1).

SEM images of **8** display rough and porous surfaces, whereas the EDX spectrum contains a peak at 2.8 eV assignable to Pd nanoparticles locating on the surface of the supporting materials (see Figures S10 and S11). In addition, despite differences in surface areas, total pore volumes, and pore size distributions, TEM images in Figure 6 of PdNp@poly-POSS-T_n (**5**−**8**) reveal well-dispersed Pd nanoparticles with average sizes of 6.2−6.5 nm, which further confirm effective stabilization of Pd nanoparticles by the polymeric POSS-based supports (vide supra).

Supported Palladium Nanoparticles for Aerobic Alcohol Oxidation. To evaluate the catalytic activities of PdNp@poly-POSS-T_n (**5**−**8**), we initially investigated oxidation of benzyl alcohol to benzaldehyde. In toluene, 0.43 mol % Pd of **5**−**8** catalyzed aerobic oxidation of benzyl alcohol at 80 °C to afford benzaldehyde as a sole product in quantitative yields after 5 h (entries 1−4; Table 2). It should be noted that, as a controlled experiment, no oxidation occurred in the absence of Pd catalyst (entry 14).

Under the same conditions, with the water solvent, poly-POSS-T_{mix} provides a lower benzaldehyde yield of 85% (entry 5). Recently, Rostamnia and co-workers have demonstrated that the use of water and Pluronic (P123) emulsion enhanced yields of the oxidized products by improving the solubility of hydrophobic alcoholic substrates and preventing the aggregation of Pd nanoparticles.[58−60] On the basis of these findings, 6 wt % P123 in water was investigated as the reaction medium. With 0.43 mol % Pd, PdNp@poly-POSS-T_8 (**5**) afforded 72% yield of benzaldehyde, while PdNp@poly-POSS-T_{10}, T_{12}, and T_{mix} (**6**−**8**) resulted in quantitative yields (TOF = 46.5 h^{-1}, entries 6−9). To investigate the role of P123, TEM images of the used catalyst **8** from catalytic oxidation reactions with and without P123 were compared in which no significant changes in average Pd nanoparticle sizes were observed (see Figure S12). Thus, it is most likely that P123 facilitates substrate solubility rather than prevents nanoparticle agglomeration. Meanwhile, when PdNp@poly-POSS-T_{mix} (no PEG-200) in entry 10 was used as a catalyst, 71% product yield was obtained. Reduced catalytic activities of **5** and **10** are attributed to their lower amounts of mesopores, surface areas, and total pore volumes, as compared to **6**−**8**. To demonstrate the role of POSS, other solid supports were also investigated. Under the same conditions, Pd nanoparticles stabilized on activated charcoal (Pd/C) and PMMA (Pd/PMMA) afforded the oxidized product in 66% and 45% yields, respectively (entries 11 and 12). Furthermore, with the PdO catalyst, no benzalydehyde product was detected (entry 13).

On the basis of simpler preparation (i.e., no need for purifications), the catalyst PdNp@poly-POSS-T_{mix} (**8**) was selected for further studies. Various benzyl alcohol derivatives were examined as substrates in the aerobic oxidation reactions

DOI: 10.1021/acsami.7b03910
ACS Appl. Mater. Interfaces 2017, 9, 12812−12822

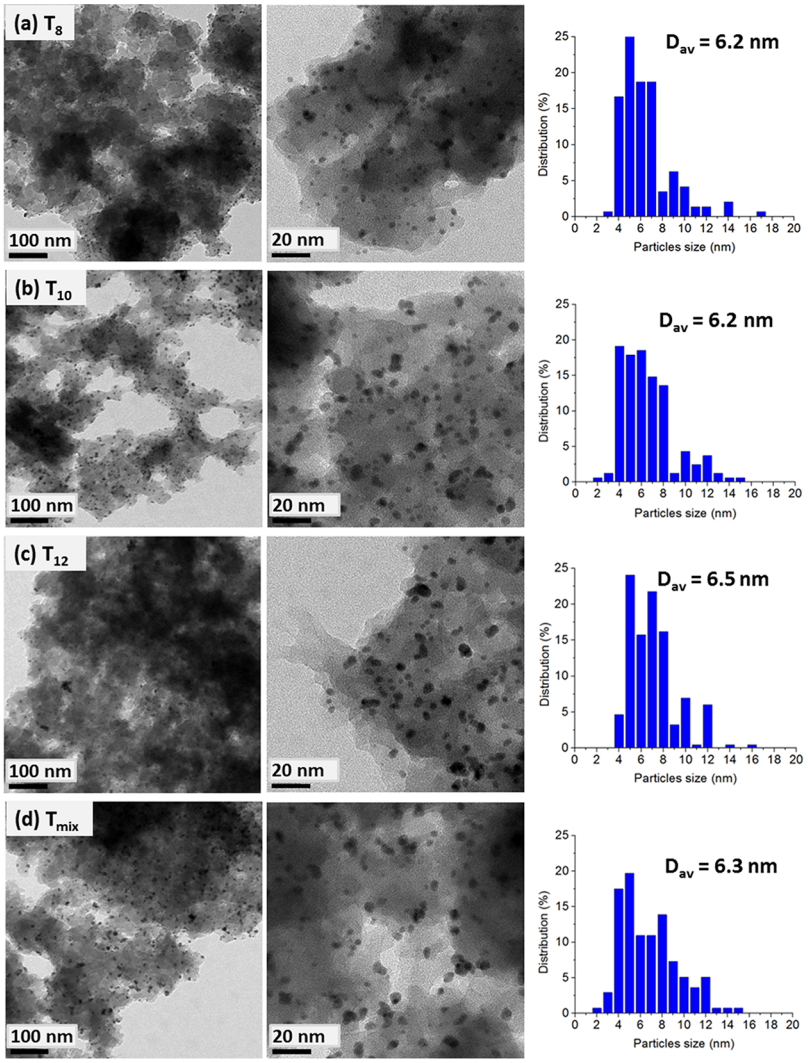

Figure 6. TEM images of PdNp@poly-POSS-T_n (n = 8, 10, 12, and mix; **5**–**8**) at scale bars of 100 and 20 nm.

(Table 3). Under optimal conditions, while the hydroxyl-substituted benzyl alcohol was quantitatively converted to the corresponding aldehyde after 6 h (entry 2), the methoxy-substituted benzyl alcohols and cinnamyl alcohol afforded moderate to high conversions at higher Pd loadings (entries 3–6). On the contrary, only a trace amount (<5%) of electron-deficient benzyl alcohol derivatives including 4-nitro, 4-bromobenzyl alcohols, and 2-furfuryl alcohol was oxidized. Conversions of these electron-deficient substrates were significantly improved in the presence of K_2CO_3 (1 equiv) additive, giving the corresponding aldehyde products in 88–94% yields (entries 7–9). These findings are consistent with previous results, in which a base promotes deprotonation of a Pd-bound alcohol[61] and/or β-H elimination.[62] Unfortunately, more challenging aliphatic alcohol 1-hexanol could not be oxidized under the catalytic conditions investigated.

Hot filtration tests (see Scheme S1) and MP-AES analysis of the reaction filtrate confirm the heterogeneous nature of the catalyst with minimal Pd leaching (<0.2 ppm). For reusability study, after each cycle, catalyst **8** was recovered *via* centrifugation followed by simple decantation to remove the supernatant. After being washed with EtOH, the solid **8** was used in the next catalytic run. It should be noted that the catalytic reactions in the reusability study were up-scaled and the amount of **8** used in the first catalytic run was increased from 0.43 mol % (entry 9, Table 2) to 0.65 mol % to make up for catalyst losses after each catalyst recovery. The results revealed no significant loss in activities after five reaction cycles (Figure 7). TEM analysis of the used catalyst **8** shows well-dispersed Pd nanoparticles with some aggregation resulting in a slightly larger average nanoparticle size of 7.3 nm (Figure S13 and Table 4). To gain insights into the oxidation states of Pd species, the XPS spectra of the as-prepared and used catalysts **8** were measured (Figures 8 and S14), respectively. The XPS spectra of both materials contain two main peaks with binding energies of ca. 335.0 and 340.3 eV, assignable to Pd $3d_{5/2}$ and Pd $3d_{3/2}$, respectively. The binding energies of deconvoluted peaks suggest that both Pd(0) and Pd(II) species are present on the POSS-based support. The small shoulder peaks at $E_b \approx$ 336.4 eV ($3d_{5/2}$) and 341.7 ($3d_{3/2}$) are assigned to PdO species formed on the surface.[55,63] The ratios of Pd(0)/Pd(II) species estimated from the relative peak areas in the XPS spectra are essentially the same for both as-prepared and used catalysts (Table 4). In agreement with the results from reusability studies, the XPS analysis (see Figure S14) confirms that no significant degradation of Pd nanoparticles (*via* oxidation) occurs over the course of the catalytic reaction.

DOI: 10.1021/acsami.7b03910
ACS Appl. Mater. Interfaces 2017, 9, 12812–12822

Table 2. Catalytic Activities toward Aerobic Alcohol Oxidation[a]

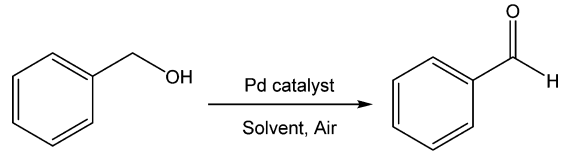

entry[a]	catalyst	solvent	yield (%)[b]
1	PdNp@poly-POSS-T_8	toluene	>99
2	PdNp@ poly-POSS-T_{10}	toluene	>99
3	PdNp@ poly-POSS-T_{12}	toluene	>99
4	PdNp@ poly-POSS-T_{mix}	toluene	>99
5	PdNp@ poly-POSS-T_{mix}	water	85
6[c]	PdNp@ poly-POSS-T_8	water/P123	72
7[c]	PdNp@ poly-POSS-T_{10}	water/P123	95
8[c]	PdNp@ poly-POSS-T_{12}	water/P123	>99
9[c]	PdNp@ poly-POSS-T_{mix}	water/P123	>99
10[c]	PdNp@ poly-POSS-T_{mix} (no PEG-200)	water/P123	71
11[c]	Pd/C	water/P123	66
12[c]	PdNp/PMMA	water/P123	45
13[c]	PdO	water/P123	0
14[c]	poly-POSS-T_{mix}	water/P123	0

[a]Reaction conditions: 1.0 mmol of benzyl alcohol, 2.0 mL of solvent, 0.43 mol % Pd (the amount of Pd on supporting materials was determined by MP-AES; Table S1), reaction time = 5 h. [b]Product yield was determined using GC−MS with anisole or hexamethylbenzene as internal standard. [c]2 mL of H_2O with P123 (6 wt %, 0.12 g).

Table 3. Substrate Scope for Aerobic Alcohol Oxidation Catalyzed by PdNp@poly-POSS-T_{mix} (8) in Water[a]

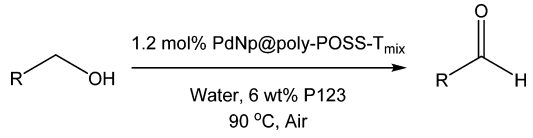

entry[a]	R−	time (h)	yield (%)[b]
1[c]	C_6H_5−	6	>99
2[c]	4-HOC_6H_4−	6	>99
3	2-$CH_3OC_6H_4$−	6	70
4	3-$CH_3OC_6H_4$−	6	90
5	4-$CH_3OC_6H_4$−	6	81
6	C_6H_5CH=CH−	6	95
7[d]	4-$NO_2C_6H_4$−	96	91
8[d]	4-BrC_6H_4−	48	88
9[d]	2-furyl−	6	94

[a]Reaction conditions: 0.50 mmol of RCH_2OH, 2.0 mL of H_2O with P123 (6 wt %, 0.12 g), 1.2 mol % Pd (14 mg of **8**) at 90 °C with air bubbling. [b]GC yield. [c]0.43 mol % Pd (5.2 mg of **8**). [d]With 1 equiv of K_2CO_3 additive.

CONCLUSION

Polymeric POSS-based porous materials, poly-POSS-T_n [n = 8 (**1**), 10 (**2**), 12 (**3**), and mix (**4**)], were prepared *via* free radical polymerization from the corresponding pure forms of MMA-POSS-T_n (n = 8, 10, 12) and the mixture form (n = mix). BET analysis revealed that POSS cage sizes exert a significant effect on polymer surface areas and porosities, as poly-POSS-T_{12} (**3**) possesses the highest surface areas, pore volumes, and also amount of mesopores, as compared to other poly-POSS-T_n. Interestingly, although these differences show no effect on Pd nanoparticles stabilization, they have an influence on the catalytic activities toward Pd-catalyzed aerobic alcohol oxidation. In particular, due to higher surface areas, pore volumes, and amount of mesopores, PdNp@poly-POSS-T_n [n = 10 (**6**), 12 (**7**), and mix (**8**)] were more effective heterogeneous oxidation catalysts than PdNp@poly-POSS-T_8 (**5**) in the P123/water medium. In addition, the substrate scope study revealed that electron-rich benzyl alcohol derivatives were more readily oxidized than the related electron-withdrawing substrates. Catalyst **8** can also be reused for at least five reaction cycles without a significant loss in activities.

This work, for the first time, provides insights into the effects of POSS cage sizes on POSS-based polymer properties and consequently their efficiency as catalyst supports for Pd-catalyzed aerobic alcohol oxidation. These findings should pave a way for the preparation of POSS-based materials for stabilization of metal nanoparticles. Efforts to include other stabilizing functional groups at the POSS organic linkers and investigation of different catalytic reactions are ongoing in our laboratory.

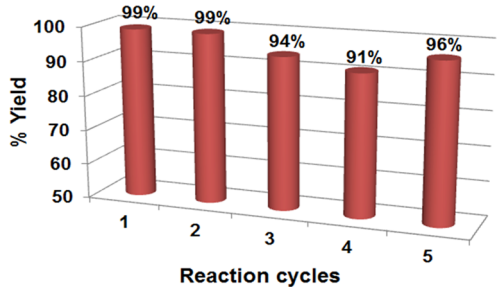

Figure 7. Reusability studies of **8**.

Table 4. Pd Nanoparticles on the As-Prepared and the Used Catalyst 8

entry	catalysts	mean particle size diameter by volume measured using TEM (nm)[a]	oxidation state of surface Pd (XPS) (Pd(0)/Pd(II))
1	**8**	6.3	2.1
2	used **8**	7.3	2.2

[a]The average Pd nanoparticle sizes on the poly-POSS-T_{mix} support obtained by specified number of particles count.

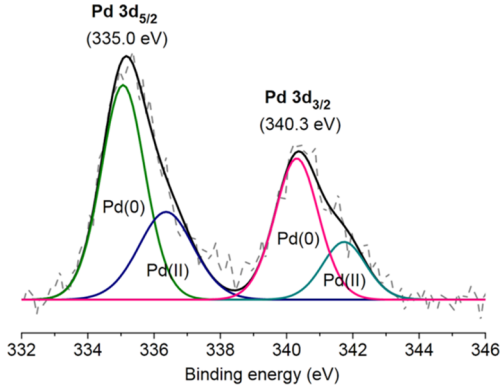

Figure 8. XPS analysis for Pd 3d spectra of Pd nanoparticles on the surface of freshly prepared **8**.

DOI: 10.1021/acsami.7b03910
ACS Appl. Mater. Interfaces 2017, 9, 12812−12822

■ ASSOCIATED CONTENT

Supporting Information

The Supporting Information is available free of charge on the ACS Publications website at DOI: 10.1021/acsami.7b03910.

FT-IR spectra and PXRD patterns of MMA-POSS-T_8, MMA-POSS-T_{10}, and MMA-POSS-T_{12}; FT-IR, ^{29}Si CP/MAS NMR spectra, DSC, and TGA curves of materials **1**−**4**; and EDX, XPS spectra, SEM, and TEM images of materials **4** and **8** and the reaction images of palladium with/without supported materials (PDF)

■ AUTHOR INFORMATION

Corresponding Author

*Tel.: +66-2-2015126. Fax: +66-2-3547151. E-mail: vuthichai.erv@mahidol.ac.th.

ORCID

Vuthichai Ervithayasuporn: 0000-0002-1999-2463

Notes

The authors declare no competing financial interest.

■ ACKNOWLEDGMENTS

This research is financially supported by two grants from the Thailand Research Fund: RSA5780058 (for P.Sa.) and RSA5980018 (for V.E.). We also gratefully acknowledge the Center of Excellence for Innovation in Chemistry (PERCH-CIC), Faculty of Science, Mahidol University, and Mahidol University under the National Research Universities Initiative, the Nanotechnology Center (NANOTEC), NSTDA, Ministry of Science and Technology, Thailand, through its program of Center of Excellence Network.

■ REFERENCES

(1) Croissant, J. G.; Cattoen, X.; Wong Chi Man, M.; Durand, J.-O.; Khashab, N. M. Syntheses and Applications of Periodic Mesoporous Organosilica Nanoparticles. *Nanoscale* **2015**, *7*, 20318−20334.

(2) Sanchez, C.; Belleville, P.; Popall, M.; Nicole, L. Applications of Advanced Hybrid Organic-Inorganic Nanomaterials: from Laboratory to Market. *Chem. Soc. Rev.* **2011**, *40*, 696−753.

(3) Oral, A.; Tasdelen, M. A.; Demirel, A. L.; Yagci, Y. Poly(methyl methacrylate)/Clay Nanocomposites by Photoinitiated Free Radical Polymerization using Intercalated Monomer. *Polymer* **2009**, *50*, 3905−3910.

(4) Zhang, C.; Babonneau, F.; Bonhomme, C.; Laine, R. M.; Soles, C. L.; Hristov, H. A.; Yee, A. F. Highly Porous Polyhedral Silsesquioxane Polymers. Synthesis and Characterization. *J. Am. Chem. Soc.* **1998**, *120*, 8380−8391.

(5) Roll, M. F.; Kampf, J. W.; Kim, Y.; Yi, E.; Laine, R. M. Nano Building Blocks *via* Iodination of $[PhSiO_{1.5}]_n$, Forming $[p\text{-}IC_6H_4SiO_{1.5}]_n$ (n = 8, 10, 12), and a New Route to High-Surface-Area, Thermally Stable, Microporous Materials *via* Thermal Elimination of I_2. *J. Am. Chem. Soc.* **2010**, *132*, 10171−10183.

(6) Sodkhomkhum, R.; Ervithayasuporn, V. Synthesis of Poly(siloxane/double-decker Silsesquioxane) *via* Dehydrocarbonative Condensation Reaction and Its Functionalization. *Polymer* **2016**, *86*, 113−119.

(7) Tanaka, K.; Chujo, Y. Advanced Functional Materials Based on Polyhedral Oligomeric Silsesquioxane (POSS). *J. Mater. Chem.* **2012**, *22*, 1733−1746.

(8) Chimjarn, S.; Kunthom, R.; Chancharone, P.; Sodkhomkhum, R.; Sangtrirutnugul, P.; Ervithayasuporn, V. Synthesis of aromatic functionalized cage-rearranged silsesquioxanes (T_8, T_{10}, and T_{12}) *via* nucleophilic substitution reactions. *Dalton Trans.* **2015**, *44*, 916−919.

(9) Ervithayasuporn, V.; Pornsamutsin, N.; Prangyoo, P.; Sammawutthichai, K.; Jaroentomeechai, T.; Phurat, C.; Teerawatananond, T. One-Pot Synthesis of Halogen Exchanged Silsesquioxanes: Octakis(3-bromopropyl)octasilsesquioxane and Octakis(3-iodopropyl)octasilsesquioxane. *Dalton Trans.* **2013**, *42*, 13747−13753.

(10) Jaroentomeechai, T.; Yingsukkamol, P.-k.; Phurat, C.; Somsook, E.; Osotchan, T.; Ervithayasuporn, V. Synthesis and Reactivity of Nitrogen Nucleophiles-Induced Cage-Rearrangement Silsesquioxanes. *Inorg. Chem.* **2012**, *51*, 12266−12272.

(11) Kunthom, R.; Jaroentomeechai, T.; Ervithayasuporn, V. Polyhedral Oligomeric Silsesquioxane (POSS) Containing Sulfonic Acid Groups as a Metal-Free Catalyst to Prepare Polycaprolactone. *Polymer* **2017**, *108*, 173−178.

(12) Hanprasit, S.; Tungkijanansin, N.; Prompawilai, A.; Eangpayung, S.; Ervithayasuporn, V. Synthesis and Isolation of Non-Chromophore Cage-Rearranged Silsesquioxanes from Base-Catalyzed Reactions. *Dalton Trans.* **2016**, *45*, 16117−16120.

(13) Nischang, I.; Brüggemann, O.; Teasdale, I. Facile, Single-Step Preparation of Versatile, High-Surface-Area, Hierarchically Structured Hybrid Materials. *Angew. Chem., Int. Ed.* **2011**, *50*, 4592−4596.

(14) Wei, Z.; Luo, X.; Zhang, L.; Luo, M. POSS-Based Hybrid Porous Materials with Exceptional Hydrogen Uptake at Low Pressure. *Microporous Mesoporous Mater.* **2014**, *193*, 35−39.

(15) Li, J.-G.; Chu, W.-C.; Kuo, S.-W. Hybrid Mesoporous Silicas and Microporous POSS-Based Frameworks Incorporating Evaporation-Induced Self-Assembly. *Nanomaterials* **2015**, *5*, 1087.

(16) Zhang, L.; Yang, Q.; Yang, H.; Liu, J.; Xin, H.; Mezari, B.; Magusin, P. C. M. M.; Abbenhuis, H. C. L.; Santen, R. A. v.; Li, C. Super-Microporous Organosilicas Synthesized from Well-Defined Nanobuilding Units. *J. Mater. Chem.* **2008**, *18*, 450−457.

(17) Pawlak, T.; Kowalewska, A.; Zgardzińska, B.; Potrzebowski, M. J. Structure, Dynamics, and Host−Guest Interactions in POSS Functionalized Cross-Linked Nanoporous Hybrid Organic−Inorganic Polymers. *J. Phys. Chem. C* **2015**, *119*, 26575−26587.

(18) Kim, H.; Han, B.; Choo, J.; Cho, J. Three-Dimensional Porous Silicon Particles for Use in High-Performance Lithium Secondary Batteries. *Angew. Chem.* **2008**, *120*, 10305−10308.

(19) Ma, J.; Lv, L.; Zou, G.; Zhang, Q. Fluorescent Porous Film Modified Polymer Optical Fiber via "Click" Chemistry: Stable Dye Dispersion and Trace Explosive Detection. *ACS Appl. Mater. Interfaces* **2015**, *7*, 241−249.

(20) Zhou, H.; Ye, Q.; Neo, W. T.; Song, J.; Yan, H.; Zong, Y.; Tang, B. Z.; Hor, T. S. A.; Xu, J. Electrospun Aggregation-Induced Emission Active POSS-based Porous Copolymer Films for Detection of Explosives. *Chem. Commun.* **2014**, *50*, 13785−13788.

(21) Rekha, P.; Sahoo, U.; Mohanty, P. Click-Based Porous Inorganic-Organic Hybrid Material (PHM) Containing Cyclophosphazene Unit and Their Application in Carbon Dioxide Capture. *RSC Adv.* **2014**, *4*, 34860−34863.

(22) Stein, A.; Melde, B. J.; Schroden, R. C. Hybrid Inorganic−Organic Mesoporous Silicates-Nanoscopic Reactors Coming of Age. *Adv. Mater.* **2000**, *12*, 1403−1419.

(23) Ervithayasuporn, V.; Kwanplod, K.; Boonmak, J.; Youngme, S.; Sangtrirutnugul, P. Homogeneous and Heterogeneous Catalysts of Organopalladium Functionalized-Polyhedral Oligomeric Silsesquioxanes for Suzuki−Miyaura Reaction. *J. Catal.* **2015**, *332*, 62−69.

(24) Leng, Y.; Liu, J.; Zhang, C.; Jiang, P. A Polyhedral Oligomeric Silsesquioxane (POSS)-Bridged Oxo-Molybdenum Schiff Base Complex with Enhanced Heterogeneous Catalytic Activity in Epoxidation. *Catal. Sci. Technol.* **2014**, *4*, 997−1004.

(25) Leng, Y.; Liu, J.; Jiang, P.; Wang, J. POSS-Derived Mesostructured Amphiphilic Polyoxometalate-based Ionic Hybrids as Highly Efficient Epoxidation Catalysts. *ACS Sustainable Chem. Eng.* **2015**, *3*, 170−176.

(26) Alves, F.; Scholder, P.; Nischang, I. Conceptual Design of Large Surface Area Porous Polymeric Hybrid Media Based on Polyhedral Oligomeric Silsesquioxane Precursors: Preparation, Tailoring of Porous Properties, and Internal Surface Functionalization. *ACS Appl. Mater. Interfaces* **2013**, *5*, 2517−2526.

(27) Létant, S. E.; Maiti, A.; Jones, T. V.; Herberg, J. L.; Maxwell, R. S.; Saab, A. P. Polyhedral Oligomeric Silsesquioxane (POSS)-Stabilized Pd Nanoparticles: Factors Governing Crystallite Morphology and Secondary Aggregate Structure. *J. Phys. Chem. C* **2009**, *113*, 19424−19431.
(28) Moitra, N.; Kanamori, K.; Shimada, T.; Takeda, K.; Ikuhara, Y. H.; Gao, X.; Nakanishi, K. Synthesis of Hierarchically Porous Hydrogen Silsesquioxane Monoliths and Embedding of Metal Nanoparticles by On-Site Reduction. *Adv. Funct. Mater.* **2013**, *23*, 2714−2722.
(29) Scholder, P.; Nischang, I. Miniaturized Catalysis: Monolithic, Highly Porous, Large Surface Area Capillary Flow Reactors Constructed *in situ* from Polyhedral Oligomeric Silsesquioxanes (POSS). *Catal. Sci. Technol.* **2015**, *5*, 3917−3921.
(30) Moitra, N.; Kanamori, K.; Ikuhara, Y. H.; Gao, X.; Zhu, Y.; Hasegawa, G.; Takeda, K.; Shimada, T.; Nakanishi, K. Reduction on Reactive Pore Surfaces as a Versatile Approach to Synthesize Monolith-Supported Metal Alloy Nanoparticles and Their Catalytic Applications. *J. Mater. Chem. A* **2014**, *2*, 12535−12544.
(31) Moitra, N.; Matsushima, A.; Kamei, T.; Kanamori, K.; Ikuhara, Y. H.; Gao, X.; Takeda, K.; Zhu, Y.; Nakanishi, K.; Shimada, T. A New Hierarchically Porous Pd@HSQ Monolithic Catalyst for Mizoroki-Heck Cross-Coupling Reactions. *New J. Chem.* **2014**, *38*, 1144−1149.
(32) Mohapatra, S.; Chaiprasert, T.; Sodkhomkhum, R.; Kunthom, R.; Hanprasit, S.; Sangtrirutnugul, P.; Ervithayasuporn, V. Solid−State Synthesis of Polyhedral Oligomeric Silsesquioxane-Supported N-Heterocyclic Carbenes/Imidazolium salts on Palladium Nanoparticles: Highly Active and Recyclable Catalyst. *ChemistrySelect* **2016**, *1*, 5353−5357.
(33) Simon, M.-O.; Li, C.-J. Green chemistry oriented organic synthesis in water. *Chem. Soc. Rev.* **2012**, *41*, 1415−1427.
(34) Brink, G.-J. t.; Arends, I. W. C. E.; Sheldon, R. A. Green, Catalytic Oxidation of Alcohols in Water. *Science* **2000**, *287*, 1636−1639.
(35) Zhancheng, M.; Hengquan, Y.; Yong, Q.; Yajuan, H.; Guang, L. Palladium Nanoparticles Confined in the Nanocages of SBA-16: Enhanced Recyclability for the Aerobic Oxidation of Alcohols in Water. *J. Mol. Catal. A: Chem.* **2010**, *331*, 78−85.
(36) Uozumi, Y.; Nakao, R. Catalytic Oxidation of Alcohols in Water under Atmospheric Oxygen by Use of an Amphiphilic Resin-Dispersion of a Nanopalladium Catalyst. *Angew. Chem., Int. Ed.* **2003**, *42*, 194−197.
(37) Li, Y.-A.; Yang, S.; Liu, Q.-K.; Chen, G.-J.; Ma, J.-P.; Dong, Y.-B. Pd(0)@UiO-68-AP: Chelation-Directed Bifunctional Heterogeneous Catalyst for Stepwise Organic Transformations. *Chem. Commun.* **2016**, *52*, 6517−6520.
(38) Chen, J.; Zhang, Q.; Wang, Y.; Wan, H. Size-Dependent Catalytic Activity of Supported Palladium Nanoparticles for Aerobic Oxidation of Alcohols. *Adv. Synth. Catal.* **2008**, *350*, 453−464.
(39) Chen, G.-J.; Wang, J.-S.; Jin, F.-Z.; Liu, M.-Y.; Zhao, C.-W.; Li, Y.-A.; Dong, Y.-B. Pd@Cu(II)-MOF-Catalyzed Aerobic Oxidation of Benzylic Alcohols in Air with High Conversion and Selectivity. *Inorg. Chem.* **2016**, *55*, 3058−3064.
(40) Karimi, B.; Khorasani, M.; Vali, H.; Vargas, C.; Luque, R. Palladium Nanoparticles Supported in the Nanospaces of Imidazolium-Based Bifunctional PMOs: The Role of Plugs in Selectivity Changeover in Aerobic Oxidation of Alcohols. *ACS Catal.* **2015**, *5*, 4189−4200.
(41) Ervithayasuporn, V.; Chimjarn, S. Synthesis and Isolation of Methacrylate- and Acrylate-Functionalized Polyhedral Oligomeric Silsesquioxanes (T_8, T_{10}, and T_{12}) and Characterization of the Relationship between Their Chemical Structures and Physical Properties. *Inorg. Chem.* **2013**, *52*, 13108−13112.
(42) Li, L.; Liang, R.; Li, Y.; Liu, H.; Feng, S. Hybrid Thiol−ene Network Nanocomposites Based on Multi(meth)acrylate POSS. *J. Colloid Interface Sci.* **2013**, *406*, 30−36.
(43) Xing, Y.; Peng, J.; Xu, K.; Lin, W.; Gao, S.; Ren, Y.; Gui, X.; Liang, S.; Chen, M. Polymerizable Molecular Silsesquioxane Cage Armored Hybrid Microcapsules with In Situ Shell Functionalization. *Chem. - Eur. J.* **2016**, *22*, 2114−2126.
(44) Mi, Y.; Zhou, W.; Li, Q.; Zhang, D.; Zhang, R.; Ma, G.; Su, Z. Detailed Exploration of Structure Formation of an Epoxy-based Monolith with Three-Dimensional Bicontinuous Structure. *RSC Adv.* **2015**, *5*, 55419−55427.
(45) Forbes, L. M.; Omahony, A. M.; Sattayasamitsathit, S.; Wang, J.; Cha, J. N. Polymer End-Group Mediated Synthesis of Well-Defined Catalytically Active Platinum Nanoparticles. *J. Mater. Chem.* **2011**, *21*, 15788−15792.
(46) Aymonier, C.; Bortzmeyer, D.; Thomann, R.; Mülhaupt, R. Poly(Methyl methacrylate)/Palladium Nanocomposites: Synthesis and Characterization of the Morphological, Thermomechanical, and Thermal Properties. *Chem. Mater.* **2003**, *15*, 4874−4878.
(47) Esumi, K.; Tano, T.; Meguro, K. Preparation of Organo Palladium Particles from Thermal Decomposition of Its Organic Complex in Organic Solvents. *Langmuir* **1989**, *5*, 268−270.
(48) Tano, T.; Esumi, K.; Meguro, K. Preparation of Organo-palladium Sols by Thermal Decomposition of Palladium. *J. Colloid Interface Sci.* **1989**, *133*, 530−533.
(49) Peng, J.; Xu, K.; Cai, H.; Wu, J.; Lin, W.; Yu, Z.; Chen, M. Can an Intact and Crystalline Octakis(methacryloxypropyl) Silsesquioxane be Prepared by Hydrolysis-Condensation of a Trimethoxysilane Precursor? *RSC Adv.* **2014**, *4*, 7124−7131.
(50) Kim, S.-W.; Park, J.; Jang, Y.; Chung, Y.; Hwang, S.; Hyeon, T.; Kim, Y. W. Synthesis of Monodisperse Palladium Nanoparticles. *Nano Lett.* **2003**, *3*, 1289−1291.
(51) Yang, J.; Tian, C.; Wang, L.; Fu, H. An Effective Strategy for Small-Sized and Highly-Dispersed Palladium Nanoparticles Supported on Graphene with Excellent Performance for Formic Acid Oxidation. *J. Mater. Chem.* **2011**, *21*, 3384−3390.
(52) Wang, Z.; Leng, S.; Wang, Z.; Li, G.; Yu, H. Nanostructured Organic−Inorganic Copolymer Networks Based on Polymethacrylate-Functionalized Octaphenylsilsesquioxane and Methyl Methacrylate: Synthesis and Characterization. *Macromolecules* **2011**, *44*, 566−574.
(53) Markovic, E.; Clarke, S.; Matisons, J.; Simon, G. P. Synthesis of POSS−Methyl Methacrylate-Based Cross-Linked Hybrid Materials. *Macromolecules* **2008**, *41*, 1685−1692.
(54) Mantz, R. A.; Jones, P. F.; Chaffee, K. P.; Lichtenhan, J. D.; Gilman, J. W.; Ismail, I. M. K.; Burmeister, M. J. Thermolysis of Polyhedral Oligomeric Silsesquioxane (POSS) Macromers and POSS−Siloxane Copolymers. *Chem. Mater.* **1996**, *8*, 1250−1259.
(55) Sing, K. S. W.; Everett, D. H.; Haul, R. A. W.; Moscou, L.; Pierotti, R. A.; Rouquerol, J.; Siemieniewska, T. Reporting Physisorption Data for Gas/Solid Systems with Special Reference to the Determination of Surface Area and Porosity. *Pure Appl. Chem.* **1985**, *57*, 603−619.
(56) Thommes, M.; Kaneko, K.; Neimark Alexander, V.; Olivier James, P.; Rodriguez-Reinoso, F.; Rouquerol, J.; Sing Kenneth, S. W. Physisorption of Gases, with Special Reference to the Evaluation of Surface Area and Pore Size Distribution. *Pure Appl. Chem.* **2015**, *87*, 1051.
(57) Alves, F.; Nischang, I. Tailor-Made Hybrid Organic−Inorganic Porous Materials Based on Polyhedral Oligomeric Silsesquioxanes (POSS) by the Step-Growth Mechanism of Thiol-Ene "Click" Chemistry. *Chem. - Eur. J.* **2013**, *19*, 17310−17313.
(58) Rostamnia, S.; Doustkhah, E.; Karimi, Z.; Amini, S.; Luque, R. Surfactant-Exfoliated Highly Dispersive Pd-Supported Graphene Oxide Nanocomposite as a Catalyst for Aerobic Aqueous Oxidations of Alcohols. *ChemCatChem* **2015**, *7*, 1678−1683.
(59) Piao, Y.; Jang, Y.; Shokouhimehr, M.; Lee, I. S.; Hyeon, T. Facile Aqueous-Phase Synthesis of Uniform Palladium Nanoparticles of Various Shapes and Sizes. *Small* **2007**, *3*, 255−260.
(60) Dun, R.; Wang, X.; Tan, M.; Huang, Z.; Huang, X.; Ding, W.; Lu, X. Quantitative Aerobic Oxidation of Primary Benzylic Alcohols to Aldehydes Catalyzed by Highly Efficient and Recyclable P123-Stabilized Pd Nanoclusters in Acidic Aqueous Solution. *ACS Catal.* **2013**, *3*, 3063−3066.

DOI: 10.1021/acsami.7b03910
ACS Appl. Mater. Interfaces 2017, 9, 12812−12822

(61) Mueller, J. A.; Goller, C. P.; Sigman, M. S. Elucidating the Significance of β-Hydride Elimination and the Dynamic Role of Acid/Base Chemistry in a Palladium-Catalyzed Aerobic Oxidation of Alcohols. *J. Am. Chem. Soc.* **2004**, *126*, 9724−9734.
(62) Dell'Anna, M. M.; Mali, M.; Mastrorilli, P.; Cotugno, P.; Monopoli, A. Oxidation of Benzyl Alcohols to Aldehydes and Ketones under Air in Water using a Polymer Supported Palladium Catalyst. *J. Mol. Catal. A: Chem.* **2014**, *386*, 114−119.
(63) Rahul, R.; Singh, R. K.; Bera, B.; Devivaraprasad, R.; Neergat, M. The Role of Surface Oxygenated-Species and Adsorbed Hydrogen in the Oxygen Reduction Reaction (ORR) Mechanism and Product Selectivity on Pd-based Catalysts in Acid Media. *Phys. Chem. Chem. Phys.* **2015**, *17*, 15146−15155.

DOI: 10.1021/acsami.7b03910
ACS Appl. Mater. Interfaces 2017, 9, 12812−12822

ChemComm

COMMUNICATION

View Article Online
View Journal | View Issue

Cite this: *Chem. Commun.*, 2017, 53, 12108

Received 24th August 2017,
Accepted 17th October 2017

DOI: 10.1039/c7cc06647c

rsc.li/chemcomm

Silsesquioxane cages as fluoride sensors†

Supphachok Chanmungkalakul,[a] Vuthichai Ervithayasuporn, *[a] Sasikarn Hanprasit,[a] Manlika Masik,[a] Nicha Prigyai[a] and Suda Kiatkamjornwong[bc]

Pyrene functionalized silsesquioxane cages (PySQ) not only provide significant fluorescence from pyrene–pyrene excimers with a very large Stokes shift ($\Delta\lambda$ = 143 nm, 69 930 cm^{-1}) in DMSO but also exhibit fluoride capture results coincidentally with a π–π* fluorescence enhancement. On the other hand, PySQ-F$^-$ in THF significantly exhibits π–π* fluorescence quenching and a color change can be observed with the naked eye from light yellow to deep orange by forming a charge-transfer (CT) complex among the pyrenyl rings. Moreover, PySQ selectively captures F$^-$ with a response time of <2 min and with a very low detection limit (1.61 ppb), while ^{19}F NMR is used to confirm encapsulation of F$^-$ with $\Delta\delta$ = 19 ppm.

Silsesquioxanes (SQs) are classified as hybrid inorganic–organic materials with the empirical formula $RSiO_{3/2}$, where R is an organic group, *e.g.* aryl, alkyl or vinyl. Typically, SQs can exist in many structural forms (*e.g.*, random, ladder, and cage-like structures). However, cage-like octameric structures (T_8) are among the most promising starting points for further elaboration,[1] and are used widely in many applications: bioconjugations,[2] electronics,[3] catalysis,[4] and nanocomposites.[5] A conventional method to prepare a silsesquioxane cage is to use catalytic tetrabutylammonium fluoride (TBAF) (<5 mol%).[6] For example, Laine *et al.* used F$^-$ to cleave Si–O–Si bonds that can turn polysilsesquioxanes into SQ cages.[7a] They have exquisitely explained that the cage reformation definitely involves multiple steps of complex formation and intermediates leading to complex equilibria.[7b] On the other hand, higher concentrations of F$^-$, *e.g.*, >50 mol%, and TBAF can lead to SQ encapsulated F$^-$.[8]

Considering the silsesquioxane cage as a model, molecular modeling suggests that there is a void within the cage that may be accessible to trap small ions.[9] However, until recently, there was no experimental evidence that such trapping could occur until Päch and Stosser demonstrated that γ-irradiation patterns of H_8T_8 led to hydrogen-encapsulated T_8 cages.[10] Then, Bassindale and Taylor used TBAF to prepare cubic SQs,[8c] coincidentally discovering F$^-$ encapsulation. Later, Bowers *et al.* investigated F$^-$ encapsulated in SQs by using mass spectrometry.[8b]

As a consequence, we sought to attach fluorophores to an SQ cage starting from octavinylsilsesquioxane (OVS) as a model study of fluoride encapsulation. This fluorescent POSS capsule may not only be key to solve the mystery of fluoride encapsulation, but fluoride sensing is also obtained as a side result. The fluoride ion is one of the typical biological anions in the human body and most bones contain fluoride in the form of fluorapatite.[11] The consumption of only a suitable amount of fluoride is recommended, and excessive fluoride intake is the main cause of several dental and skeletal diseases.[12] Traditional methods used to investigate fluoride sensing include the electrode method, NMR analysis, and chemosensors. However, upon comparing those among methods, fluorometric or colorimetric methods are the most practical, with simple preliminary screening and less instrumental analysis compared to others.[13] It is worth mentioning that one popular type of fluoride chemosensor uses the chemical benefits of thermodynamically stable Si–F and B–F.[14]

Herein, pyrene functionalized silsesquioxane cages (PySQ) were successfully synthesized, which can provide different fluorescence properties depending on the polarity of the solvent. For example, PySQ in DMSO potentially generates a significant fluorescence of the pyrene–pyrene excimer through space, while π–π* fluorescence emission of PySQ in THF can be dominant. Upon the addition of the fluoride ion, the highly negatively charged F$^-$ was pulled into the confined silsesquioxane cage through the electrostatic interactions of electron deficient elements (*i.e.*, silicon).[15] Subsequently, the fluoride ion was centralized within a silsesquioxane cage, which can also compress the cage.[8c] Therefore, fluorescence responses of PySQ to F$^-$ in DMSO and THF can

[a] *Department of Chemistry, Center of Excellence for Innovation in Chemistry (PERCH-CIC), and Center of Intelligent Materials and Systems, Nanotec Center of Excellence, Faculty of Science, Mahidol University, Rama VI road, Ratchathewi, Bangkok 10400, Thailand. E-mail: vuthichai.erv@mahidol.ac.th*

[b] *Faculty of Science, Chulalongkorn University, Phayathai Road, Bangkok 10330, Thailand*

[c] *Division of Science, The Royal Society of Thailand, Sanam Suepa, Dusit, Bangkok 10300, Thailand*

† Electronic supplementary information (ESI) available: Experiments, characterizations and spectroscopic studies. See DOI: 10.1039/c7cc06647c

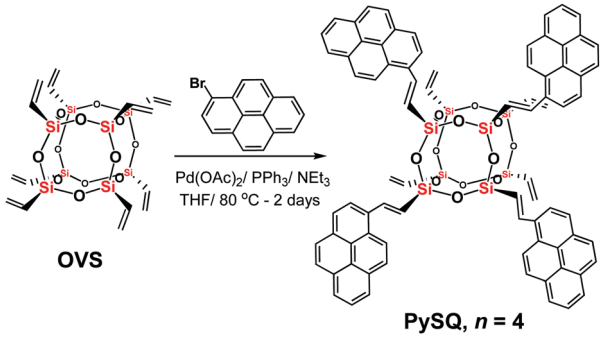

Scheme 1 Synthesis of a pyrene functionalized-silsesquioxane cage (PySQ) *via* the Heck reaction.

also be used to detect the fluoride ion by turning the fluorescence ON–OFF and OFF–ON, respectively, including detection by the naked eye.

The modified synthetic approach of PySQ is shown in Scheme 1.[16] The pyrene rings are conjugated to the OVS cage through the Heck reaction to obtain PySQ as a bright yellow solid (41% yield). Matrix assisted laser desorption ionization time-of-flight (MALDI-TOF) is shown in Fig. S1 (ESI†). The results show a normal distribution of a T_8 product with four substitutions; $n = 4$ is the most abundant species.

The sensor cannot be a good one without good selectivity. Thus, PySQ selectivity was tested for F^-, Cl^-, NO_2^-, CN^-, N_3^-, SCN^-, HSO_4^- and ClO_4^- by adding an excess amount (150 eq.) to PySQ in DMSO and THF. Only the fluoride ion was found to exhibit significant changes. Interestingly, in selectivity tests, PySQ displays solvent dependent fluorescence (see Fig. S2, ESI†). In Fig. 1a, the red-shift emission (λ_{max} = 494 nm, Φ_p = 0.30) of PySQ in DMSO solution shows a very large Stokes shift ($\Delta\lambda$ = 143 nm, 69 930 cm^{-1}) confirming the presence of pyrene–pyrene excimer.[14c] Upon addition of excess TBAF, the emission spectrum of PySQ in DMSO dramatically shifts to the blue region as shown in Fig. S2b (ESI†). As a result of concentration dependent fluorescence, Fig. 1, the emission of π–π* (λ_{max} = 396 nm) is enhanced, but the excimer fluorescence (λ_{max} = 494 nm) is suppressed to finally give Φ_p = 0.60 and 0.76, when fluoride is provided from THF and H_2O media, respectively. This result strongly confirms that F^- plays a crucial role in reorganizing the cage geometry to support π–π* fluorescence emissions of individual pyrene groups. We suggested that the excimer fluorescence (stacked pyrene–pyrene dimer) of PySQ in DMSO must be blocked upon fluoride addition as shown in Fig. 2b, while maintaining π–π* fluorescence of sole pyrenes for long periods of time as shown in Fig. 3. This can also be confirmed from the color change and fluorescence quenching under UV radiation of the PySQ solid-state before and after TBAF addition (see Fig. S3, ESI†), thus inhibiting the bright blue emission (λ_{max} = 494 nm) in DMSO, but with the purple emission (λ_{max} = 396 nm) of the pyrene portion being activated simultaneously (see Fig. S4, ESI†). Hence, PySQ in DMSO can be described as a "turn-on" sensor for fluoride.

As can be seen in Fig. 2a, PySQ in THF also displays solvent dependent fluorescence, compared to DMSO. The excimer

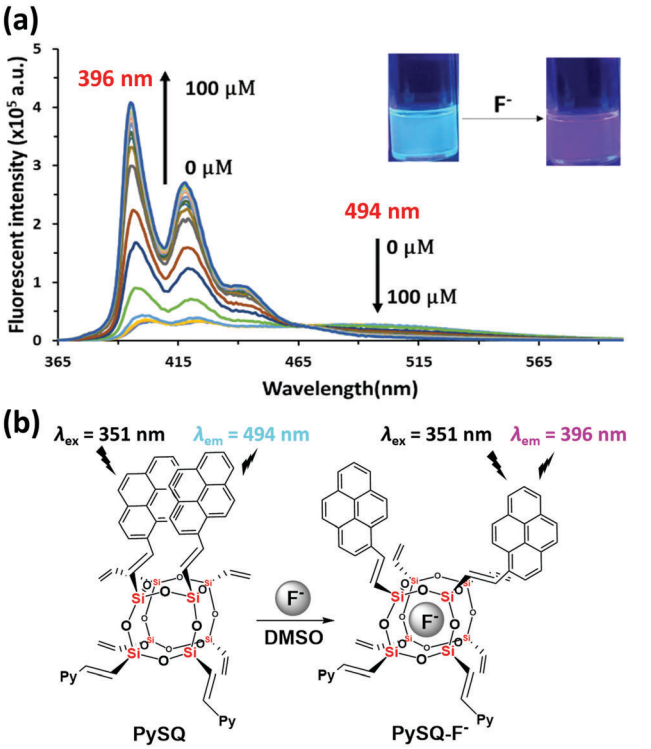

Fig. 1 (a) The emission spectra of PySQ (5.6 μM in DMSO) upon addition of TBAF and (b) the principle of a "turn-on" sensor for fluoride detection under UV radiation.

emission of PySQ in THF becomes weaker and moves to shorter wavelengths than that in DMSO, but has a much higher quantum efficiency (*e.g.*, λ_{max} = 421 nm, Φ_p = 0.65 in THF). Interestingly, the excimer emission disappeared after fluoride addition, while π–π* fluorescence emissions from pyrene still existed although they were shifted to the blue region. Moreover, the response of PySQ in THF to F^- contrasts with that in DMSO: instead of enhanced fluorescence, the addition of F^- to THF solution quenches emission (Fig. 2a) to give Φ_p = 0.08 and 0.57, for F^- from THF and H_2O media, respectively. Laine and co-workers also suggested that the F^- catalyzed rearrangement of silsesquioxane in THF is highly complicated and involves the equilibration of many intermediates.[7b] In this report, F^- must participate in cage reorganization by inhibiting both π–π* and excimer fluorescence emissions among the pyrene groups. Consequently, PySQ in THF is a "turn-off" sensor for F^- (Fig. 2a). However, Fig. 2b shows a very fast response time of around 2 min in DMSO, even though PySQ in THF had a very long response time (>50 min). Thus, DMSO is a better solvent than THF for studying the concentration dependent fluorescence and kinetic studies.

PySQ was studied for its dynamic change upon addition of an excess amount of tetrabutylammonium fluoride (TBAF) solution (150 eq.) in every experiment in order to make the reaction a pseudo 1st order reaction. The fluorescence intensity point was measured at λ_{em} = 396 nm, at a concentration of 5.6 μM in DMSO, a slit width of 1 nm, and λ_{ex} = 351 nm. The observed rate constants of the reaction at 25, 35 and 45 °C were 0.007,

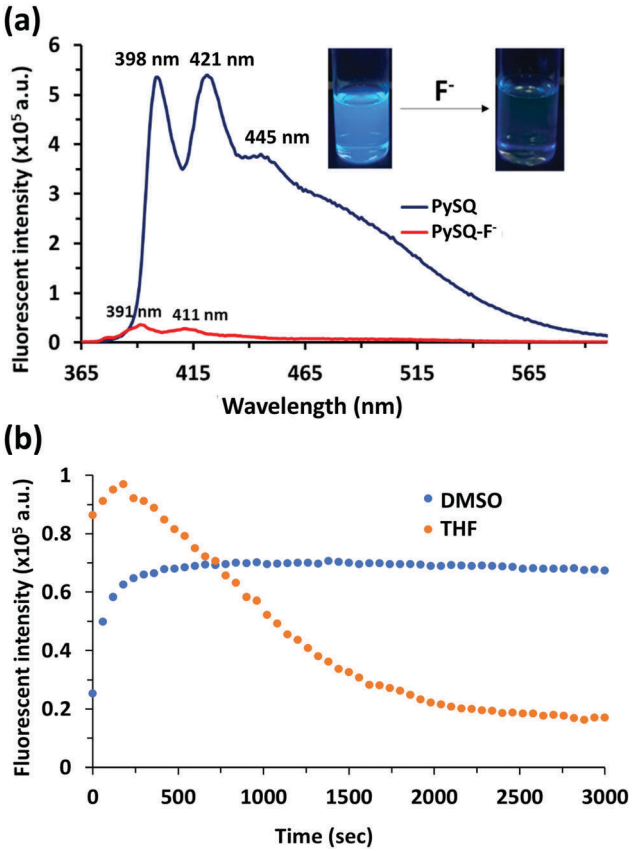

Fig. 2 (a) The emission spectra of PySQ (5.6 μM in THF) upon excess addition (150 eq.) of TBAF in THF and (b) the changes of fluorescence intensity of PySQ in DMSO and THF upon excess addition (150 eq.) of TBAF at λ_{em} = 396 and 398 nm in DMSO and THF, respectively, where λ_{ex} = 351 nm for both solvents.

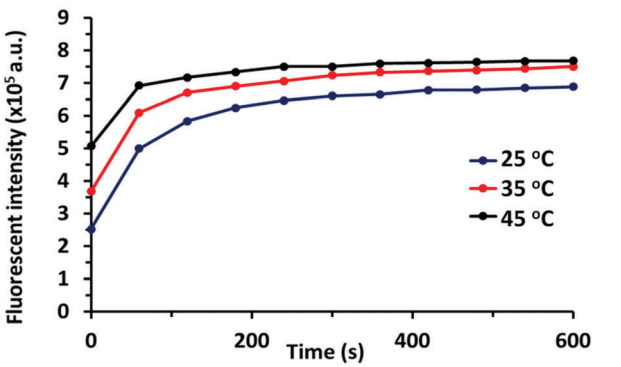

Fig. 3 Changes in fluorescence changes (λ_{ex} = 351 nm and λ_{em} = 396 nm) with time and temperature of 5.6 μM PySQ in DMSO upon addition of excess TBAF (150 eq.).

0.005 and 0.003 s^{-1}, respectively (see Fig. S5, ESI†). The observed rate constants at each temperature were plotted with the Arrhenius equation. Using the Arrhenius equation, the activation energy of fluoride ion encapsulation in PySQ was found to be −33 kJ mol^{-1} and the pre-exponential constant was 1.2 × 10^{-3} s^{-1}. An Eyring–Polanyi plot was also applied and the result was obtained as $\Delta H^{\ddagger}$ = −36 kJ mol^{-1} and $\Delta S^{\ddagger}$ = −0.41 kJ mol^{-1} (see Fig. S5, ESI†). There was a reaction model with a negative value of activation energy, as reported by Shinomura and co-workers. The potential-energy barrier for any process cannot be negative, so the negative value must specify some complexity in the process.[17] The association constant (K_a), calculated using the Benesi–Hildebrand plot,[18] of PySQ-F^- is 3.3 × 10^4 M^{-1} (see Fig. S6, ESI†). From titration results, the equivalent point for TBAF/PySQ was 72% w/w or 93% mol. In this case, the proportional equivalent point is nearly 1 : 1 (see Fig. S7, ESI†).

In Fig. 4a, PySQ in THF upon addition of TBAF also displays solvent and concentration dependent UV-visible absorption and the color of the PySQ solution changed from very light yellow (λ_{abs} = 394 nm) to deep orange (λ_{abs} = 501) (see Fig. S8, ESI†), while PySQ in DMSO remains the same as a light yellow colored solution. It was suggested that a charge transfer complex[19] of pyrene–pyrene can be stabilized by F^- in THF (see Fig. 4b) and a change of color responses can be clearly observed with the naked eye.

PySQ-F quenched emission in THF is similar to the emission spectrum of 1-bromopyrene (see Fig. S18, ESI†). In order to confirm the interactions between fluoride and silicon, PySQ-F^- was simply prepared by adding 0.1 M TBAF/PySQ at 72% w/w according to the titration results. The reaction was stirred for 16 h in THF.[8a] Then, the evaporation of the solvent gave a deep orange powder of the PySQ-F^- product, and no further purification was needed.[20] This obtained PySQ-F^- complex can be confirmed by solid state ^{29}Si CP/MAS NMR spectroscopy. PySQ solely appears at δ −77.8 ppm, while PySQ-F^- appears at a higher

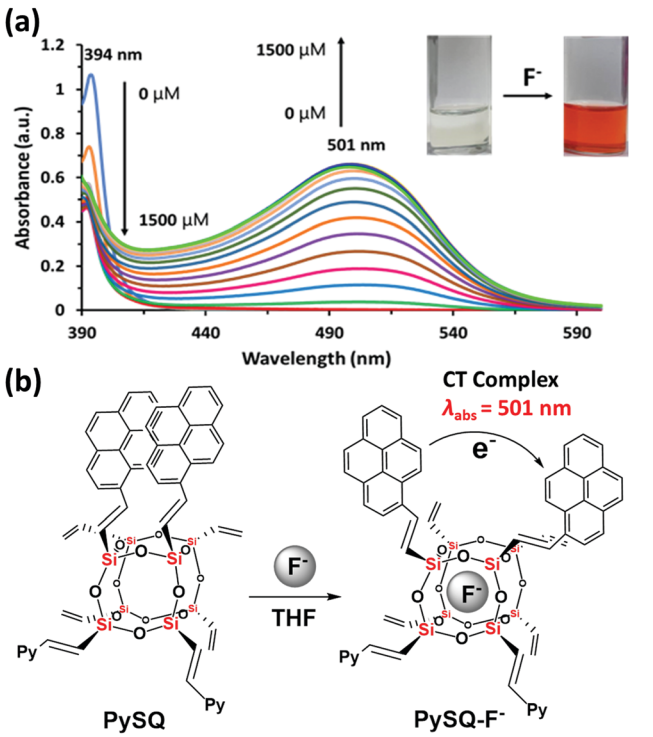

Fig. 4 (a) The UV-visible absorption spectrum at λ = 501 nm for 56 μM of PySQ in THF upon addition of 0.01 M TBAF in THF and (b) the principle of a "turn-on" sensor for fluoride changes detected by the naked eye.

field of δ −79.6 ppm. The trend of chemical shifts of PySQ was in agreement with previous reports after encapsulating the fluoride.[8a,b] X-ray powder diffraction (XRD) also shows compression of the *d*-spacing after TBAF addition from 2.91 Å to 2.89 Å with no indication of cage destruction, which is similar to a previous report (see Fig. S19, ESI†).[8c] Moreover, ^{19}F NMR in DMSO-d_6 shows an upfield signal from the neat TBAF at δ −105 to −124 ppm after mixing with PySQ (see Fig. S20, ESI†).

In conclusion, pyrene functionalized silsesquioxane cages were successfully synthesized, which can provide different fluorescence, mainly depending on the type of solvent used. PySQ in DMSO potentially generates a significant fluorescence of a pyrene–pyrene excimer through-space, while π–π* fluorescence emission of sole pyrene groups on PySQ in THF can be dominant. Upon addition of fluoride into PySQ in both DMSO and THF solutions, PySQ not only provided fluorescence enhancement, but also rendered fluorescence quenching as well. We suggest that in fluoride encapsulation by PySQ in low polarity solvents, *e.g.*, THF, both excimer and π–π* fluorescence emissions were diminished and a charge transfer (CT) complex could be instead occurred, which can be observed with the naked eye as a color change from light yellow to deep orange, as well as fluorescence quenching under UV radiation. On the other hand, PySQ with fluoride encapsulation in high polarity solvents, *e.g.*, DMSO or DMSO/H_2O, increased the pyrene–pyrene distance by diminishing pyrene–pyrene excimer fluorescence, with enhanced π–π* fluorescence emission; the encapsulation in DMSO could be confirmed by thermodynamic values. However, the quenched fluorescence of PySQ in THF needs further investigation and a clear explanation should be presented in the near future.

This research was financially supported by the Thailand Research Fund (RSA5980018 and DPG6080001), the Center of Excellence for Innovation in Chemistry (PERCH-CIC), and the National Nanotechnology Center (NANOTEC), NSTDA, Ministry of Science and Technology, Thailand, through its program of Center of Excellence Network. S. C. thanks for partially financial support from TRF IRG5980007.

Conflicts of interest

There are no conflicts to declare.

Notes and references

1 (*a*) S. Hanprasit, N. Tungkijanansin, A. Prompawilai, S. Eangpayunga and V. Ervithayasuporn, *Dalton Trans.*, 2016, **45**, 16117; (*b*) S. Chimjarn, R. Kunthom, P. Chancharone, R. Sodkhomkhum, P. Sangtrirutnugul and V. Ervithayasuporn, *Dalton Trans.*, 2015, **44**, 916; (*c*) V. Ervithayasuporn and S. Chimjarn, *Inorg. Chem.*, 2013, **52**, 13108; (*d*) Y. Kaneko, M. Shoiriki and T. Mizumo, *J. Mater. Chem.*, 2012, **22**, 14475–14478; (*e*) D. B. Cordes, P. Lickiss and F. Rataboul, *Chem. Rev.*, 2010, **110**, 2081.

2 (*a*) S. Hörner, S. Knauer, C. Uth, M. Jöst, V. Schmidts, H. Frauendorf, C. M. Thiele, O. Avrutina and H. Kolmar, *Angew. Chem., Int. Ed.*, 2016, **55**, 14842; (*b*) Z. Zhou and Z.-R. Lu, *Nanomedicine*, 2014, **9**, 2387.

3 (*a*) K. Tanaka and Y. Chujo, *J. Mater. Chem.*, 2012, **22**, 1733; (*b*) M. Yoon, Lo, C. Zhen, M. Lauters, G. E. Jabbour and A. Sellinger, *J. Am. Chem. Soc.*, 2007, **129**, 5808.

4 (*a*) R. Kunthom, T. Jaroentomeechai and V. Ervithayasuporn, *Polymer*, 2017, **108**, 173; (*b*) Y. Zhou, G. Yang, C. Lu, J. Nie, Z. Chen and J. Ren, *Catal. Commun.*, 2016, **75**, 23; (*c*) L. A. Bivona, O. Fichera, L. Fusaro, F. Giacalone, M. Buaki-Sogo, M. Gruttadauria and C. Aprile, *Catal. Sci. Technol.*, 2015, **5**, 5000.

5 (*a*) P. Sangtrirutnugul, T. Chaiprasert, W. Hunsiri, T. Jitjaroendee, P. Songkhum, K. Laohhasurayotin, T. Osotchan and V. Ervithayasuporn, *ACS Appl. Mater. Interfaces*, 2017, **9**, 12812; (*b*) P. Żak, M. Majchrzak, G. Wilkowski, B. Dudziec, M. Dutkiewicz and B. Marciniec, *RSC Adv.*, 2016, **6**, 10054; (*c*) S. Mohapatra, T. Chaiprasert, R. Sodkhomkhum, R. Kunthom, S. Hanprasit, P. Sangtrirutnugul and V. Ervithayasuporn, *ChemistrySelect*, 2016, **1**, 5353; (*d*) T. Maegawa, Y. Irie, H. Imoto, H. Fueno, K. Tanaka and K. Naka, *Polym. Chem.*, 2015, **6**, 7500.

6 (*a*) A. Miyazato, C. Pakjamsai and Y. Kawakami, *Dalton Trans.*, 2010, **39**, 3239; (*b*) A. R. Bassindale, D. J. Parker, M. Pourny, P. G. Taylor, P. N. Horton and M. B. Hursthouse, *Organometallics*, 2004, **23**, 4400.

7 (*a*) M. Z. Asuncion and R. M. Laine, *J. Am. Chem. Soc.*, 2010, **132**, 3723; (*b*) J. C. Furgal, T. Goodson and R. M. Laine, *Dalton Trans.*, 2016, **45**, 1025–1039.

8 (*a*) Y. El Aziz, P. G. Taylor, A. R. Bassindale, S. J. Coles and M. B. Pitak, *Organometallics*, 2016, **35**, 4004–4013; (*b*) S. E. Anderson, D. J. Bodzin, T. S. Haddad, J. A. Boatz, J. M. Mabry, C. Mitchell and M. T. Bowers, *Chem. Mater.*, 2008, **20**, 4299; (*c*) A. R. Bassindale, M. Pourny, P. G. Taylor, M. B. Hursthouse and M. E. Light, *Angew. Chem., Int. Ed.*, 2003, **42**, 3488.

9 (*a*) T. Kudo, T. Taketsugu and M. S. Gordon, *J. Phys. Chem. A*, 2011, **115**, 2679; (*b*) D. Hossain, S. R. Gwaltney, C. U. Pittman Jr. and S. Saebo, *Chem. Phys. Lett.*, 2009, **467**, 348–353.

10 M. Päch and R. Stosser, *J. Phys. Chem. A*, 1997, **101**, 8360.

11 S. Amini, A. Masic, L. Bertinetti, J. S. Teguh, J. S. Herrin, X. Zhu, H. Su and A. Miserez, *Nat. Commun.*, 2014, **5**, 3187.

12 H. Aboubakr, H. Brisset, O. Siri and J.-M. Raimundo, *Anal. Chem.*, 2013, **85**, 9968–9974.

13 (*a*) Y. Zhou, J. F. Zhang and J. Yoon, *Chem. Rev.*, 2014, **114**, 5511; (*b*) P. Thiampanya, N. Muangsin and B. Pulpoka, *Org. Lett.*, 2012, **14**, 4050; (*c*) C. Suksai and T. Tuntulani, *Chem. Soc. Rev.*, 2003, **32**, 192.

14 (*a*) A. Roy, D. Kand, T. Saha and P. Talukdar, *Chem. Commun.*, 2014, **50**, 5510–5513; (*b*) X. Y. Liu, D. R. Bai and S. Wang, *Angew. Chem., Int. Ed.*, 2006, **45**, 5475; (*c*) L. Gai, H. Chen, B. Zou, H. Lu, G. Lai, Z. Li and Z. Shen, *Chem. Commun.*, 2012, **48**, 10721.

15 (*a*) S. Mihail, Y. Wang and M. Dieng, *ECS Trans.*, 2013, **45**, 29; (*b*) R. R. Pappalardo, E. S. Marcos and M. F. Lopez-Ruiz, *J. Am. Chem. Soc.*, 1993, **115**, 3722.

16 X. H. Yang, T. Giovenzama, B. Felid, G. E. Jabbour and A. Sellinger, *J. Mater. Chem.*, 2012, **22**, 12689.

17 T. Shimimura, K. L. Tölle, J. Smid and M. Szware, *J. Am. Chem. Soc.*, 1967, **89**, 796–803.

18 H. Benesi and J. Hildebrand, *J. Am. Chem. Soc.*, 1947, **71**, 2703–2707.

19 S. Zheng, H. Phillips, E. Geva and B. D. Dunietz, *J. Am. Chem. Soc.*, 2012, **134**, 6944.

20 Y. El Aziz, A. R. Bassindale, P. G. Taylor, P. N. Horton, R. A. Stephenson and M. B. Hursthouse, *Organometallics*, 2012, **31**, 6032–6040.

ChemPubSoc Europe

DOI: 10.1002/slct.201702597

Chemistry SELECT Full Papers

Materials Science inc. Nanomaterials & Polymers

Heterogeneous Pd/POSS Nanocatalysts for C–C Cross-Coupling Reactions

Vetiga Somjit,[a] Michel Wong Chi Man,[b] Armelle Ouali,[b] Preeyanuch Sangtrirutnugul,[a] and Vuthichai Ervithayasuporn*[a]

An insoluble solid support of *N* – heterocyclic imidazolium-functionalized cage-like silsesquioxane (SQ); Bim-SQ, was synthesized by nucleophilic substitution of octakis(3-chloropropyl)octasilsesquioxane with an excess bis-(imidazol-1-yl) methane and investigated as a new organic-inorganic hybrid support. In the presence of Bim-SQ, Pd(II) from $[PdCl_4]^{2-}$ can be stabilized *via* both electrostatic interactions and imidazole-*N*-coordination, giving an amorphous material of Pd(II)@Bim-SQ. Subsequent *in situ* reduction of Pd(II)@Bim-SQ during Suzuki – Miyaura cross-coupling reactions afforded monodispersed Pd nanoparticles (2.33 ± 1.50 nm) stablized on Bim-SQ support, PdNp@Bim-SQ with Pd loading up to 14% *w/w*. Catalytic studies revealed that the pre-catalyst Pd(II)@Bim-SQ was active heterogeneous catalyst for Suzuki – Miyaura cross-coupling reactions, having the maximum TOFs of 5400 h^{-1} under mild conditions and in aqueous ethanol medium. Furthermore, PdNp@Bim-SQ was also shown to be an efficient catalyst for Heck reactions. Simple catalyst recovery and reusability of PdNp@Bim-SQ for at least 5 catalytic cycles without loss of activity were also demonstrated.

Introduction

Palladium – catalyzed carbon – carbon cross-coupling reactions (e.g. Suzuki – Miyaura,[1] Heck,[2] and Sonogashira reaction)[3] are the most popular reactions and have been widely used for building up a complex structure in both organic and material syntheses.[4] Based on their importance, the design of Pd catalysts for C – C coupling reactions, especially the preparation of highly active catalysts with low Pd loadings, represents a key aspect of research.[5] In particular, convenient catalyst preparation, catalyst's recyclability, and environmental friendly catalytic conditions constitute important catalyst features.[6] Heterogeneous Pd catalysts stabilized on supporting materials (e.g. graphene,[7] chitosan,[8] and silica)[9] have been developed in order to improve the catalytic activities. For example, Gruttadauria *et al.* successfully prepared the palladium nanoparticles supported on silica-based materials,[10] while Veisi *et al.* also found that catalytic activities of Pd can be enhanced by highly porous (mesoporous) silica.[11]

Along the same line, organic-inorganic hybrid materials of polyhedral oligomeric silsesquioxanes (POSS) or cage-like silsesquioxanes (SQ) have been investigated as supports for metal catalysts,[12] as a result of their exceptional thermal stability[13] and ease of surface functional group modification.[14] Not only the SQ cages contain the smallest inorganic silica core, but their molecular structures were also decorated with a wide variety of functional organic groups (e.g. alkyl,[15] aryl,[16] vinyl,[17] acrylate,[18] and hydroxyl groups).[19] Owing to their tunable organic-inorganic structure/property relationships,[23] SQ have been incorporated in a number of novel complex structures for a wide range of applications (e.g. sensors,[20] electronic devices,[21] and catalysts).[22] For catalytic applications, palladium nanoparticles supported on porous cross-linked silsesquioxanes catalyzed aerobic alcohol oxidation in water.[24] Zhang *et al.* also reported the synthesis of Pd(II) supported on SQ functionalized with Schiff base ligands for Suzuki – Miyaura cross-coupling reaction.[25] Our group has recently shown that Pd(II) complexes supported by pyridine – triazole-functionalized SQ were highly active homogeneous and heterogeneous catalysts, depending on the amount of pyridine-triazole ligands on SQ.[28]

N – Heterocyclic carbene (NHC) ligands are known as highly effective stabilizing ligands[26] due to their strong π-electron-donating nitrogen atoms.[25] Furthermore, the *N* – heterocyclic ligands are also able to activate Pd catalysts for C–C coupling reactions.[27] For example, Pd(II) supported on NHC-functionalized SQ can be simply prepared *via* solid-state annealing.[29] To further broaden aspects of the SQ application in catalysis, it is very important to design a new type of support materials possessing a good stabilizing ligand, which produces efficient catalysts and works under an environmentally benign medium. In this work, the insoluble imidazolium/imidazole ligands derived from SQ can be freshly prepared as a novel support

[a] *V. Somjit, Prof. Dr. P. Sangtrirutnugul, Prof. Dr. V. Ervithayasuporn*
Department of Chemistry
Center of Excellence for Innovation in Chemistry (PERCH-CIC)
and Center for Inorganic and Materials Chemistry, Faculty of Science
Mahidol University
Rama VI road, Ratchathewi District, Bangkok 10400, Thailand
E-mail: vuthichai.erv@mahidol.ac.th
maldiniandg@hotmail.com
Homepage: http://chemistry.sc.mahidol.ac.th/en/people/faculty/vuthichai-ervithayasuporn/

[b] *Dr. M. Wong Chi Man, Dr. A. Ouali*
Institut Charles Gerhardt Montpellier
UMR5253 CNRS-ENSCM-UM
8, rue de l'école normale, 34296 Montpellier, France

Supporting information for this article is available on the WWW under https://doi.org/10.1002/slct.201702597

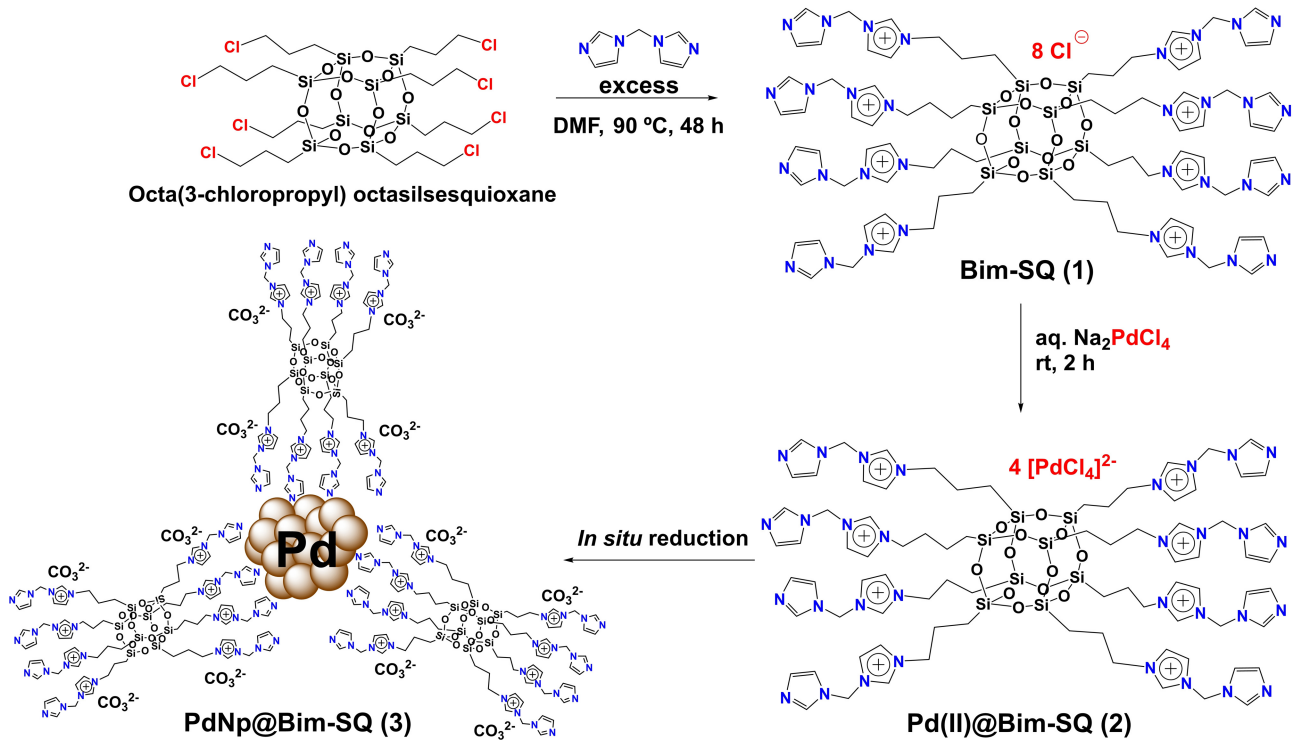

Scheme 1. Synthetic approach to prepare Bim-SQ (**1**), the pre-catalyst of Pd(II)@Bim-SQ (**2**), and PdNp@Bim-SQ (**3**).

material to stabilize the pre-catalyst Pd(II) species as well as monodispersed Pd nanoparticles formed *in situ* during Suzuki–Miyaura reaction *via* both electrostatic interactions and *N*-coordinations. Moreover, this palladium nanocomposite can be also used as a heterogeneous catalyst for Heck reactions in aqueous media. Furthermore, the reusability of the catalyst was also evaluated.

Results and Discussion

A mixture of octakis(3-chloropropyl)octasilsesquioxane[31] and an excess amount of bis-(imidazol-1-yl)methane[32] in *N,N*–dimethylformamide (DMF) at 90 °C afforded the bis-imidazole/imidazolium functionalized-SQ; Bim-SQ (**1**), as a white insoluble precipitate, in 97% yield after 48 h (Scheme 1). It should be noted that this synthesis is simple to operate as the precipitate **1** can be isolated by a simple filtration because of their insolubility in organic and aqueous solvents.

The formation of **1** was confirmed by FT-IR spectrum (Figure 1). Material **1** as shown in Figure 1c reveals an absorption band associated with asymmetric Si–O–Si stretching vibration at 1034 cm^{-1},[33] indicating the existence of cubic silsesquioxane structure with some opening of cage-like structure.[34] Moreover, the disappearance of the wagging vibration band at 1252 cm^{-1} of chlorine groups ($-CH_2Cl$) together with the concomitant appearance of a lower shift at 1635 cm^{-1} attributable to the C=N vibration band confirm a complete substitution on the SQ precursor, as well as the incorporation of bis-imidazole in material **1**.

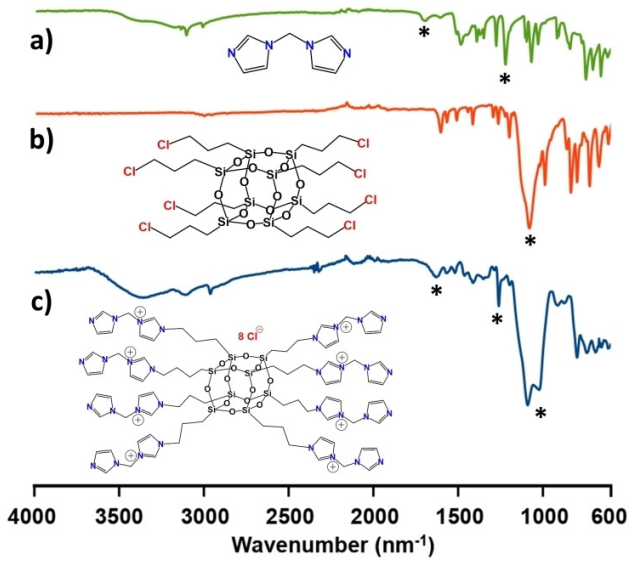

Figure 1. FT-IR spectra of a) bis-imidazole, b) octakis(3-chloropropyl)octasilsesquioxane, and Bim-SQ (**1**).

The ^{13}C CP/MAS NMR spectrum of **1** (Figure 2a) exhibits the chemical shifts consisting of aromatic and aliphatic carbon centers. In addition, the chloromethyl signal of SQ precursor at *ca.* 47.02 ppm[35] completely disappears, indicating a successful substitution of aromatic imidazole rings on SQ. However, the chemical shifts of aliphatic side chains at 9.56, 23.95, 26.00, 52.53, and 58.11 ppm suggest the presence of two different

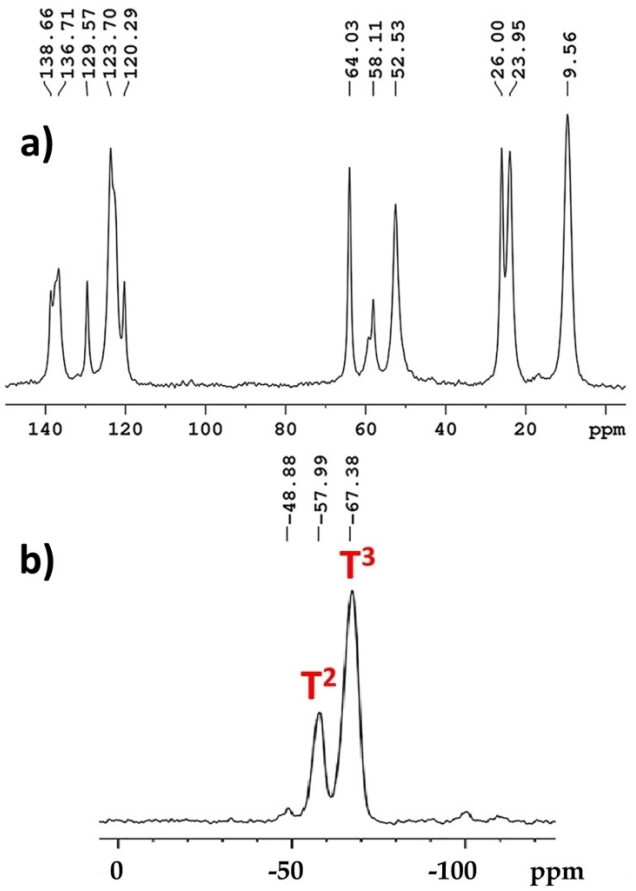

Figure 2. a) ^{13}C and b) ^{29}Si CP/MAS NMR spectra of Bim-SQ (**1**).

propyl chains of the organic substituents.[36] It is possible that moisture from air may simultaneously cause the hydrolysis reaction leading to the formation of a hydroxypropyl substituent along with the desired imidazolium side chains.

Furthermore, ^{29}Si CP/MAS NMR spectrum of **1** (Figure 2b) revealed two signals at −67.38 and −57.99 ppm, corresponding to T^3 and some partially opening-cage silsesquioxane of T^2, respectively.[38] According to strong nucleophilicity of nitrogen atom on imidazole rings, it may induce the cleavage of the inorganic Si−O bonds of the silsesquioxane cage during the substitution reaction.[39] TGA curve of **1** in air (Figure S2) shows the decomposition in four mass loss steps, in which the first step of mass loss (8%) before 150 °C indicates water evaporation. This result confirms the hydrophilic nature of Bim-SQ **1**, consistent with imidazolium linkages showing strong moisture absorption.

When material **1** was dispersed in an aqueous solution of Na_2PdCl_4 (0.0124 M) with vigorous stirring for 2 h at room temperature (Scheme 1), the orange solution gradually became to colorless whereas the precipitate, the pre-catalyst **2**, became dark orange. This immediate change of dispersed solid support from white to orange provided an evidence for successful anionic exchanges between chloride (Cl^-) and $[PdCl_4]^{2-}$ anions (Figure S1). The high amount of Pd loading (21% *w*/*w*) of **2** was also determined by Inductively Coupled Plasma Mass Spectrometer (ICP−MS) (Table S1). Scanning electron microscopy (SEM) image of **2** (Figure 3) shows an aggregation of the particles, while Energy dispersive spectroscopy (EDS) spectrum of **2** contains a new signal at *ca.* 2.85 keV (Figure 3g), which can be attributed to the presence of Pd (Figure 3f) distributing throughout the surface of the supporting materials compared to the EDS spectrum of SQ support, as shown in Figure S3.

The reduction of Pd(II) to Pd(0) nanoparticles supported on Bim-SQ can occur during Suzuki−Miyaura cross-coupling reactions (Scheme 1). In the presence of phenylboronic acid under strong alkaline solutions, Pd(II) of the pre-catalyst **2**, which appeared as an orange precipitate, was rapidly transformed to Pd(0) nanocomposites as evidenced by the formation of a dark grey precipitate of the active catalyst PdNp@Bim-SQ (**3**) with Pd loading of 14% *w/w.* In order to confirm the existence of Pd nanoparticles over the solid support, EDS image of **3** (Figure S4) shows well-distributed Pd throughout the SQ support. Transmission electron microscopy (TEM) images (Figure 4) of **2** and **3** illustrate that the *in situ* reduction reaction produced uniformly-dispersed Pd nanoparticles with an average size of 2.33 ± 1.50 nm (Figures 4c and 4d).

To study the oxidation states of palladium on the materials, the narrow scanned X-ray photoelectron microscopy (XPS) spectrum (Figure S6) of **2** reveals Pd(II) as a main species on the surface materials based on the appearance of two signals of Pd $3d_{5/2}$ and Pd $3d_{3/2}$ at *ca.* 336.7 and *ca.* 341.9 eV, respectively. After *in situ* reduction of **2**, the resulting catalyst **3** features signals at *ca.* 335.3 and *ca.* 340.5 eV suggesting that both Pd(0) and Pd(II) species are present on the solid support (Figure 5). Moreover, the full XPS spectra of materials **2** and **3** also show the disappearance of the chloride signals after the *in situ* reduction (Figure S7). Indeed, there was an anion exchange during the reduction between the residual carbonate (CO_3^{2-}) and Cl^- ions. Moreover, XPS spectra (Figure S8) of N species on both materials **2** and **3** contain a key signal at *ca.* 399.0 eV assignable to N 1s, which can be deconvoluted into two signals of sp^2 N (*ca.* 398.5 eV) and quaternary N (*ca.* 401.5 eV) of imidazole and imidazolium ligands, respectively. Therefore, the information of quaternary N signal confirmed the formation of cationic linkages on SQ-based support.

In general, the starting material of octakis(3-chloropropyl)octasilsesquioxane is soluble in various organic solvents and highly crystalline as suggested by single crystal X-ray diffraction.[31] Interestingly, functionalization with bis(imidazol-1-yl) methane in DMF immediately results in a white precipitate of Bim-SQ **1**, which is insoluble in organic solvents while the powder X-ray diffraction (XRD) spectrum of **1** reveals its highly crystalline nature (Figure 6a). On the basis of these results, we speculate that Bim-SQ **1** led to the formation of strong electrostatic interactions of imidazolium salts among functionalized SQ molecules, compared to neutral imidazole ligands.[29] In addition, the same appearance of a broad diffraction in **1, 2,** and **3** (Figure 6) centered at $2\theta = 22$ ° can be ascribed to the existence of a cage-like structure of SQ in those solid materials. The *d*-spacing value under this reflection can be calculated to 0.41 nm of Si-O–Si bonds in a SQ cage. However, after introducing Pd, both materials **2** and **3** completely became

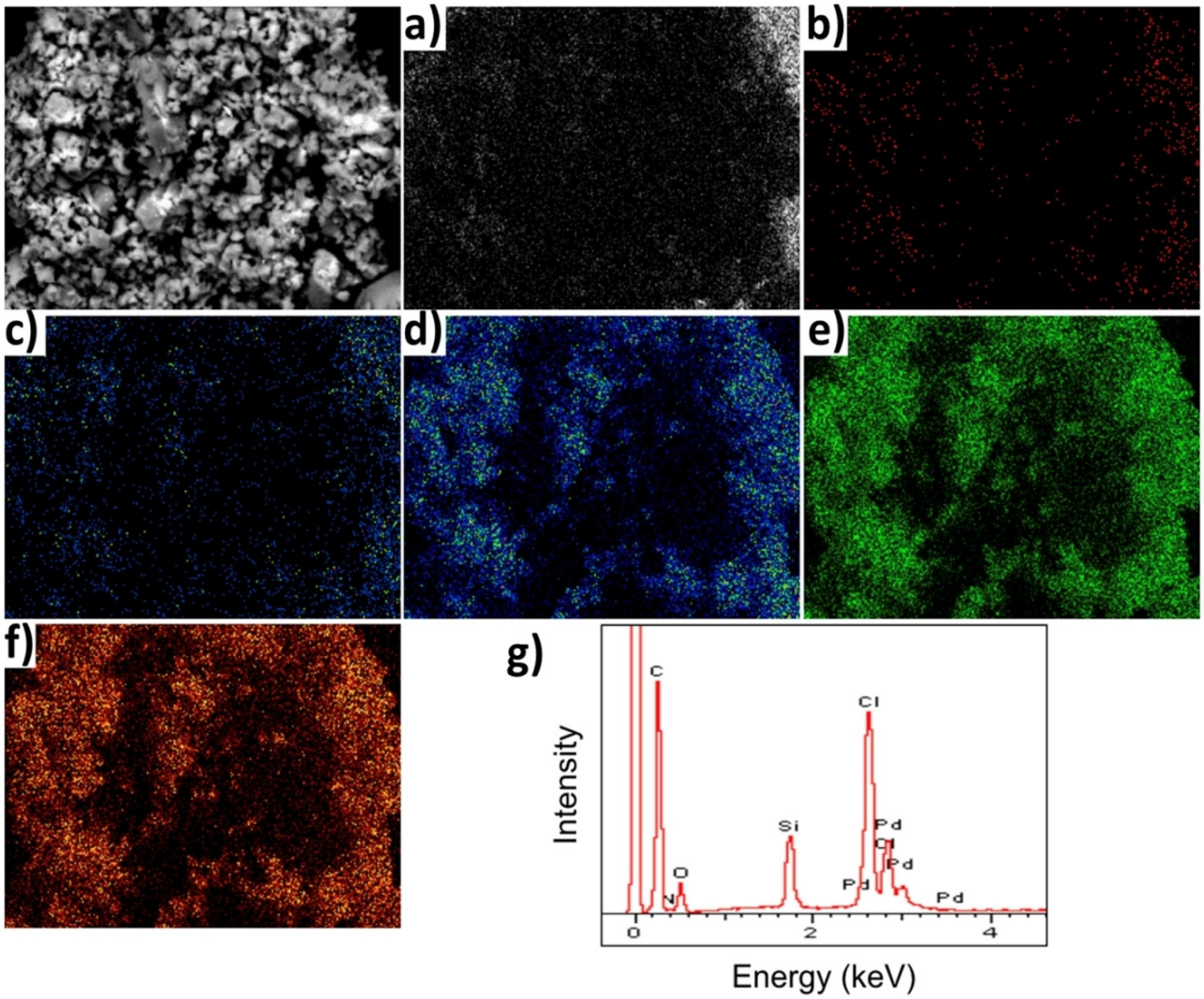

Figure 3. EDS mapping of a) carbon, b) nitrogen, c) oxygen, d) silicon, e) chlorine, and f) palladium in Pd(II)@Bim-SQ (**2**) and g) its EDS pattern.

amorphous. This result strongly supported that ionic crystalline solids, which are responsible for self-assembly of insoluble Bim-SQ **1** support were replaced with Pd-ligand interactions in amorphous nanocomposites **2** and **3**.

To evaluate the catalytic activity of catalyst **2**, the Suzuki–Miyaura cross coupling of aryl halides with phenyl boronic acid was chosen as the model reaction (Table 1). Under typical conditions (in aqueous ethanol solution at 60 °C in the presence of a base), iodobenzene substrate was more reactive than the corresponding bromide and chloride analogs (entries 1–3). This result is in accordance with the reactivity generally observed in such couplings.[40] Arylation of various aryl bromides bearing either electron-withdrawing (entries 4–6 and 12) or electron-donating (entries 7–11) substituents was performed. All expected coupled products could be obtained in good (71%) to quantitative yields within short reaction times (6 min to 5 h). The pre-catalyst **2** exhibited the highest activity with the maximum TOFs of 5400 h^{-1} in the case of 4-bromoacetophenone (Table 1, entry 4). Moreover, to investigate the steric effect of substrates on the activity, the reaction rates of methoxy-substituted aryl bromides were compared (entries 7–9). Under the same reaction conditions, the lowest catalytic performance was observed when using more hindered 2-bromoanisole as the substrate (entry 6 bearing an *ortho*-substituent). Furthermore, 4-bromoaniline and 1-bromonaphtalene required longer reaction times to achieve 86% and 99% yields of the coupled products, respectively (entries 11–12). The reusability of the catalyst **3** was investigated using 4-bromoacetophenone and phenylboronic acid as the substrates at 60 °C for 1 h. The results indicated that catalyst **3** could be reused up to 5th cycles without a loss of the catalytic activities (Figure S9) and the catalyst was easily separated from the reaction mixture by simple centrifugation.

In addition, the heterogeneous catalyst **3** was evaluated for Heck reactions showing active catalytic activities at 100 °C in aqueous acetonitrile under alkaline conditions (Table 2). Cross-coupling products were obtained quantitatively from iodobenzene and various aryl bromides after 20 h (entries 1–4). As

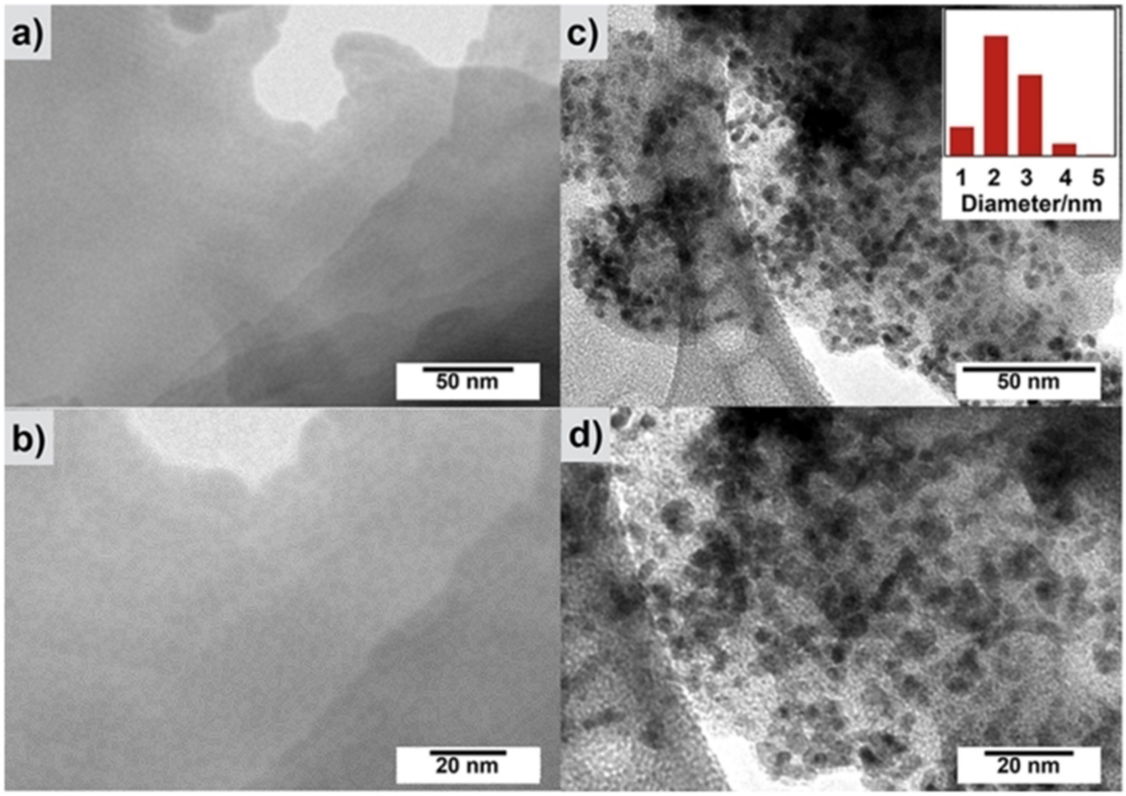

Figure 4. TEM images of Pd(II)@Bim-SQ (**2**) at scale bar of a) 50 and b) 20 nm and PdNp@Bim-SQ (**3**) at scale bar c) 50 nm and d) 20 nm. Histogram obtained considering 180 particles.

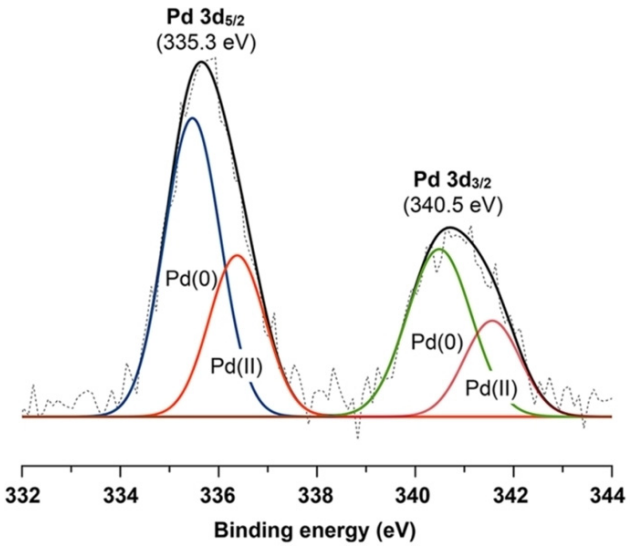

Figure 5. XPS analysis for Pd 3*d* spectrum on PdNp@Bim-SQ (**3**).

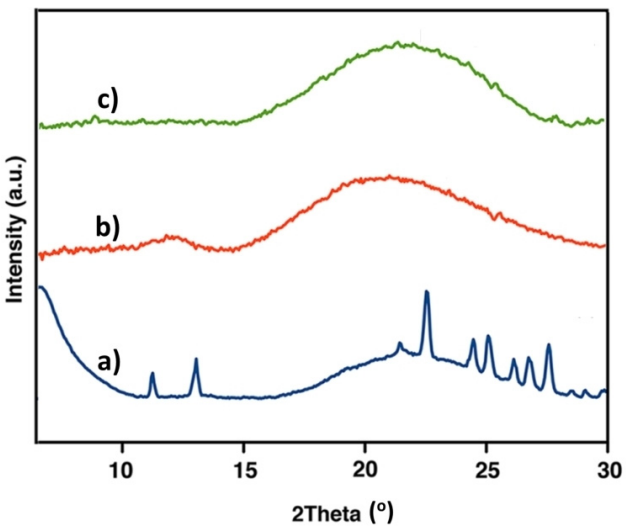

Figure 6. XRD spectra of a) Bim-SQ (**1**), b) Pd(II)@Bim-SQ (**2**), and c) PdNp@Bim-SQ (**3**).

expected, chlorobenzene was much less reactive and only 20% conversion could be obtained under the same conditions (entry 5). The results suggested that catalyst **3** could be successfully used as heterogeneous catalysts for both Suzuki–Miyaura and Heck cross-coupling reactions. In addition, hot filtration test (Figure S10) and ICP–MS analysis of the filtrate from the reaction confirmed the stabilization of the heterogeneous catalysts with minimal palladium leaching (< 0.2 ppm). The distribution of Pd over the catalyst **3**, evaluated by SEM-EDS analysis (Figure S4), revealed a uniform dispersion of Pd nanoparticles on the material surface. Meanwhile after five

Table 1. Catalytic activities of **2** toward Suzuki – Miyaura cross-coupling reaction.[a]

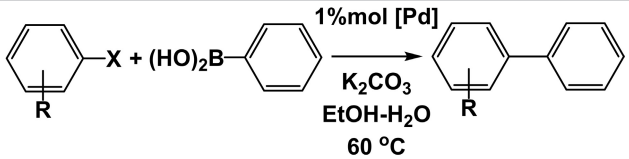

Entry	Substrate (R – Ar – X)	Time (h)	Yield (%)[b]	TOF (h^{-1})
1	Iodobenzene	0.3	100	1566
2	Bromobenzene	0.5	100	1260
3	Chlorobenzene	20	19	
4	4-Bromoacetophenone	0.1	100	5400
5	1-Bromo-4-nitrobenzene	1	71	
6	4-Bromobenzaldehyde	1.5	100	273
7	4-Bromoanisole	0.5	100	1290
8	2-Bromoanisole	4	99	
9	3-Bromoanisole	1	96	420
10	4-Bromotoluene	5	98	
11	4-Bromoaniline	20	86	
12	1-Bromonaphthalene	20	99	

[a] Aryl halides (0.2 mmol), phenylboronic acid (36.6 mg, 0.3 mmol), K_2CO_3 (41.5 mg, 0.3 mmol) and palladium catalyst **2** (1.01 mg, 1%mol Pd) in 1:1 mixture of EtOH:H_2O (2 mL) at 60 °C for the given time. [b] Determined by GC-MS using hexamethylbenzene as the internal standard. X = I, Br, Cl

Table 2. Catalytic activities of **3** toward Heck cross-coupling reaction.[a]

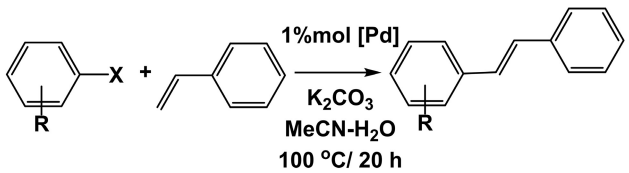

Entry	Substrate (R – Ar – X)	Yield (%)[b]
1	Iodobenzene	100
2	Bromobenzene	100
3	4-Bromoacetophenone	100
4	4-Bromotoluene	98
5	Chlorobenzene	19

[a] Aryl halides (0.1 mmol), styrene (17.2 µL, 0.2 mmol), K_2CO_3 (27.7 mg, 0.2 mmol) and palladium catalyst **3** (0.76 mg, 1%mol Pd) in 2:1 mixture of MeCN:H_2O (2 mL) at 100 °C for 20 h. [b] Determined by GC-MS using hexamethylbenzene as the internal standard. X = I, Br, Cl

reaction cycles the reused catalyst **3** still showed a well-dispersed Pd nanoparticles with a small amount of aggregation at the corner of the surface (Figure S11f).

Conclusions

Hybrid organic-inorganic materials of *N*-heterocyclic imidazole/imidazolium functionalized-SQ were successfully prepared and found as an insoluble, highly crystalline solid support. Subsequently, Pd(II) can be loaded into the support material **1** *via* an ionic exchange reaction, which became the amorphous Pd(II)@Bim-SQ of pre-catalyst **2**. *In situ* reduction during Suzuki – Miyaura cross-coupling reaction resulted in Pd nanoparticles, stabilized by *N* – heterocyclic ligands from SQ, PdNp@Bim-SQ (**3**). Based on TEM, EDS, and ICP-MS, Pd nanoparticles were well dispersed over SQ network with an average size of 2.33 ± 1.50 nm and Pd loading up to 14% *w/w*. The pre-catalyst **2** generally exhibited high catalytic efficiency for Suzuki – Miyaura reactions with the maximum TOFs of 5400 h^{-1} under mild aqueous ethanol conditions. Similarly, PdNp@Bim-SQ (**3**) can also be used as heterogeneous catalysts for Heck cross-coupling reaction giving excellent yields. Convenient catalyst separation *via* simple centrifugation, minimal Pd leaching, and reusability made the heterogeneous catalyst **3** a promising catalytic materials for Pd-catalyzed cross-coupling reactions.

Acknowledgements

This research was financially supported by the Thailand Research Fund (RSA5980018 and IRG5980007), Center of Excellence for Innovation in Chemistry (PERCH-CIC), and Office of the Higher Education Commission (OHEC), Ministry of Education. V.S. also thanks the student financial supports from the Development and Promotion of Science and Technology Talents Project (DPST).

Conflict of Interest

The authors declare no conflict of interest.

Keywords: Heterogeneous catalysis · Nanoparticle · Palladium · POSS · Silsesquioxane · Silica

[1] N. Miyaura, A. Suzuki, *Chem. Rev.* **1995**, *95*, 2457–2483.
[2] I. P. Beletskaya, A. V. Cheprakov, *Chem. Rev.* **2000**, *100*, 3009–3066.
[3] R. Chinchilla, C. Nájera, *Chem. Rev.* **2007**, *107*, 874–922.
[4] A. Suzuki, *J. Organometal. Chem.* **1999**, *576*, 147–168.
[5] a) N. T. S. Phan, M. V. D. Sluys, C. W. Jones, *Adv. Synth. Catal.* **2006**, *348*, 609–679; b) Y. M. A. Yamada, S. M. Sarkar, Y. Uozumi, *J. Am. Chem. Soc.* **2012**, *134*, 3190–3198.
[6] a) A. R. Siamaki, A. E. R. S. Khder, V. Abdelsayed, M. S. El-Shall, B. F. Gupton, *J. Catal.* **2011**, *279*, 1–11; b) S. Bhattacharya, A. Srivastava, S. Sengupta, *Tetrahedron Lett.* **2005**, *46*, 3557–3560; c) C. J. O'Brien, E. A. B. Kantchev, C. Valente, N. Hadei, G. A. Chass, A. Lough, A. C. Hopkinson, M. G. Organ, *Chem. Eur. J.* **2006**, *12*, 4743–4748.
[7] a) Y. Nishina, J. Miyata, R. Kawai, K. Gotoh, *RSC Adv.* **2012**, *2*, 9380–9082; b) Y. S. Feng, X. Y. Lin, J. Had, H. J. Xu, *Tetrahedron* **2014**, *70*, 5249–5253.
[8] T. Baran, A. Menteş, *J. Mol. Struct.* **2017**, *1134*, 591–596.
[9] a) B. Basu, S. Paul, *Appl. Organometal. Chem.* **2013**, *27*, 588–594; b) M. Trilla, G. Borja, R. Pleixats, M. W. C. Man, C. Bied, J. J. E. Moreau, *Adv. Synth. Catal.* **2008**, *350*, 2566–2574.
[10] S. Pavia, E. Ballerini, L. A. Bivona, F. Giacalone, C. Aprile, L. Vaccaro, M. Gruttadauria, *Adv. Synth. Catal.* **2013**, *355*, 2007–2018.
[11] H. Veisi, A. A. Manesh, N. Eivazi, A. R. Faraji, *RSC Adv.* **2015**, *5*, 20098–20107.
[12] a) K. Naka, M. Sato, Y. Chujo, *Langmuir* **2008**, *24*, 2719–2726; b) C. H. Lu, F. C. Chang, *ACS Catal.* **2011**, 481–488; c) L. Geng, Y. Li, Z. Qi, H. Fan, Z. Zhou, R. Chen, Y. Wang, J. Huang, *Catal. Commun.* **2016**, *82*, 24–28.
[13] M. Nowacka, C. Fischer, A. Kowalewska, M. Hebda, K. Hodor, *Eur. Polym. J.* **2017**, *86*, 17–28.
[14] G. Chen, Y. Zhou, X. Weng, J. Li, S. Sue, Y. Liu, Q. Wang, J. Wang, *Sci. Rep.* **2015**, *5*, 11236.
[15] a) H. Liu, Q. Zhu, L, Feng, B. Yao, S. Feng, *J. Mol. Struct.* **2013**, *1032*, 29–34; b) F. X. Perrin, D. M. Panaitescu, A. N. Frone, C. Radovics, C. Nicolae, *Polymer* **2013**, *54*, 2347–2354.
[16] a) F. J. Feher, T. A. Budzichowski, *J. Organometl. Chem.* **1989**, *373*, 153–163; b) M. E. Wright, D. A. Schorzman, F. J. Feher, R. H. Jin, *Chem. Mater.* **2003**, *15*, 264–268.

[17] B. Yang, H. Xu, J. Wang, S. Gang, C. Li, *J. Appl. Polym. Sci.* **2007**, *106*, 320–326.
[18] a) H. J. Ben, Y. Fan, Y. J. Shi, R. Liu, Y. Chen, X. K. Ren, S. Jiang, *Dyes Pigm.* **2017**, *137*, 584–592; b) J. Jiao, P. Lv, L. Wang, Y. Cai, P. Lui, *Polym. Eng. Sci.* **2015**, 565–572.
[19] C. Nio, G. Wu, C. Zhu, B. Yao, *J. Phys. Chem. C* **2010**, *114*, 13471–13476.
[20] a) S. Chanmungkalakul, V. Ervithayasuporn, S. Hanprasit, M. Masik, N. Prigyaia, S. Kiatkamjornwong, *Chem. Commun.* **2017**, *53*, 12108–12111; b) D. Wang, S. Feng, H. Liu, *Eur. Polym. J.* **2016**, *22*, 14319–14327.
[21] R. H. Lee, H. H. Lai, *Eur. Polym. J.* **2007**, *43*, 715–724.
[22] a) R. Kunthom, T. Jaroentomeechai, V. Ervithayasuporn, *Polymer* **2017**, *108*, 173–178; b) L. Gardella, A. Basso, M. Prato, O. Monticelli, *ACS Appl. Mater. Interfaces* **2013**, *5*, 7688–7692; c) P. Scholder, I. Nischang, *Catal. Sci. Technol.* **2015**, *5*, 3917–3921; d) D. Lu, J. Zhao, Y. Leng, P. Jiang, C. Zhang, *Catal. Commun.* **2016**, *83*, 27–30.
[23] D. B. Cordes, P. D. Lickiss, F. Rataboul, *Chem. Rev.* **2010**, *110*, 2081–2173.
[24] P. Sangtrirutnugul, T. Chaiprasert, W. Hunsiri, T. Jitjaroendee, P. Songkhum, K. Laohhasurayothin, T. Osotchan, V. Ervithayasuporn, *ACS Appl. Mater. Interfaces* **2017**, *9*, 12812–12822.
[25] C. Zhang, Y. Leng, P. P. Jiang, D. Lu, *RSC Adv.* **2016**, *6*, 57183–57189.
[26] S. Roy, K. C. Mondal, H. W. Roesky, *Acc. Chem. Res.* **2016**, *49*, 357–369.
[27] a) K. Tanaka, F. Ishiguro, Y. Chujo, *J. Am. Chem. Soc.* **2010**, *132*, 17649–17651; b) A. Ahmadi, C. McBride, J. J. Freire, A. Kajetanowicz, J. Czaban, K. Grela, *J. Phys. Chem. A* **2011**, *115*, 12017–12024.
[28] a) L. A. Bivona, F. Giacalone, E. Carbonell, M. Gruttadauria, C. Aprile, *ChemCatChem* **2016**, *8*, 1685–1691; b) J. G. Huddleston, A. E. Visser, W. M. Reichert, H. D. Willauer, G. A. Broker, R. D. Rogers, *Green Chemistry* **2001**, *3*, 156–164; b) H. Itoh, K. Naka, Y. Chujo, *J. Am. Chem. Soc.* **2004**, *126*, 3026–3027.
[29] V. Ervithayasuporn, K. Kwanplod, J. Boonmak, S. Youngme, P. Sangtrirutnugul, *J. Catal.* **2015**, *332*, 62–69.
[30] S. Mohapatra, T. Chaiprasert, R. Sodkhomkhum, R. Kunthom, S. Hanprasit, P. Sangtrirutnugul, V. Ervithayasuporn, *ChemistrySelect* **2016**, *1*, 5353.
[31] B. Marciniec, M. Dutkiewicz, H. Maciejewski, M. Kubicki, *Organometallics* **2008**, *27*, 793–794.
[32] X. Zhao, T. Wu, X. Bu, P. Feng, *Dalton Trans* **2011**, *40*, 8072–8074.
[33] S. Dirè, E. Borovin, F. Ribot, *Handbook of Sol-Gel Science and Technology* (Eds.: L. Klein et al.), Springer International Publishing, Switzerland, **2016**, pp. 1–34.
[34] E. S. Park, H. W. Ro, C. V. Nguyen, R. L. Jaffe, D. Y. Soon, *Chem. Mater.* **2008**, *20*, 1548–1554.
[35] S. Hanprasit, N. Tungkijanansin, A. Prompawilai, S. Eangpayung, V. Ervithayasuporn, *Dalton Trans.* **2016**, *45*, 16117–16120.
[36] S. Chimjarn, R. Kunthom, P. Chancharone, R. Sodkhomkhum, P. Sangtrirutnugul, V. Ervithayasuporn, *Dalton Trans.* **2015**, *44*, 916–919.
[37] J. Nichols, J. Terzic, E. G. Bittle, O. B. Korneta, L. E. De Long, J. W. Brill, G. Cao, S. S. A. Seo, *Appl. Phys. Lett.* **2013**, *102*, 141908.
[38] M. Itoh, F. Oka, M. Suto, S. D. Cook, N. Auner, *Int. J. Polym. Sci.* **2012**, *2012*, 1–17.
[39] T. Jaroentomeechai, P. Yingsukkamol, C. Phurat, E. Somsook, T. Osotchan, V. Ervithayasuporn, *Inorg. Chem.* **2012**, *51*, 12266–12272.S.
[40] A. F. Little, C. Dai, G. C. Fu, *J. Am. Chem. Soc.* **2000**, *122*, 4020–4028.

Submitted: November 2, 2017
Revised: December 29, 2017
Accepted: December 29, 2017

Catalysis Letters (2018) 148:779–786
https://doi.org/10.1007/s10562-017-2286-z

Chiral Pyrrolidine Bridged Polyhedral Oligomeric Silsesquioxanes as Heterogeneous Catalysts for Asymmetric Michael Additions

Torsak Luanphaisarnnont[1] · Sasikarn Hanprasit[1] · Vetiga Somjit[1] · Vuthichai Ervithayasuporn[1]

Received: 9 November 2017 / Accepted: 21 December 2017 / Published online: 30 December 2017

Abstract

A chiral pyrrolidine bridged polyhedral oligomeric silsesquioxane (SQ) was synthesized, characterized, and used as an effective heterogeneous catalyst. The synthesis involves two simple steps: nucleophilic substitution between benzylchloride functionalized SQ and imidazoyl pyrrolidine carboxylate and subsequent deprotection. The catalyst was isolated by simple filtration. The SQ-supported chiral pyrrolidine catalyst was used as a heterogeneous catalyst in an asymmetric Michael addition into nitrostyrenes under room temperature and neat condition, giving the product in excellent yields (85–91%), diastereoselectivities (up to 99:1) and enantioselectivities (95–98%). The catalyst can be recycled by a simple filtration without a significant loss in its reactivity and selectivity.

Graphical Abstract

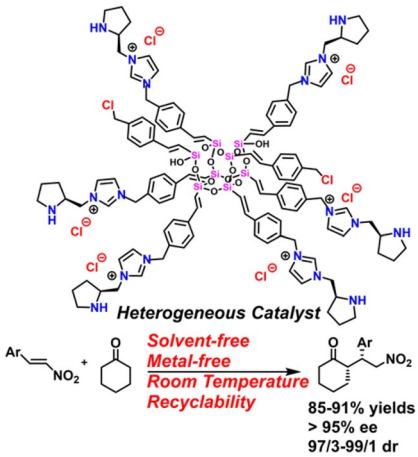

Keywords Silsesquioxane · POSS · Asymmetric catalysis · Michael reaction · Heterogeneous catalysis

1 Introduction

Development of efficient catalysis for organic transformations has been among major challenges in chemistry [1]. The use of inorganic support for heterogeneous catalysis has gained attention over organic materials due to their outstanding mechanical and thermal stabilities [2]. Although silica gel has been the most widely used support for chiral catalysts [3–5], recent research investigations have shown that an ordered nanostructure of mesoporous silica can also be used

Electronic supplementary material The online version of this article (https://doi.org/10.1007/s10562-017-2286-z) contains supplementary material, which is available to authorized users.

✉ Vuthichai Ervithayasuporn
vuthichai.erv@mahidol.ac.th; maldiniandg@hotmail.com

[1] Department of Chemistry, Center of Excellence for Innovation in Chemistry (PERCH-CIC), and Center for Inorganic and Materials Chemistry, Faculty of Science, Mahidol University, 272 Rama VI Road, Ratchathewi District, Bangkok 10400, Thailand

as a support for catalyst, exhibiting high catalytic activities in both symmetric and asymmetric organic reactions [6–12]. Polyhedral oligomeric silsesquioxanes (POSS) or cage-like silsesquioxanes (SQ) with a well-defined nanostructure, composed of a silica (Si–O) core with the highest organic functionalities [13–15], have also been studied and used as sensors [16], electronic materials [17], and alternative catalyst supports [18–20]. Recent works showed that SQ could be applied in C–C bond coupling reactions [21–23], oxidations [24], multicomponent coupling reactions [25], carbon dioxide fixation reactions [26], and polymerizations [27, 28]. Despite many reports on the use of SQ as a catalyst support, the development of SQ-supported chiral catalysts for heterogeneous asymmetric reactions has been limited. An organorhodium-functionalized SQ, which was used as a bifunctional heterogeneous catalyst for an asymmetric transfer hydrogenation of aromatic ketones, has been reported [29]. To the best of our knowledge, there is no report on the use of chiral SQ as a heterogeneous catalyst in asymmetric C–C bond forming reactions.

Catalytic asymmetric Michael reactions are one of the most important and useful asymmetric C–C bond forming reactions [30, 31]. Many chiral pyrrolidine catalysts have been developed for asymmetric homogeneous Michael addition into nitrostyrenes [32, 33]. Developments of heterogeneous catalysts by attachment of chiral pyrrolidines on modified organic and inorganic materials have also been studied [34–39]. However, a chiral heterogeneous pyrrolidine-modified SQ catalyst has not been well investigated. Herein, a chiral pyrrolidine bridged polyhedral oligomeric SQ was synthesized, characterized, and used as a heterogeneous catalyst for asymmetric Michael additions of cyclohexanones into nitrostyrenes. Furthermore, the chiral pyrrolidine loading of SQ catalyst were determined to be much greater than any previous silicon-based materials.

2 Experimental

2.1 Chemicals and Instruments

Di-*tert*-butyl dicarbonate was purchased from Tokyo Chemical Industry, while imidazole, L-proline, *trans*-β-nitrostyrene, *trans*-4-methoxy-β-nitrostyrene, *trans*-4-fluoro-β-nitrostyrene, *trans*-4-chloro-β-nitrostyrene, and anhydrous toluene were purchased from Sigma Aldrich and used without additional purification. The commercial grades of ethyl acetate, methylene chloride, methanol and hexane were further distilled. Precoated silica gel 60 F254 plates and silica gel (No. 60) used for chromatography were purchased from Merck & Co., Inc.

The FT-IR spectra were collected using an attenuated total reflectance technique with Bruker model Alpha spectrometer. HPLC analysis was performed on Waters 2695 Separation Modules with Waters 2487 Dual λ Absorbance Detector using a Chiralpak AD-H column purchased from Daicel Chemical Industries, Ltd.

The ^{13}C and ^{29}Si CP/MAS NMR spectra were acquired at 60 MHz frequency with AVANCE 300 MHz Digital NMR Spectrometer (Bruker Biospin; DPX-300). A 7 mm triple resonance probe, a sample spinning rate of 5 kHz with a contact time of 2 ms, and pulse delay of 5 s were used. The pulses and the spectra were calibrated using commercially available samples of 2,2-dimethyl-2-silapentan-5-sulfonate, glycine and adamantine, for ^{29}Si and ^{13}C, respectively. Fourier transform nuclear magnetic resonance spectra in solution phase were obtained by using a Bruker-Ascend™ 400 and Bruker-AV 500 high-resolution magnetic resonance spectrometers for ^{1}H (400 MHz) and (500 MHz) nuclei, respectively. Powder X-ray diffraction was performed by Bruker D8 Advance with a monochromatic Cu K_α radiation at $\lambda = 0.154$ nm. Applied voltage and current were used at 40 kV and 30 mA, respectively. The mode of recorded system was operated with $2\theta = 5.00–40.00$ (scan rate $= 0.005° \ s^{-1}$). Thermogravimetric analyses (TGA) were performed on a TG 209F3 instrument in Al_2O_3 pans and carried out under oxygenated atmosphere on heating at 10 °C/min in a range of 35 and 800 °C.

2.2 Preparation of Catalysts

2.2.1 Synthesis of SQ-Supported Chiral Pyrrolidine Procatalyst (2)

Under argon atmosphere, octa(4-(chloromethyl)styryl)octasilsesquioxane [40, 41] (0.30 g, 0.18 mmol) and *tert*-butyl (*S*)-2-((1*H*-imidazol-1-yl)methyl)pyrrolidine-1-carboxylate [42] (1.13 g, 4.52 mmol) were mixed in 4 mL of dried toluene. The solution was kept at 70 °C and stirred for 24 h. The precipitate was filtered and washed with CH_2Cl_2, methanol, and ethyl ether, respectively, and dried under vacuum. The Boc-protected SQ-supported product was obtained as a pale yellow solid (0.51 g, 0.135 mmol, 75% yield). Procatalyst **2** was further quantified through CHN microanalysis and found to be 2.14 mmol/g of pyrrolidine-based imidazolium cation based on nitrogen percentage. ^{29}Si CP/MAS NMR: δ − 67.89, − 77.43 ppm; ^{13}C CP/MAS NMR: δ 154.8, 148.0, 136.9, 129.9, 127.4, 123.0, 79.4, 56.9, 52.4, 46.8, 28.4, 23.4 ppm.

2.2.2 Synthesis of SQ-Supported Chiral Pyrrolidine Catalyst (3)

The Boc-protected SQ-supported catalyst **2** (0.51 g, 0.135 mmol) was deprotected using 5 M HCl in ethanol (10 mL) with vigorously stirring at room temperature for 4 h. The reaction was subsequently neutralized with NEt_3 (3 mL). The reaction was filtered, and the solid catalyst

was washed with ethanol and ethyl ether and dried under vacuum at room temperature to afford the desired product as a solid (0.39 g, 0.129 mmol, 96% yield). Catalyst **3** was further quantified through CHN microanalysis and found to be 2.28 mmol/g of pyrrolidine-based imidazolium cation based on nitrogen percentage. ^{29}Si CP/MAS NMR: δ − 59.92, − 68.14, − 78.03 ppm; ^{13}C CP/MAS NMR: δ 147.8, 136.8, 127.8, 123.0, 58.4, 52.7, 46.6, 28.8, 24.1, 21.6 ppm.

2.3 Catalytic Testing for Asymmetric Michael Addition

The SQ-supported catalyst **3** (7.5 mg, 0.0029 mmol), nitrostyrene (75 mg, 0.5 mmol), and cyclohexanone (0.4 mL) were added to a reaction flask. The reaction was stirred at room temperature for 24 h. The reaction mixture was filtered and washed with ethyl acetate. The combined filtrate was concentrated. Flash column chromatography (hexanes/ethyl acetate = 3:1) provided the γ-nitroketone as a solid.

3 Result and Discussion

3.1 Preparation of Catalysts

The synthesis approach for SQ-supported (*S*)-1-((pyrrolidin-2-yl)methyl)-1*H*-imidazolium chloride, the SQ-supported catalyst (**3**), was depicted in Scheme 1. Firstly, SQ-supported (*S*)-1-((1-(*tert*-butoxycarbonyl)pyrrolidin-2-yl)methyl)-1*H*-imidazolium chloride, the SQ-supported procatalyst (**2**), can be synthesized from a substitution reaction between octa(4-(chloromethyl)styryl)octasilsesquioxane (**1**) [40, 41] and *tert*-butyl (*S*)-2-((1*H*-imidazol-1-yl)methyl)pyrrolidine-1-carboxylate [42] under thermal activation in 75% yield, subsequently followed by a Boc deprotection under acidic condition to obtain SQ-supported catalyst **3** in 96% yield. It

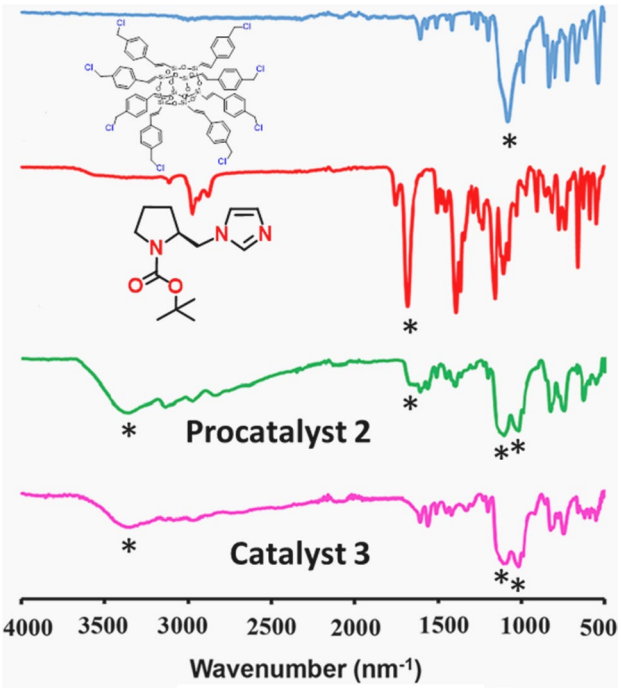

Fig. 1 IR spectra of starting materials, procatalyst **2**, and catalyst **3**

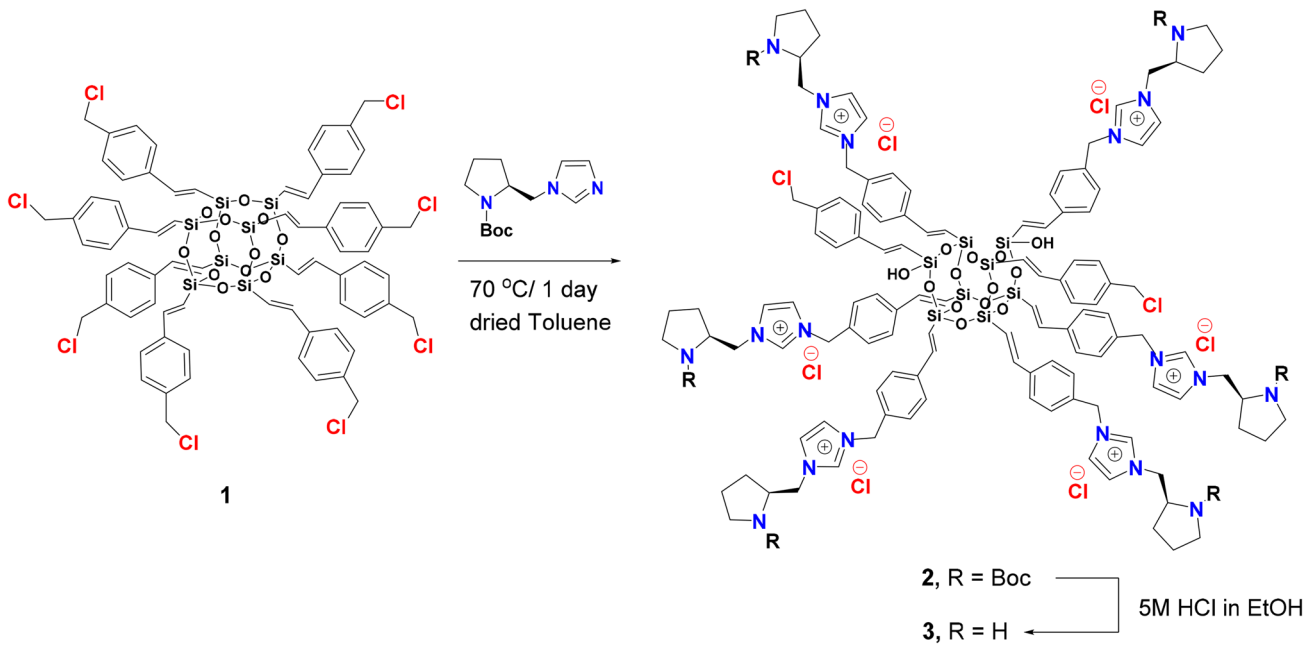

Scheme 1 Synthesis of a chiral pyrrolidine bridged polyhedral oligomeric SQ, the SQ supported catalyst (**3**)

is noteworthy that the syntheses of the procatalyst **2** and the catalyst **3** require no templating reagents and the isolation processes involve only a simple filtration because of their insolubility in organic and aqueous solvents.

3.2 Catalyst Characterizations

The formations of procatalyst **2** and the catalyst **3** were confirmed by IR, NMR, TGA, XRD, and CHN methods. The FT-IR spectra of **2** as shown in Fig. 1 showed a key C=O stretching vibration band at 1683 cm^{-1} corresponding to the presence of Boc–pyrrolidine moieties. This absorption band is absent in the IR spectra of **3** (Fig. 1), confirming the removal of Boc protecting group. Both **2** and **3** also exhibited overlapped C–N stretching vibrations of pyrrolidine rings at 1150 cm^{-1}among two distinct asymmetrical Si–O–Si stretching vibrations at 1100 and 1020 cm^{-1} arising for more disordered polyhedral SQ cages, which differ from a perfect T_8 cage of **1** with a very strong broad band at 1030 cm^{-1} [43]. The presence of a broad O–H band (3000–3700 cm^{-1}) can be assigned to SiOH units, which also confirmed the presence of some cage-degradation resulting in open siliceous structures with silanols groups such as T^1 [R-Si$(OSi)_1(OH)_2$] and T^2 [R-Si$(OSi)_2(OH)$]. These disordered cages from partial cage opening could be explained by the strong nucleophilicity of the sp^2 nitrogen on the imidazole, which increased the chance of the cleavage of Si–O bonds at a SQ core [44].

The NMR results (Fig. 2) also agreed well with the IR spectra. To confirm a successful substitution of substituted imidazole on **1**, ^{13}C CP/MAS NMR spectrum of **2** (Fig. 2a)

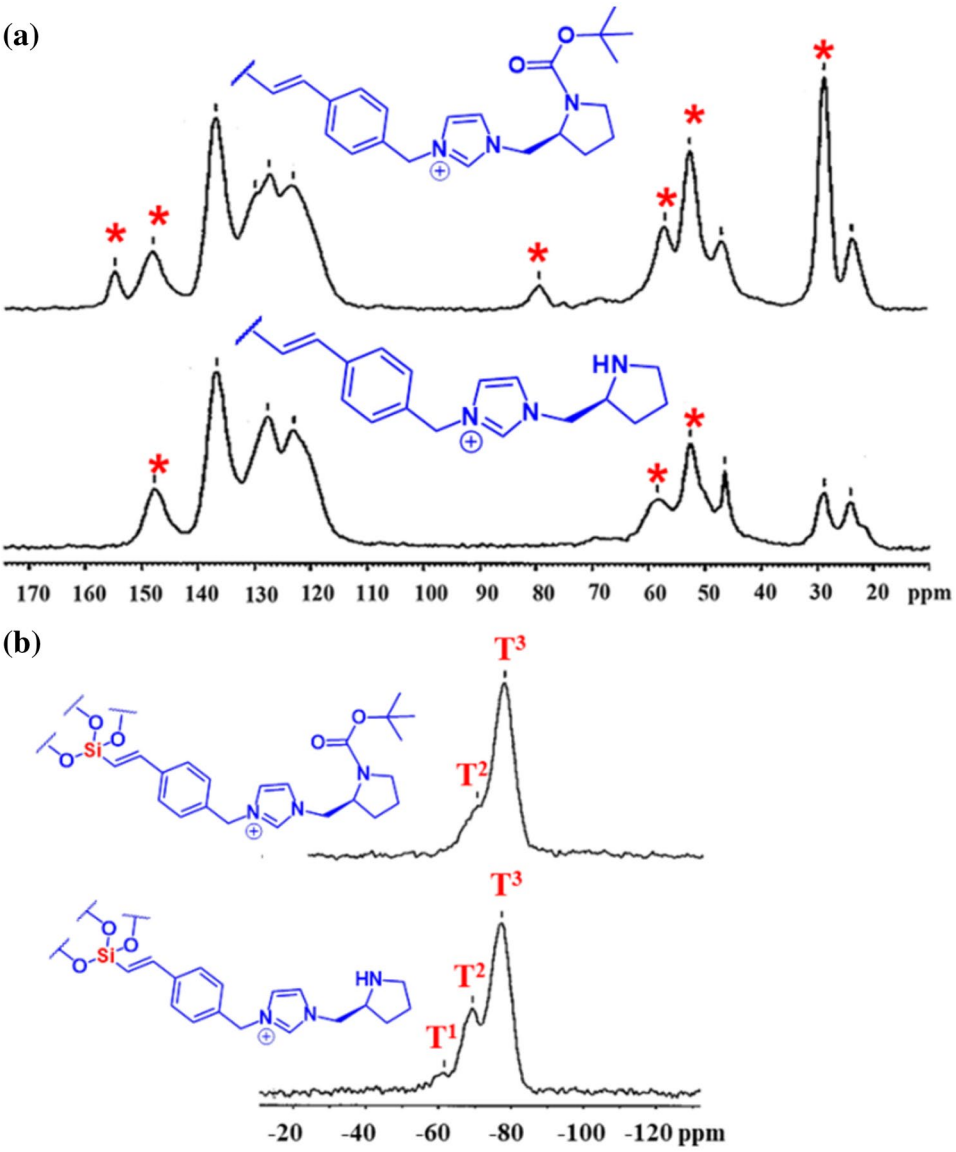

Fig. 2 **a** ^{13}C and **b** ^{29}Si CP/MAS NMR spectra of procatalyst **2** and catalyst **3**

exhibited two key signal sets corresponding to imidazolium (148.0 ppm) and Boc–pyrrolidine rings (154.8, 79.4, 56.9, 52.4, and 28.4 ppm). The absence of the signals at 154.8, 79.4, and 28.4 ppm in the ^{13}C CP/MAS NMR spectrum of **3** (Fig. 2a) confirmed the complete removal of the Boc protecting group. The ^{29}Si CP/MAS NMR spectra were used to probe into the core structures of **2** and **3** (Fig. 2b). The signals of catalyst **3** at −77, −68, and −59 ppm corresponded to the T^3 [R-Si(OSi)$_3$] and some partially cage-opening silsequioxanes (T^2 and T^1), respectively.

TGA of **2** and **3** (Fig. 3) confirmed the existence of the hydrophilic imidazolium and silanol moieties, which can strongly absorb moisture, on both materials. The TGA curves showed 5% weight loss between 25 and 120 °C; therefore, the reformulated ceramic yields of **2** and **3** were 13.7 and 17.9 wt%, respectively, versus the calculated values of 14.9 and 18.3 wt%, respectively. The derivative weight loss of **2** (Fig. 3) showed an additional peak at 150–215 °C confirmed the degradation of Boc groups on **2**. This peak was absent in the curve of **3** (Fig. 3).

According to the XRD spectra of **2** and **3** in Fig. 4, both materials exhibited an amorphous nature with a key characteristic reflection at $2\theta = 21.0°$, which can be converted to a 4.22 Å of *d*-value. This value indicated the existence of a SQ (Si–O–Si) cage [27]. When compared with that of the SQ-supported procatalyst **2**, the reflection of the SQ catalyst **3** was shifted from $2\theta = 7.3°$–$8.5°$, and the *d*-spacing

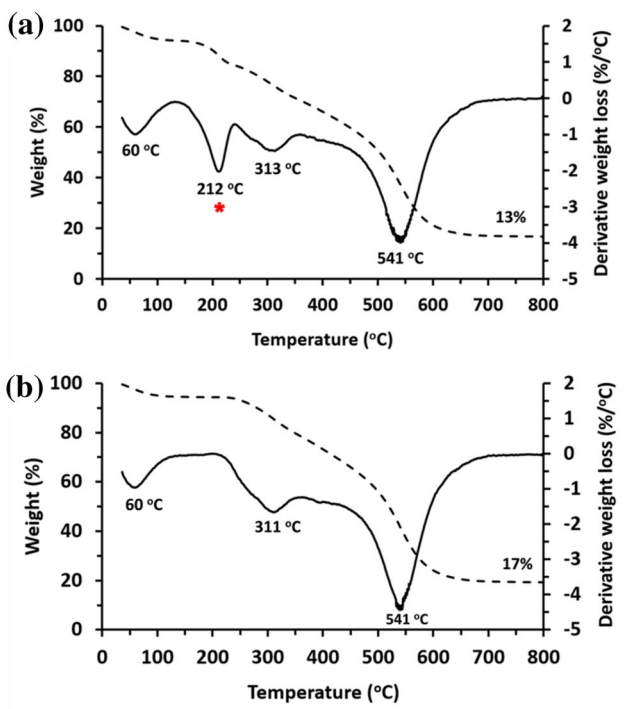

Fig. 3 TGA and derivative weight loss curves of **a** procatalyst **2** and **b** catalyst **3**

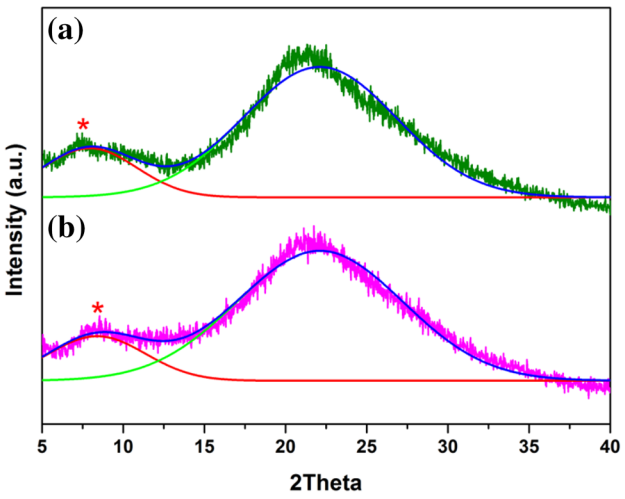

Fig. 4 XRD spectra of **a** procatalyst **2** and **b** catalyst **3**

is decreased to about 1.70 Å. This shift confirmed a successful removal of the Boc protecting group on **2**. In order to confirm the number of active sites of pyrrolidine-based imidazole on SQ, catalyst **3** was simply quantified through CHN microanalysis. Its carbon-to-nitrogen (C:N) mass ratio was found to be 6.09, compared to a calculated value of 5.95 for the SQ with six chiral pyrrolidine rings. This result suggested that the number of active chiral pyrrolidine rings on the SQ core in **3** is approximately 6.

3.3 Catalytic Testing for Asymmetric Michael Addition

To test for the effectiveness and efficiency of the SQ scaffold as a support for chiral catalysts, the SQ-supported chiral catalyst **3** was used in an asymmetric Michael addition reaction of cyclohexanone into nitroolefins (Table 1). The amount of catalyst **3** is 0.57 mol%, which is approximately equal to 3.4 mol% active chiral pyrrolidine rings. Both electron-rich and electron-poor nitrostyrenes work well in the reaction, giving the corresponding products in excellent yields, diastereoselectivities and enantioselectivities. The slightly lower yield of electron-rich substrate may be due to the lower electrophilicity of the substrate. The high yields and selectivities were similar to those obtained from the homogeneous catalysis [32] and silica–gel-supported catalyst [35], suggesting that the SQ core did not interfere with the active chiral pyrrolidine ring. It is noteworthy that the SQ-supported catalyst was more efficient at catalyzing the reaction, yielding similar yields and selectivities even with a lower amount of the active chiral pyrrolidine rings and a shorter reaction time. When compared with the homogeneous catalyst, the SQ-supported catalyst was also easier to

Table 1 Asymmetric Michael additions of cyclohexanone catalyzed by the SQ-supported chiral catalyst **3**

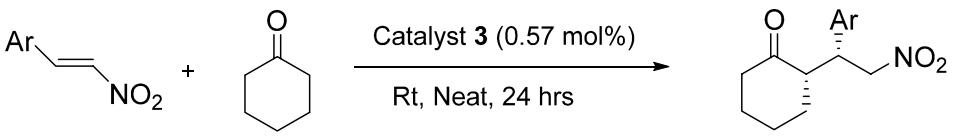

Entry[a]	Product	Yield[b] (%)	dr[c]	ee[d] (%)
1	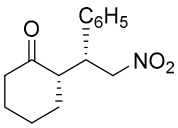	90	98:2	98
2	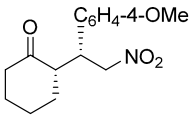	85	97:3	97
3	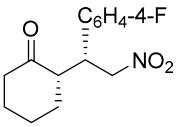	90	99:1	97
4	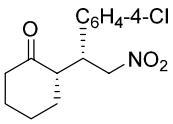	91	99:1	95

[a]Nitroolefin (0.5 mmol), cyclohexanone (0.4 mL) and **3** (0.57 mol%) under neat reaction condition at room temperature for 24 h

[b]Isolated yields

[c]Diastereomeric ratio, dr (syn:anti), determined by ^{1}H NMR spectroscopy of the crude product

[d]Determined by HPLC using a Chiralpak AD-H column

handle with a simple filtration to separate the catalyst from the reaction mixture and without need for solvents.

The recyclability of the SQ-supported catalyst **3** was investigated by subjecting it into a new reaction for multiple cycles (Table 2). The catalyst can be used for at least four cycles with a minimal loss in yields and selectivities. This result showed the high robustness of the SQ as a catalyst support. To further study the durability of the SQ-supported catalyst **3**, a leaching test and a filtration test were performed, and their results suggested that no catalytically active species leached out form the SQ-supported catalyst **3** during the reaction. A preliminary study on the basic kinetic behavior of the catalyst was performed by monitoring the product yield at different times (Fig. S5). The formation of the product plateaued after around 24 h. The turnover number of the catalyst after 24 h could be calculated to be approximately 158. A further kinetic investigation to study the detailed behavior of the SQ-supported catalyst, particularly at the beginning of the reaction, is currently being investigated.

Table 2 Recycling experiments of the catalyst **3**

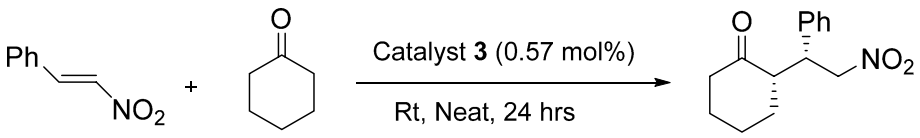

Cycle	Yield (%)	dr	ee (%)
1	90	98:2	98
2	88	98:2	97
3	89	98:2	98
4	85	97:3	95

4 Conclusion

The chiral pyrrolidine bridged cage-like SQ catalyst was synthesized and characterized. The catalyst was used to effectively and efficiently catalyze the Michael addition reactions of cyclohexanone into nitroolefins with excellent yields and selectivities at room temperature. The catalyst could be recycled by a simple filtration with a minimal loss in the yields and selectivities, which confirms the effectiveness and robustness of the SQ core as a heterogeneous scaffold for chiral catalysts. Further applications of SQ cage as a support for other chiral catalysts is undergoing and will be reported in due course.

Acknowledgements This research was supported by Thailand Research Fund (MRG5980118 for T.L.), the Central Instrument Facility, the Faculty of Science, Mahidol University, and the Center of Excellence for Innovation in Chemistry (PERCH-CIC), Office of the Higher Education Commision (OHEC), Ministry of Education. S.H. thanks a graduate student financial support from TRF IRG5980007.

References

1. Beller M, Renken A, van Santen RA (2012) Catalysis: from principles to applications. Wiley, Weinheim
2. Liu H, Zheng S, Nie K (2005) Macromolecules 38:5088
3. Soai K, Watanabe M, Yamamoto A (1990) J Org Chem 55:4832
4. Heckel A, Seebach D (2000) Angew Chem Int Ed 39:163
5. Fraile JM, Mayoral JA, Serrano J, Pericas MA, Sola L, Castellnou D (2003) Org Lett 5:4333
6. Kawasaki T, Araki Y, Hatase K, Suzuki K, Matsumoto A, Yokoi T, Kubota Y, Tatsumi T, Soai K (2015) Chem Commun 51:8742
7. Cheng T, Zhao Q, Zhang D, Liu G (2015) Green Chem 17:2100
8. del Pozo C, Corma A, Iglesias M, Sánchez F (2011) Green Chem 13:2471
9. Croissant JG, Cattoën X, Durand JO, Man MWC, Khashab NM (2016) Nanoscale 8:19945
10. Hosseini HG, Doustkhah E, Kirillova MV, Rostamnia S, Mahmoudi G, Kirillov A (2017) Appl Catal A 548:96
11. Rostamnia S, Gholipour B, Hossenini HG (2016) Process Saf Environ Prot 100:74
12. Rostamia S, Hossieni HG, Doustkhah E (2015) J Organomet Chem 791:18
13. Cordes DB, Lickiss PD, Rataboul F (2010) Chem Rev 110:2081
14. Hanprasit S, Tungkijanansin N, Prompawilai A, Eangpayung S, Ervithayasuporn V (2016) Dalton Trans 45:16117
15. Chimjarn S, Kunthom R, Chancharone P, Sodkhomkhum R, Sangtrirutnugul P, Ervithayasuporn V (2015) Dalton Trans 44:916
16. Chanmungkalakul S, Ervithayasuporn V, Hanprasit S, Masik M, Prigyai N, Kiatkamjornwong S (2017) Chem Commun 53:12108
17. Ervithayasuporn V, Abe J, Wang X, Matsushima T, Murata H, Kawakami Y (2010) Tetrahedron 66:9348
18. Zheng W, Lu C, Yang G, Chen Z, Nie J (2015) Catal Commun 62:34
19. Moreau JJE, Vellutini L, Man MWC, Bied C (2003) Chem Eur J 9:1594
20. Duchateau R (2002) Chem Rev 102:3525
21. Bivona LA, Giacalone F, Carbonell E, Gruttadauria M, Aprile C (2016) ChemCatChem 8:1685
22. Zhang C, Leng Y, Jiang P, Lu D (2016) RSC Adv 6:57183
23. Mohapatra S, Chaiprasert T, Sodkhomkhum R, Kunthom R, Hanprasit S, Sangtrirutnugul P, Ervithayasuporn V (2016) ChemistrySelect 1:5353
24. Sangtrirutnugul P, Chaiprasert T, Hunsiri W, Jitjaroendee T, Songkhum P, Laohhasurayotin K, Osotchan T, Ervithayasuporn V (2017) ACS Appl Mater Interfaces 9:12812
25. Safaei-Ghomi J, Nazemzadesh SH, Shahbazi-Alavi H (2016) Appl Organomet Chem 30:911
26. Bivona LA, Fichera O, Fusaro L, Giacalone F, Buaki-Sogo M, Gruttaduaria M, Aprile C (2015) Catal Sci Technol 5:5000
27. Kunthom R, Jaroentomeechai T, Ervithayasuporn V (2017) Polymer 108:173
28. Pochwala M, Bialek M, Franczyk A, Marciniec B, Czaja K (2016) Eur Polym J 79:121
29. Tang S, Jin R, Zhang H, Yao H, Zhuang J, Liu G, Li H (2012) Chem Commun 48:6286
30. Berner OM, Tedeschi L, Enders D (2002) Eur J Org Chem 2002:1877
31. Almasi D, Alonson DA, Najera C (2007) Tetrahedron: Asymmetry 18:299
32. Ishii T, Fujioka S, Sekiguchi Y, Kotsuki H (2004) J Am Chem Soc 126:9558
33. Reyes-Rangel G, Vargas-Caporali J, Juaristi E (2017) Tetrahedron 73:4707

34. Du J, Shuai B, Tao M, Wang G, Zhang W (2016) Green Chem 18:2625
35. Li P, Wang L, Zhang Y, Wang G (2008) Tetrahedron 64:7633
36. Luo S, Mi X, Zhang L, Liu S, Xu H, Cheng JP (2006) Angew Chem Int Ed 45:3093
37. Tian J, Zhang C, Qi X, Yan X, Li Y, Chen L (2015) Catal Sci Technol 5:724
38. Qi X, Tian J, Li Y, Chen L, Yan X (2015) Catal Commun 71:70
39. Liu J, Li P, Zhang Y, Ren K, Wang L, Wang G (2010) Chirality 22:432
40. Harrison PG, Hall C (1997) Main Group Met Chem 20:515
41. Cheng G, Vautravers NR, Morris RE, Cole-Hamilton DJ (2008) Org Biomol Chem 6:4662
42. Wang L, Tang R, Yang H (2013) J Korean Chem Soc 57:591
43. Fina A, Tabuani D, Carniato F, Frache A, Boccaleri E, Camino G (2006) Thermochim Acta 440:36
44. Jaroentomeechai T, Yingsukkamol PK, Phurat C, Somsook E, Osotchan T, Ervithayasuporn V (2012) Inorg Chem 51:12266

Journal of Photochemistry and Photobiology A: Chemistry 358 (2018) 215–225

Contents lists available at ScienceDirect

Journal of Photochemistry and Photobiology A: Chemistry

journal homepage: www.elsevier.com/locate/jphotochem

Green synthesis of fluorescent N,O-chelating hydrazone Schiff base for multi-analyte sensing in Cu^{2+}, F^- and CN^- ions

Neeraj Saini[a], Nicha Prigyai[a], Chidchanok Wannasiri[a], Vuthichai Ervithayasuporn[a,*], Suda Kiatkamjornwong[b,c]

[a] Department of Chemistry, Center of Excellence for Innovation in Chemistry (PERCH-CIC), Center for Inorganic and Materials Chemistry, Faculty of Science, Mahidol University, Rama VI Road, Ratchathewi District, Bangkok 10400, Thailand
[b] Faculty of Science, Chulalongkorn University, Phayathai Road, Bangkok 10330, Thailand
[c] FRST, Division of Science, The Royal Society of Thailand, Sanam Suepa, Dusit, Bangkok 10300, Thailand

ARTICLE INFO

Article history:
Received 31 January 2018
Received in revised form 1 March 2018
Accepted 12 March 2018
Available online 13 March 2018

Keywords:
Dehydroacetic acid
1,8-Naphthalimide
Fluorescence
Copper
Fluoride
Cyanide

ABSTRACT

A colorimetric and fluorometric hydrazone Schiff's base derived from dehydroacetic acid by three-steps and high-yield syntheses under green approach employing ethanol as a solvent has been prepared. Multi-analyte sensing for both metal cation (Cu^{2+}) and anions (F^- and CN^-), with high sensitivity and competitive selectivity, was encountered. The sensing mechanism of anion detection found to be deprotonation of N—H and O—H moieties in the presence of ions. However, metal cation like copper(II) ions chelation with sensor, leads to diminish intra-molecular charge transfer (ICT) with chelation induced quenching of fluorescence (CHQF). Contrary, anionic interaction ensued in heightened ICT as well as photo-induced electron transfer (PET) processes. The Job's plots interpretation rendered stoichiometry of 2:1 with Cu^{2+}/F^- and 1:1 with CN^-. Moreover, the detection limits of 0.962 ppm (Cu^{2+}), 0.023 ppm (F^-) and 0.073 ppm (CN^-) were much lower than WHO guidelines. Further, either water or methanol was employed to differentiate F^-/CN^- ions with sensor in THF, with prominent visible naked eye and fluorometric responses.

1. Introduction

Constructing dual responsive chemosensors for the efficient and selective recognition of metal ions as well as anions simultaneously are still a challenging task for the scientific community [1–3]. Nowadays, research scenario has been focused more on developing optical signaling probes due to high competitive selectivity, rapid naked eye detection in ambient light and economical testing, over conventional detection methods [4,5]. Various receptor molecules interacting through unidirectional hydrogen bonding [6,7], ions induced Si-O bond cleavage reactions [8], molecular encapsulation [9], chelation [10] etc. displaying either colorimetric or fluorometric responses, have been contrived and tested toward ions [11]. But the majority of them exhibited severe limitations such as non-discrimination between fluoride and cyanide ions, interference from other competing ions specially acetate ions, long time to response and/or irreversibility [12–15]. On the other side, deprotonation based sensing probes display higher selectivity with stable optical responses [16,17]. As an example, Pu et al. [18] accounted various diarylethene based chemosensors for fluoride and copper ions in acetonitrile. However, Wan and co-workers described a phenol derived indicator system with dual optical responses toward fluoride and risky cyanide ions. Even though, these systems were excellent examples of chemosensors but effective only in pure organic environments limiting their application to off-site detection. In addition, aqueous analysis suffers from solvent competition and probe insolubility, ensuing sensing of ions an uphill battle [19,20]. Probes that can effectively detect multiple ions in aqueous medium are highly desirable but still quite rare [21,22]. Further, synthetic methodologies followed in the previous reports involve the use of hazardous chemicals such as pyridines, dioxanes, nitrobenzene, etc. with high temperature and tedious extraction processes [1,15,18]. This puts a negative impact on the development of economical sensing probes as well as on human health.

It has been well demonstrated that both metal ions as well as anions are crucial constituents in various biological, manufacturing and metallurgical processes [23–26]. In particular, copper ions act as cofactor and active site constituent in various metalloenzymes due to its versatile redox and binding properties [27–29]. Also, fluoride ions

* Corresponding author.
E-mail address: vuthichai.erv@mahidol.ac.th (V. Ervithayasuporn).

https://doi.org/10.1016/j.jphotochem.2018.03.018
1010-6030/

have been a crucial constituent in toothpastes and drinking water. It precludes dental caries [30]. However, over intake of fluoride ions is deuced for many medical ailments such as fluorosis, osteoporosis or even urolithiasis [31,32]. Similarly, excess concentration of cyanide ions poses hazardous impingement on the living systems [33–35]. For these reasons, an impetus always exists for the development of economical optical probes that assist in maintaining a periodic check and in-turn regulate ion's concentration in the ecosystem [36,37].

Majorly, 1,8-naphthalimide moiety has been exploited as fluorophore unit in different sensing systems due to eminent quantum yields, proficient photo-stability and prominent Stokes' shift [38,39]. Moreover, pyran ring systems have evinced biocompatibility, scuttling unexampled dimensions of sensor application in biological system. Additionally, a pyrone derivative such as dehydroacetic acid based receptor system puts forth excellent chelation based sensing of metal ions [40,41]. Literature survey revealed that there is still paucity of dual responsive sensors that can selectively detect copper ions in addition to differentiating fluoride and cyanide ions within same measurement method. To work on this site, a cost efficient dual responsive chemosensor, based on 1,8-naphthalimide and hydroxylpyrones ring system with a hydrazone linker, has been synthesized in ethanol under ambient temperature conditions. Apparently, due to paramagnetic behavior, Cu^{2+} ions N,O-chelation with **4**, resulted in diminished ICT process and complete quenching of emission intensity. Besides, anions induced deprotonation elicit the internal charge transfer (ICT) and PET processes. In the present report, NMR titration experiments delineated the deprotonation based recognition mechanism. Sensor **4** loaded paper strip experimentation revealed the practical applicability *via* portable sensor kit for on-site detection of multi-analytes in aqueous medium. Additionally, it has been demonstrated that both deionized water and methanol assisted in selective discrimination of F^- and CN^- ions with **4**, in THF. Indeed, the fluorescent N,O-chelation successfully demonstrated that an efficient sensing probe has been synthesized under a green solvent like ethanol that can effectively detect multiple analytes generating instantaneous optical responses.

2. Experimental

2.1. Materials and instrumentations

4-Bromo-1,8-naphthalic anhydride, *n*-butylamine, 2-methoxyethanol, 3-acetyl-4-hydroxy-6-methyl-pyran-2-one hydrazine hydrate (80%), DMSO-d_6 and chloroform-d_1 were incurred from Sigma Aldrich. Tetrabutylammonium salts of different anions and metal perchlorates were bought from TCI chemicals and dried prior to use. Ethanol and THF employed for the synthesis or analysis were used as supplied without further purification. Water utilized in the analysis processes was obtained from Millipore system and deionized prior to use. Commercially available toothpaste (Colgate) and mineral water (Nestle) were purchased and analyzed for ions. All the metal ions and anions were incurred by the dissolution of their respective TBA salts in deionized water. Melting point was measured with the open capillary tube method using a GALLENKAMP variable heater melting point apparatus. ESI-Mass (negative mode) was calculated employing a microTOF-Q III instrument. UV–vis spectra were measured using a slit width of 1.0 nm and matched quartz cells on a Shimadzu UV-2600 UV–vis spectrophotometer. Fluorescence spectra and quantum yield (filter glass 2.5, dark offset) were recorded with a HORIBA Fluoro Max Plus Spectrofluorometer. ^1H and $^{13}C\{^1H\}$ NMR spectra were incurred on a Bruker 500 MHz spectrometry using TMS as an internal reference. NMR chemical shifts were reported in ppm and referenced to residual protonated solvent. Tetrabutylammonium salts and metal perchlorates were used for anion and cation studies, respectively.

2.2. Preparations

2.2.1. Synthesis of 6-bromo-2-butyl-benzoisoquinoline-1,3-dione (**2**)

4-Bromo-1,8-naphthalic anhydride (0.277 g, 1 mmol) was dissolved in ethanol (20 mL). Later, *n*-butylamine (0.073 g, 1 mmol) was dropwise added to the ethanolic solution. The reaction mixture was refluxed with gentle stirring for 12 h, in an oil bath. The resulting mixture was allowed to cool to room temperature and concentrated under vacuum. The crude product was filtered down and washed 3–4 times by ethanol. Recrystallization of **2** in ethanol obtained a white crystalline solid. m.p. 103–104 °C. yield: 0.295 g (89%). ^1H NMR (400 MHz, $CDCl_3$, 25 °C, TMS) δ (ppm): 8.63–8.61 (dd, 1H, ArH), 8.55–8.52 (dd, 1H, ArH), 8.39–8.37 (d, 1H, ArH), 8.02–8.00 (d, 1H, ArH), 7.83–7.79 (t, 1H, ArH), 4.16–4.12 (t, 2H, CH_2), 1.72–1.64 (m, 2H, CH_2), 1.46–1.36 (m, 2H, CH_2), 0.96–0.92 (t, 3H, CH_3) as shown in Fig. S1. $^{13}C\{^1H\}$ NMR (400 MHz, $CDCl_3$, 25 °C, TMS) δ (ppm): 163.68 (C12), 163.66 (C1), 133.25 (C9/C3), 132.08 (C5), 131.27 (C8), 130.66 (C7), 130.26 (C4), 129.03 (C6), 128.17 (C2), 123.24 (C10), 122.38 (C11), 40.54 (C13), 30.32 (C14), 20.54 (C15), 14.01 (C16) as depicted in Fig. S2.

2.2.2. Synthesis of 2-butyl-6-hydrazinyl-benzoisoquinoline-1,3-dione (**3**)

Compound **2** (0.332 g, 1 mmol) was dissolved in 25 mL of ethanol followed by the addition of 80% hydrazine hydrate (0.3 mL, 3.3 mmol). The resulting solution was refluxed with stirring for 3 h in an oil bath. Finally, the precipitated orange colored crude product was collected under vacuum suction and washed with ethanol. Recrystallization of **3** was carried out in acetonitrile to obtain an orange crystalline solid. m.p. 220–223 °C. yield: 0.241 g (85%). ^1H NMR (400 MHz, $CDCl_3$, 25 °C, TMS) δ (ppm): 9.10 (s, 1H, NH), 8.59–8.57 (d, 1H, ArH), 8.40–8.38 (d, 1H, ArH), 8.27–8.25 (d, 1H, ArH), 7.63–7.59 (t, 1H, ArH), 7.23–7.21 (d, 1H, ArH), 4.65 (s, 2H, NH_2), 4.01–3.97 (t, 2H, CH_2), 1.60–1.53 (m, 2H, CH_2), 1.36–1.27 (m, 2H, CH_2), 0.92–0.88 (t, 3H, CH_3) as shown in Fig. S3. $^{13}C\{^1H\}$ NMR (400 MHz, $CDCl_3$, 25 °C, TMS) δ (ppm): 163.79 (C12), 162.94 (C1), 153.19 (C7), 134.22 (C9), 130.58 (C3), 129.30 (C5), 128.23 (C4), 124.13 (C2), 121.75 (C11), 118.45 (C6), 107.40 (C10), 104.01 (C8), 38.93 (C13), 29.86 (C14), 19.87 (C15), 13.77 (C16) as depicted in Fig. S4.

2.2.3. Synthesis of 2-butyl-6-(2-(1-(4-hydroxy-6-methyl-2-oxo-pyran-3-yl)-ethylidene)-hydrazinyl)-benzoisoquinoline-1,3-dione (**4**)

Compound **3** (0.283 g, 1 mmol) and 3-acetyl-4-hydroxy-6-methyl-pyran-2-one (0.168 g, 1 mmol) were added in ethanol (25 mL). The mixture was refluxed with continuous stirring at 100 °C. After refluxing for 12 h, the reaction mixture was left to cool at room temperature and concentrated under vacuum. The crude product was further purified by recrystallization with acetonitrile-hexane mixture (95:5) to give a novel compound **4** (0.345 g) as yellow crystalline solid. m.p. 253–254 °C. yield: 0.345 g (80%). ^1H NMR (400 MHz, $CDCl_3$, 25 °C, TMS) δ (ppm): 15.52 (s, 1H, OH), 8.62–8.60 (d, 1H, ArH), 8.50–8.48 (d, 1H, ArH), 8.19–8.17 (d, 1H, ArH), 7.99 (s, 1H, NH), 7.74–7.70 (t, 1H, ArH), 7.13–7.11 (d, 1H, ArH), 5.89 (s, 1H, ArH), 4.15–4.11 (t, 2H, CH_2), 2.77 (s, 3H, $-CH_3$), 2.20 (s, 3H, $-CH_3$), 1.72–1.64 (m, 2H, CH_2), 1.46–1.36 (m, 2H, CH_2), 0.96–0.92 (t, 3H, $-CH_3$) as shown in Fig. S5. $^{13}C\{^1H\}$ NMR (400 MHz, $CDCl_3$, 25 °C, TMS) δ (ppm): 178.62 (C17), 166.38 (C15), 164.39 (C14), 163.89 (C1/C12), 163.04 (C18), 144.78 (C7), 133.57 (C9), 131.68 (C3), 129.55 (C5), 126.40 (C4), 125.53 (C2), 123.74 (C11), 119.91 (C6), 115.59 (C10), 107.35 (C8), 104.30 (C16), 97.09 (C13), 40.42 (C19), 30.44 (C20), 20.61 (C23), 20.27 (C21), 15.99 (C22), 14.06 (C24) as depicted in Fig. S6. HRMS (ESI): $[M - H]^-$ calcd for $[C_{24}H_{22}N_3O_5]^-$, *m/z* 432.1559; found *m/z* 432.1583 (Fig. S7).

2.3. General spectroscopic procedures

2.3.1. UV–vis and fluorometric measurements of **4** with Cu^{2+}

Stock solution of **4** (2×10^{-5} M) in THF (10 mL) & perchlorate salts of metal ions (4×10^{-4} M) in deionized water (5 mL) were prepared. UV–vis spectrometric study involved sequential addition of 20–300 μL of Cu^{2+} ions into the solution of **4** (2 mL) in a cuvette. On the other side, fluorometric study involved the gradual addition of 20–500 μL of Cu^{2+} ions into the solution of **4** (2 mL) in a cuvette. The obtained solutions were stirred for 1 min and UV–vis/fluorometric spectra were collected at room temperature by adjusting slit width parameters to 2/2 nm and 5/5 nm, respectively.

2.3.2. Job plot measurements

Stock solutions of sensor **4** (10^{-4} M) in THF (10 mL) & $Cu(ClO_4)_2$ (10^{-4} M) in deionized H_2O (10 mL) were prepared. A solution of sensor **4** in varying amounts i.e. 0.5, 0.45, 0.40, 0.35, 0.30, 0.25, 0.20, 0.15, 0.10, 0.05 and 0 mL were transferred to individual volumetric flasks (5 mL). Later, Cu^{2+} solution, 0, 0.05, 0.10, 0.15, 0.20, 0.25, 0.30, 0.35, 0.40, 0.45 and 0.5 mL, was added to a solution of sensor **4** separately. Finally, each flask was made up to 5 mL with THF. Then, individual flask solution was immixed for 1 min and transferred to fluorescence cuvette (2 mL). All the fluorescence spectra were recorded at room temperature.

2.3.3. UV–vis and fluorometric measurements of **4** with F^-/CN^-

Stock solution of **4** (2×10^{-5} M) in THF (10 mL) & TBA salts of anions (4×10^{-4} M) in deionized water (5 mL) were prepared. UV–vis spectrometric study involves sequential addition of 5–120 μL of F^-/20–400 μL of CN^- ions into the solution of **4** (2 mL) in a cuvette. On the other side, fluorometric study involve the gradual addition of 5–150 μL of F^-/10–400 μL of CN^- ions into the solution of **4** (2 mL) in a cuvette. The incurred solutions were stirred for 1 min, prior to recording UV–vis/fluorometric spectra at room temperature, using slit width of 2/2 nm and 5/5 nm respectively.

2.3.4. Job plot measurements

Stock solutions of sensor **4** (10^{-4} M) in THF (10 mL) & TBA-X (X-F^- and CN^-) salts (10^{-4} M) in deionized H_2O (10 mL) were prepared. Different volumes of sensor **4** i.e. 0.5, 0.45, 0.40, 0.35, 0.30, 0.25, 0.20, 0.15, 0.10, 0.05 and 0 mL were measured and transferred to volumetric flasks of 5 mL capacity. Additionally, 0, 0.05, 0.10, 0.15, 0.20, 0.25, 0.30, 0.35, 0.40, 0.45 and 0.5 mL of the F^-/CN^- solution were added to above solution separately. Finally, every flask was filled up to 5 mL mark with THF. Then, individual solutions were mixed thoroughly for 1 min and later pipette out (2 mL) to fluorescence cuvette. Fluorescence spectra were obtained at room temperature.

2.3.5. Competitive experiments

Stock solution of **4** (2×10^{-5} M) in THF (10 mL) & perchlorate salts of metal ions (4×10^{-4} M)/TBA salts of anions (4×10^{-4} M) in deionized water (5 mL) were prepared. Fluorometric competitive study involved initial addition of 100 μL of relevant anions/200 μL of metal ions to the solution of **4** (2 mL) in a cuvette, followed by the addition of 100 μL of F^- or CN^-/200 μL of Cu^{2+} ions, respectively. After stirring the solutions for 1 min, emission spectra were recorded employing a slit width of 5/5 nm.

3. Result and discussions

3.1. Synthesis methodology of **4**

Initially, two reactive precursor compounds i.e. 6-bromo-2-butyl-benzoisoquinoline-1,3-dione (**2**) and 2-butyl-6-hydrazinyl-benzoisoquinoline-1,3-dione (**3**), have been consecutively synthesized employing ethanol as reaction medium [42–45]. Later condensation reaction between compound **3** and 3-acetyl-4-hydroxy-6-methyl-pyran-2-one in 1:1 ratio in ethanol for 12 h results in the formation of deep yellow solution of novel hydrazone Schiff's base product (80% yield) i.e. 2-butyl-6-(2-(1-(4-hydroxy-6-methyl-2-oxo-pyran-3-yl)ethylidene)hydrazinyl)-benzoisoquinoline-1,3-dione (**4**), as shown in Scheme 1. Ambient temperature conditions were used to conclude the condensation reaction. Further isolation of the pure compounds were achieved through recrystallization in pure ethanol rather than tedious column chromatography. The detailed experimental procedures and the characterizations of **4** are described in above.

3.2. Colorimetric responses of **4** with Cu^{2+}

The changes observed in the absorption spectral pattern of **4** with the addition of different metal ions in THF/H_2O are shown in Fig. 1. It is inferred from the absorbance plots that with the addition of 2 equiv. of different metal ions (except for Cu^{2+}), the absorption band at 412 nm undergoes slightly red shift (8 nm), with a minor change in the absorption intensity. Contrary to this, with the addition of Cu^{2+} (2 equiv.) to the solution of **4**, the ICT absorption band at 412 nm was completely vanished and solution color changed from yellow to colorless (Fig. 1 Inset). This in turn pointed out that chelation of Cu^{2+} ions with **4** ensued in reduced electron density, leading to diminished ICT process [46]. Hence, sensor **4** showed high selectivity towards Cu^{2+} ions over other common metal ions.

To obtain further insight into the binding characteristics of Cu^{2+} with **4**, spectrophotometric titration experiments were conducted with Cu^{2+} ions in aqueous-organic solution. Upon sequential

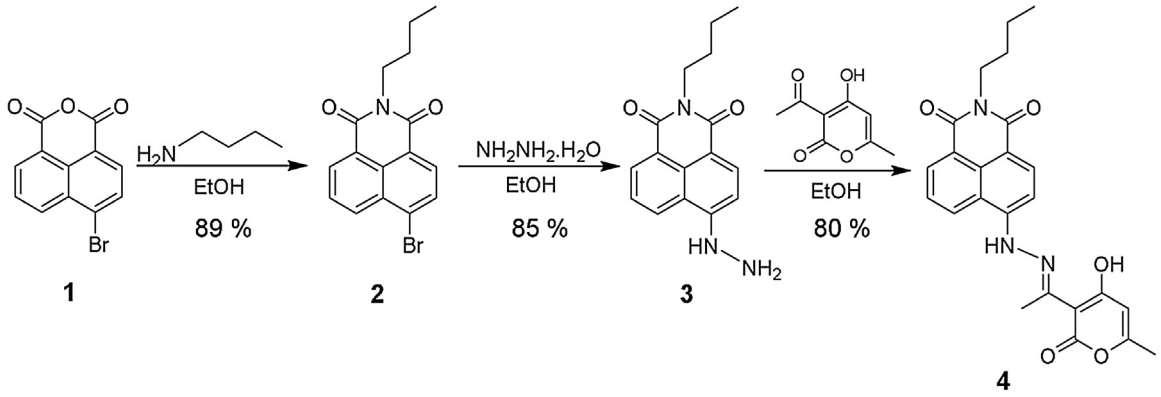

Scheme 1. Synthetic approach to prepare the hydrazone Schiff base of chemosensor **4** derived from 1,8-naphthalimide and dehydroacetic acid.

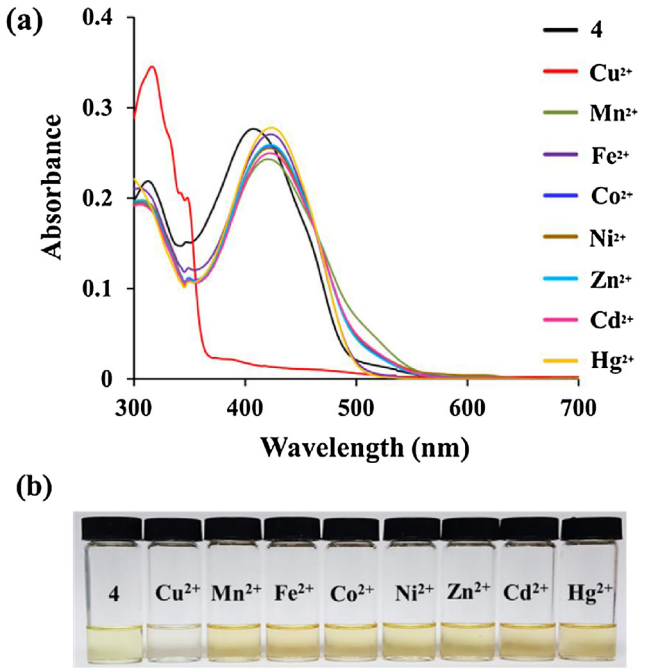

Fig. 1. Absorbance spectra (a) of **4** (2×10^{-5} M) with the comportment of 2 equiv. of different metal ions in THF/H_2O; (b) Inset: changes in the color observed (bottom) with the addition of different metal ions (2 equiv.) to the solution of **4** (2×10^{-5} M) solution in ambient light.

accession of Cu^{2+} to a solution of **4**, the ICT absorption band at 412 nm undergoes a slight bathochromic shift (3 nm) with a simultaneous uninterrupted decrease in the absorbance intensity, that halts at 3 equiv. of Cu^{2+} ions (Fig. 2). A clear isosbestic point was indicated at 355 nm ascertaining the existence of equilibrium between the two species i.e. **4** and **4** + Cu^{2+}, during the titration experiment. As a result, yellow solution of **4** slowly changed to colorless solution (Fig. 2 Inset).

3.3. Colorimetric responses of 4 with F^- and CN^-

To investigate the colorimetric response patterns of **4** (2×10^{-5} M in THF) with anions, the UV–vis absorbance experiments were conducted with tetrabutylammonium salts (TBA–X: X = F^-, Cl^-, Br^-, I^-, CN^-, SCN^-, AcO^-, ClO_4^-, HSO_4^-, $H_2PO_4^-$, NO_2^-, CO_3^{2-}) of various anions, (Fig. 3). Visual inspection of **4** solution, before and after the addition of anions displayed noticeable color changes only with F^- and CN^- ions, which confirmed existence of strong interaction exist between **4** and F^-/CN^- ions. Additionally, comportment of the OH group in vicinity of hydrazone group offered additional interaction site for F^- and CN^- ions. On the other hand, the addition of other anions to the solution of **4** did not bring on any appreciable color changes. Also, absorption spectrum of **4** showed absorbance maxima at 412 nm due to intra-molecular charge transfer phenomenon (ICT) i.e. $n \rightarrow \pi^*$ transitions [15]. Addition of 1 equiv. of various anions (except for F^- and CN^- ions), the absorption spectra of **4** did not display any substantial change with minor fluctuation in absorbance intensity at 412 nm. However, with F^- ions (1 equiv.), the ICT absorption band at 412 nm (1.6×10^4 L mol^{-1} cm^{-1}) underwent a drastic decrease and ultimately split up into two adjacent bands positioned at 408 nm and 428 nm. Simultaneously, two new absorption maxima at 580 and 620 nm, with prominent bathochromic shift (172 nm and 192 nm respectively), were observed as depicted in Fig. 3. This leads to visible naked eye color change of solution **4** from yellow to blue in ambient light; Fig. 3 Inset. Similarly, addition of CN^- ions (1 equiv.) to the solution **4**, ensued in two new bands at 581 nm and 622 nm with diminished 412 nm band. Herein, the solution color shows perceptible changes from yellow to violet. These remarked changes in the absorption spectra with F^-/CN^- ions were due to the deprotonation and subsequent ameliorated electron donor propensity of N-/O- moiety, within the receptor molecule, resulting in heightened ICT process [46,47]. Thus, **4** emerged as a relevant probe for naked-eye recognition of F^- and CN^- ions, with noticeably chromogenic changes, in aqueous-organic medium.

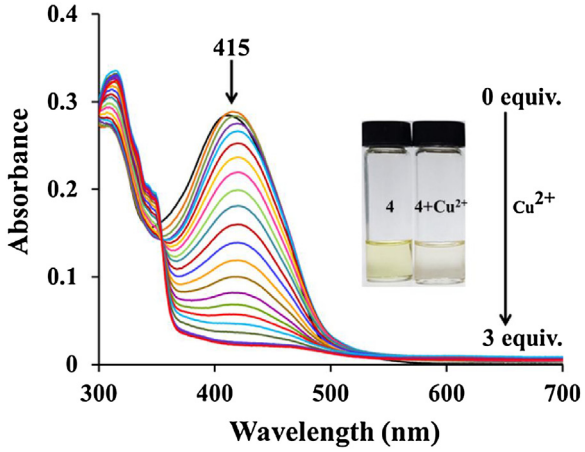

Fig. 2. Absorbance titration spectra of **4** (2×10^{-5} M) with various concentrations of Cu^{2+} (0–3 equiv.) in THF/H_2O; Inset: the color of **4** (left) and **4** + Cu^{2+} (right) upon the addition of 3 equiv. of Cu^{2+}.

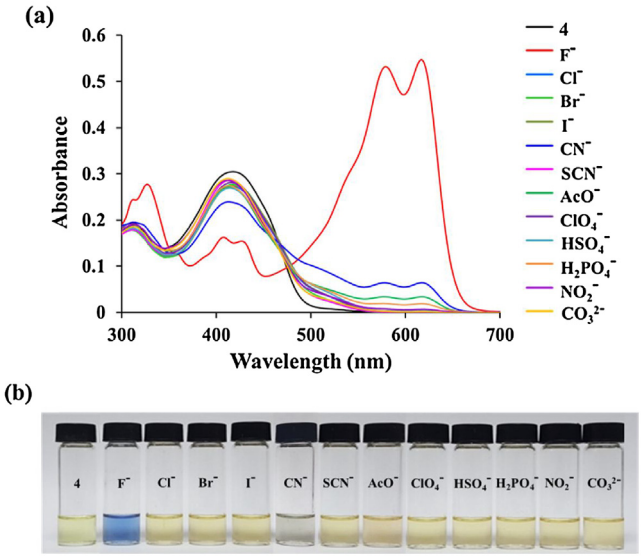

Fig. 3. Absorbance spectra (a) of **4** (2×10^{-5} M) with the addition of 1 equiv. of different anions in THF/H_2O; (b) Inset: color change noticed (bottom) in sensor **4** (2×10^{-5} M) solution with anions (1 equiv.).

UV-vis titration experiments were carried out to determine the sensitivities of **4** toward F^- and CN^- ions. As shown in Fig. S8(a), following spectroscopic changes observed when a solution of **4** in THF were treated with increasing quantities of TBAF solution in deionized water. Upon sequential addition of TBAF to **4**, the band at 412 nm progressively decreased, whereas two new bands with peak positions at 580 nm and 620 nm displayed a gradual increase and attained its maximum absorbance intensity at 1.2 equiv. of F^- ions. The yellow solution of **4** slowly changed to blue color solution, Fig. S8(a) Inset. An isosbestic point at 480 nm further ensured that equilibrium exists between **4** and **4** + F^- species, during the course

of the titration. As demonstrated in Fig. S8(b), addition of TBACN to **4,** also displayed a similar pattern as that of F^- with a decrease in band at 412 nm and simultaneously increases in two new bands positioned at 581 nm and 622 nm. Herein, an isosbestic point was observed at 482 nm affirming existence of equilibrium between **4** and **4** + CN^- species. The solution color slowly changes from yellow to violet with the incremental addition of 0–3.5 equiv. of CN^-, Fig. S8(b) Inset. Therefore, it was reasoned out that F^- or CN^- ions, induced deprotonation of O—H and N—H moieties, resulting in the prolonged conjugation in **4**. Due to meliorated electronic delocalization, the energy required for *p–p* transitions scale down, ensuing two new absorption bands at around 580 nm and 620 nm.

3.4. Fluorometric responses of **4** with Cu^{2+}

The emission intensity changes observed in the spectra of **4** induced by cations, such as Cu^{2+}, Mn^{2+}, Fe^{2+}, Co^{2+}, Ni^{2+}, Zn^{2+}, Cd^{2+}, Hg^{2+} are shown in Fig. 4. Addition of Cu^{2+} ions to the solution of **4** ensued a sudden sharp decrease in the emission intensity at 520 nm compared to other competitive metal ions. The fluorescence color changed from bright green to dull blue with Cu^{2+} ions only (Fig. 4 Inset). It was interpreted that complete quenching of emission intensity was observed as a consequence of paramagnetic behavior of Cu^{2+} ions [46].

To work out the detection range and correlation between fluorescence responses of sensor **4** at 520 nm and Cu^{2+} ion concentration, fluorescence titration experiments were performed. It was remarked that incremental addition of Cu^{2+} (0–5 equiv.) to a solution of **4**, results in consistent decreases in emission intensity at 520 nm with a slightly bathochromic shift (10 nm), as depicted in Fig. 5. The solution color changed from yellow to colorless in Cu^{2+}, with the fluorescence color change from bright green to dull blue (Fig. 5 Inset). Further, detection limits were calculated based on fluorometric titration results observed at

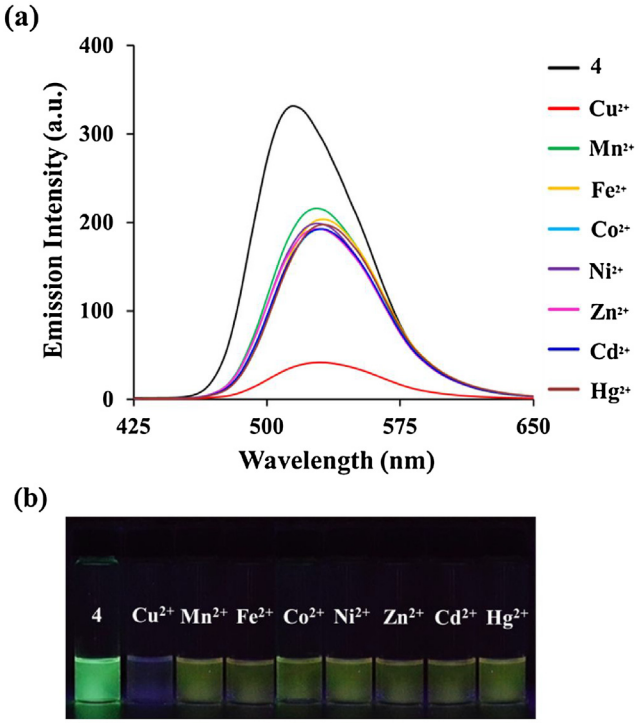

Fig. 4. Emission spectral pattern (a) of **4** (2×10^{-5} M) obtained with the addition of 2 equiv. of different metal ions in THF/H_2O; (b) Inset: color change observed (bottom) upon the addition of different metal ions (2 equiv.) to the sensor **4** (2×10^{-5} M) solution, under the UV-lamp (365 nm).

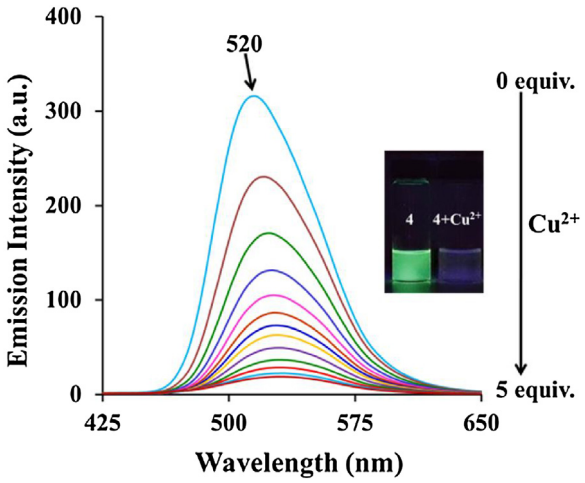

Fig. 5. Emission titration spectrum of **4** (2×10^{-5} M) in the presence of incremental concentrations of Cu^{2+} ions (0–5 equiv.) in THF/H_2O; Inset: the color of **4** (left) and **4** + Cu^{2+} (right) with 5 equiv. of Cu^{2+} ions.

maximum wavelength, employing formulation $3\sigma/C$; where, σ corresponds to the standard deviation of the blank and C is the slope of each titration curve and found to be 0.962 ppm.

Further, competitive experiments were carried out to establish the selectivity of **4** toward Cu^{2+} ions. As shown in Fig. 6, sensor **4** was treated 2 equiv. of Cu^{2+} in the presence of other metal ions (Mn^{2+}, Fe^{2+}, Co^{2+}, Ni^{2+}, Zn^{2+}, Cd^{2+}, Hg^{2+}) of the same concentration. The fluorescence quenching pattern obtained evidently ensued that other common competing metal ions have relatively negligible interference.

Job's plot was delineated based on the fluorescence intensity of **4** at 530 nm, against the molar fraction of **4,** maintaining the constant total concentration, to obtain the binding ratio between **4** and Cu^{2+}. The maxima was attained when the molar fraction of (**4**)/[(**4**) + (Cu^{2+})], was 0.67, indicating that the stoichiometric ratio of **4** with Cu^{2+} to be 2:1 Fig. S9(a). As interaction of **4** with Cu^{2+} ions, resulted in drastic change in the emission intensity therefore emission titration experiments were employed to calculate the association constant and quenching constant. Association constant were calculated according to the Benesi–Hildebrand equation as follows:

$$1/(I - I_o) = 1/\{K(I_{max} - I_o)[\text{Ion}]^n\} + 1/[I_{max} - I_o]$$

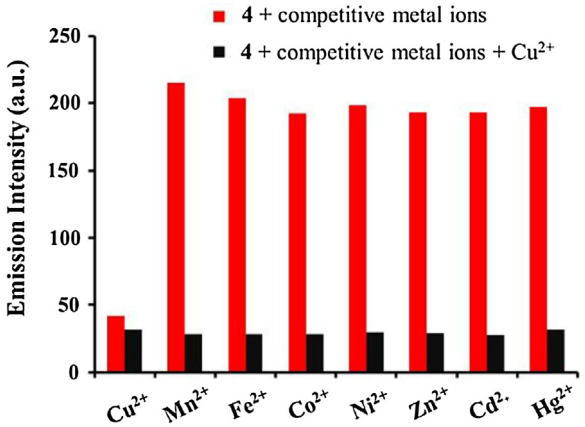

Fig. 6. Relative emission intensity bar graph showing competitive selectivity of **4** (2×10^{-5} M) toward Cu^{2+} (2 equiv.) in the presence of other competing metal ions (2 equiv.) in THF/H_2O.

I_0 relates to the fluorescence of **4** without any ion, I is the fluorescence recorded with ion, I_{max} corresponds to the fluorescence in the presence of added $[Ion]_{max}$ and K is the association constant. which was calculated from the slope of the straight line of the B-H plot of $1/(I - I_0)$ against $1/[Ion]^n$. The association constant value of **4** with Cu^{2+} was determined from the emission intensity plots measured at 530 nm. The association constant (K_a) of **4** with Cu^{2+} were calculated to be 1.26×10^5 L mol^{-1}, Fig. S10(a). Moreover, to elucidate the quenching phenomenon in **4** with Cu^{2+} ions, the Stern-Volmer (S-V) plot, a graph was plotted between intensity ratio, I_o/I and concentration of Cu^{2+} ions as shown in Fig. S11(a). The slope of the obtained straight line (R^2 0.9765 for Cu^{2+}) rendered the quenching constant, $K_{S\text{-}V}$ 2.04×10^5 mol L^{-1} for Cu^{2+}. This deciphered that quenching of emission intensity in the interactive ground state **4** + Cu^{2+}, was the entirely active process [47,48]. Additionally, noticeable decrease in the quantum yield value of **4** from 4.24 to 1.54; in Fig. S12(a) was obtained. Thus, detectable fluorescence quenching was observed only with Cu^{2+} ions compared to all other metal ions.

3.5. Fluorometric responses of 4 with F^- and CN^-

Next, to further examine the dual-mode recognition behavior of **4** toward anions, the fluorometric experiments were performed at an excitation wavelength of 412 nm, under ambient conditions. Initially, the fluorescence spectra were recorded in the presence of various anions (F^-, Cl^- Br^-, I^-, CN^-, SCN^-, AcO^-, ClO_4^-, HSO_4^-, $H_2PO_4^-$, NO_2^-, CO_3^{2-}) as shown in Fig. 7 and the results show that the fluorescence of **4** was quenched significantly only with F^- and CN^- ions, with a minor bathochromic shift (5 nm). Anion induced deprotonation of N—H and O—H groups at the receptor site, facilitate lone pair of nitrogen/oxygen for heightened PET process [46], leading to quenching of emission intensity.

Fluorometric titration experiments were also conducted to investigate parameters such as detection limit and the results obtained are shown in Fig. S13(a). A consistent decline with a slightly bathochromic shift (5 nm) in the emission intensity at 515 nm was observed for **4**, when the F^- concentration increased from 0–1.5 equiv. The solution color changed from bright yellow to deep blue in F^- with the fluorescence color change from bright green to dark, Fig. S13(a) Inset. The detection limit was found to be 0.023 ppm. These results were further ascertained through decreased quantum yield value from 4.24 to 1.41 with F^- (1 equiv.) as shown in Fig. S12(b). Further, **4** solution was titrated with CN^- ions and it was observed that the sequential addition of 0–3.5 equiv. of CN^- ions, resulted in consistent decrement in the emission intensity at 519 nm with a slightly red shift of 8 nm, with fluorescence color changes from bright green to dull green, Fig. S13 (b) & Inset. The detection limit was calculated to be 0.073 ppm. Quantum yield value of **4** dropped down to 1.59 with CN^- (1 equiv.); Fig. S12(c).

In order to ascertain the selectivity of **4** toward recognition of F^-/CN^- ions, competitive experiments with 1 equiv. of F^- and 1 equiv. of other common competitive anions (Cl^-, Br^-, I^-, SCN^-, AcO^-, ClO_4^-, HSO_4^-, $H_2PO_4^-$, NO_2^-, CO_3^{2-}) were performed. It was observed that the fluorescence intensity of **4** with F^- was not significantly interfered even in the presence of competing anions Fig. 8(a). The fluorescence quenching observed with F^- was not affected with all of the competing anions together. Similar fluorescence experiments were carried out to confirm the selective nature of **4** toward CN^- ions in the presence of other anions. Addition of 1 equiv. of CN^- to a solution of **4**, in the presence of relevant anions (1 equiv.), still quenched the fluorescence affirming that competitive anions have negligible interference in the recognition of CN^- ions; Fig. 8(b). These results revealed the high selectivity of **4** for the recognition of F^-/CN^- ions.

Continuous variation methodology was followed to determine the fluorogenic quantitative sensing ability of **4** toward F^-/CN^- ions. As deduced from the Job's plot of **4** with F^- and CN^- anions, the maxima was achieved when the molar fractions of (**4**)/

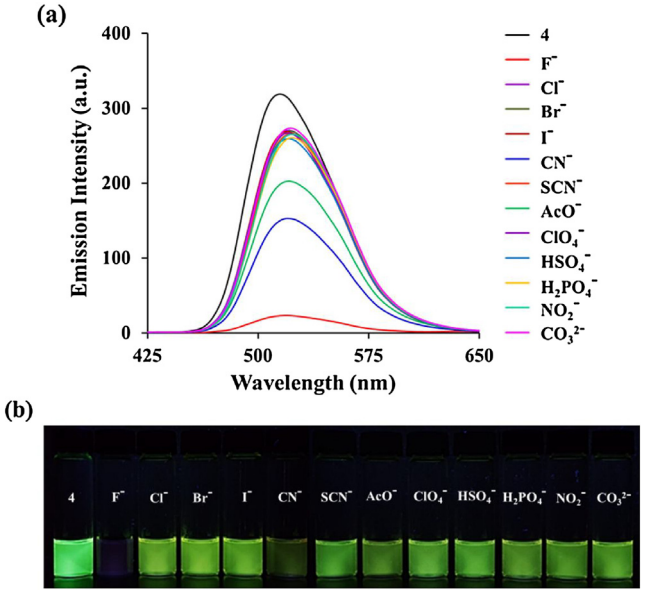

Fig. 7. Emission spectra (a) of **4** (2×10^{-5} M) with the addition of 1 equiv. of various anions in THF/H_2O solution; (b) Inset: color change observed (bottom) upon the addition of various anions (1 equiv.) to the sensor **4** (2×10^{-5} M) solution, under UV-lamp (365 nm).

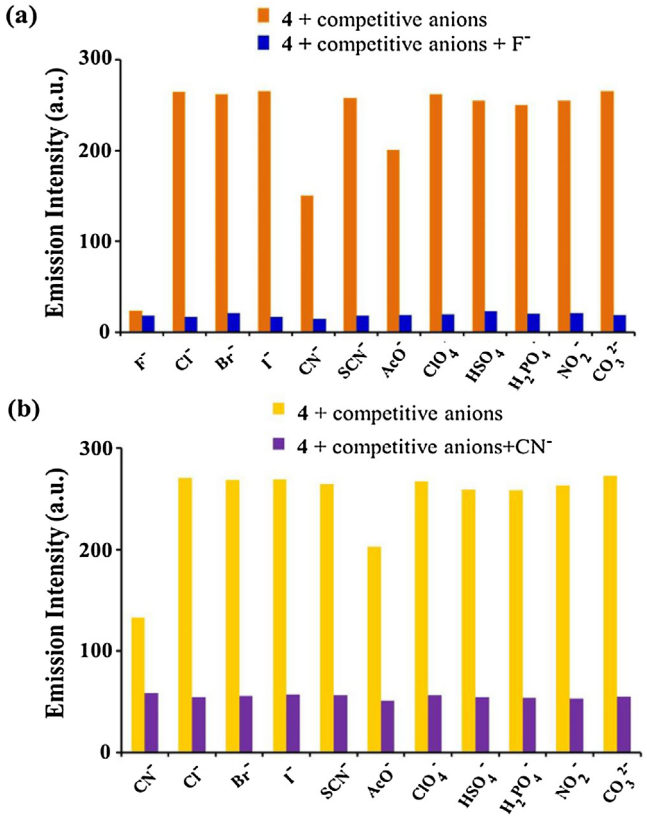

Fig. 8. Relative emission intensity bar graphs showing competitive selectivity of **4** (2×10^{-5} M) toward (a) F^- (1 equiv.) and (b) CN^- (1 equiv.) in the presence of competing anions (1 equiv.).

[(**4**) + (F^-)] and (**4**)/[(**4**) + (CN^-)], were 0.69 and 0.5 respectively, indicating that the ratios of **4** with F^- (2:1) and CN^- (1:1) were achieved in Fig. S9(b) and (c). The association constant (K_a) of **4** with F^- and CN^- was calculated to be 1.5×10^5 L mol^{-1} and 0.62×10^5 L mol^{-1}, respectively, using the Benesi–Hildebrand equation, Fig. S10(b) and (c). From the association constant values, it is interpreted that the F^- has the higher fluorescence binding affinity compared with CN^- towards **4**. The detection limit of **4** was found to be 1.2×10^{-6} M for F^- and 2.79×10^{-6} M for CN^-. An almost straight line (R^2 0.9879/0.9864 for F^-/CN^-) with quenching constants, $K_{S\text{-}V}$: 3.54×10^5 $molL^{-1}$/2.41×10^5 $molL^{-1}$ for F^-/CN^-, respectively; Fig. S11(b) and (c), further support the enhanced PET process.

3.6. Mechanism of interaction of *4* with ions

In order to elucidate the bonding interaction of Cu^{2+} ions with **4**, NMR titration experiments were performed, in DMSO-d_6 as shown in Fig. S14. Initially, sequential addition of Cu^{2+} ions (0–5 equiv.) to the **4**, resulted into complete disappearance of O—H (δ 15.51 ppm) proton signal. Additionally, aliphatic protons in vicinity of hydrazone group and other aromatic ring protons undergoing upfield shift, a redistribution of electric charge on the naphthalimide rings was encountered upon interaction with Cu^{2+} ion [49,50]. These observations clearly indicated that two sensor molecules encircled the Cu^{2+} ions copper ions in a square planar geometry, with N/O atoms of hydrazone/hydroxy groups, respectively, as interacting sites [46,51,52] Interpretation of the experiment data affirmed the proposed mechanism and related 2:1 stoichiometry.

Further to gain insight into the sensing mode of **4** toward F^-/CN^- ions, NMR titration experiments were performed in $CDCl_3$ and changes observed in the ^{1}H NMR spectra were depicted in Fig. 9. Initially, F^- ions (0–1 equiv.) were gradually added to **4** and corresponding spectra were analyzed. It was noticed that with the addition of 0.2 equiv. of F^- to **4**, the resonance signal related to O—H and N—H proton at δ 15.51 ppm/7.99 ppm vanished completely; Fig. 9(a). Thus, it was concluded that F^- ions interacted with **4** through deprotonation of N—H and O—H moieties [50,52,53]. Beside this, other aromatic ring protons also displayed prominent up-field chemical shifts. These chemical shifts were encountered as a consequence of deprotonation, which resulted in increased electron density leading to enhanced ICT process within the receptor molecule [54,55]. Later, with the addition of 1 equiv. of F^- ions, a very weak signal appeared at 16.51 ppm, which affirmed the existence of $[FHF]^-$ dimer species [56]. This dimer formation further supports that deprotonation took place upon interaction of **4** with F^- ions. These results confirmed that F^- ions interact with hydrazone as well as hydroxyl group protons, as shown in Fig. 9(a) Inset.

Moreover, similar interaction mechanism between **4** and CN^- ions was concluded from the NMR titration experiment. Different equivalents (0–1 equiv.) of TBACN were sequentially added to the solution of **4** in $CDCl_3$ and the observed ^{1}H NMR spectra were shown in Fig. 9(b). When 0.2 equiv. CN^- was added, the signal existing for the proton of O—H and N—H groups at 15.51 ppm/7.99 ppm disappeared immediately, which evidently showed that deprotonation occur instantaneously [54,55]. The other aromatic protons resonance signals undergoes a gradual upfield shift due to the shielding effect. Based on the analysis and interpretation of ^{1}H NMR titration spectra, we proposed a potential mechanism for the interaction between receptor **4** and CN^- as depicted in Fig. 9(b) Inset. Thus, **4** behaves as a highly sensitive chemosensor for both F^- and CN^- ions in aqueous-organic medium.

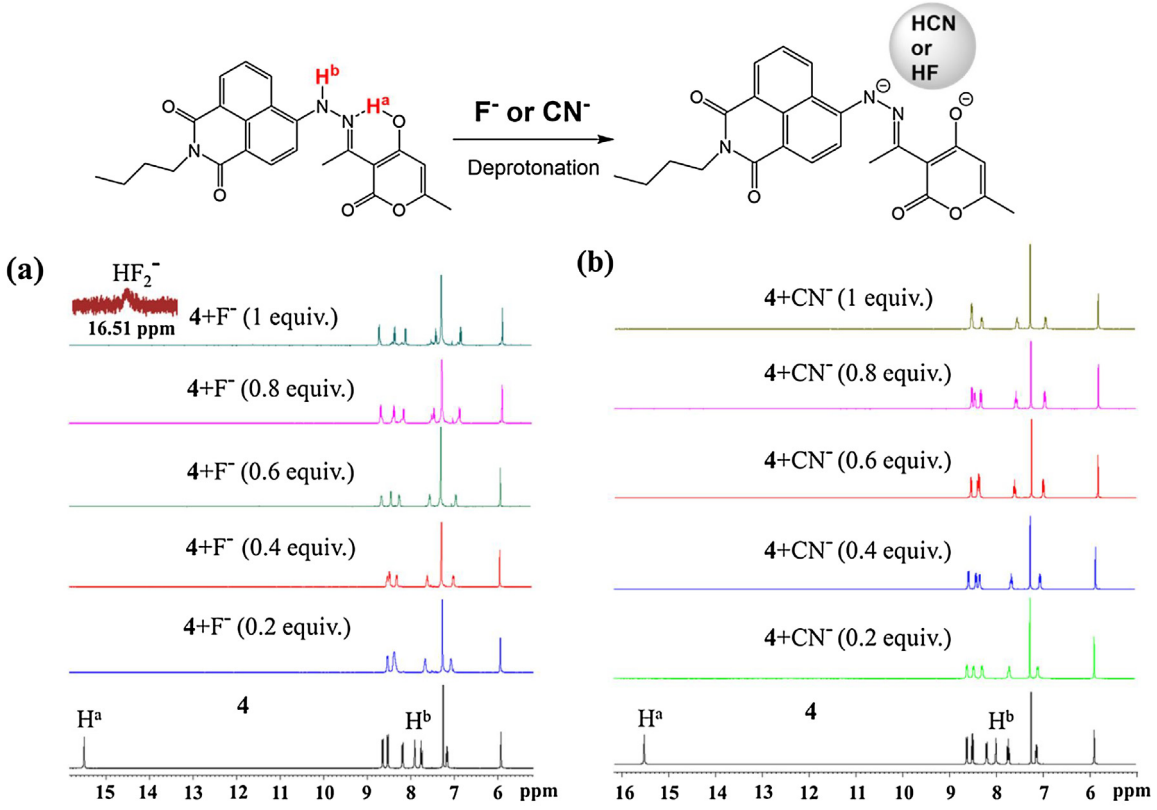

Fig. 9. ^{1}H NMR titration plot of **4** with (a) F^- (0–1 equiv.) and (b) CN^- (0–1 equiv.) in $CDCl_3$. Inset: Deprotonation phenomenon in **4**, with F^-/CN^- ions.

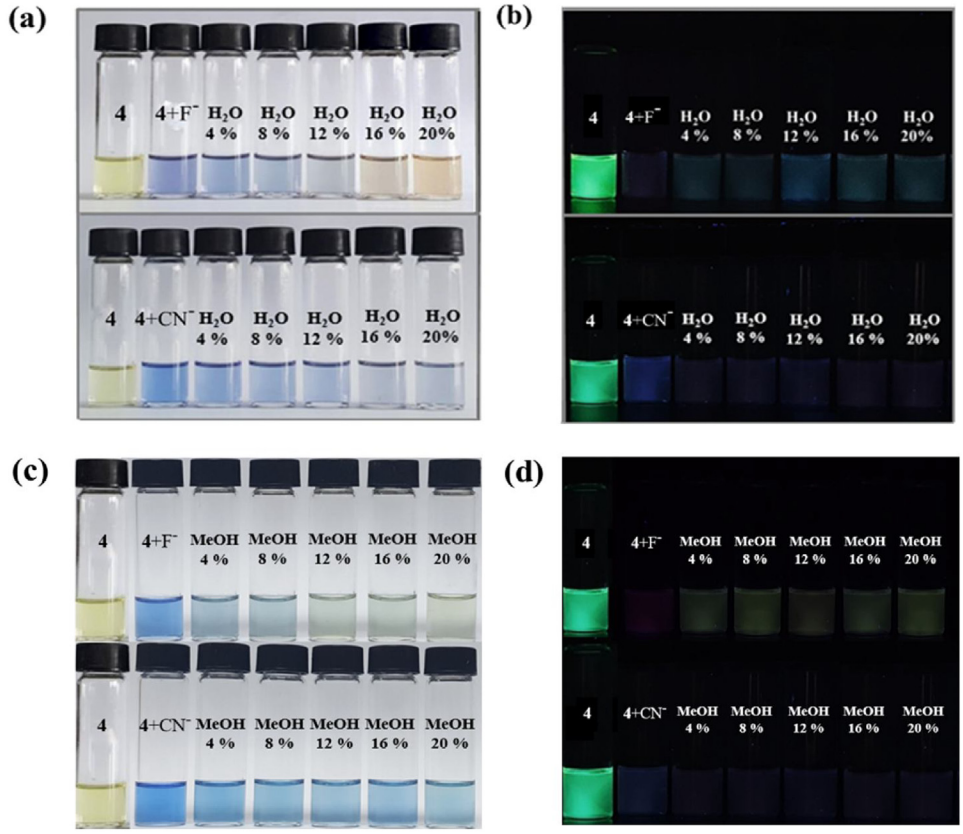

Fig. 10. Photographs of **4** (10^{-3} M) with F^- and CN^- ions (4×10^{-4} M) in THF solution, under ambient light/UV lamp with (a)/(b) H_2O (0–5 equiv.) and (c)/(d) MeOH (0–5 equiv.), respectively.

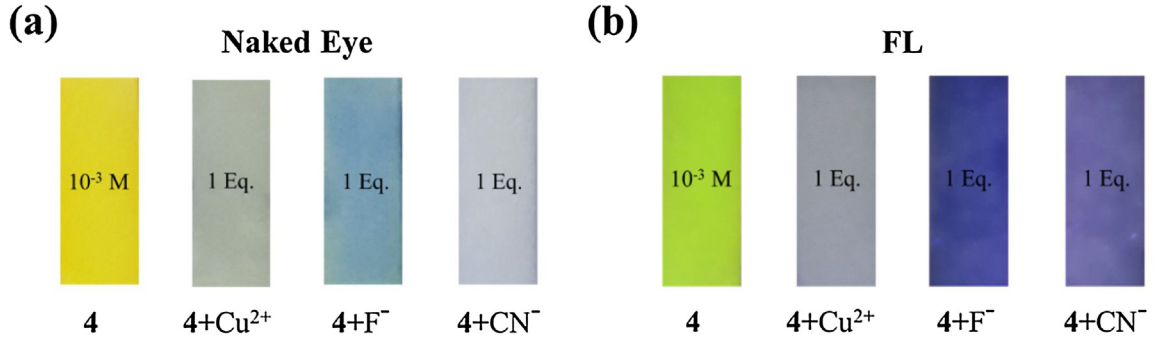

Fig. 11. Photographs of paper strips of **4** (10^{-3} M) with Cu^{2+}, F^- and CN^- ions (4×10^{-4} M) in THF/H_2O solution under (a) ambient (b) UV radiation.

3.7. Discrimination with deionized water/methanol

Both colorimetric and fluorometric spectral patterns undergo a significant change with the addition of deionized water to the **4** + F^-/**4** + CN^- THF solution. During the colorimetric experiments, successive addition of deionized water (5 equiv.) to the **4** + F^- solution, ensued in visible naked eye color change from blue to orange Fig. 10(a). As plotted in Fig. S15(a), following colorimetric changes were observed as a result of drastic decrease in the absorption intensity of bands at 580/581 nm and 620/622 nm. In contrast only, slight change in the intensity of blue color was observed in **4** + CN^- solution. However, during the fluorometric experimentation, Fig. S16(a), addition of F^- ions (1 equiv.) to **4** solution, resulted in complete quenching of the emission intensity, but gradual addition of deionized water (0–5 equiv.) to this

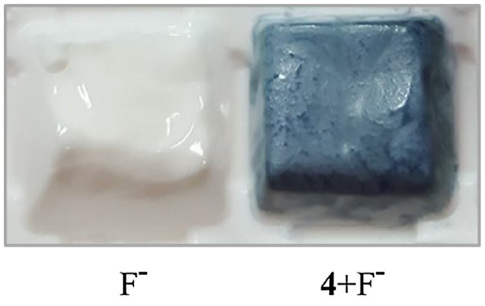

Fig. 12. Photographs of visible naked eye color of commercial toothpaste (NaF, 20 mg/kg); white and with **4** (10^{-3} M in THF); blue, under ambient light. (For interpretation of the references to colour in this figure legend, the reader is referred to the web version of this article.)

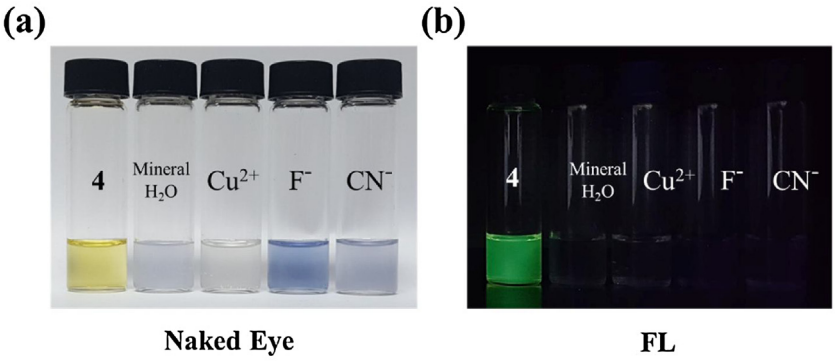

Fig. 13. Photographs of fluoridated mineral water (F^-, 0.5 mg/L) with **4** (2×10^{-5} M) in the presence of Cu^{2+}, F^- and CN^- ions (1.5, 0.07 (less than 0.08) and 2 mg/L, WHO permissible limits) under (a) ambient (b) UV radiation.

solution, again leads to the enhancement in emission intensity. On the other side, minimum emission intensity was observed with the addition of CN^- (3 equiv.) to a solution of **4**. Later, sequential addition of deionized water (0–5 equiv.) to the **4** + CN^- solution, resulted in thorough quenching of the emission intensity Fig. 10(b). Similar colorimetric and fluorometric experiments shown in Figs. S15(b) and S16(b), were performed with methanol. Addition of methanol (0–5 equiv.) to **4** + F^- solution, resulted in visible naked eye color change from blue to grey as shown in Fig. 10(c). However, no detectable color change was observed in **4** + CN^- solution. Interpretation of fluorometric results revealed that of **4** + F^- solution showed slight increase in emission intensity from completely quenched state. Contrary to this, residual fluorescence of **4** + CN^- solution undergoes complete quenching, Fig. 10(d). Since F^- ions exhibits high hydration energy and strong electronegativity [19], as a result significant solvent competitiveness exists, ensuing in reduced interaction between **4** and F^- ions. As a consequence, in the presence of deionized water/methanol, intra-molecular charge transfer (ICT) process gets diminished, contributing to visible naked eye color changes. However, PET process become more favorable leading to slight restoration of fluorescence [46]. Hence, deionized water or methanol could be used for the colorimetric as well as fluorometric discrimination of the two anions in organic medium.

4. Practical applications

4.1. Paper strips experiments

To ascertain the solid-state sensing ability of **4**, sensor loaded paper strips (Whatman filter paper no.1) were developed for the real-time analysis of Cu^{2+}, F^- and CN^- ions in aqueous medium. Initially, filter papers (3×1 cm^2) were plunged with **4** (10^{-3} M) solution for about 5 mins and then dried off completely. Later, aqueous solution of Cu^{2+} ions were added on the loaded paper strips, the color of the paper strip changed immediately from yellow to colorless under ambient light as shown in Fig. 11(a). Similarly, with F^- and CN^- ions in water solution, the color changed from yellow to dark blue/gray, respectively. Under UV lamp (λ_{ex} = 412 nm), an apparent color change of **4** from bright green to dark occurred immediately, Fig. 11(b). The observed color changes were due to the deprotonation phenomenon observed in **4** with $Cu^{2+}/F^-/CN^-$ ions. Thus, sensor **4** has demonstrated both naked eye color and fluorometric recognition efficiency for metal ion as well as anions in the solid phase. Competitive metal ions and anions have not posed any interference during the paper strip experimentation. Hence, sensor **4** loaded paper strips can be conveniently used for the recognition of $Cu^{2+}/F^-/CN^-$ ions, without any additional equipmentation.

4.2. Real samples analysis

As established earlier, sensor **4** responds selectively for fluoride ions in solid state as well. In order to validate solid state applicability in practical samples, commercially available products such as toothpaste were analyzed for fluoride ions contents. A gram of toothpaste was treated with **4** (10^{-3} M, 400 μL), sample color changes immediately from white to blue, ascertaining the presence of fluoride ions (20 ppm) as shown in Fig. 12.

Further, Cu^{2+} as well as F^-/CN^- ions were analyzed in fluoridated mineral water to corroborate competitive selectivity. Commercially available fluoridated mineral water (F^-, 0.5 mg/L) was supplemented with Cu^{2+} (2 mg/L), F^- (1.5 mg/L) and CN^- (0.07 mg/L) ions. Detectable ions solutions (1 mL) were treated separately with **4** (1 equiv. for Cu^{2+} and F^-, 15 equiv. for CN^-) in the presence of major constituent of mineral water such as Na^+, Mg^{2+} Ca^{2+} salts. Prominent visible naked eye color changes from yellow to colorless (Cu^{2+}) and blue (F^-/CN^-) was observed as shown in Fig. 13(a). Additionally, emission intensity undergoes completely quenching, depicted in Fig. 13(b). Thus, it has been successfully established that **4** displayed high competitive selectivity for ions in commercial commodities within WHO defined limits.

5. Conclusions

In ratiocination, a novel dehydroacetic acid based hydrazone Schiff's base sensor from three-step and high-yield syntheses under green approach like ethanol solvent has been prepared that exhibited high sensitivity and selectivity for Cu^{2+}, F^- and CN^- ions, within WHO accentuated detection limits. The presence of two receptor sites in a molecular sensor revealed instantaneous optical responses with ions. Sensor possessing N,O chelation with Cu^{2+} ions accounted for reduced ICT process, resulting in disappearance of absorption band at 412 nm. This brought on yellow color solution to colorless. However, with F^- and CN^- ions, two new absorption bands at 580/620 nm and 581/622 nm, imparting blue/violet color to the solution, respectively, were observed. As anions induced deprotonation resulted in enhanced ICT within the molecules. Emission intensity was substantially quenched in the presence of detectable metal ions as well as anions, due to inherent paramagnetism and enhanced PET process, respectively. Competitive experiments result further uncovered that common competing ions had negligible effect on the selective sensing of Cu^{2+}, F^- and CN^- ions, under ambient conditions. Deprotonation phenomenon of N—H and O—H moieties in the presence of ions was ascertained through ^1H NMR titration experiments. Job's plots interpretation worked out 2:1 (Cu^{2+}/F^-) and 1:1 (CN^-) stoichiometry with sensor molecule. Sensor displayed strong binding affinity for Cu^{2+}/F^- compared to CN^-, as deduced from the B–H plots.

Additionally, deionized water or methanol, effectively discriminate the F^- ions with noticeable color variation from blue to orange/grey, respectively, in THF. Moreover, slight restoration of fluorescence was also observed. Contrary to this, with CN^- ions, complete quenching of emission intensity, with no visible naked eye color change, were encountered. Paper strip experimentation further established the practical applicability for on-site detection of ions in aqueous medium. Analysis of ions in the commercial commodities further established the competitive selectivity of sensor. Thus, sensor emerged out as an economical alternative for the aqueous analysis of Cu^{2+}, F^- and CN^- ions.

Acknowledgements

The research work was supported by the Mahidol University for postdoctoral fellowship and financially supported by the Thailand Research Fund (RSA5980018 and DPG6080001), the Center of Excellence for Innovation in Chemistry (PERCH-CIC), Office of the Higher Education Commission, Ministry of Education (OHEC), and the Nanotechnology Center (NANOTEC), NSTDA, Ministry of Science and Technology, Thailand, through its program of Center of Excellence Network.

Appendix A. Supplementary data

Supplementary data associated with this article can be found, in the online version, at https://doi.org/10.1016/j.jphotochem.2018.03.018.

References

[1] L. Wan, Q. Shu, J. Zhu, S. Jin, N. Li, X. Chen, S. Chen, A new multifunctional Schiff-based chemosensor for mask-free fluorimetric and colorimetric sensing of F^- and CN^-, Talanta 152 (2016) 39–44.
[2] H.J. Lee, S.J. Park, H.J. Sin, Y.J. Na, C. Kim, A selective colorimetric chemosensor with an electron-withdrawing group for multi-analytes CN^- and F^-, New J. Chem. 39 (2015) 3900–3907.
[3] J.H. Hu, J.B. Li, J. Qi, Y. Sun, Selective colorimetric and turn-on fluorimetric detection of cyanide using an acylhydrazone sensor in aqueous media, New J. Chem. 39 (2015) 4041–4046.
[4] P.D. Beer, P.A. Gale, Anion recognition and sensing the state of the art and future perspectives, Angew. Chem. Int. Ed. 40 (2001) 486–516.
[5] S.K. Kim, J. Yoon, A new fluorescent PET chemosensor for fluoride ions, Chem. Commun. 7 (2002) 770–771.
[6] C.F. Wan, Y.J. Chang, C.Y. Chien, Y.W. Sie, C.H. Hu, A.T. Wu, A new multifunctional Schiff base as a fluorescence sensor for Fe^{2+} and F^- ions, and a colorimetric sensor for Fe^{3+}, J. Lumin. 178 (2016) 115–120.
[7] V.K. Harikrishnan, S.M. Basheer, N. Joseph, A. Sreekanth, Colorimetric and fluorimetric response of salicylaldehyde dithiosemicarbazone towards fluoride, cyanide and copper ions: spectroscopic and TD-DFT studies, Spectrochim. Acta Part A: Mol. Biomol. Spectrosc. 182 (2017) 160–167.
[8] Q. Song, A. Bamesberger, L. Yang, H. Houtwed, H. Cao, Excimer–monomer switch: a reaction-based approach for selective detection of fluoride, Analyst 139 (2014) 3588–3592.
[9] S. Chanmungkalakul, V. Ervithayasuporn, S. Hanprasit, M. Masik, N. Prigyaia, S. Kiatkamjornwong, Silsesquioxane cages as fluoride sensors, Chem. Commun. 53 (2017) 12108–12111.
[10] R. Kunthom, P. Piyanuch, N. Wanichacheva, V. Ervithayasuporn, Cage-like silsesequioxanes bearing rhodamines as fluorescence Hg^{2+} sensors, J. Photochem. Photobiol., A 356 (2018) 248–255.
[11] C. Suksai, T. Tuntulani, Chromogenic anion sensors, Chem. Soc. Rev. 32 (2003) 192–202.
[12] G.J. Park, G.R. You, Y.W. Choi, C. Kim, A naked-eye chemosensor for simultaneous detection of iron and copper ions and its copper complex for colorimetric/fluorescent sensing of cyanide, Sens. Actuators B 229 (2016) 257–271.
[13] A.S. Gupta, A. Garg, K. Paul, V. Luxami, Differential sensing of fluoride and cyanide ions by using Dicyano substituted benzimidazole probe, J. Lumin. 173 (2016) 165–170.
[14] A.R. Chowdhury, B.G. Roy, S. Jana, T. Weyhermuller, P. Banerjee, A simple cleft shaped hydrazine-functionalized colorimetric new Schiff base chemoreceptor for selective detection of F^- in organic solvent through PET signaling: development of a chemoreceptor based sensor kit for detection of fluoride, Sens. Actuator B 241 (2017) 706–715.
[15] M. Boiocchi, L.D. Boca, D.E. Gomez, L. Fabbrizzi, M. Licchelli, E. Monzani, Nature of urea-fluoride interaction: incipient and definitive proton transfer, J. Am. Chem. Soc. 126 (2004) 16507–16514.
[16] S.V. Bhosale, M.B. Kalyankar, S.J. Langford, A core-substituted naphthalene diimide fluoride sensor, Org. Lett. 11 (2009) 5418–5421.
[17] M.S. Kumar, S.L.A. Kumar, A. Sreekanth, Highly selective fluorogenic anion chemosensors: naked-eye detection of F^- and AcO^- ions in natural water using a test strip, Anal. Methods 5 (2013) 6401–6410.
[18] Y. Fu, C. Fan, G. Liu, S. Pu, A colorimetric and fluorescent sensor for Cu2+ and F− based on a diarylethene with a 1,8-naphthalimide Schiff base unit, Sens. Actuators B 239 (2017) 295–303.
[19] N. Kumari, S. Jha, S. Bhattacharya, Colorimetric probes based on anthraimidazolediones for selective sensing of fluoride and cyanide ion *via* intramolecular charge transfer, J. Org. Chem. 76 (2011) 8215–8222.
[20] B. Garg, T. Bisht, S.M.S. Chauhan, 2,2′-Diaminoazo-benzene, a potential scaffold for the synthesis of bis-ureas and thioureas: solution phase anion sensing and binding studies, Sens. Actuators B 168 (2012) 318–328.
[21] A. Bamesberger, C. Schwartz, Q. Song, W. Han, Z. Wang, H. Cao, Rational design of a rapid fluorescent approach for detection of inorganic fluoride in MeCN-H2O: a new fluorescence switch based on N-aryl-1,8-naphthalimide, New J. Chem. 38 (2014) 884–888.
[22] S.M. Kim, M. Kang, I. Choi, J.J. Lee, C. Kim, A highly selective colorimetric chemosensor for cyanide and sulfide in aqueous solution: experimental and theoretical studies, New J. Chem. 40 (2016) 7768–7778.
[23] P.A. Gale, T. Gunnlaugsson, Preface: supramolecular chemistry of anionic species themed issue, Chem. Soc. Rev. 39 (2010) 3595–3596.
[24] P.A. Gale, Anion receptor chemistry: highlights from 2008 and 2009, Chem. Soc. Rev. 39 (2010) 3746–3771.
[25] Q. Wang, Y. Xie, Y. Ding, X. Li, W. Zhu, Colorimetric fluoride sensors based on deprotonation of pyrrole–hemiquinone compounds, Chem. Commun. 46 (2010) 3669–3671.
[26] T. Gunnlaugsson, M. Glynn, G.M. Tocci, P.E. Kruger, F.M. Pfeffer, Anion recognition and sensing using luminescent and colorimetric sensors, Coord. Chem. Rev. 250 (2006) 3094–3117.
[27] D. Udhayakumari, S. Velmathi, M.S. Boobalan, Novel chemosensor for multiple target anions: the detection of F^- and CN^- ion *via* different approach, J. Fluor. Chem. 175 (2015) 180–184.
[28] Y.W. Choi, J.J. Lee, G.R. You, S.Y. Lee, C. Kim, Chromogenic naked-eye detection of copper ion and fluoride, RSC Adv. 5 (2015) 86463–86472.
[29] X. Yang, W. Zhang, Z. Yi, H. Xu, J. Wei, L. Hao, Highly sensitive and selective fluorescent sensor for copper(II) based on salicylaldehyde Schiff-base derivatives with aggregation induced emission and mechanoluminescence, New J. Chem. 41 (2017) 11079–11088.
[30] J.T. Yeh, P. Venkatesan, S.P. Wu, A highly selective turn-on fluorescent sensor for fluoride and its application in imaging of living cells, New J. Chem. 38 (2014) 6198–6204.
[31] Y. Ma, Y. Zhao, F. Zhang, T. Jiang, X. Wei, H. Shen, R. Wang, Z. Shi, Two new chemosensors for fluoride ion based on perylene tetra-(alkoxycarbonyl) derivatives, Sens. Actuators B 241 (2017) 735–743.
[32] E.J. Cho, B.J. Ryu, Y.J. Lee, K.C. Nam, Visible colorimetric fluoride ion sensors, Org. Lett. 7 (2005) 2607–2609.
[33] A. Ghosh, K. Mukherjee, S.K. Ghosh, B. Saha, Sources and toxicity of fluoride in the environment, Res. Chem. Intermed. 39 (2013) 2881–2915.
[34] Y. Fu, C. Fan, G. Liu, S. Pu, A colorimetric and fluorescent sensor for Cu^{2+} and F^- based on a diarylethene with a 1,8-naphthalimide Schiff base unit, Sens. Actuators B 239 (2017) 295–303.
[35] Q. Gao, L. Ji, Q. Wang, K. Yin, J. Li, L. Chen, Colorimetric sensor for highly sensitive and selective detection of copper ion, Anal. Methods 9 (2017) 5094–5100.
[36] G.T. Spence, P.D. Beer, Expanding the scope of the anion templated synthesis of interlocked structure, Acc. Chem. Res. 46 (2013) 571–586.
[37] E.S. Figueroa, M.E. Moragues, E. Climent, A. Agostini, R.M. Manez, F. Sancenon, Chromogenic and fluorogenic chemosensors and reagents for anions. A comprehensive review of the years 2010–2011, Chem. Soc. Rev. 42 (2013) 3489–3613.
[38] M.H. Lee, B. Yoon, J.S. Kim, J.L. Sessler, Naphthalimide trifluoroacetyl acetonate: a hydrazine-selective chemodosimetric sensor, Chem. Sci. 4 (2013) 4121–4126.
[39] M. Kumar, N. Kumar, V. Bhalla, A naphthalimide based chemosensor for Zn^{2+}, pyrophosphate and H_2O_2: sequential logic operations at the molecular level, Chem. Commun. 49 (2013) 877–879.
[40] T.I. Kashar, A.H.E. Sehli, Synthesis characterization, antimicrobial and anticancer activity of Zn(II), Pd(II) and Ru(III) complexes of dehydroacetic acid hydrazine, J. Chem. Pharm. Res. 5 (2013) 474–483.
[41] S. Kannan, M. Sivagamasundari, R. Ramesh, Y. Liu, Ruthenium(II) carbonyl complexes of dehydroacetic acid thiosemicarbazone: synthesis, structure, light emission and biological activity, J. Organomet. Chem. 693 (2008) 2251–2257.
[42] Z. Zhang, J. Wu, Z. Shang, C. Wang, J. Cheng, X. Qian, Y. Xiao, Z. Xu, Y. Yang, Photocalibrated NO release from N-nitrosated napthalimides upon one-Photon or two-photon irradiation, Anal. Chem. 88 (2016) 7274–7280.
[43] J. Gan, H. Tian, Z. Wang, K. Chen, J. Hill, P.A. Lane, M.D. Rahn, A.M. Fox, D.D.C. Bradley, Synthesis and luminescence properties of novel ferrocene–naphthalimides dyads, J. Organomet. Chem. 645 (2002) 168–175.
[44] J.W. Pavlik, V. Ervithayasuporn, S. Tantayanon, Synthesis of some pyrano[2,3-c] pyrazoles, J. Heterocycl. Chem. 48 (2011) 710–714.
[45] J.W. Pavlik, V. Ervithayasuporn, J.C. MacDonald, S. Tantayanon, The photochemistry of some pyranopyrazoles, Arkivoc 8 (2009) 57–68.

[46] H. Yang, H. Song, Y. Zhu, S. Yang, Single chemosensor for multiple analytes: chromogenic and fluorogenic detection for fluoride anions and copper ions, Tetrahedron Lett. 53 (2012) 2026–2029.
[47] K.D. Bhatt, H.S. Gupta, B.A. Makwana, D.J. Vyas, D. Maity, V.K. Jain, Calix receptor edifice; Scrupulous turn off fluorescent sensor for Fe(III), Co(II) and Cu (II), J. Fluoresc. 22 (2012) 1493–1500.
[48] C.B. Murphy, Y. Zhang, T. Troxler, V. Ferry, J.J. Martin, W.E. Jones, Probing forster and dexter energy-transfer mechanisms in fluorescent conjugated polymer chemosensors, J. Phys. Chem. 108 (2004) 1537–1543.
[49] A.S. Murugan, E.R.A. Noelson, J. Annaraj, Solvent dependent colorimetric, ratiometric dual sensor for copper and fluoride ions: real sample analysis, cytotoxicity and computational studies, Inorg. Chem. Acta 450 (2016) 131–139.
[50] L. Zang, H. Shang, D. Wei, S. Jiang, A multi-stimuli-responsive organogel based on salicylidene Schiff base, Sens. Actuators B 185 (2013) 389–397.
[51] W. Wang, Q. Wen, Y. Zhang, X. Fei, Y. Li, Q. Yang, X. Xu, Simple naphthalimide-based fluorescent sensor for highly sensitive and selective detection of Cd^{2+} and Cu^{2+} in aqueous solution and living cells, Dalton Trans. 42 (2013) 1827–1833.
[52] Y.M. Hijji, B. Barare, A.P. Kennedy, R. Butcher, Synthesis and photophysical characterization of a Schiff base as anion sensor, Sens. Actuators B 136 (2009) 297–302.
[53] V. Reena, S. Suganya, S. Velmathi, Synthesis and anion binding studies of azo-Schiff bases: selective colorimetric fluoride and acetate ion sensors, J. Fluor. Chem. 153 (2013) 89–95.
[54] S. Mukherjee, A.K. Paul, Pyrene based chemosensor for selective sensing of fluoride in aprotic and protic environment, J. Fluoresc. 25 (2015) 1461–1467.
[55] S.M. Kumar, K. Dhahagani, J. Rajesh, K. Anitha, G. Chakkaravarthi, N. Kanakachalam, M. Marappan, G. Rajagopal, Synthesis, structural analysis and cytotoxic effect of copper (II)-thiosemicarbazone complexes having heterocyclic bases: a selective naked eye sensor for F^- and CN^-, Polyhedron 85 (2015) 830–840.
[56] I.G. Shenderovich, H. Limbach, S.N. Smirnov, P.M. Tolstoy, G.S. Denisov, N.S. Golubev, H/D isotope effects on the low-temperature NMR parameters and hydrogen bond geometries of $(FH)_2F^-$ and $(FH)_3F^-$ dissolved in CDF_3/CDF_2Cl, Phys. Chem. Chem. Phys. 4 (2002) 5488–5497.

Volume 9 | Number 40 | 28 October 2018 | Pages 7719–7884

Chemical Science

rsc.li/chemical-science

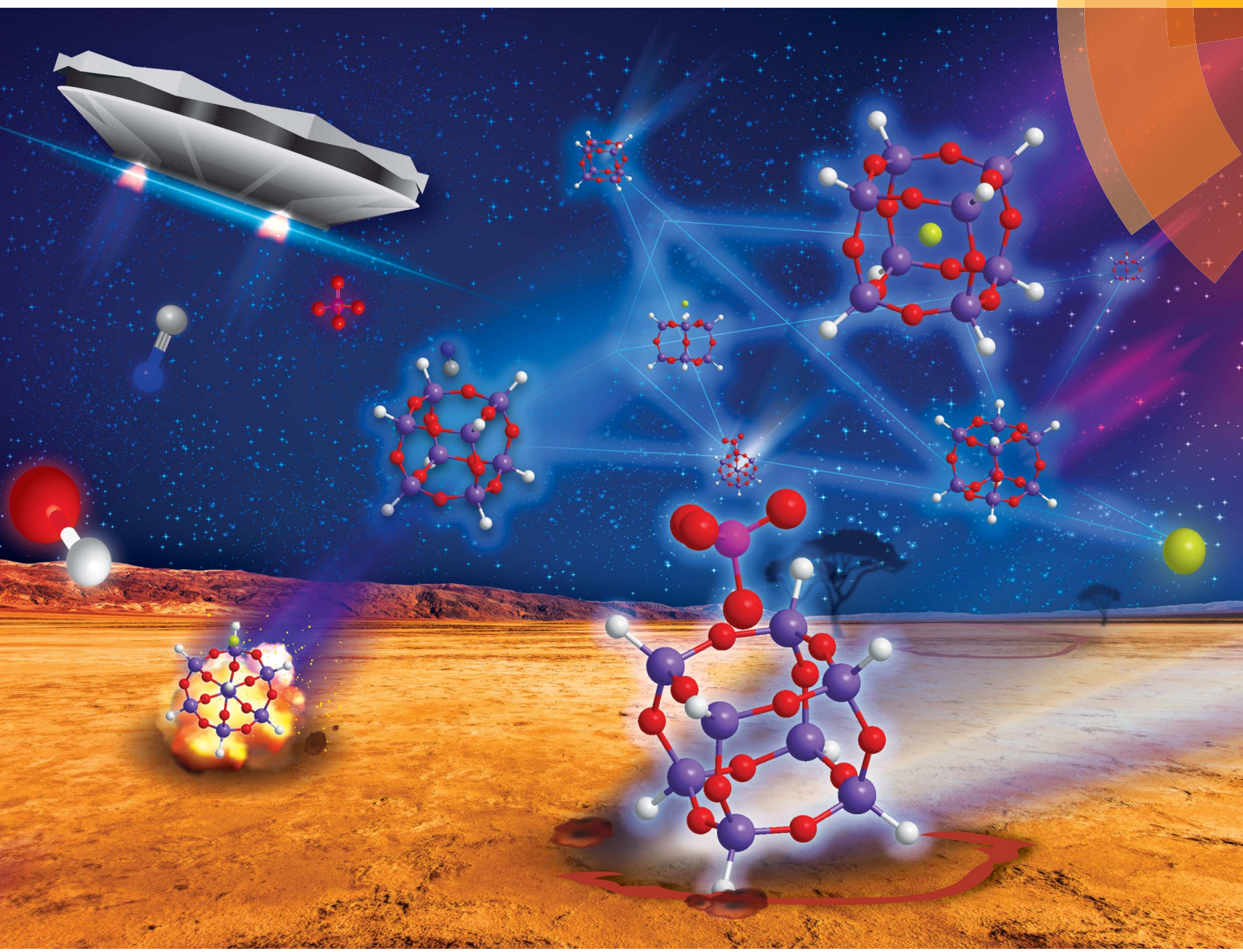

ISSN 2041-6539

ROYAL SOCIETY OF CHEMISTRY

EDGE ARTICLE
Vuthichai Ervithayasuporn *et al.*
Anion identification using silsesquioxane cages

Chemical Science

EDGE ARTICLE

View Article Online
View Journal | View Issue

Cite this: *Chem. Sci.*, 2018, **9**, 7753

All publication charges for this article have been paid for by the Royal Society of Chemistry

Anion identification using silsesquioxane cages†

Supphachok Chanmungkalakul,[a] Vuthichai Ervithayasuporn, *[a] Patcharaporn Boonkitti,[a] Alisa Phuekphong,[a] Nicha Prigyai,[a] Sumana Kladsomboon[b] and Suda Kiatkamjornwong[cd]

Received 5th July 2018
Accepted 13th September 2018

DOI: 10.1039/c8sc02959h

rsc.li/chemical-science

Anthracene-conjugated octameric silsesquioxane (AnSQ) cages, prepared *via* Heck coupling between octavinylsilsesquioxane (OVS) and 9-bromoanthracene, thermodynamically display intramolecular excimer emissions. More importantly, these hosts are sensitive to each anionic guest, thereby resulting in change of anthracene excimer formation, displaying the solvent-dependent fluorescence and allowing us to distinguish up to four ions such as F^-, OH^-, CN^- and PO_4^{3-} by fluorescence spectroscopy. Depending on the solvent polarity, for example, both F^- and CN^- quenched the fluorescence emission intensity in THF, but only F^- could enhance the fluorescence in all other solvents. The presence of PO_4^{3-} results in fluorescence enhancements in high polarity solvents such as DMSO, DMF, and acetone, while OH^- induces enhancements only in low polarity solvents (*e.g.* DCM and toluene). A picture of the anion recognizing ability of AnSQ was obtained through principal component analysis (PCA) with NMR and FTIR confirming the presence of host–guest interactions. Computational modeling studies demonstrate the conformation of host–guest complexation and also the change of excimer formation. Detection of F^-, CN^- and OH^- by AnSQ hosts in THF is noticeable with the naked eye, as indicated by strong color changes arising from charge transfer complex formation upon anion addition.

Introduction

Silica is one of the most naturally abundant compounds on the Earth. It is used in building materials, electronic devices, in environmental remediation, and in chemical industry.[1] Silica gel is a commonly used laboratory sorbent for chromatographic separations, the binding properties of which can be tailored through surface functionalization.[2] For example, amine groups appended to the silica surface allow for chemical adsorption of CO_2, which generates a chelating group allowing sequestration of metal ions.[3,4] Interestingly, the mode of adsorption for organic molecules by silica is still controversial. While a mechanism has been postulated[5] and the outstanding capacity and absorptivity properties of silica are well-known,[6,7a] very few studies have been devoted to determine the actual role of silica in the adsorption of organic species.[7b,c] This may relate to the poor solubility of these sorbents in water or organic solvents, hindering investigations using solution phase techniques (fluorescent emission, UV-vis absorption or nuclear magnetic resonance).[8]

Polyhedral oligomeric silsesquioxanes (POSS) or silsesquioxane (SQ) cages may be considered as representative molecules for silica due to their closely related empirical formulae ($RSiO_{1.5}$).[9] These systems consist of a rigid cage-like silica framework with organic groups attached to the periphery. The properties of these inorganic–organic hybrid molecules (*e.g.*, solubility) can be altered or tailored to specific applications through changing the organic functionalities.[10] The higher solubility of SQ relative to silica allows for more facile characterization and study of these systems at the molecular level.[11] Accordingly, technological applications of SQ as biocompatible materials,[12] organic light emitting diodes (OLEDs),[13] hybrid polymer[14] porous materials for CO_2 capture,[15] in nitroaromatics detection,[16] and catalysts[17] have arisen over the last decade.

Polyhedral SQ cages can be considered as host molecules, whereby guest species (atoms, ions or molecules) can interact through encapsulation by the internal cavity, or through facial interactions. Solid state encapsulation of fluoride ion within a SQ cage[18] led to further computational studies, which suggested that encapsulation is enhanced if the cage is electron deficient.[19] SQs appended with conjugated pendant organic substituents (*e.g.*, vinyl, phenyl) containing electron withdrawing $-CF_3$ groups exhibited diffusive negative contours at the exterior and more condensed positive contours within the

[a]*Department of Chemistry, Center of Excellence for Innovation in Chemistry (PERCH-CIC), Center for Inorganic and Materials Chemistry, Faculty of Science, Mahidol University, Rama VI Road, Ratchathewi, Bangkok 10400, Thailand. E-mail: vuthichai.erv@mahidol.ac.th; vuthichai.erv@mahidol.edu*

[b]*Department of Radiological Technology, Faculty of Medical Technology, Mahidol University, Nakhon Pathom 73170, Thailand*

[c]*Faculty of Science, Chulalongkorn University, Phayathai Road, Bangkok 10330, Thailand*

[d]*FRST, Division of Science, The Royal Society of Thailand, Sanam Suepa, Dusit, Bangkok 10300, Thailand*

† Electronic supplementary information (ESI) available: Experiments, characterization and spectroscopic studies. See DOI: 10.1039/c8sc02959h

cage interior. In comparison, cages appended with aliphatic electron donating substituents exhibited condensed negative contours within the interior, rendering fluoride ingress less favorable.[19] These data have been exploited by Aziz *et al.* for the preparation of many silsesquioxane-based receptor systems,[20] in addition to fluorescent sensors based on pyrene-conjugated silsesquioxane cages for fluoride detection.[21]

Anion recognition studies form an integral part of modern sensor design and research. While host–guest recognition processes mostly rely on weak non-covalent interactions (*e.g.*, hydrogen bonding, π–π interactions), protonation, deprotonation and nucleophilic substitution are also important modes underlying sensor function.[22,23] This work highlights design of a SQ cage coupled with fluorophores as a host for anion sensing. Recognition by the approach of anions through the face of the octahedral (O_h) cage causes changes in the fluorophore environment, as observed by fluorescence perturbations. Anthracene was chosen as the fluorophore based on past work by James *et al.*, who integrated it into his glucose sensor platform for monitoring of blood-sugar levels in diabetic patients.[24] Commonly used in photochemistry,[25] anthracene and its derivatives exhibit numerous fluorescence modes (*e.g.* types of excimers: twisted, side to face in T-shape and end-overlapped).[26] As the fluorescence response of anthracene-containing molecules depends on the spacing of these motifs and the nature of the linkages, not on their concentration,[27a] appending multiple anthracene groups to the periphery of the octahedral SQ of the T_8 cage allows for the possibility of significant geometry distortion (and hence sensing), on exposure to complementary anions.[27b]

In this work, the synthesis of an anthracene-conjugated octameric silsesquioxane (AnSQ) is presented. The anion recognition ability of this host was probed through monitoring of fluorescence emission and UV-vis absorption changes, on exposure. Complementary *in silico* calculations for T_8 cages provide insights into the flexibility of anthracenes with variations in the spacer, along with electrostatic potential mapping of the AnSQ cage interior to determine the potential for, and likely mode of, anion ingress.

Results and discussion

Synthesis

The AnSQ cage (Scheme 1) was prepared in 86% yield through a Heck-coupling reaction between octavinylsilsesquioxane (OVS) and 9-bromoanthracene. The MALDI-TOF spectrum (Fig. S1†) with *trans*-2-3-(4-*tert*-butylphenyl)-2-methyl-2-propenylidenemalononitrile (DCTB) as a matrix showed the distribution of products, with that corresponding to $n = 4$ being the most abundant. Increasing the ratio of 9-bromoanthracene to OVS under these synthetic conditions did not significantly alter the product distribution. Calcd for 4 substitutions of anthracene units in a silsesquioxane T8 cage ($n = 4$), calcd for $C_{72}H_{56}O_{12}Si_8$ + H^+: m/z 1338.203 [M + H^+]. Found: m/z 1338.110.

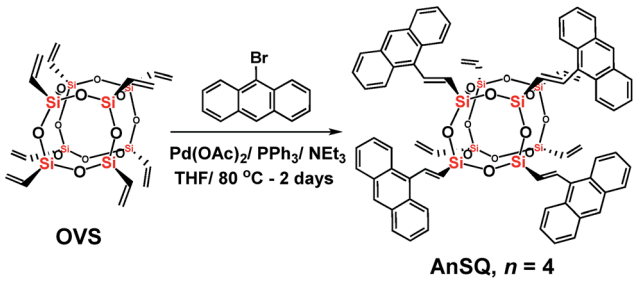

Scheme 1 Synthesis of anthracene-conjugated octameric silsesquioxane (AnSQ) cages.

Solvent and anion effects on excimer formation

Anthracene derivatives possess solvent-dependent properties; change of solvent will slightly affect the absorption λ_{max} (Fig. 1a), the intensity of both absorption and emission.[34c,d] For example, 9-bromoanthracene used as a fluorescent labeling of AnSQ, its emissive intensity mostly increases with increase of solvent polarity as shown in Fig. 1b. Interestingly, 9-bromoanthracene in THF as a solvent showed very broad fluorescence emission. This phenomenon suggests that THF can also induce an intermolecular interaction among 9-bromoanthracene molecules leading to an aggregation with multilayer π–π stacks, even at low concentrations. Moreover, a solid state of 9-

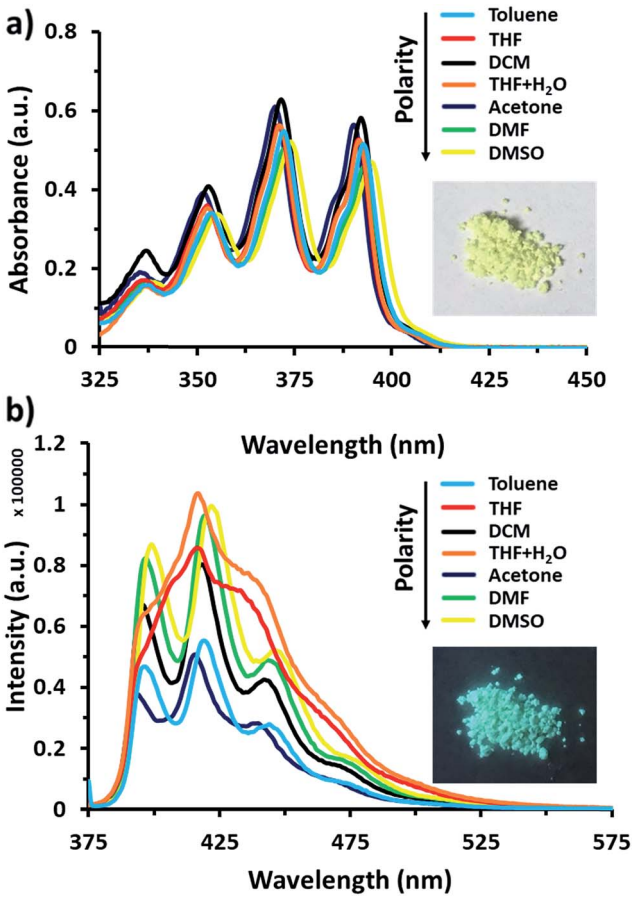

Fig. 1 (a) UV-vis absorption of 9-bromoanthracene at 60 μM and a picture under visible light, (b) fluorescence emission of 9-bromoanthracene at 60 μM with λ_{ex} = 370 nm and a picture under UV light.

bromoanthracene shines a bright blue fluorescence (Fig. 1a) under UV radiation, confirming the presence of intermolecular excimer. However, after SQ cages coupled with anthracene functions, the fluorescence emission of AnSQ shown in Fig. 2b is significantly shifted to longer wavelengths with a larger Stokes shift ($\Delta\lambda$ = 85 nm), compared to 9-bromoanthracene (with a Stokes shift of $\Delta\lambda$ = 55 nm), as well as AnSQ in solid state emits a bright green fluorescence under UV light (Fig. 6b). This result confirms that strongly intramolecular interactions among adjacent anthracene groups (Fig. 2a) on AnSQ are thermodynamically favorable and simply found in all solvents as shown in Fig. 2b.[28a]

Such fluorescence emissions of AnSQ cage can be of two types: molecular and excimer emissions (Fig. 2a). The molecular emission, or π–π* fluorescence, of a fluorophore will show multiple peaks,[28b] whilst an excimer emission from an excited dimer shows a broad peak at a longer wavelength. In contrast to the solubility nature of 9-bromoanthracene, AnSQ is highly soluble in non-polar solvents, because the fluorescence intensity increased in low polar solvents (Fig. 2b). However, AnSQ tends to aggregate in high polar solvents like DMF or DMSO showing poor fluorescence intensity, as well as the intramolecular excimeric formation of adjacent anthracene functions on AnSQ can be instead interrupted by intermolecular π–π stacks of anthracene units with other AnSQ cages. To illustrate the effect of anion addition, fluorescence emission measurements of pristine AnSQ were first conducted in several solvents (Fig. 3). The emission intensities obtained could then be compared to those resulting from AnSQ in each solvent, after anion addition. As shown in Table 1, emission intensity and quantum yield generally decrease as the solvent polarity increases. Significant changes in λ_{max} of the AnSQ emission did not, however, correlate with solvent polarity. The trends in fluorescence intensity and quantum yield exhibited for AnSQ are reasonably consistent with those from previous work.[30] The quantum yield measurements are provided in Fig. S3.†

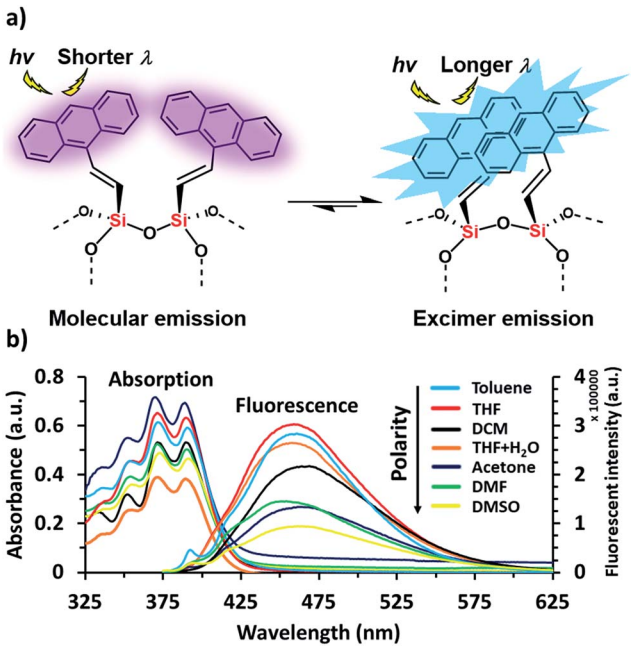

Fig. 2 (a) Demonstration of thermodynamically stable of the excimer on AnSQ and (b) UV-vis absorption and fluorescence emission at λ_{ex} = 370 nm of AnSQ in various solvents at a concentration of 6 μM.

The fluorescence emission of AnSQ in the presence of 100 equiv. of anions in 6 μM of AnSQ, and all anion salts dissolved in THF except for PO_4^{3-} which was dissolved in DI, was measured once equilibrium was reached (18 hours post-addition). Therefore, the results are highlighted as λ_{max} values in Table 1, in addition to quantum yields. In contrast to a previous study focusing on fluoride sensing,[21] significant changes in AnSQ emission occur in the presence of other anions in addition to fluoride (OH^-, PO_4^{3-} and CN^-). Addition of these to AnSQ in various solvents results in noticeable fluorescence emission perturbations (Fig. 3 and Table 1), manifested as the enhancement, quenching or Stokes shift of the fluorescence maxima. As an example, AnSQ in a moderately polar solvent (THF) exhibits a fluorescence wavelength maximum (λ_{max}) at 457 nm with a quantum yield (Φ_P) of 0.297. Addition of F^- results in lowering a Stokes shift of $\Delta\lambda$ = 60 nm with significant quenching to OFF (Φ_P = 0.004), confirming the formation of fluoride encapsulation by a SQ cage.[21] We hypothesize that intramolecular excimer fluorescence of AnSQ was strongly disturbed by fluoride ion leading to reorganize the SQ cage framework and finally distort an excimer. This result would turn off the radiative transitions by the formation of "ion-induced aggregates" or "aggregation-caused quenching" (ACQ). Thereby, AnSQ became non-emissive in the aggregates even under highly diluted THF solution. Exposure of AnSQ to OH^-, PO_4^{3-} and CN^- results in similar λ_{max} shifts (to 441, 442 and 429 nm, respectively) and changes in quantum yield (Φ_P = 0.210, 0.302 and 0.009, respectively). While F^-, OH^- and CN^- addition results in fluorescence quenching, PO_4^{3-} affords a slight enhancement in intensity. On the other hand, in highly polar DMSO, AnSQ exhibits a λ_{max} at 464 nm with Φ_P = 0.158. The presence of either F^- or PO_4^{3-} results in enhancing a quantum efficiency, while OH^- and CN^- addition gives lower a Stokes shift of λ_{max} values to shorter wavelengths, with a bare change in quantum yields.

The results in Fig. 3 and Table 1 highlight the influence of solvent polarity on fluorescence emission. This is highlighted by a comparison of the quantum yields for AnSQ in pure THF (Φ_P = 0.297) with those obtained in THF/water (95 : 5 v/v, Φ_P = 0.428). Addition of F^- to AnSQ in pure THF results in OFF fluorescence (Φ_P = 0.004), whilst the same guest in THF/H_2O results in enhanced fluorescence intensity (Φ_P = 0.581) and a λ_{max} shift to shorter wavelengths. Similarly, AnSQ exposure to CN^- and OH^- in THF results in quenching, although enhancements occur in THF/H_2O, mirroring the behavior in DMSO. Although CN^- and F^- quench AnSQ fluorescence in THF and enhance it in THF/H_2O, only F^- affords fluorescence enhancements in toluene (Φ_P = 0.394 to 0.975) and DCM (Φ_P = 0.260 to 0.591). Hydroxide addition to AnSQ in THF results in decrease in fluorescence intensity and lowers a Stokes shift to shorter wavelengths ($\Delta\lambda_{max}$ = −16 nm), with similar behavior occurring in DMSO. Phosphate, while not measurable in

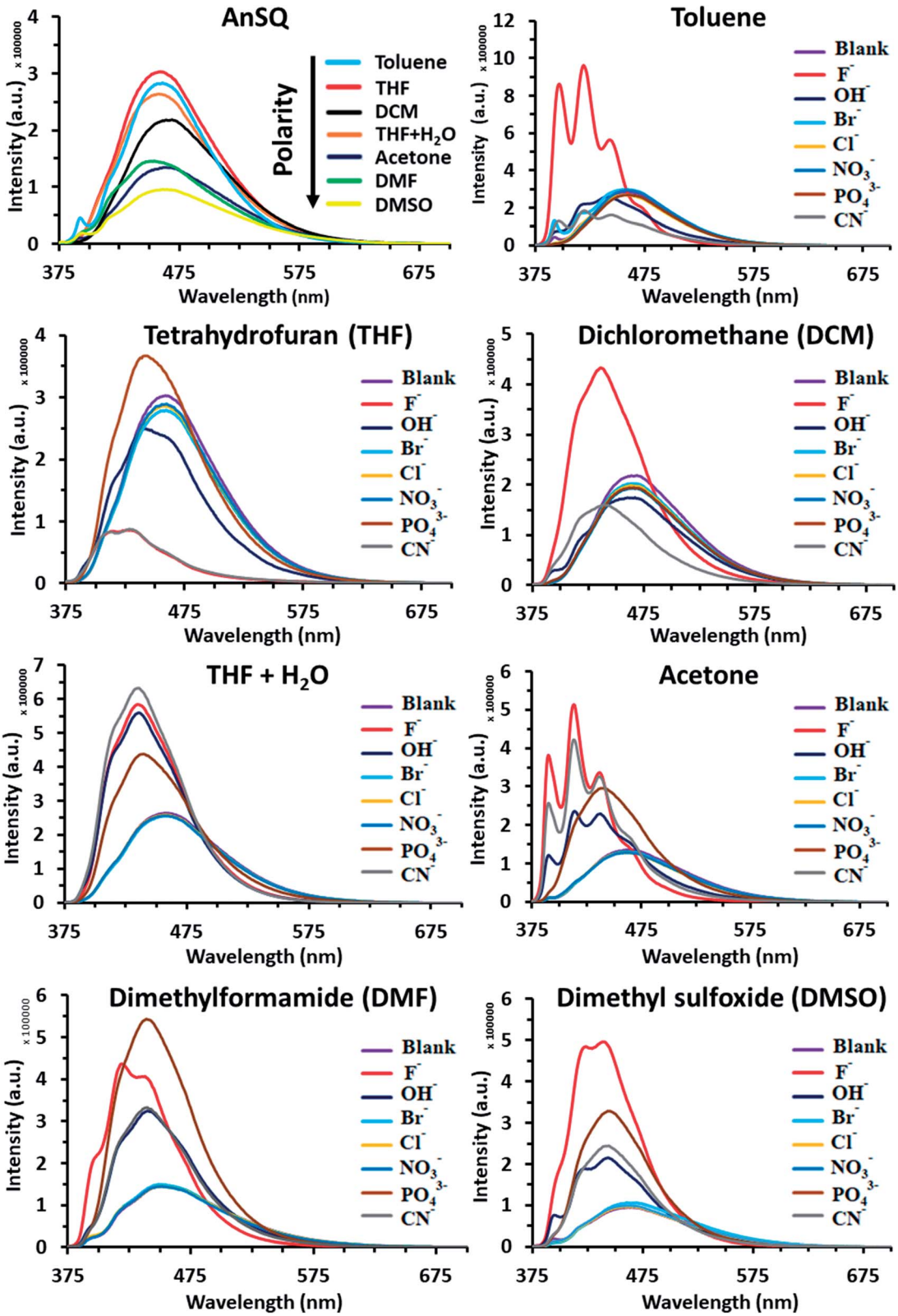

Fig. 3 Fluorescence emission spectra (λ_{ex} = 370 nm) of AnSQ in various solvents before and after addition of guest anions (100 equiv.). Reaction time was set to 18 hours to ensure equilibrium was reached.

toluene and DCM due to insolubility, affords slight enhancements in AnSQ emission intensity in THF. Additions of PO_4^{3-} in THF and THF/H_2O did not provide the different spectrum. Although anion detection of AnSQ in aqueous solution is not feasible due to the precipitation of AnSQ host, use of a binary solvent system in THF/water (95 : 5 v/v) would provide the same

Table 1 Fluorescence wavelength maxima (λ_{max}) and quantum yields (Φ_P) of AnSQ in various solvents at $\lambda_{ex} = 370$ nm before and after addition of guest anions (100 equiv.). Reaction time was set to 18 hours to ensure equilibrium was reached

	Fluorescence wavelength maxima (λ_{max}; nm) and quantum yields (Φ_P) on anion addition							
Solvents	Control	F^-	OH^-	Br^-	Cl^-	NO_3^-	PO_4^{3-}	CN^-
DMSO	464, 0.158	440, 0.344	443, 0.131	460, 0.152	464, 0.136	460, 0.166	447, 0.242	444, 0.133
DMF	454, 0.283	419, 0.848	440, 0.288	449, 0.292	451, 0.314	452, 0.219	439, 0.646	440, 0.353
Acetone	464, 0.187	413, 0.460	414, 0.193	460, 0.324	459, 0.196	462, 0.224	442, 0.469	413, 0.324
THF + H_2O	458, 0.428	435, 0.581	435, 0.405	457, 0.316	458, 0.381	457, 0.399	440, 0.528	436, 0.417
DCM	469, 0.260	436, 0.591	469, 0.396	466, 0.267	466, 0.263	465, 0.269	466, 0.277	436, 0.201
THF	457, 0.297	430, 0.004	441, 0.210	459, 0.323	458, 0.332	460, 0.322	442, 0.302	429, 0.009
Toluene	461, 0.394	419, 0.975	441, 0.475	459, 0.423	459, 0.391	460, 0.450	461, 0.351	420, 0.398

trend of results, if it is still homogeneous, such as DMSO and DMSO/water. Only THF and THF/water provided different results.

The differences in the fluorescence behavior of AnSQ may be due to the nature of the excimer formed in each solvent system and on guest exposure, such as solubility and ion-induced molecular and excimer emissions.[28b] For example, poorly soluble solvents might lead to an aggregation of AnSQ, perturbing excimer emission within a SQ cage. A previous report found that approach of an acetonitrile solvent molecule to a SQ cage occurs from the most electronegative center (N atom),[31] consistent with the findings by Anderson *et al.*[19] While the approach of negatively charged species to the positive surface of silicon atoms in SQ cage should be favorable, repulsive forces between the guest and lone pairs of oxygen atoms within a T_8 cage will become prevalent at close distances. Such repulsive forces can result in cage distortion, which in turn alters the geometry of the excimer interactions. Emission from anthracenes can occur from two types of emissive states: excimeric anthracene emission and monomeric anthracene emission.[32,33] The shift between both states can be easily observed by fluorescence spectral changes, in that monomer emission will occur at the lowest Stokes shift or shorter wavelengths while excimer emission wavelength depends on the solvent type.[34a] Addition of fluoride ions to AnSQ results in fluorescence enhancements in all solvents apart from THF, which, being moderately polar, is expected to give rise to charge transfer complex formation. Some increases in fluorescence intensity coincide with lower quantum efficiencies as a consequence of the quantum measurements being based on the emission area to absorption area ratio. As suggested by Narikiyo *et al.*, excimer formation of fluorophores on SQ cages relies on system rigidity, with excimer and molecular fluorescence emission being controllable through the selection of appropriate solvents and guests.[34b]

Response time

The effects of solvent on the interaction between AnSQ and anionic guests (*e.g.* Cl^-, Br^-, NO_3^-, F^-, CN^-, OH^-, and PO_4^{3-}) were evaluated on the basis of fluorescence response. Theoretically, an increase in solvent polarity may result in rate enhancements in the case of charged reactants. Reaction rates were measured by addition of 100 equiv. of anions to 6 μM of AnSQ, ensuring pseudo 1st order kinetics. Fluorescence changes were monitored at an excitation wavelength (λ_{ex}) of 370 nm with maximum emission wavelength fixed according to Table 1. Observations were carried out for 20 min time periods at 30 s intervals, for comparative purposes. Only four anions (*e.g.* F^-, CN^-, OH^-, and PO_4^{3-}) resulted in significant fluorescence intensity changes in high polarity solvents (DMSO, DMF and acetone), in contrast to slow reaction kinetics occurring in low polarity solvents (Table 2). However, F^-, CN^- and PO_4^{3-} provided fine patterns of change in fluorescence intensity (Fig. S4a and b†). Addition of OH^- provided a fluctuating pattern of fluorescent response suggesting that OH^- may induce Si–O cleavage and cage rearrangement resulting in several intermediates.[9c–e,10b,10e,11,27b] Other guest anions (Cl^-, Br^- and NO_3^-) give rise to only minimal fluorescence responses, as shown in Fig. S4c and d† and Table 1, which change the fluorescence in the same trend, so these three anions cannot be identified with AnSQ.

Anion identification

Principal component analysis (PCA) was used to create association fingerprints for anions with AnSQ.[35,36] Input data were emission spectra obtained at $\lambda_{ex} = 370$ nm of the sample minus the blank in each solvent (acetone, DCM, DMF, DMSO, THF, THF/H_2O and toluene). In each solvent, spectra of 6 μM AnSQ were measured before and after addition of 100 equiv. anions

Table 2 Kinetic constants (k) highlighting the fluorescence responses of AnSQ to anionic guests (100 equiv.) ($\lambda_{ex} = 370$ nm)

	Kinetic constant (k) × 10^{-3} s^{-1}			
Solvent	F^-	OH^-	CN^-	PO_4^{3-}
DMSO	1.3	0.2	0.7	1.3
DMF	2.2	0.3	0.7	0.8
Acetone	2.2	0.5	1.2	0.9
THF + H_2O	0.5	0.3	0.6	0.3
DCM	1.6	0.3	0.3	0.1
THF	−0.1	0.2	0.5	0.3
Toluene	1.4	0.1	0.7	0.04

(F^-, OH^-, NO_3^-, CN^-, PO_4^{3-}, Cl^-, Br^-). As in previous experiments, samples were allowed to equilibrate for 18 hours prior to measurement. As expected, spectral changes occurred on anion addition, as shown in Fig. 3. The software Laboratory Virtual Instrument Engineering Workbench (LabVIEW) was used to create PCA graphs. PCA data were obtained from these spectra as the differences in fluorescence intensity (ΔI) from 400 to 500 nm over 10 nm intervals, with data being the result of five repeat experiments. The obtained PC contributions were PC1 = 91.7%, PC2 = 8.1% for acetone, PC1 = 98.2%, PC2 = 1.7% for DMSO, PC1 = 93.0%, PC2 = 7.0% for THF and PC1 = 92.9%, PC2 = 6.8% for toluene. The grouping in PC1 for toluene indicates that AnSQ can be used as a sensor for F^- in this solvent (see Fig. S6† for PCA data of all anions). So, the combination of PCA and fluorescence changes of AnSQ can be used to create a dendrogram for anion detection as shown in

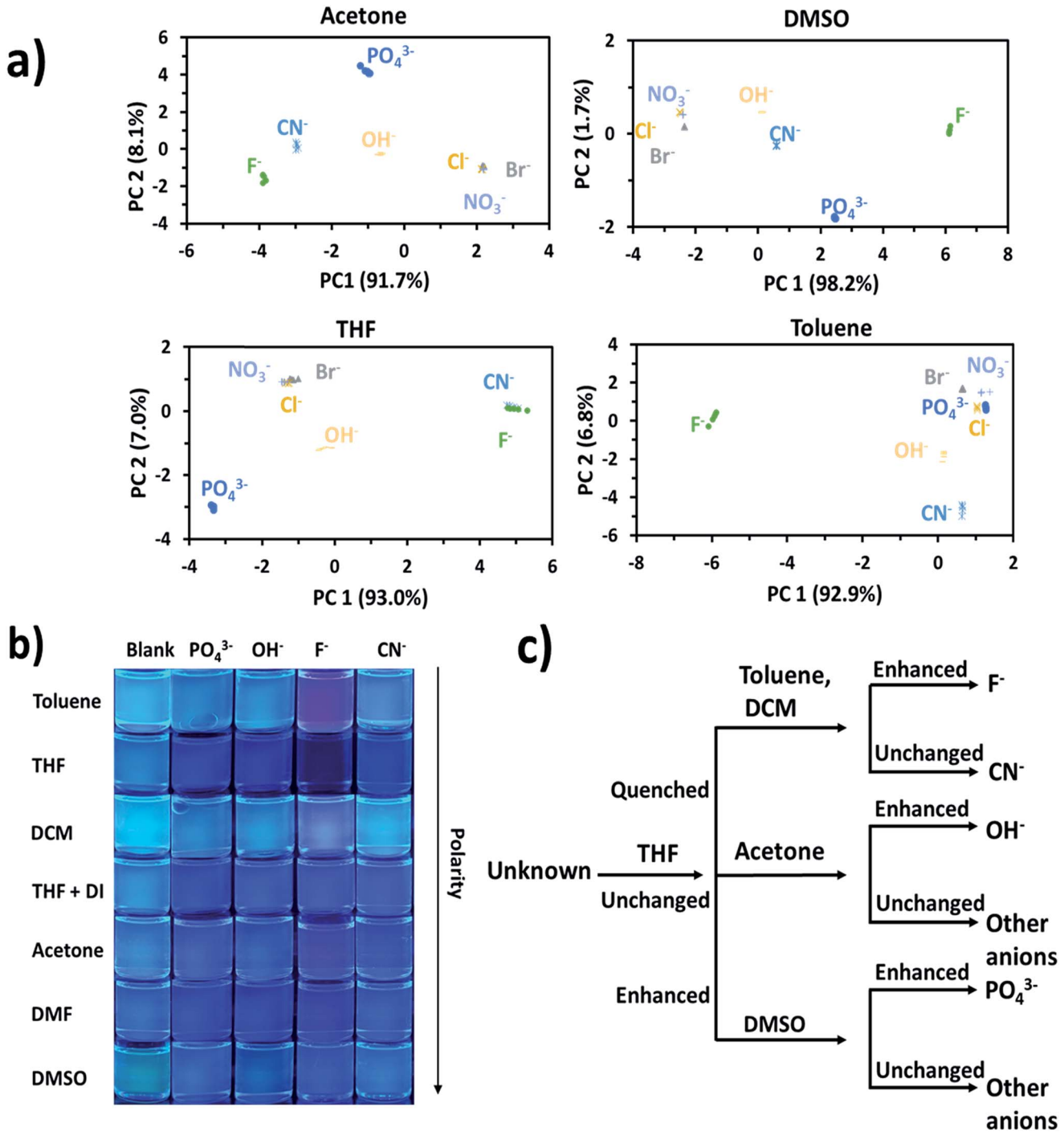

Fig. 4 (a) PCA results for AnSQ anion association in different solvents, (b) photographs of AnSQ–guest solution under UV radiation, and (c) dendrogram of AnSQ response behaviour obtained from fluorescence spectra (Table 1).

Fig. 4c. In practical use, the unknown anion may be tested with AnSQ in THF first; the obtained spectral change could lead to the next solvent choice. At this state, AnSQ may not be suitable for use with multiple anion solution due to some limitations: notably, that fluoride binds much more strongly than other anions in all solvents, which is considered to be a very competitive anion.

Quantitative analysis of anion detection

The reaction between AnSQ and anions could presumably occur *via* a coordination complex, as well as the polarity of solvents had affected to the rate of reactions.[37] Acetone, DMF, DMSO and toluene were selected as solvents for the determination of detection limits due to the fast kinetics of anion association (Fig. 5 and S7†). For AnSQ (6.0 μM) in DMSO, the detection limit for F^- detection was 1.001 ppb. Responses to other anions were less marked: 5.61, 2.04 and 4.54 ppb for OH^-, CN^- and PO_4^{3-}, respectively (Fig. S10†). In DMF for the same AnSQ concentration, detection limits were higher (1.65, 26.9, 12.1 and 59.5 ppb) for F^-, OH^-, $CN^-$and PO_4^{3-}, respectively. In acetone, AnSQ detection limits for all anions apart from PO_4^{3-} (10.2 ppb) were higher than in DMF, and in toluene only F^- (9.57 ppb) showed good sensitivity. Thus solvent polarity is an important factor affecting anion binding, and these results afford useful insights into solvent selection for detection of anionic analytes.

Results in Fig. 5 and S7† indicate that, with anion addition, molecular emission intensity increases at the expense of excimer emission. Anion binding strengths, as calculated from Benesi–Hildebrand plots from titration data (Fig. S9†), were

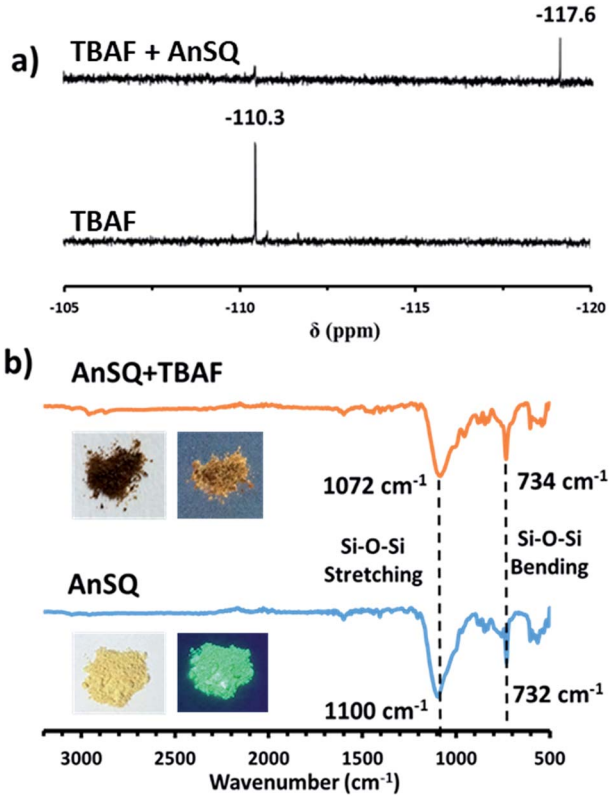

Fig. 6 (a) ^{19}F NMR spectra for titration of AnSQ with TBAF using DMSO-d_6 as the solvent and $CFCl_3$ as a calibration agent, (b) FTIR spectra of AnSQ before and after addition of TBAF (1 equiv.) with inset pictures of AnSQ under visible (left) and UV lights (right).

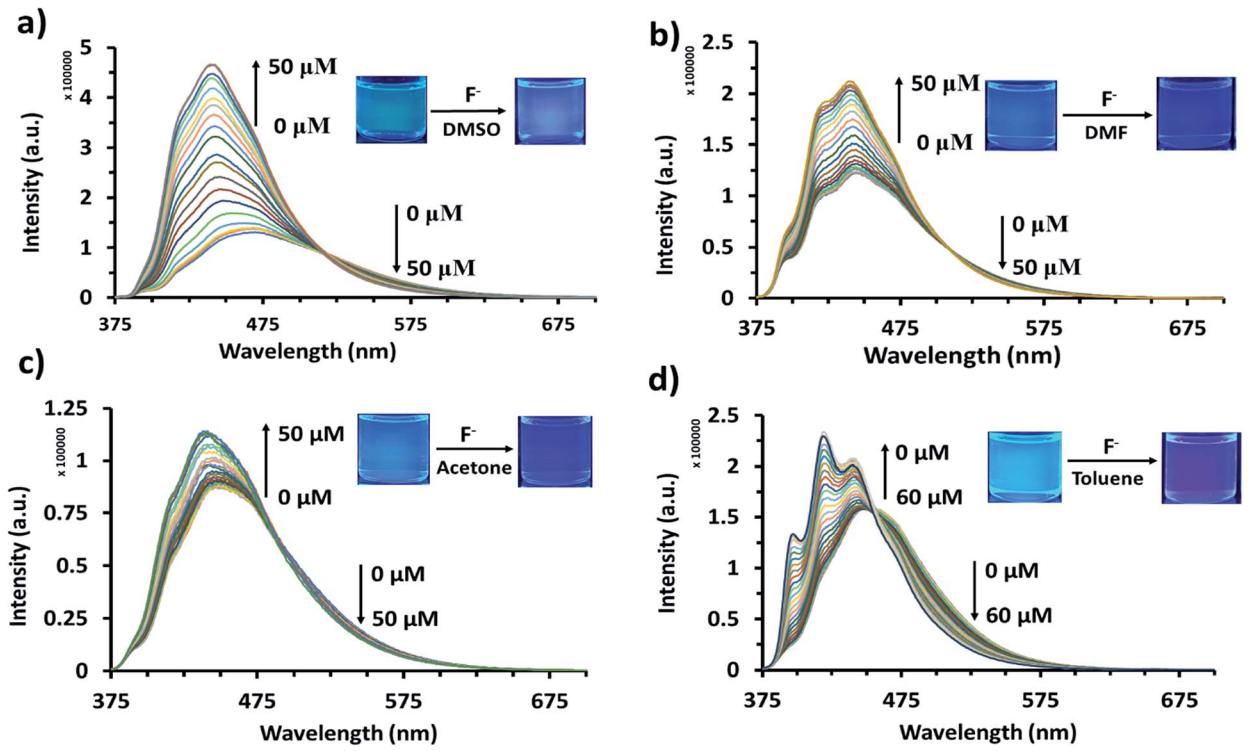

Fig. 5 Fluorescence titration of AnSQ (6 μM) with TBAF (λ_{ex} = 370 nm) after 2 min of addition for each point in (a) DMSO, (b) DMF, (c) acetone, and (d) toluene after 5 min of addition for each point.

3333, 173, 263 and 697 M^{-1} for F^-, OH^-, CN^- and PO_4^{3-}, respectively. Selectivity for F^- can be explained on the basis of cage encapsulation, as confirmed by ^{19}F NMR experiments (Fig. 6a). Addition of TBAF to AnSQ in DMSO-d_6 results in substantial upfield chemical shift changes of the F^- resonance, relative to that of uncomplexed TBAF. So, the chemical shift further upfield in the ^{19}F NMR spectra and the outstanding binding constant can confirm the encapsulation of fluoride in the cage.

FTIR result (Fig. 6b) of AnSQ in the solid state shows the key signal of Si–O–Si stretching vibrational frequency at 1100 cm^{-1}, confirming the existence of a cage framework. Upon addition of 1 equiv. TBAF, an absorption band associated with Si–O bond stretching of AnSQ appears in the lower energy at 1072 cm^{-1}. This result suggested the formation of [AnSQ + F^-] complex through very strong host–guest interactions as the Si–O bond strength decreases, while Si–F bonds form. Solution studies also suggest that only fluoride is thermodynamically capable of being encapsulated by the cage (Fig. 7), whereas other anions may interact solely with the cage surface. This is because the Si–O–Si stretching vibrational frequency of AnSQ diplays minor changes with all anions except fluoride as shown in Fig. S11† confirming weaker host–guest interactions at the SQ cage.[28c]

UV-vis spectroscopy

UV-visible absorption measurements of AnSQ in THF with various anions supported the change of anthracene excimer type on association (Fig. 8). 100 equiv. of the anions was added to 6 μM of AnSQ and left for 18 hours. The UV-vis absorption spectra of AnSQ are most perturbed in the presence of F^-, CN^- and OH^-, as a consequence of excimer changes.[29] Absorbance of AnSQ shows two major peaks at λ_{abs} = 370 and 390 nm, and after addition of F^- and CN^- the peak at λ_{abs} = 370 nm alone

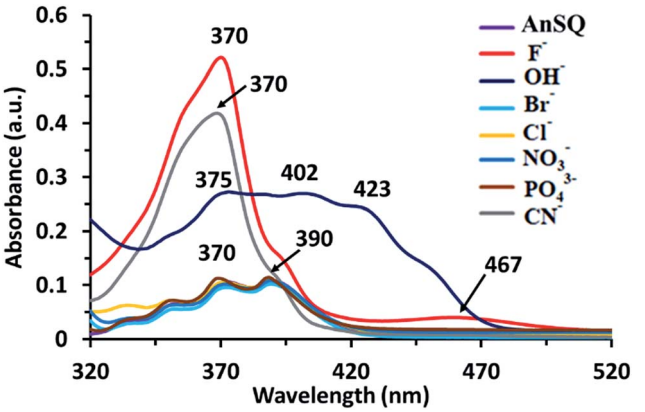

Fig. 8 UV absorptions of AnSQ (6 μM) in THF before and after anion addition at 18 hours (100 equiv.).

predominates, while λ_{abs} = 375, 402 and 423 nm are prevalent on OH^- addition. The flexibility of SQ allows for distortion to occur on anion association, giving rise to various types of anthracene excimers as reflected by the number and position of absorption bands. These absorptions can provide insights into anion discrimination by host systems.[25,29] Interestingly, absorbance bands in the visible region for OH^- show a red shift to λ_{abs} = 402 and 423 nm, while F^- addition also results in visible light absorbance at 467 nm. This suggests that F^-, CN^- and OH^- led to reorganize of SQ framework forming charge transfer complexes; such complexes have been documented for anthracene itself in mid-polarity solvents.[38] SQs appended with aromatic motifs are able to form charge transfer complexes, both ligand to ligand and ligand to cage types.[39,40] This is evident by the naked eye detection of F^- and OH^- by AnSQ in THF, as indicated by changes in absorption in the visible region.[21] While charge transfer complex formation in SQs can

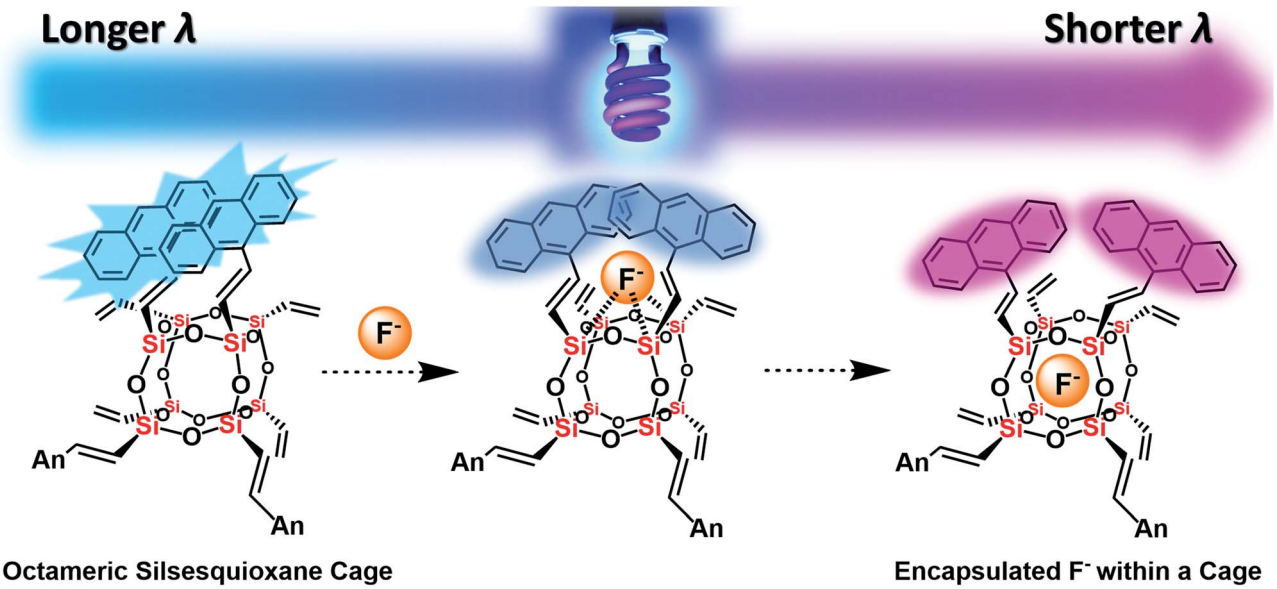

Fig. 7 The plausible mechanism of fluoride capture by AnSQ involving facial interaction followed by encapsulation and its fluorescent characters.

occur in the absence of anions, only F^-, OH^-, and CN^- were found to induce charge transfer complex formation in AnSQ, as evident by their purple, pink, and yellow solution colors (Fig. 9). The results from UV-vis titration of AnSQ with F^-, OH^- and CN^- showed limits of detection being 0.452, 1.01 and 1.56 ppm respectively (Fig. S8†).

Computational studies

As a starting point the pristine molecular T_8 structure with hydrogen atoms as R groups was created using ArgusLab chemistry software, for use in Gaussian 03. Geometry optimizations of pristine T_8 were done using Gaussian 03 incorporating density functional theory (DFT) including B3LYP with the LanL2MB basis set. After optimization, the cubic T_8H_8 structure was obtained, and the H atoms replaced with 9-vinyl anthracenes, creating the T_8R_8 framework. Electrostatic potential surface calculations were done utilizing density functional theory (DFT) including B3LYP with the LanL2MB basis set (Fig. S5†). Structural and energy optimizations of SQs were achieved by MM2 minimization with free bond rotation and ion mobility, while minimizing steric hindrance. Eight 9-vinyl anthracenes peripheral SQ (T_8R_8) was used as a representative to be the ideal molecule for studying the excimer behaviour.

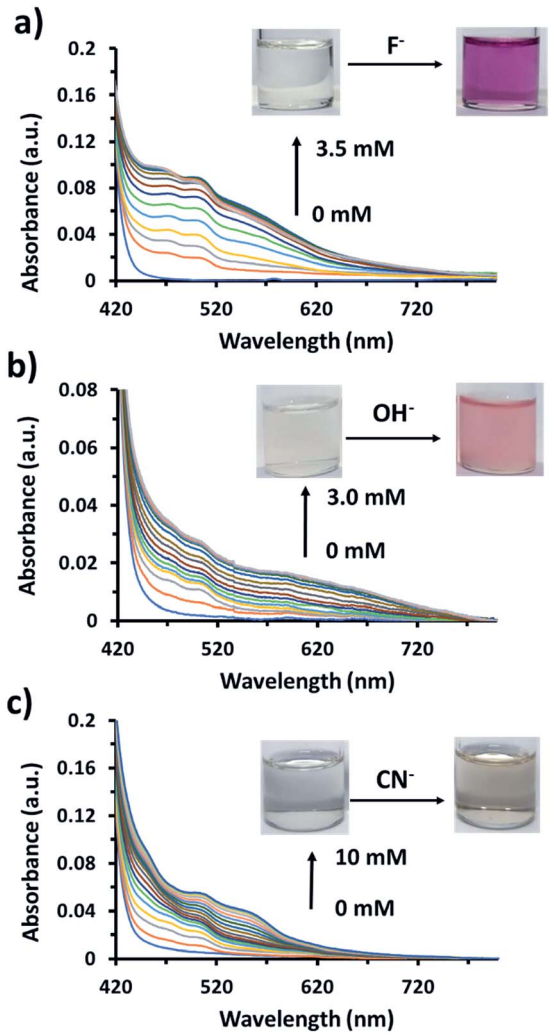

Fig. 9 UV-visible titration of 60 μM of AnSQ in THF upon addition of (a) fluoride, (b) hydroxide, and (c) cyanide ions within 2 min of addition for each point.

Electrostatic potential calculations indicate that the surface of T_8R_8 has a positive contour, providing the opportunity for anions to approach the cage.[19] The anthracene excimer formations in T_8R_8, as studied by MM2 minimization with no constraints on ion movement or bond rotation but including minimization of steric hindrance, were performed by placement of anions (F^-, Cl^-, Br^-, OH^-, CN^-, PO_4^{3-}, NO_3^-) either on the cage surface or in the interior. As shown in Fig. 10 the T_8R_8 cage responded well in the case of encapsulated F^- or surface placed OH^- (relative total energies −59.74 and −53.31 kcalmol^{-1}, respectively). Fluoride encapsulation thus involves at least 2 steps, formation of a kinetic product from the facial anion approach, and subsequent encapsulation affording the thermodynamic product (Fig. 10).[21] The relative energies of anion-cage association events are shown in Fig. 10a and b and in surface association the results are in accordance with those of Anderson *et al.*[19] with the addition of anions resulting in cage stabilization relative to pristine T_8R_8, as reflected by the negative total energies. The AnSQ minimalization studies suggest that cage distortion occurs as a consequence of two interactions: attraction between the positive surface and anionic guest, and repulsion between anions and T_8 oxygen lone pairs. These forces thus influence anthracene excimer formation as a result of cage distortion and excimer rearrangement (Fig. 10). As suggested by Narikiyo *et al.*, the emission of fluorophores on SQs could be controlled by solvent polarity,[34b] but for more rigid SQ systems such as AnSQ emission changes also result from anion association. Anion association by AnSQ promotes molecular emission at the expense of excimer emission.

Valiev *et al.* had done the calculation on anthracene excimers. Briefly, the formation of anthracene excimers is classified into 5 types: slipped-parallel (off-set), graphite-like, T-species, X-species and end-overlapped.[26,37b] By the minimalization with no solvation, the results show that, even with no solvent effect, the addition of anions to the T_8 cage can change from graphite-like to slipped-parallel or end-overlapped, which can explain the increase of fluorescence after anion addition in most cases of AnSQ. In practice when the solvent effects are also involved, the conformation of anthracene formation could be simply detected by the UV spectroscopy technique. The UV-vis absorption measurement of AnSQ is in agreement with those calculations. In THF, the addition of F^- and CN^- changed the UV-vis absorption from multiple peaks into one dominant peak at λ_{max} = 370 nm (Fig. 8), which relates to the change from slipped-parallel into graphite-like formation which has more π–π stacking, providing quenching emission. In higher polar solvents such as DMF, the UV-vis absorption of AnSQ has also increased upon anion addition indicating the formation of charge transfer complexes among anthracene units on AnSQ, in other words it changes from off-set into end-overlapped or non-excimer (Fig.S8a†).

It is worth mentioning that the LUMO state of conjugated T_8 cages with fluorophores is highly electron deficient.[41–43] The

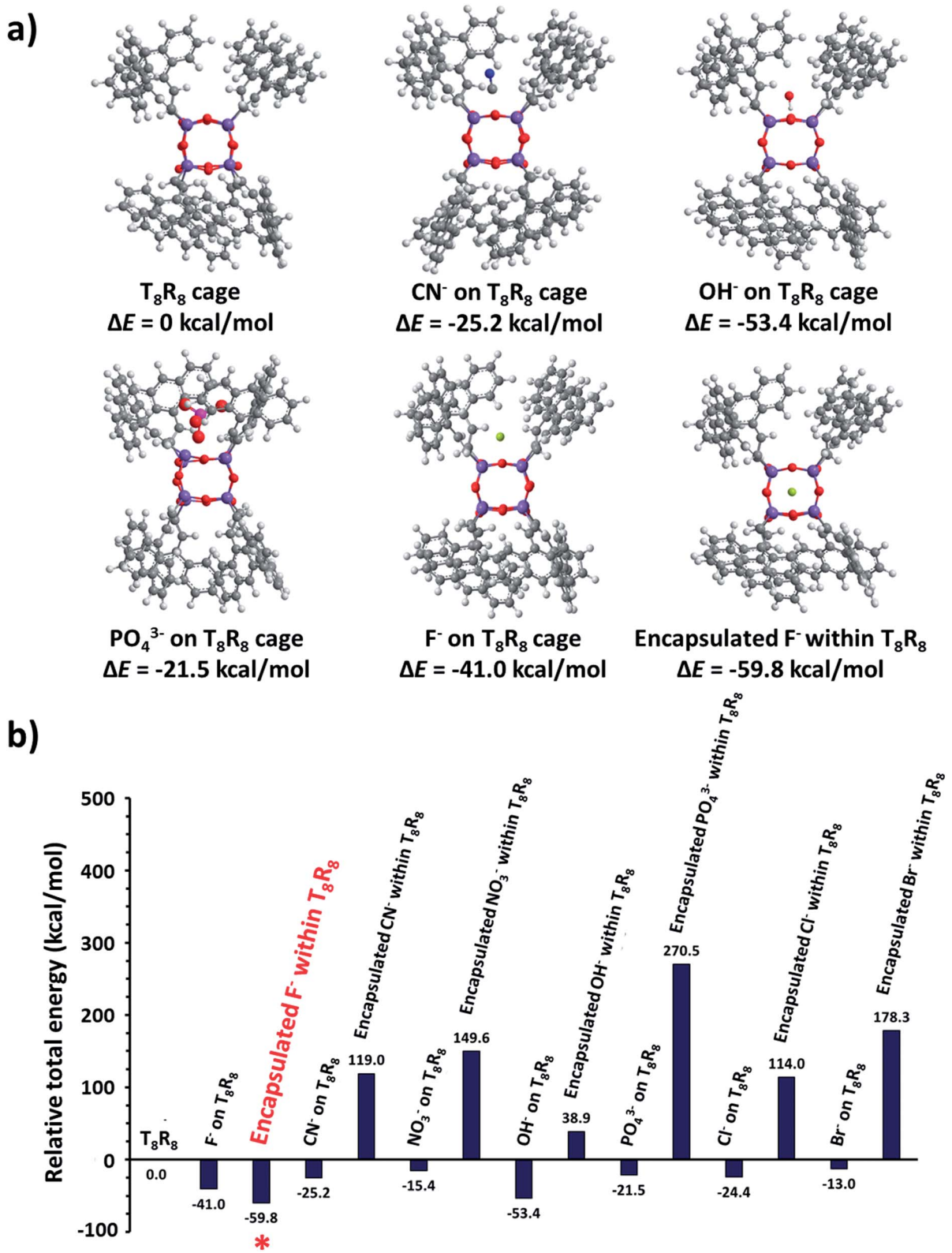

Fig. 10 (a) Potential host–guest anion complex formation by T_8R_8 as determined by computational molecular modelling and (b) the relative total energy (ΔE) of complexes in comparison with that of T_8R_8.

calculated LUMO of T_8R_8 and T_8H_8 also pointed out of a cage (Fig. 11), which is the reason that it is possible to hypothesize about interactions between anions and SQ cages. As suggested by the results in this work, anions such as F^-, OH^-, CN^- and PO_4^{3-} would interact through the surface of the SQ cage, but only fluoride could be thermodynamically trapped inside the T_8R_8 cage.

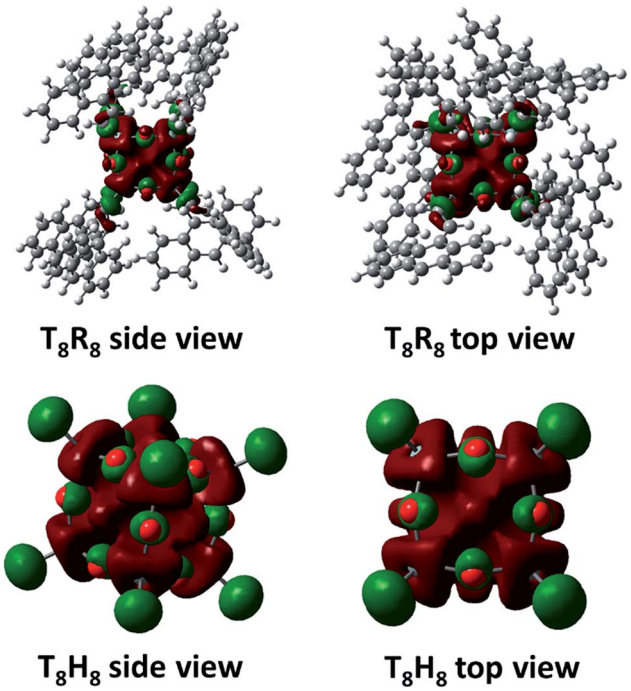

Fig. 11 LUMO of T_8R_8 and T_8H_8 from DFT calculation.

Conclusions

Anthracene-conjugated octameric silsesquioxane (AnSQ) cages were successfully prepared through Heck coupling reactions. These materials strongly exhibited the large Stokes shift of fluorescence emission behavior, suggesting the presence of intramolecular excimer formation. The emission intensity of AnSQ and the quantum yield show inverse relationships to solvent polarity. Kinetic studies of AnSQ fluorescence response on exposure to anions (F^-, CN^-, OH^-, and PO_4^{3-}) indicate that association is more rapid in polar solvents such as DMSO, DMF and acetone than in less polar solvents. Other halide and nitrate ions, however, show no significant response in any of the solvents. Both F^- and CN^- addition results in fluorescence quenching in THF, although the presence of fluoride enhances fluorescence in all other solvents. Phosphate enhances fluorescence only in highly polar solvents such as DMSO, DMF, and acetone, whilst OH^- response is only enhanced in low polarity solvents (*e.g.* DCM and toluene). Emission spectral changes depend on anion association and solvent polarity, which cause shifting between monomer and excimer emission modes. Such pathways of anionic identification are rationalized by a dendrogram, formulated by principal component analysis using fluorescence intensities, anions, and solvents, as variants. Changes in the excimer type on anion addition indicated that only F^-, OH^-, and CN^- association with AnSQ facilitated naked eye detection in THF (λ_{abs}= 498, 471 and 500 nm), respectively. These results confirmed the formation of charge transfer complexes among anthracene units in AnSQ. Electrostatic potential surface mapping of AnSQ provided a rationale for anion attraction to the cage, causing the excimer distortion with minimization affording relative total energies of anion–host combinations. Of these, only encapsulation of F^- was deemed feasible on energy grounds, with other anions exhibiting cage surface interactions.

This study confirmed the feasibility of functionalization of SQ with four anions in fluorescence mode and three anionic species by the naked eye. Using the SQ core as a molecular sensor thus opens up many possibilities for the development of modern functional anion recognition systems. Furthermore, the behavior of AnSQ toward fluoride in THF, with lowering of fluorescence intensity but production of intense purple color confirmed the formation of SQ charge transfer complexes. Further studies on these complexes are currently underway.

Conflicts of interest

There are no conflicts of interest to declare.

Acknowledgements

This research project was supported by the Thailand Research Fund (RSA5980018 and DPG6080001), the Center of Excellence for Innovation in Chemistry (PERCH-CIC), the Office of the Higher Education Commission (OHEC), Ministry of Education and CIF Grant, Faculty of Science, Mahidol University. We would like to give a big thank to Assoc. Prof. Dr Christopher Smith for academic suggestion and language correction.

Notes and references

1 (*a*) S. Ghose, T. M. McNerney and B. Hubbard, *Biotechnol. Bioeng.*, 2004, **87**, 413–423; (*b*) A. V. Kislev, Y. S. Nikitin, R. S. Petrova, K. D. Shcherbakova and Y. I. Yashin, *Anal. Chem.*, 1964, **36**, 1526–1533; (*c*) I. P. Ting and W. M. Dugger, *Anal. Biochem.*, 1965, **12**, 571–578.
2 (*a*) H. T. Fan, X. Fan, J. Li, M. Guo, D. Zhang, F. Yan and T. Sun, *Ind. Eng. Chem. Res.*, 2012, **51**, 5216–5223; (*b*) Q. Hua, W. Lu, S. Zheng, Y. Zhang, W. Zhang, D. Wu and Y. Shen, *Thermochim. Acta*, 2017, **656**, 53–58.
3 M. J. Al-Marri, M. M. Khader, M. Tawfik, G. Qi and E. P. Giannelis, *Langmuir*, 2015, **31**, 3569–3576.
4 W. Jung, J. Park, W. Won and K. S. Lee, *Energy*, 2018, **150**, 950–964.
5 J. Fujiki, K. Yogo and E. Furuya, *Fuel*, 2018, **215**, 463–467.
6 N. K. Sandhu, D. Pudasainee, P. Sarkar and R. Gupta, *Ind. Eng. Chem. Res.*, 2016, **55**, 2210–2220.
7 (*a*) T. M. Budnyak, A. Gładysz-Płaska, A. V. Strizhak, D. Sternik, I. V. Komarov, M. Majdan and V. A. Tertykh, *ACS Appl. Mater. Interfaces*, 2018, **10**, 6681–6693; (*b*) P. N. E. Diaboya and E. D. Dikio, *Microporous Mesoporous Mater.*, 2018, **266**, 252–267; (*c*) T. L. R. Mota, A. P. Marques de Oliveira, E. H. M. Nunes and M. Houmard, *Microporous Mesoporous Mater.*, 2017, **253**, 177–182.
8 J. T. Andersson, *Anal. Chem.*, 1987, **59**(17), 2207–2209.
9 (*a*) N. Oguri, Y. Egawa, N. Takeda and M. Unno, *Angew. Chem., Int. Ed.*, 2016, **55**, 9336–9339; (*b*) R. Kunthom, T. Jarentomeechai and V. Ervithayasuporn, *Polymer*, 2017, **86**, 113–119; (*c*) S. Chimjarn, R. Kunthom, P. Chancharone,

R. Sodkhomkhum, P. Sangtrirutnugul and V. Ervithayasuporn, *Dalton Trans.*, 2015, **44**, 916–919; (*d*) V. Ervithayasuporn and S. Chimjarn, *Inorg. Chem.*, 2013, **52**, 13108–13112; (*e*) T. Jaroentomeechai, P. Yingsukkamol, C. Phurat, E. Somsook, T. Osotchan and V. Ervithayasuporn, *Inorg. Chem.*, 2012, **51**, 12266–12272.

10 (*a*) M. Janeta, Ł. John, J. Ejfler, T. Lis and S. Szafert, *Dalton Trans.*, 2016, **45**, 12312; (*b*) S. Hanprasit, N. Tungkijanansin, A. Prompawilai, S. Eangpayung and V. Ervithayasuporn, *Dalton Trans.*, 2016, **45**, 16117–16120; (*c*) V. Ervithayasuporn, R. Sodkhomkhum, T. Teerawatananond, C. Phurat, P. Phinyocheep, E. Somsook and T. Osotchan, *Eur. J. Inorg. Chem.*, 2013, 3292–3296; (*d*) V. Ervithayasuporn, T. Tomeechai, N. Takeda, M. Unno, A. Chaiyanurakkul, R. Hamkool and T. Osotchan, *Organometallics*, 2011, **30**, 4475–4478; (*e*) V. Ervithayasuporn, X. Wang and Y. Kawakami, *Chem. Commun.*, 2009, 5130–5132.

11 J. C. Furgal, J. H. Jung, T. Goodson and R. M. Laine, *J. Am. Chem. Soc.*, 2013, **135**, 12259–12269.

12 (*a*) A. Noureddine and C. J. Brinker, *Chem. Eng. J.*, 2018, **340**, 125–147; (*b*) N. Kanfar, A. Mehdi, P. Dumy, S. Ulrich and J.-Y. Winum, *Chem.–Eur. J.*, 2017, **23**, 17867; (*c*) M. E. Pérez-Ojeda, B. T. Á. Rol, M. D. Chiara, I. García-Moreno and J. L. Chiara, *Chem.–Eur. J.*, 2013, **19**, 6630–6640.

13 (*a*) X. H. Yang, T. Giovenzana, B. Feild, G. E. Jabbour and A. Sellinger, *Mater. Chem.*, 2012, **22**, 12689; (*b*) V. Ervithayasuporn, J. Abe, X. Wang, T. Matsushima, H. Murata and Y. Kawakami, *Tetrahedron*, 2010, **66**, 9348–9355.

14 (*a*) R. Sodkhomkhum and V. Ervithayasuporn, *Polymer*, 2016, **86**, 113–119; (*b*) Y. Kaneko, H. Imamura, T. Sugioka and Y. Sumida, *Polymer*, 2016, **92**, 250–255; (*c*) Z. Wang, Y. Li, X.-H. Dong, K. Guo, H. Su, K. Yue, X. Yu, C. Wesdemiotis, S. Z. D. Cheng and W. B. Zhang, *Chem. Sci.*, 2013, **4**, 1345–1352.

15 D. Wang, W. Yang, S. Feng and H. Liu, *RSC Adv.*, 2016, **6**, 13749–13756.

16 D. Wang, L. Li, W. Yang, Y. Zuo, S. Feng and H. Liu, *RSC Adv.*, 2014, **4**, 59877–59884.

17 (*a*) P. Sangtrirutnugul, T. Chaiprasert, W. Hunsiri, T. Jitjaroendee, P. Songkhum, K. Laohhasurayotin, T. Osotchan and V. Ervithayasuporn, *ACS Appl. Mater. Interfaces*, 2017, **9**, 12812–12822; (*b*) V. Somjit, M. W. C. Man, A. Ouali, P. Sangtrirutnugul and V. Ervithayasuporn, *ChemistrySelect*, 2018, **3**, 753–759; (*c*) S. Mohapatra, T. Chaiprasert, R. Sodkhomkhum, R. Kunthom, S. Hanprasit, P. Sangtrirutnugul and V. Ervithayasuporn, *ChemistrySelect*, 2016, **1**, 5353–5357; (*d*) V. Ervithayasuporn, K. Kwanplod, J. Boonmak, S. Youngme and P. Sangtrirutnugul, *J. Catal.*, 2015, **332**, 62–69; (*e*) T. Luanphaisarnnont, S. Hanprasit, V. Somjit and V. Ervithayasuporn, *Catal.Lett.*, 2018, **148**, 779.

18 A. R. Bassindale, M. Pourny, P. G. Taylor, M. B. Hursthouse and M. E. Light, *Angew. Chem., Int. Ed.*, 2003, **42**, 3488–3490.

19 S. E. Anderson, D. J. Bodzin, T. S. Haddad, J. A. Boatz, J. M. Mabry, C. Mitchell and M. T. Bowers, *Chem. Mater.*, 2008, **20**, 4299–4309.

20 Y. El Aziz, A. R. Bassindale, P. G. Taylor, P. N. Horton, R. A. Stephenson and M. B. Hursthouse, *Organometallics*, 2012, **31**, 6032–6040.

21 S. Chanmungkalakul, V. Ervithayasuporn, S. Hanprasit, M. Masik, N. Prigyai and S. Kiatkamjornwong, *Chem. Commun.*, 2017, **53**, 12108–12111.

22 (*a*) R. Sodkhomkhum, M. Masik, S. Watchasit, C. Suksai, J. Boonmak, S. Youngme, N. Wanichacheva and V. Ervithayasuporn, *Sens. Actuators, B*, 2017, **245**, 665–673; (*b*) B. W. Tresca, O. B. Berryman, L. N. Zakharov, D. W. Johnson and M. M. Haley, *Supramol. Chem.*, 2016, **28**, 37–44.

23 A. Raja Sekhar, M. A. Kaloo and J. Sankar, *Org. Biomol. Chem.*, 2015, **13**, 10155–10161.

24 J. D. Larkin, K. A. Frimat, T. M. Fyles, S. E. Flower and T. D. James, *New J. Chem.*, 2010, **34**, 2922.

25 H. Liu, L. Yao, B. Li, X. Chen, Y. Gao, S. Zhang, W. Li, P. Lu, B. Yang and Y. Ma, *Chem. Commun.*, 2016, **52**, 7356–7359.

26 C. Zhao, X. Cai, Z. Ma, J. Shi, L. Xu and H. Wang, *J. Photochem. Photobiol., A*, 2018, **355**, 318–325.

27 (*a*) P. K. Lekha and E. Prasad, *Chem.–Eur. J.*, 2010, **16**, 3699–3706; (*b*) J. C. Furgal, T. Goodson and R. M. Laine, *Dalton Trans.*, 2016, **45**, 1025–1039.

28 (*a*) D. W. Cho, M. Fujitsuka, K. H. Choi, M. J. Park, U. C. Yoon and T. Majima, *J. Phys. Chem. B*, 2006, **110**, 4576–4582; (*b*) E. V. Bichenkova, A. R. Sardarian, A. N. Wilton, P. Bonnet, R. A. Bryce and K. T. Douglas, *Org. Biomol. Chem.*, 2006, **4**, 367–378; (*c*) E. S. Park, H. W. Ro, C. V. Nguyen, R. L. Jaffe and D. Y. Yoon, *Chem. Mater.*, 2008, **20**, 1548–1554.

29 I. Penso, E. A. Cechinatto, G. Machado, C. Luvison, C. H. Wanke, O. Bianchi and M. R. F. Soares, *J. Non-Cryst. Solids*, 2015, **428**, 82–89.

30 J. W. Verhoeven, *Pure Appl. Chem.*, 1990, **62**, 1585–1596.

31 A. N. Bilyachenko, V. N. Khrustalev, Y. V. Zubavichus, A. V. Vologzhanina, G. S. Astakhov, E. I. Gutsul, E. S. Shubina and M. M. Levitsky, *Cryst. Growth Des.*, 2018, **18**, 2452–2457.

32 H. Liu, L. Yao, B. Li, X. Chen, Y. Gao, S. Zhang, W. Li, P. Lu, B. Yang and Y. Ma, *Chem. Commun.*, 2016, **52**, 7356–7359.

33 J. E. Norton and J. L. Brédas, *J. Am. Chem. Soc.*, 2008, **130**, 12377–12384.

34 (*a*) E. V. Bichenkova, A. R. Sardarian, A. N. Wilton, P. Bonnet, R. A. Bryce and K. T. Douglas, *Org. Biomol. Chem.*, 2006, **4**, 367–378; (*b*) H. Narikiyo, M. Gon, K. Tanaka and Y. Chujo, *Mater. Chem. Front.*, 2018, **2**, 1449; (*c*) W. H. Melhuish, *J. Phys. Chem.*, 1961, **65**, 229–235; (*d*) Z. Guo, S. Jin and B. Liu, *Spectrochim. Acta, Part A*, 2007, **66**, 672–675.

35 X. Zhou, J. Nie and B. Du, *ACS Appl. Mater. Interfaces*, 2017, **9**, 20913–20921.

36 S. Stewart, M. A. Ivy and E. V. Anslyn, *Chem. Soc. Rev.*, 2014, **43**, 70–84.

37 (*a*) E. D. Hughes and C. K. Ingold, *J. Chem. Soc.*, 1935, 244; (*b*) R. R. Valiev, K. B. Kopbalina, V. N. Cherepanov, N. K. Ibraev and N. A. Mazhenov, *Russ. Phys. J.*, 2014, **57**, 95–99.

38 S. Zheng, E. Geva and B. D. Dunietz, *J. Chem. Theory Comput.*, 2013, **9**, 1125–1131.
39 S. Sulaiman, A. Bhaskar, J. Zhang, R. Guda, T. Goodson and R. M. Laine, *Chem. Mater.*, 2008, **20**, 5563–5573.
40 S. Zheng, H. Phillips, E. Geva and B. D. Dunietz, *J. Am. Chem. Soc.*, 2012, **134**, 6944–6969.
41 R. M. Laine and M. F. Roll, *Macromolecules*, 2011, **44**, 1073–1109.
42 C. J. H. Schutte and J. A. Pretorius, *Proc. R. Soc. A*, 2010, **467**, 928–953.
43 T. Maegawa, Y. Irie, H. Imoto, H. Fueno, K. Tanaka and K. Naka, *Polym. Chem.*, 2015, **6**, 7500–7504.